Identification of Key Reaction Products from MoO_3 and Ethylene Glycol Mixtures Used for Attempted MoS_2 Electrodeposition and Synthesis of Bidentate Ligands and Related Group 1 and 13 Metal Complexes

By
Tanner A. George
A Thesis Submitted to
Saint Mary's University, Halifax, Nova Scotia
in Partial Fulfillment of the Requirements for
the Degree of Master of Science in Applied Science.
August, 2021, Halifax, Nova Scotia

Approved:	Dr. Jason Masuda
	Supervisor
	Department of Chemistry
Approved:	Dr. Christa Brosseau
	Supervisor
	Department of Chemistry
Approved:	Dr. Danielle Tokarz
	Supervisory Committee Member
	Department of Chemistry
Approved:	Dr. Erin Adlakha
	Supervisory Committee Member
	Department of Geology
Approved:	Dr. Francesca Kerton
	External Examiner
	Memorial University of Newfoundland
Date:	August 26th, 2021

Identification of Key Reaction Products from MoO_3 and Ethylene Glycol Mixtures Used for Attempted MoS_2 Electrodeposition and Synthesis of Bidentate Ligands and Related Group 1 and 13 Metal Complexes

By Tanner A. George

Date: August 26th, 2021

Abstract

Replication of a procedure to electrodeposit MoS_2 required use of an uncharacterized crude MoO_3 and ethylene glycol reaction mixture as a molybdenum precursor. Multiple attempts to replicate the desired "brown oil" resulted in isolating four crystals, with three being previously unknown products for this reaction. This evidence highlights possible identities for the molybdenum precursor responsible during this MoS_2 electrodeposition.

A sterically bulky phosphine-imine treated with either H_2O_2, S_8, Se^0, or reacted with 9-bromofluorene followed by one equivalent of a base made four ligand precursors that can be deprotonated to act as mono-anionic ligands for a variety of metal complexes including Li-K, Al, and In. The four ligands undergo tautomerization revealing 2-4 isomers observed by ^{1}H, ^{13}C, and ^{31}P NMR spectroscopy, with two of these supported by SC-XRD analysis. Alkali metal complexes showed diverse η^2 to η^{4+6} interactions with the delocalized phosphonium fluorenylide and η^1/η^2 with 2,6-diisopropylphenyl aromatic ring systems.

Acknowledgements

I am pretty surprised this thesis happened and that I am where I am looking back to where I used to be. In my third year I had the chance to take mostly all of the second-year chemistry courses, and I'm very grateful for the Professors, peers, and lab instructors I've met, grown with, and learned from. Jason and Christa were both extremely kind to me and others in our first upper year chemistry courses, and very quickly Inorganic and Analytical chemistry became many of our favorite courses for both incredibly cool and informative content, and the friendly, hilarious community that formed within the classes and labs. Every teacher I had within Saint Mary's University gave me unique and valuable lessons and I'm very happy to continue working alongside everyone in the coming years as I work towards my PhD doing what I do best. It isn't possible to explain the value I've gotten from the dozens of relationships, courses, and experiences I've had at this school, and I'm extremely glad I had a hunch this school is where I belong.

I likely wouldn't have entered university if it wasn't for my Father's support, starting to save very early in life to ensure I could get my first degree without any financial worries, something very few people are lucky to receive. I'm very grateful you convinced me not to take that first year off out of high school, beginning when I did allow me to experience so many amazing times with great friends and it allowed me to find my way (very slowly, but surely) into Jason's lab, a place that feels like a home away from home. I know I wouldn't *want* to do what I do now if it wasn't for my Mother. Your love and curiosity for nature was always inspirational to me growing up from the time I couldn't talk until today. You were always encouraging me to explore and question plants, animals, rocks, and space averaged out into a Son fascinated by nature and excited to explore it with instruments, methods, and fundamentals I could have only dreamt of as a kid. Whether it

was pretty chunks of quartz, letting me pick carrots months early to check if they were done, the cubic zirconium crystal I accidentally fed the dog, or gross bugs I wanted nothing to do with, you made sure to show me everything you possibly could about this world and the curiosity you instilled is something I identify with as a core part of who I will always be.

Thank you for being an incredible big sister Ashley. You were my first idol in many ways because you took the time to teach me how to begin existing before I could talk. I know I wasn't grateful when I was young for all your love and support, but I couldn't be more grateful than I am now. Thank you so much for being hilarious, kind, sweet, and wise from being the first kid making all the mistakes first so I could learn what not to do.

Thank you, Lilia, for absolutely everything you've helped me with including growing as a person, taking care of everything I've been too busy to handle, and for your constant love, support, and emotional wisdom. I love you very much.

If I listed all the friends that helped me get to, and complete this journey, I'd need at least another page or two. Thank you, Jenn(s), Bailey, Jacob, Ryan, Robert, Ernlie, Krish, Carter, Maddy, Kaleigh, Jake, Megan, and every other great friend and mentor that helped me learn and laugh through the good and bad. Thank you, Marc, Robin, Haydn, Ryan, Jess, Tabatha, Kerri, David, Griffin, and Bradley for being the best friends I could ask for. I'm looking forward to growing old and continuing to hang out with you all in the future!

Thank you, Christa, Jason(s), Mitch, Erin, Danielle, Rob, Marc, Mary, Kai, Kathy, Cory, Luke, Ivan, Laurel, Clarissa, Richard, Alyssa, Elizabeth, Patricia, and Xiang, for making Saint Mary's University an incredible place for science and thank you all for helping me learn about nature and the many incredible methods available to study this beautiful world I'm happy to have met you all in!

Table of Contents

Table of Abbreviations

°	Degrees
°C	degrees Celsius
µA	Microampere
µL	Microliter
μ_n	bridging ligand (n = # metal atoms bridged, often 2 or just "µ")
2D-MoS_2	two-dimensional molybdenum disulfide, the material is in fact 3D; however, the single sheet (S-Mo-S 3 atom layer) is what is deemed a "2D" material
A	Ampere
BPA	bisphenol-A
Bu	Butyl
C	coulomb (A/s)
Calc.	Calculations
CE	counter electrode
Cp	cyclopentadien-yl or -ide
Cp*	pentamethylcyclopentadien-yl or -ide
Cp*H	Pentamethylcyclopentadiene
CpH	Cyclopentadiene
CVD	chemical vapor deposition
d	Doublet
DCM	dichloromethane, CH_2Cl_2
Dipp	2,6-Diisopropylphenyl
EA	Elemental Analysis (carbon, hydrogen, and nitrogen in this work)
eq	equivalents - often referring to reagents, impurities, or atoms
Et	Ethyl
Et_2O	diethyl Ether, $(C_2H_5)_2O$
Fc	$Fe(\eta^5\text{-}Cp)_2$ ferrocene
Flu	The $C_{13}H_8R$ anion fluoren-yl,-ide with various 9-substitutions. If R is phosphorus this also refers to the fluorenylide (P=Flu)
FluH	The $C_{13}H_9R$ fragment of neutral fluorene
g	Gram
HER	hydrogen evolution reaction
hr	Hour
I	current (Ampere, commonly units like A, µA) A = C/s
iPr	Isopropyl
j	current density (Ampere/surface area^2, A/m^{2,} µA/cm^2, etc.)
J	coupling constant
kg	Kilogram
L	liter
mA	milliampere
mg	milligram

mL	milliliter
mV	millivolts
nA	nanoampere
NMR	Nuclear Magnetic Resonance
PAH	polyaromatic hydrocarbon
Ph	Phenyl, C_6H_5R group where R = P, C, N, O, etc.
PLA	polylactic acid
PP13-TFSI	N-methyl-N-propyl piperidinium (= PP13) bis(trifluoromethane)sulfonimide (= TFSI)
PTFE	polytetrafluoroethylene
s	singlet
sat.	saturated
SC-XRD	single crystal X-ray diffraction
SERS	surface enhanced Raman spectroscopy
SPE	screen printed electrode
STP	standard temperature and pressure
RE	reference electrode
temp	temperature
THF	tetrahydrofuran
UV-Vis	ultraviolet-visible (commonly referring to spectroscopy)
V	voltage, volts
WE	working electrode
α	alpha, typically "Kα", referring to a type of X-ray radiation or the α-position (adjacent) by a given group and an angle value.
β	beta, the β-position (two away) relative to a given functional group and also a crystallographic angle value.
γ	gamma, the γ-position (three away) relative to a given functional group and also a crystallographic angle value.
δ	ppm, parts per million
Δ	mostly heat, rarely change
ε	molar attenuation coefficient (UV-Vis)
η	hapticity of metal-conjugated system interactions
θ	theta, used to define an angle of some degrees (°) within crystallography; one major axis of rotation
Φ	theta, used to define an angle of some degrees (°) within crystallography; one major axis of rotation
κ	kappa, coordination number for multidentate ligands
λ	lambda, wavelength of light
π	pi, referring to bonds between two atoms and their "π" electron orbitals
σ	sigma, typically referring to bonding interaction
Ω	omega, used to denote Ohms for resistance

List of Figures

List of Schemes

List of Tables

1. Chapter 1: Introduction

Many important applications rely on a foundation of synthetic chemistry, and exploratory work is necessary to understand how materials will behave and more importantly how they can begin to be used. In this work, three projects were undertaken that relied heavily on producing materials via synthetic methods. These methods included published procedures as in the case of Chapter 3, while Chapters 4 and 5 contain newly discovered procedures. These three projects aimed to produce materials for different applications (3/4/5 = molecular detection/precursors/catalysis); however, the central unifying factor is exploratory synthetic chemistry.

The scope of this project is primarily focused with the production and characterization of new materials which can be explored more in future work as precursors for MoS_2 electrodeposition (chapter 3), ligand transfer precursors (chapter 4), and complexes that are ready to be tested for use as co-polymerization and ring-opening polymerization catalysts (chapter 5). The direction of the project in chapter 3 came from the unexpected difficulty in reproduction of a key molybdenum precursor during the process of attempting to reproduce MoS_2 via an electrodeposition described by Murugesan et al. This precursor is not detailed to any great extent and irreversibly will decompose upon hydrolysis. The identity remains unknown; however, some evidence regarding the identity has been uncovered. The other projects have less direct problems, with end goals addressing the ever-present problem of producing value-added products from renewable sources. These final projects also seek to explore unique bonding motifs not previously explored to any

great extent for different organometallic systems, which indirectly could result in unseen value if the ligands prove to be effective.

This thesis is composed of 6 chapters. The first two chapters overview and each project, the problems each seeks to address, and tools used to explore the chemical systems studied. Chapter 2 introduces literature, history, and specific reasons for choosing to each research project. Following the bulk of experimental work in chapters 3-5, chapter 6 ends the thesis with a mix of speculation and possible future direction for continued study for each of these chemical systems.

Chapter 3, entitled *"X-Ray Structural Evidence for Monomeric, Dimeric, Polymeric and Octameric Clusters Derived from the Reaction of Molybdenum Trioxide with Ethylene Glycol"*, is about research, which took an unexpected turn upon realization that a literature procedure did not work as effectively as was reported. Various gaps in necessary information needed to properly repeat the procedure led to a variety of discoveries, which themselves are worthy of report. The literature procedure, in short, claimed to provide a method of electrochemically depositing non-amorphous molybdenum disulfide thin films on glassy carbon using a solution containing an ionic liquid, a dithiol, and a poorly characterized molybdenum precursor. The attempt to replicate this work resulted in various discoveries which offer insight into where future research should focus to achieve a reliable, consistent, well understood electrodeposition of crystalline, thickness-controlled molybdenum disulfide for *many* important applications.

Chapter 4, entitled *"Alkali Metal Amide Salts of a Bulky Nitrogen Tethered Phosphonium Fluorenylide Ligand"*, focuses on the synthetic preparation of a new

structure of bidentate ligand based around the very useful donor properties of a neutral phosphonium-fluorenide. Deprotonation of the ligand affords a monoanionic amide ligand which bonds to a metal, allowing the electron delocalized fluorenide donor to shield the metal center with anywhere between 0- to 6-electron donation. Low energy transformations between each degree of donation via haptotropic π-bonding of the metal cation with the conjugated electron rich ring system of the fluorenide donor may improve stability. The resultant ligand produced alkali metal complexes that are prime precursors for producing organometallic complexes via metathesis reactions.

Chapter 5, entitled *"Dimethyl Aluminum and Indium Complexes of Oxygen, Sulfur, and Selenium Substituted Phosphine-Imine Ligands"*, is similar to chapter 4, though rather than studying the phosphonium-fluorenide ligand and alkali metals mentioned previously, this project focuses instead on chalcogen (O, S, Se) substitution on phosphorus rather than fluorenide substitution and the metals studied are from group 13; aluminum and indium. The ligands containing the phosphine oxide, sulfide, and selenide donor similarly undergo deprotonation forming monoanionic amides. In this case, use of trimethyl aluminum or indium as a metal precursor results in loss of methane. This forms cyclic structures with both nitrogen and oxygen/sulfur/selenium coordinated to each metal ion, forming a tetrahedral structure with the remaining two methyl ligands bound to the metal.

Each of these projects utilize problem solving necessary from a synthetic chemistry perspective to produce and understand materials that may have potential applications such as a material to split hydrogen from water (chapter 3), precursors for forming potential organometallic catalysts (chapter 4), and preparation of biodegradable plastic production

(chapter 5). The projects within this thesis are primarily concerned with fundamental synthetic exploration of materials rather than the study of their applications. Every element can be used in a way that benefits society, and this exploration into various metal compounds has provided insight into identity, properties and problems associated with each preparation.

The structure of the chapters 3-5 follow a similar format including first a descriptive title, an abstract detailing the purpose of the study and major findings, an introduction to the related topics covered within the work to place each project within the appropriate context of related literature, and the results and discussion follow with a final conclusion and references. In each chapter results and discussion, presentation of a general overview of synthesis precedes discussion of characterization or use of the materials produced. The experimental section detailing preparation and sourcing of various solvents and reagents is followed with a breakdown of different equipment and instruments used to prepare and analyze the material produced in the chapter. In each case, the final subsection of the experimental is a detailed synthesis of each material along with characteristic Nuclear Magnetic Resonance (NMR) spectroscopy, Single Crystal X-ray Diffraction (SC-XRD) spectroscopy, Elemental Analysis (EA), or other relevant properties. Following this is the final conclusions and general summary of the projects with references last. For each major chapter (3-5) Supplementary Information (SI) is available within an appendix document that will be frequently addressed throughout the projects. In general, some images, spectra (mainly NMR and IR), crystallography, and information relating to modified syntheses and more is available within this additional document.

2. Chapter 2: Background and Theory

Section 2.1 - Molybdenum Disulfide: Properties, Applications and Production

2.1.1 Properties of MoS_2

Molybdenum sulfides (crystalline MoS_x, x = 2, 3, amorphous MoS_x, $2 < x < 3$) have been widely studied due to vast interest across many industries (health, energy, technology)[1] owing to the ability of these materials to undergo useful light-matter interactions. Molybdenum disulfide (MoS_2) receives a lot of focus in the energy and technology sectors due to its various useful polymorphs (Tetragonal (D_{3d}) = 1T, Hexagonal (D_{3h}) = 2H, Rhombohedral (C^5_{3v}) = 3R)[2] with conducting (1T) and semiconducting (2H, 3R) properties. Molybdenum disulfides form 3-atom thick sheets with a S-Mo-S sandwich structure resulting in basal planes of sulfur and edge sites of both sulfur and molybdenum.

Different polymorphs possess different chemical and optical interactions, and structural morphology also plays a significant role in the observed properties of MoS_2. For example, semiconducting materials such as 2H- and 3R-MoS_2 possess a small bandgap, and the energy required to promote electrons from valence to conduction bands within a solid crystalline material allows for effective charge transfer properties. For 1T-MoS_2, there exists overlap of valence and conduction band energies resulting in conductivity. A single monolayer 2D-2H-MoS_2 possesses a direct bandgap of ~1.9 V, while few layered MoS_2 has an indirect bandgap of ~1.3 V.[1] The direct bandgap means that 2D-2H-MoS_2 requires only photon excitation for promote electrons from the valence to conduction bands, allowing current to flow. In contrast, the indirect bandgap, in addition to photon excitation, also requires an excitation propagating through the crystalline lattice to promote the valence

electrons to the conduction band. Sheets of 2D-MoS_2 have properties that make it uniquely desirable, and likewise, each polymorph of MoS_2 offers potential benefit for different applications.

2.1.2 Applications of MoS_2

Each polymorph of MoS_2 possesses several interactions with both light and matter that allow for many different uses when alone, or combined with other materials such as ZnO,[3,4] Fe_3O_4,[5] FeS_2,[6,7] graphene,[8] copper foil,[9] or gold nanoparticles[10] (Table 2.1). Some of these applications include energy generation and storage (hydrogen evolution reaction (HER), battery storage, solar photocatalysis),[1] environmental remediation,[5] supercapacitors,[6] and more recently, as a substrate for the enhancement of inelastically scattered light (Figure 2.1) used for the detection of trace molecules via Surface Enhanced Raman Spectroscopy (SERS).[11]

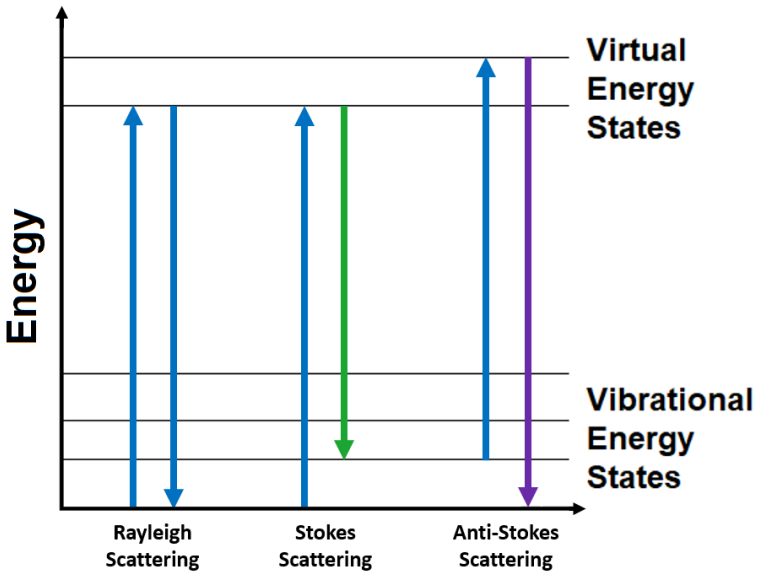

Figure 2.1 Jablonski diagram illustrating the absorption and re-emission of a photon by matter. The more common elastic Rayleigh scattering upon irradiation results in emission of a photon of the same energy as the incident wavelength.

Many studies have examined polymorphs of MoS_2 with differing morphologies and substrates or co-catalysts for the evolution of hydrogen gas from dilute acid.[9,12,13] Use of conductive 1T-MoS_2 and mixed materials incorporating MoS_2 for harnessing solar energy to split water into H_2 and O_2 is also possible due to properties such as high durability and the ability of 1T-MoS_2 to act as an effective charge transfer catalyst transferring solar energy into splitting water, forming hydrogen gas.[1] Platinum is often employed for hydrogen evolution from splitting water because of how efficient platinum is at transferring electrons necessary for protons to adsorb on the metal surface. This is followed by either combination of two adsorbed hydrogen atoms, or combination of an adsorbed hydrogen atom with an electron and proton from acidic solutions forming the hydrogen gas. Completing this splitting process rapidly with low energy inputs is necessary, but sustainability issues with platinum create the need to find alternate materials that can perform these crucial sustainable energy processes as well or better than platinum. Crystalline MoS_2 on its own or with additional materials have been found to be competitive.[14]

Table 2.1 Preparation and application of various polymorphs and mixed materials containing MoS_2.

Material	Synthesis	Application	Ref.
1T	NaK exfoliation followed by H_2O or [*p*-$RC_6H_4N_2^+$][BF_4^-] capping agents.	SERS	[15]
2H-MoS_2/ZnO	Na_2MoO_4•$2H_2O$ + thiourea in H_2O + citric acid monohydrate	SERS	[3]
MoS_2/ZnO	autoclave reduction of $(NH_4)_6Mo_7O_{24}$ and sulfur powder with hydrazine hydrate to prepare MoS_2, second step uses $Zn(O_2CCH_3)_2(H_2O)_2$ and hydrazine hydrate stirring with the suspended MoS_2, finally annealing for 2 hr at 500 °C	Photocatalytic pollutant degradation	[4]
1T/2H-Au	Sonicate EtOH suspension of 2H MoS_2, centrifuge, then add supernatant to SC-CO_2 = 1T/2H MoS_2. Combine and heat with $HAuCl_4$ + 1-amino-9-octadecene in EtOH/hexane, centrifuge, wash, and dry.	HER/SERS	[10]
1T	Top-down (Alkali metal intercalation) and bottom up (hydrothermal, CVD, electrodeposition)	HER, batteries, supercapacitors, photocatalysis	[1]
MoS_2/Fe_3O_4	Autoclave $FeCl_3$•$6H_2O$ with $Na(O_2CCH_3)$ with polyvinylpyrrolidone, then mixed prepared Fe_3O_4 solid with $(NH_4)_6Mo_7O_{24}$•$4H_2O$ and thiourea in water and autoclave again.	Water treatment: heavy metal decontamination (Pb/Hg)	[5]
MoS_2/FeS_2	Anodic oxidation of Mo foil to MoO_x in NaF/$H_2C_2O_4$/Na_2SO_4 in water. Autoclave foil with KSCN to afford MoS_2. Mixing ferric chloride and sodium dodecyl sulfate with thiourea in water and autoclaving with the Mo-MoS_2 foil immersed. Mo-FeS_2 control without oxidation and sulfurization of Mo foil	Supercapacitor	[6]
MoS_2/FeS_2	Chemical vapor deposition	HER	[7]
3R	Heat MoO_3 + S_8 + K_2CO_3 flux to 550 °C	HER	[2]
3R-Cu	Direct sputter deposition at 300 °C using radio frequency magnetron sputtering	HER	[9]

2.1.3 Production of MoS_2

Considering MoS_2 can be usefully utilized in many applications, the ability to selectively manufacture specific polymorphs and desired morphologies of MoS_2 reliably

through facile- and scalable methods is desirable in comparison to expensive or scale-limited methods of preparation. Some synthetic methods for preparing MoS_2 include molten S_8, MoO_3 and K_2CO_3 flux (3R),[16] alkali metal intercalation using pyrophoric reagents like NaK alloy (1T),[15] chemical vapor deposition (CVD) in a horizontal tube furnace,[7] hydrothermal growth within an autoclave,[3,5,6,10] or mechanical exfoliation and electro-ablation coupled with electron-beam lithography.[17] These methods rely on either dangerous reagents or expensive equipment and instruments with limited control over the final state of MoS_2. Optimization of these different methods has been explored in depth to produce more effective substrates or catalysts for a variety of applications, though preparation of 2D-MoS_2 still remains difficult to scale up, requiring expensive equipment to produce, orient, and isolate the single layer sheets. These methods create effective materials; however, accessibility to the required instrumentation to make the materials is limited. As a result, electrodeposition was chosen to produce MoS_2 for this thesis project due to low cost and ease of use.

2.1.4 Electrodeposition of MoS_2

Use of electrodes as substrates for deposition of MoS_2 is useful because some applications, such as splitting water, involve electrochemical processes occurring on the MoS_2 to reduce the overall energy input required. Electrodeposition of amorphous molybdenum sulfides (MoS_x $2 < x < 3$) have been reported; however, post-treatment annealing of MoS_x films in a sulfur atmosphere at high temperature is often necessary to achieve crystalline MoS_2.[13,18-22] Electrode materials are useful substrates to deposit MoS_2 because some applications like the splitting of water involve electrochemical processes

occurring at the MoS_2 edge sites for 2H-MoS_2 or basal and edge sites for 1T-MoS_2 and 3R-MoS_2 to reduce the overall energy input required via lower energy transition states. The electrochemical deposition of MoS_x tends to involve mixtures of molybdenum and sulfur precursors, electrolytes, and solvents or supporting protic sources.[21] Some precursors for the Mo and S involve the two elements in a single source such as thiomolybdates (MoS_4^{2-}) or larger Mo/S clusters. Other work has shown direct electrochemical synthesis of crystalline MoS_2 nanoflowers at 100 °C in an ionic liquid[23] using two separate sources; 1,4-butane dithiol, and a crude reaction mixture of molybdenum trioxide and ethylene glycol.[13] One source that was not referenced in this preparation, yet is crucial to understanding the molybdenum precursor is the 1973 original synthesis[24] of a dioxo molybdenum (VI) octahedral complex, formed by the same reaction used to prepare the molybdenum precursor for MoS_2 deposition with heating to 150 °C rather than 194 °C reported for the required molybdenum precursor. The octahedral molybdenum complex isolated from the similar reaction occurs with two singly deprotonated ethylene glycol ligands that, in the solid state, exist as monomers within an extensive hydrogen bonding network.[24,25]

Controlled growth via electrodeposition of MoS_2 nanocrystals with the ability to selectively form a 2D-MoS_2 monolayer would be ideal for many applications that rely on the few or monolayer MoS_2, and since this is a known growth mode for metals such as copper, MoS_2 may be deposited in similar thin sheets.[26] If this were possible under reproducible, ideal conditions, this electrochemical method would excel compared to more expensive methods that may not offer the thickness control expected with electrochemistry. Direct electrochemical synthesis of MoS_2 remains elusive, and the underlying processes of

electroreduction of the sulfur and yet-unknown molybdenum precursor into the desired crystalline MoS_2 remains unclear.

2.1.5 References

1. Jayabal, S.; Wu, J.; Chen, J.; Geng, D.; Meng, X. Metallic 1T-MoS_2 nanosheets and their composite materials: Preparation, properties and emerging applications. *Materials Today Energy* **2018**, *10*, 264-279.

2. Toh, R. J.; Sofer, Z.; Luxa, J.; Sedmidubský, D.; Pumera, M. 3R phase of MoS_2 and WS_2 outperforms the corresponding 2H phase for hydrogen evolution. *Chemical Communications* **2017**, *53*, 3054-3057.

3. Quan, Y.; Yao, J.; Yang, S.; Chen, L.; Li, J.; Liu, Y.; Lang, J.; Shen, H.; Wang, Y.; Wang, Y.; Yang, J.; Gao, M. ZnO nanoparticles on MoS_2 microflowers for ultrasensitive SERS detection of bisphenol A. *Microchim Acta* **2019**, *186*, 1-8.

4. Krishnan, U.; Kaur, M.; Kaur, G.; Singh, K.; Dogra, A. R.; Kumar, M.; Kumar, A. MoS_2/ZnO nanocomposites for efficient photocatalytic degradation of industrial pollutants. *Materials Research Bulletin* **2019**, *111*, 212-221.

5. Wang, Z.; Zhang, J.; Wen, T.; Liu, X.; Wang, Y.; Yang, H.; Sun, J.; Feng, J.; Dong, S.; Sun, J. Highly effective remediation of Pb(II) and Hg(II) contaminated wastewater and soil by flower-like magnetic MoS_2 nanohybrid. *Science of the Total Environment* **2020**, *699*, 134341.

6. Wang, Y.; Xie, Y. Electroactive FeS_2-modified MoS_2 nanosheet for high-performance supercapacitor. *Journal of Alloys and Compounds* **2020**, *824*, 153936.

7. Chen, Y.; Peng, Z.; Guo, Y.; Guan, S.; Fu, X. Novel self-supported MoS_2/FeS_2 nanocomposite as an excellent electrocatalyst for hydrogen evolution. *Solid State Sciences* **2020**, *101*, 106156.

8. Ghopry, S. A.; Alamri, M. A.; Goul, R.; Sakidja, R.; Wu, J. Z. Extraordinary Sensitivity of Surface-Enhanced Raman Spectroscopy of Molecules on MoS_2 (WS_2) Nanodomes/Graphene van der Waals Heterostructure Substrates. *Advanced Optical Materials* **2019**, *7*, 1801249.

9. Patel, M. D.; Zhang, J.; Park, J.; Choudhary, N.; Tour, J. M.; Choi, W. Directly deposited porous two-dimensional MoS_2 films as electrocatalysts for hydrogen evolution reactions. *Materials Letters* **2018**, *225*, 65-68.

10. Zheng, X.; Guo, Z.; Zhang, G.; Li, H.; Zhang, J.; Xu, Q. Building a lateral/vertical 1T-2H MoS_2/Au heterostructure for enhanced photoelectrocatalysis and surface enhanced Raman scattering. *Journal of Materials Chemistry A* **2019**, *7*, 19922-19928.

11. Langer, J.; Jimenez de Aberasturi, D.; Aizpurua, J.; Alvarez-Puebla, R. A.; Auguié, B.; Baumberg, J. J.; Bazan, G. C.; Bell, S. E. J.; Boisen, A.; Brolo, A. G.; Choo, J.; Cialla-May, D.; Deckert, V.; Fabris, L.; Faulds, K.; García de Abajo, F. Javier; Goodacre, R.; Graham, D.; Haes, A. J.; Haynes, C. L.; Huck, C.; Itoh, T.; Käll, M.; Kneipp, J.; Kotov, N. A.; Kuang, H.; Le Ru, E. C.; Lee, H. K.; Li, J.; Ling, X. Y.; Maier, S. A.; Mayerhöfer, T.; Moskovits, M.; Murakoshi, K.; Nam, J.; Nie, S.; Ozaki, Y.; Pastoriza-Santos, I.; Perez-Juste, J.; Popp, J.; Pucci, A.; Reich, S.; Ren, B.; Schatz, G. C.; Shegai,

T.; Schlücker, S.; Tay, L.; Thomas, K. G.; Tian, Z.; Van Duyne, R. P.; Vo-Dinh, T.; Wang, Y.; Willets, K. A.; Xu, C.; Xu, H.; Xu, Y.; Yamamoto, Y. S.; Zhao, B.; Liz-Marzán, L. M. Present and Future of Surface-Enhanced Raman Scattering. *ACS Nano* **2020**, *14*, 28-117.

12. Escalera-López, D.; Lou, Z.; Rees, N. V. Benchmarking the Activity, Stability, and Inherent Electrochemistry of Amorphous Molybdenum Sulfide for Hydrogen Production. *Advanced Energy Materials* **2019**, *9*, 1802614.

13. Murugesan, S.; Akkineni, A.; Chou, B. P.; Glaz, M. S.; Vanden Bout, D. A.; Stevenson, K. J. Room Temperature Electrodeposition of Molybdenum Sulfide for Catalytic and Photoluminescence Applications. *ACS Nano* **2013**, *7*, 8199-8205.

14. Kang, D.; Kim, T. W.; Kubota, S. R.; Cardiel, A. C.; Cha, H. G.; Choi, K. Electrochemical Synthesis of Photoelectrodes and Catalysts for Use in Solar Water Splitting. *Chemical Reviews* **2015**, *115*, 12839-12887.

15. Er, E.; Hou, H.; Criado, A.; Langer, J.; Möller, M.; Erk, N.; Liz-Marzán, L. M.; Prato, M. High-Yield Preparation of Exfoliated 1T-MoS_2 with SERS Activity. *Chemistry of Materials* **2019**, *31*, 5725-5734.

16. Bell, R. E.; Herfert, R. E. Preparation and Characterization of a New Crystalline Form of Molybdenum Disulfide. *Journal of the American Chemical Society* **1957**, *79*, 3351-3354.

17. Schulman, D. S.; Sebastian, A.; Buzzell, D.; Huang, Y.; Arnold, A. J.; Das, S. Facile Electrochemical Synthesis of 2D Monolayers for High-Performance Thin-Film Transistors. *ACS Applied Materials & Interfaces* **2017**, *9*, 44617-44624.

18. Ponomarev, E. A.; Neumann-Spallart, M.; Hodes, G.; Lévy-Clément, C. Electrochemical deposition of MoS_2 thin films by reduction of tetrathiomolybdate. *Thin Solid Films* **1996**, *280*, 86-89.

19. Ponomarev, E. A.; Albu-Yaron, A.; Tenne, R.; Levy-Clement, C. Electrochemical deposition of quantized particle MoS_2 thin films. *Journal of the Electrochemical Society* **1997**, *144*, L277-L279.

20. Albu-Yaron, A.; Lévy-Clément, C.; Katty, A.; Bastide, S.; Tenne, R. Influence of the electrochemical deposition parameters on the microstructure of MoS_2 thin films. *Thin Solid Films* **2000**, *361-362*, 223-228.

21. Thomas, S.; Smith, D. E.; Greenacre, V. K.; Noori, Y. J.; Hector, A. L.; Groot, C. H. (Kees) de; Reid, G.; Bartlett, P. N. Electrodeposition of MoS_2 from Dichloromethane. *Journal of the Electrochemical Society* **2020**, *167*, 106511.

22. Redman, D. W.; Rose, M. J.; Stevenson, K. J. Electrodeposition of Amorphous Molybdenum Chalcogenides from Ionic Liquids and Their Activity for the Hydrogen Evolution Reaction. *Langmuir* **2017**, *33*, 9354-9360.

23. Sakaebe, H.; Matsumoto, H. N-Methyl- N-propylpiperidinium bis(trifluoromethanesulfonyl)imide (PP13–TFSI) – novel electrolyte base for Li battery. *Electrochemistry Communications* **2003**, *5*, 594-598.

24. Schröder, F. A.; Scherle, J. Beiträge zur Chemie von Molybdän und Wolfram. XI / Contributions to the Chemistry of Molybdenum and Tungsten. XI. *Zeitschrift für Naturforschung* **1973**, *28*, 46-55.

25. Schröder, F. A.; Scherle, J.; Hazell, R. G. The structure of cis-dioxobis-(2-hydroxyethyl-1-oxo)molybdenum(VI). *Acta Crystallographica Section B* **1975**, *31*, 531-536.

26. Staikov, G. *Electrochemical Theory: Electrocrystalization;* 2009; Vol. 2, pp 32-40.

Section 2.2 - Substituted Phosphine-Imine Ligands and Organometallic Complexes

2.2.1 Historical Impact on Modern Organometallic Chemistry

Organometallic chemistry has had a very positive impact on daily life. By reducing activation energies, catalysts can lower overall energy requirements (high pressure and temperature) for the large-scale production of high demand products like many polymers, materials, medicine, and more. Organometallic chemistry has significant historical roots with many early important discoveries, including the first platinum-ethylene complex called Zeise's Salt (**1827-31**, Figure 2.2),[1] and an iron complex with two cyclopentadienide ligands (Cp, Figure 2.3 **B**) called ferrocene (**1951-52**, Figure 2.2).[2,3] Cyclopentadieneide is the monodeprotonated form of cyclopentadiene (CpH, Figure 2.3 **A**), with two of these ligands resulting in the Fe(II) oxidation state. These compounds offered insight into bonding that was previously unexpected, opening up fields of organometallic study that vastly improved and expanded chemical manipulation capabilities within the medical, petroleum, and commercial industries.

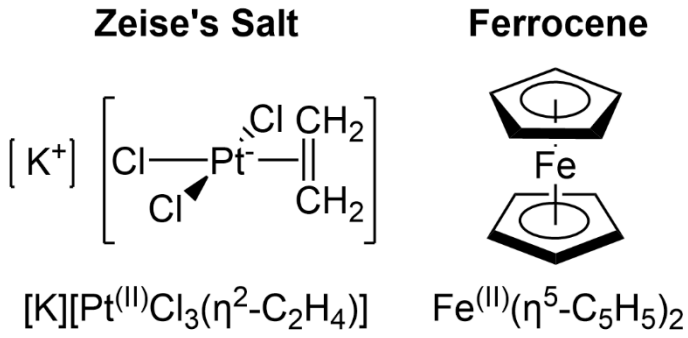

Figure 2.2 Zeise's salt $[K][PtCl_3(\eta^2\text{-}C_2H_4)]$ and Ferrocene $Fe(\eta^5\text{-}C_5H_5)_2$ with η^2 and η^5 interactions between the metal ion and the conjugated π-systems, respectively.

The former of these two complexes illustrates the earliest organic alkene metal π-bond within the platinum complex William C. Zeise discovered an example of the earliest

organometallic compound featuring what would later be known as hapticity "η" where two carbon atoms (η^2) interact with platinum via π-bonding interactions. This historically important complex is the first sign of unexpected bonding between carbon-based molecules and metallic elements. Ferrocene (Figure 2.2), discovered over a hundred years after Zeise's Salt,[2] gave rise to the understanding that not only could simple alkenes like ethylene coordinate to a metal, but bulkier aromatic compounds like cyclopentadiene (CpH, Figure 2.3 **A**) could as well. This 5-membered carbon ring with two double bonds and a methylene unit (C_5H_6), can undergo a single deprotonation forming the cyclopentadiene-ide/-yl (Cp) ligand which readily forms η^5 6π-electron donor interactions with metal atoms. In 1951 this concept was unknown, though the following year another group of researchers identified the proper structure and bonding between the Fe(II) cation and each of the two Cp ligands.[3]

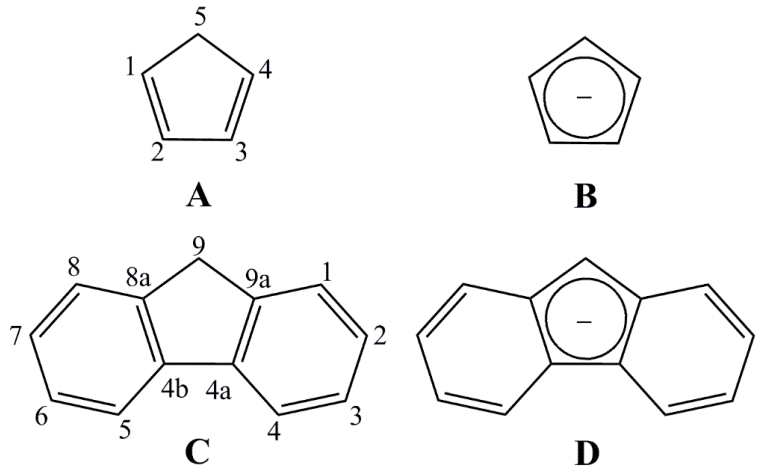

Figure 2.3 Molecular structures of cyclopentadiene (CpH, A) and fluorene (FluH, B) with their corresponding deprotonated forms cyclopentadien-ide/yl (Cp, B) and fluoren-ide/yl (Flu, D), respectively. Numbering for the general structure of CpH (A) and FluH (C) is labelled, and in each instance, deprotonation of the acidic methylene (CH_2) proton on C5 (CpH) or C9 (FluH) results in formation of a methyne (CH) at C5 and C9 as the monoanions Cp (B) and Flu (D) are formed.

This ligand is monoanionic, with sterically crowding η^5 interactions that results in compounds like $FeCp_2$ and $TiCp_2Cl_2$ being relatively stable with respect to air, moisture, and heat.[2] The cyclopentadiene ligand marked the beginning of an entire field of organometallic chemistry termed "metallocene chemistry" focused around the 5-membered Cp containing ligands and related monoanionic ligands like fluorenide ($C_{13}H_9^-$, Flu, Figure 2.3 **D**). Fluorenide, derived from deprotonation of fluorene ($C_{13}H_{10}$, FluH, Figure 2.3 **C**), is a more extended and conjugated polyaromatic hydrocarbon ligand than the simple Cp ring or small alkenes like ethylene within Zeise's salt. Derivatives of the Cp ligand can offer significant spatial shrouding around a metal atom resulting in greater stability along with the active donor potential of 2, 4, or 6 electrons through either $\eta^{1\text{-}5}$ or $\eta^{1\text{-}6}$ interactions (Figure 2.4) for Cp and Flu, respectively.

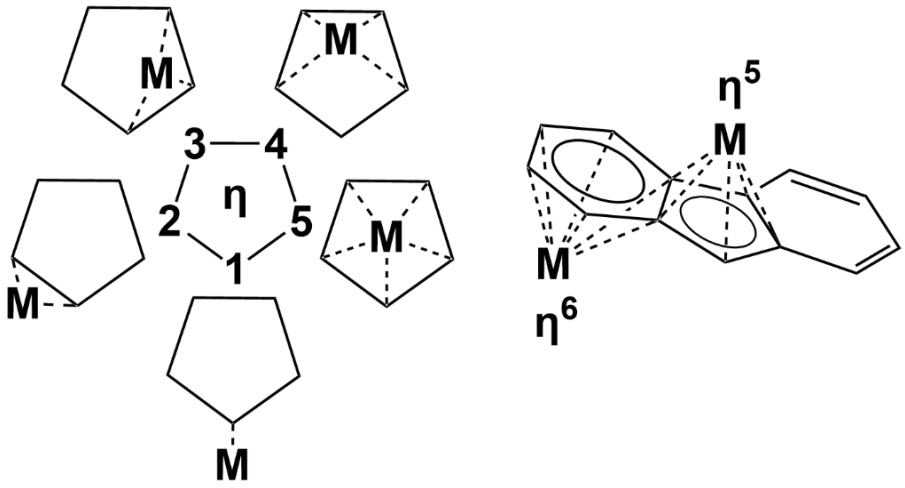

Figure 2.4 Different potential η-interactions between a metal ion M and the 5- and 6-membered aromatic rings of Cp (left, top down view) and Flu (right, perspective view).

2.2.2 The Beginning of Polyolefin-Based Plastic

More recent exploration into alkene-metal interactions resulted in the production of cheap, convenient, sterile, and moldable hydrocarbon-derived plastics (Figure 2.5, **#1-6**). Various polymerization processes using small molecular monomers like propylene are used to make plastics, with notable work by Ziegler and Nata which earned the 1961 Nobel prize in chemistry. They used a Ti/Al catalyst system to produce controlled plastic polymers like polypropylene from propylene using primarily chloride and ethyl ligands on Ti and Al, respectively.[4] Numbering for each plastic is relative to common recycling practices (Figure 2.5). This results in plastic products with very important global applications in food handling and sale, disposable hospital equipment that is contaminated upon use, and innumerable components within consumer products like phones, computers, appliances, and more.

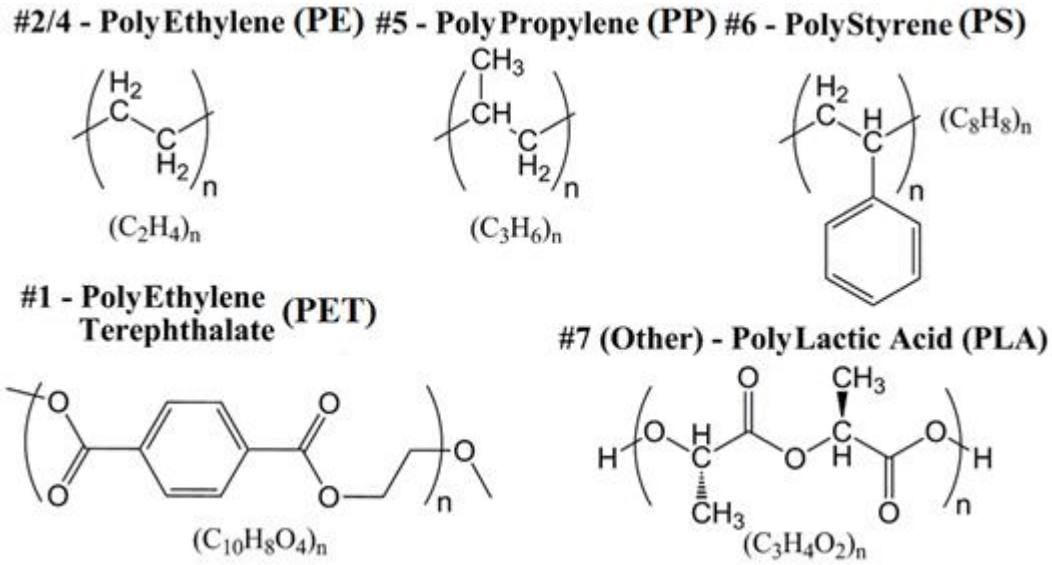

Figure 2.5 Plastic polymer subunits in common commercial products.

Later developments towards more sustainable polymerization include the use of the Cp ligands and zirconium as a monometallic catalyst system to produce more readily biodegradable plastics with an O:C ratio of 1:1 using ϵ-caprolactone or racemic lactic acid cyclic dimers (Figure 2.5, **#7**) as bioderived monomer sources rather than using petroleum derived alkenes.[5,6] Carbon-oxygen bonds are easier for chemical processes and microorganisms to break via processes such as hydrolysis, while the C-C bonds of plastics like low- and high-density polyethylene (Figure 2.5, #**2**/**4**) result in significant persistence due to the lack of environmental degradation. This slow (often mechanical) breakdown forms micro- and nano-plastics which can ad/absorb toxins and deliver them within tissues of organisms which inevitably consume them, with some managing to enter into the brain causing neurological damage within organisms like fish.[7,8] Plastic can have a harmful impact on the environment through negligent pollution; however, this sort of environmental harm resulting from poor handling of plastic wastes does not undermine the necessary value of plastic as a sanitary, durable, and cheap material for consumer items such as storage, furniture, and medical equipment. Though the history of plastic production primarily focuses on hydrocarbon chains derived from petroleum, newer work with earth-abundant metals like aluminum show the ability to perform polymerization of plant derived cyclic esters and other oxygen containing monomers, forming biodegradable polylactic acid (Figure 2.5, **#7**) and other polymers via ring opening polymerization (Figure 2.6). This research could lead to supplementing current disposable plastics with compostable alternatives, reducing the issues associated with micro- and nano-plastics.

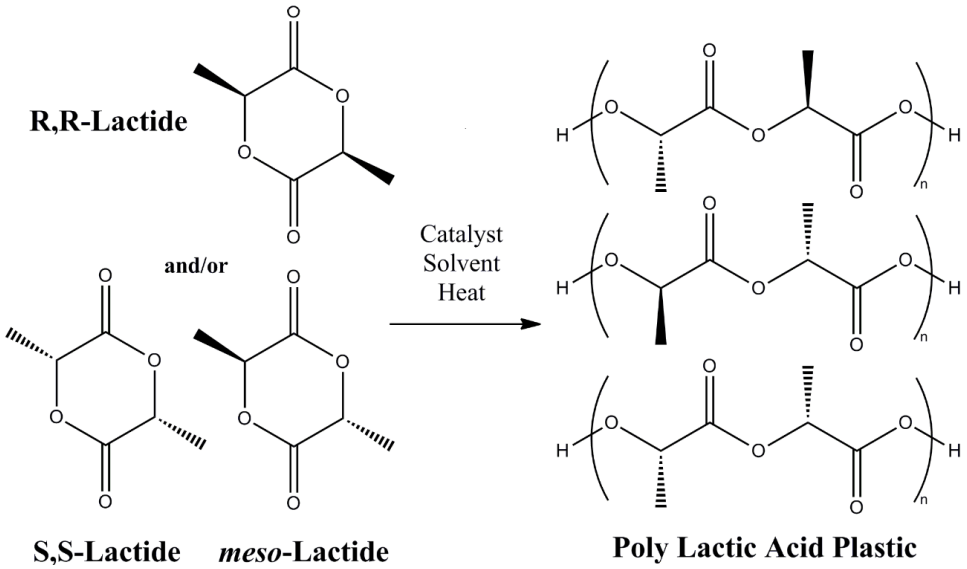

Figure 2.6 Ring-opening polymerization of various cyclic lactides into the polylactic acid plastics PLA.

One aspect of the work conducted within this thesis is the preparation of a series of aluminum- and indium-based catalyst molecules that are thought to be capable of performing the catalytic initiation step within the ring opening polymerization process necessary for production of plastics from materials such as polylactic acid. These types of group 13 catalysts are also used to catalyze copolymerization of carbon dioxide with other materials like epoxides, highlighting two environmentally important applications for these compounds that have yet to be explored in future work for the prepared and characterized catalysts detailed in Chapter 5. Seeking previously unobserved coordination around metal centers via ligand design is the primary focus of the synthetic research being conducted into new substituted phosphine-imine ligands.[9]

2.2.3 Fluorenyl and Derivatives as Organometallic Ligands

Fluorenide (Flu) on its own is a very large monoanionic ligand, making it unstable to degradation via processes such as hydrolysis, readily displacing the ligand from a metal cation (Figure 2.7). This led to the desire to effectively anchor Flu to a metal atom by transforming it into a sterically bulky bidentate ligand similar to a previously reported polymerization catalyst based on yttrium bound by a bidentate bridged Flu and tetramethyl Cp.[10] The bare Flu anion has a proton on the 5-membered ring that can readily be replaced with alternate atoms that lead to the bridging potential of the ligand. By replacing this proton with atoms that have additional chelation potential, corresponding organometallic complexes should likewise be more stable via the chelate effect due to having a greater number of atoms interacting with the orbitals of the metal ion.

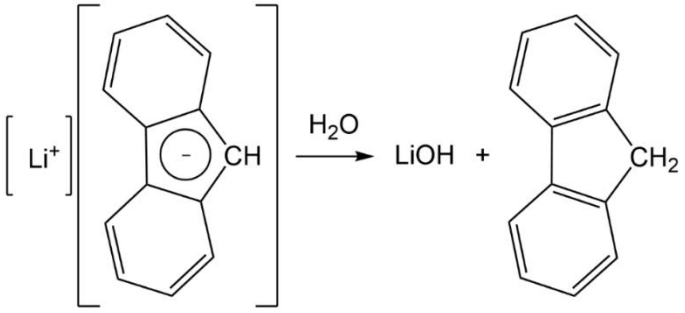

Figure 2.7 Hydrolysis of the lithium fluorenide, forming lithium hydroxide and neutral fluorene.

For increased shielding from steric bulk, binding fluorene to a tetrahedral phosphorus center allows for increased steric bulk via bulky substituents bound to phosphorus and the tendency for electron delocalization to occur, resulting in better neutral donor activity from the newly formed phosphonium fluorenide. One example of a low coordinate bond between a triphenyl phosphonium fluorenide involves a single tridentate

complex of tricarbonyl ruthenium with two instances of phenyl group ortho metalation and σ-interactions with the phosphonium fluorenylide functional group.[11] This low coordinate, η^1-interaction is attributed to the spatial bulk of the rest of the tridentate ligand and three carbonyl groups. A similar complex of tungsten tetracarbonyl with a bidentate fluorenylide also shows 2-electron σ-donor character, attributed to the tungsten ion having many ligands surrounding it preventing greater donation from the phosphonium fluorenylide donor.[12] Tungsten with four carbonyl groups is very satiated sterically and electronically, so accepting only 2-electron σ-donation from an η^1-fluorene is to be expected. This is one of the only examples of tethered diphenyl phosphonium fluorenide bidentate ligands, highlighting a literature gap this thesis work seeks to via synthesis of a bulky monoanionic bidentate phosphonium fluorenylide-amide ligand precursor and some alkali metal complexes (Figure 2.8).

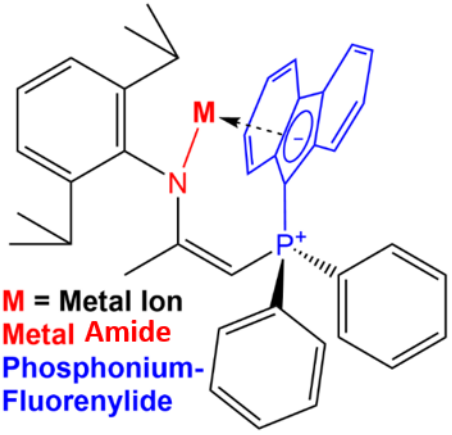

Figure 2.8 General bonding motif of organometallic complexes expected to occur with the produced phosphonium-fluorenide amide ligand supporting the alkali metal through bidentate chelation.

Of the organometallic complexes of fluorenyl-based ligands, early group 1-3 metals are very common,[13-22] though main group,[23,24] transition,[11,25-32] and rare earth[23,33-37] metal

complexes have been studied as well, this highlights the ubiquitous value of the fluorenide donor ligand, especially when coupled with a tether, bulky aromatic groups, and when used as a phosphonium fluorenide neutral donor.

2.2.4 Application and Use of Aluminum-Based Catalysts

The ability to make a complicated molecule with appreciable yields, minimal steps, and high purity is a goal in many industries (petrochemical, medical). Industry often require difficult synthetic targets, commonly made with the help of complexes of expensive and rare metals like palladium, platinum, and rhodium. These metals are effective but suffer from huge economic burdens and limited availability and accessibility. Aluminum-based molecules have been proven effective for a variety of chemical transformations and catalytic processes, enabling desirable selectivity through a wide range of geometries and structures. This regioselectivity is promising for reactions which produce racemic mixtures. A great deal of work has explored a variety of metal geometries with very promising chemical behaviour throughout, especially regarding interactions between aluminum and heteroatoms like oxygen, nitrogen, and sulfur. These compounds show precedent for forming heterocycles with exceptional functional group tolerance and regioselectivity including heterocycles like cyclic carbonates and oxazolidinones (Figure 2.9).[38-40]

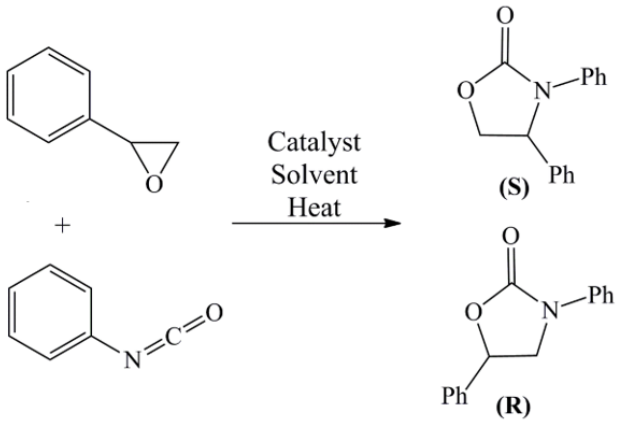

Figure 2.9 Reaction of an epoxide and isocyanate forming oxazolidinones when dissolved and heated in the presence of a catalyst system involving an alkyl ammonium halide with aluminum complexes.

This is important because rather than forming these oxazolidinone ring systems with the requirement of additional steps to protect active groups like amines, chlorides, etc., direct synthesis is possible. Formation of bonds between carbon and oxygen, nitrogen or sulfur is possible using the aluminum catalysts, and for the pharmaceutical industry, which almost solely produces heteroatom containing drug molecules, this is very important. It is favorable to understand the limits of aluminum and other abundant metal catalysts and reagents with respect to a wide scope of ligands. The less explored nature of Earth-abundant metal catalysts and the significant lack of political and socioeconomic problems associated with studying these metals makes them highly attractive elements for novel ligand exploration and will serve as the primary focus for organometallic molecules within this research.

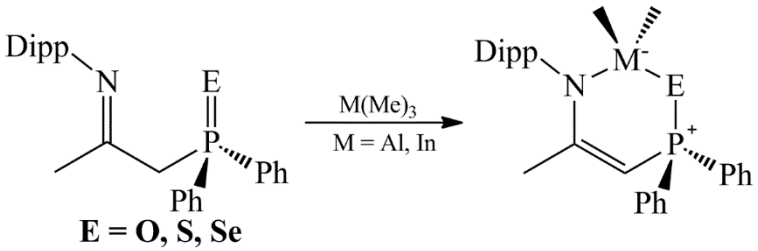

Figure 2.10 Synthesis of dimethyl group 13 metal complexes with a bidentate chalcogen substituted phosphine-imine ligand.

In addition to studying ligands and organometallic complexes of alkali metals of the type shown in Figure 2.8, oxidation of a phosphine-imine with the first three chalcogens oxygen, sulfur, and selenium (Figure 2.10) will be used to prepare a series of dimethyl aluminum and indium complexes to perform a comparison of the physical, spectroscopic, and structural properties of each compound. Future work can be done using these characterized materials to study catalytic potential for processes such as ring-opening polymerization of cyclic esters, lactones, and lactides[41-48] or cyclization of molecules like carbon dioxide with epoxides (Figure 2.11).[38-40,49-52]

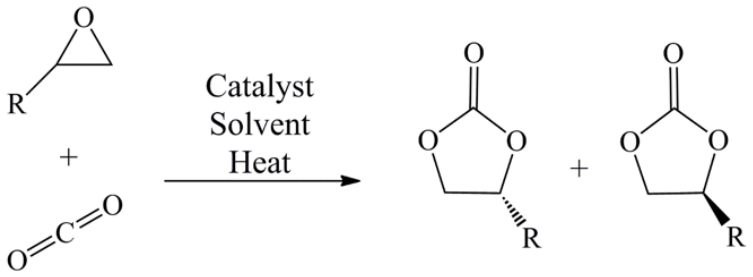

Figure 2.11 Synthesis of cyclic carbonates via ring-open insertion of CO_2 into the strained epoxide ring.

2.2.5 References

1. Zeise, W. C. Von der Wirkung zwischen Platinchlorid und Alkohol, und von den dabei entstehenden neuen Substanzen. *Annalen der Physik* **1831**, *97*, 497-541.
2. Kealy, T. J.; Pauson, P. L. A New Type of Organo-Iron Compound. *Nature* **1951**, *168*, 1039-1040.
3. Wilkinson, G.; Rosenblum, M.; Whiting, M. C.; Woodward, R. B. The Structure of Iron Bis-Cyclopentadienyl. *Journal of the American Chemical Society* **1952**, *74*, 2125-2126.
4. Natta, G.; Danusso, F. Stereoregular Polymers and Stereospecific Polymerizations. **1967**, *1*.
5. Villaseñor, E.; Gutierrez-Gonzalez, R.; Carrillo-Hermosilla, F.; Fernández-Galán, R.; López-Solera, I.; Fernández-Pacheco, A. R.; Antiñolo, A. Neutral Dimethylzirconocene Complexes as Initiators for the Ring-Opening Polymerization of ϵ-Caprolactone. *European Journal of Inorganic Chemistry* **2013**, *2013*, 1184-1196.
6. Shamiri, A.; Chakrabarti, M. H.; Jahan, S.; Hussain, M. A.; Kaminsky, W.; Aravind, P. V.; Yehye, W. A. The Influence of Ziegler-Natta and Metallocene Catalysts on Polyolefin Structure, Properties, and Processing Ability. *Materials* **2014**, *7*, 5069-5108.
7. Prüst, M.; Meijer, J.; Westerink, R. H. S. The plastic brain: neurotoxicity of micro- and nanoplastics. *Particle and Fibre Toxicology* **2020**, *17*, 24.

8. Mattsson, K.; Johnson, E. V.; Malmendal, A.; Linse, S.; Hansson, L.; Cedervall, T. Brain damage and behavioural disorders in fish induced by plastic nanoparticles delivered through the food chain. *Scientific Reports* **2017**, *7*, 11452-11457.

9. Jende, L. N.; Maichle-Mössmer, C.; Anwander, R. Rare-Earth-Metal Alkylaluminates Supported by N-Donor-Functionalized Cyclopentadienyl Ligands: C-H Bond Activation and Performance in Isoprene Polymerization. *Chemistry – A European Journal* **2013**, *19*, 16321-16333.

10. Lee, M. H.; Hwang, J. W.; Kim, Y.; Kim, J.; Han, Y.; Do, Y. The first fluorenyl ansa-yttrocene complexes: Synthesis, structures, and polymerization of methyl methacrylate. *Organometallics* **1999**, *18*, 5124-5129.

11. Arce, A.; De Sanctis, Y.; Galarza, E.; Garland, M. T.; Baggio, R. Two complexes derived from the reaction of $M_3(CO)_{12}$ clusters (M = Ru, Os) with the 9-(triphenylphosphonio)fluorenide ylide: tricarbonyl[9-(triphenylphosphonio)fluorenylidene]ruthenium and nonacarbonyl-3-fluorenylidene-2-hydrido-triangulo-triosmium(III). *Acta Crystallographica, Section C* **2013**, *69*, 363-366.

12. Bajko, Z.; Gudat, D.; Lissner, F.; Nieger, M.; Schleid, T. Ylidyl-substituted Phosphonio-benzophospholides as Chelating Ligands. *Zeitschrift für Anorganische und Allgemeine Chemie* **2004**, *630*, 1969-1976.

13. Evans, K. J.; Mansell, S. M. Synergic Deprotonation Generates Alkali-Metal Salts of Tethered Fluorenide-NHC Ligands Co-Complexed to Alkali-Metal Amides. *Chemistry – A European Journal* **2019**, *25*, 3766-3769.

14. Downing, S. P.; Danopoulos, A. A. Indenyl- and Fluorenyl-Functionalized N-Heterocyclic Carbene Complexes of Titanium and Vanadium. *Organometallics* **2006**, *25*, 1337-1340.

15. Geitner, R.; Kosygin, I.; Goerls, H.; Pahl, J.; Harder, S.; Westerhausen, M.; Langer, J. An unsymmetrical phosphonium diylide with a fluorenylidene subunit and its lithium complexes. *Journal of Coordination Chemistry* **2015**, *68*, 3302-3316.

16. Neander, S.; Tio, F. E.; Buschmann, R.; Behrens, U.; Olbrich, F. Cyclopentadienyl, indenyl, fluorenyl, and pentamethylcyclopentadienyl complexes of potassium with 18-crown-6. *Journal of Organometallic Chemistry* **1999**, *582*, 58-65.

17. Neander, S.; Körnich, J.; Olbrich, F. Novel fluorenyl alkali metal Diglyme complexes: synthesis and solid state structures. *Journal of Organometallic Chemistry* **2002**, *656*, 89-96.

18. Harder, S.; Lutz, M.; Straub, A. W. G. Silicon-Bridged Alkali-Metal and Alkaline-Earth-Metal Metallocene Complexes. *Organometallics* **1997**, *16*, 107-113.

19. Üffing, C.; Köppe, R.; Schnöckel, H. Molecular Structure of Fluorenyllithium. *Organometallics* **1998**, *17*, 3512-3515.

20. Neander, S.; Behrens, U.; Olbrich, F. Novel 18-crown-6 organometallic rubidium and cesium complexes containing cyclopentadienyl, indenyl, pentamethylcyclopentadienyl, and fluorenyl as carbanions. *Journal of Organometallic Chemistry* **2000**, *604*, 59-67.

21. Avent, A. G.; Crimmin, M. R.; Hill, M. S.; Hitchcock, P. B. Reactivity of [HC{(C(Me)N(Dipp))}(2)-Ca{N(SiMe$_3$)(2)}(THF)] (Dipp = (C$_6$H$_3$Pr$_2$)-Pr-i-2,6) with

C-H acids: Synthesis of heteroleptic calcium eta(5)-organometallics. *Journal of Organometallic Chemistry* **2006**, *691*, 1242-1250.

22. Evans, K. J.; Campbell, C. L.; Haddow, M. F.; Luz, C.; Morton, P. A.; Mansell, S. M. Lithium Complexes with Bridging and Terminal NHC ligands: The Decisive Influence of an Anionic Tether. *European Journal of Inorganic Chemistry* **2019**, *2019*, 4894-4901.
23. Roselló-Merino, M.; Mansell, S. M. Synthesis and reactivity of fluorenyl-tethered N-heterocyclic stannylenes. *Dalton Transactions* **2016**, *45*, 6282-6293.
24. Langer, J.; Kosygin, I.; Puchta, R.; Pahl, J.; Harder, S. A Soft Grip: Magnesium Complexes with a Phosphine-Modified Phosphonium Diylidic Lewis Base. *Chemistry – A European Journal* **2016**, *22*, 17425-17435.
25. Kozioł, A.; Jerzykiewicz, L. B.; Justyniak, I.; Lis, T.; Pasynkiewicz, S.; Pietrzykowski, A. New ionic fluorenylnickel complexes: Synthesis and solid state structure. *Journal of Organometallic Chemistry* **2014**, *767*, 22-26.
26. Mutseneck, E. V.; Loginov, D. A.; Perekalin, D. S.; Starikova, Z. A.; Golovanov, D. G.; Petrovskii, P. V.; Zanello, P.; Corsini, M.; Laschi, F.; Kudinov, A. R. (Tetramethylcyclobutadiene)cobalt complexes with five-electron carbo- and heterocyclic ligands. *Organometallics* **2004**, *23*, 5944-5957.
27. Schulte, P.; Behrens, U. Organometallic compounds of copper. XX - On the reaction of the alkyne copper(I) complexes [CuCl(S-alkyne)] and [Cu_2Br_2(S-alkyne)(dms)] (S-alkyne=3,3,6,6-tetramethyl-1-thiacyclohept-4-yne; dms = dimethylsulfide) with the

lithiumorganyls phenyllithium and fluorenyllithium. *Zeitschrift Fur Anorganische Und Allgemeine Chemie* **2000**, *626*, 1692-1696.

28. Edwards, A. J.; Paver, M. A.; Raithby, P. R.; Rennie, M. A.; Russell, C. A.; Wright, D. S. Preparation of copper organometallics via nucleophilic substitution of $CpCuPPh_3$: syntheses and X-ray structure determinations of $[Li(THF)_4]^+[(fluorenyl)_2CuPPh_3]^-$ and $[Cy_3PCu(\mu\text{-}C{\equiv}CtBu)_2Cu(PPh_3)_2]$ (THF = tetrahydrofuran, fluorenyl = $C_{13}H_9$). *Organometallics* **1994**, *13*, 4967-4972.
29. Freund, C.; Barros, N.; Gornitzka, H.; Martin-Vaca, B.; Maron, L.; Bourissou, D. Enforced η^1-Fluorenyl Coordination to Rhodium(I) with the $[FluPPh_2NPh]$- Ligand. *Organometallics* **2006**, *25*, 4927-4930.
30. Werle, C.; Bailly, C.; Karmazin-Brelot, L.; Le Goff, X.; Pfeffer, M.; Djukic, J. First Stabilization of 14-Electron Rhodium(I) Complexes by Hemichelation. *Angewandte Chemie-International Edition* **2014**, *53*, 9827-9831.
31. Kirillov, E.; Toupet, L.; Lehmann, C. W.; Razavi, A.; Kahlal, S.; Saillard, J.; Carpentier, J. $[(Cp{-}CMe_2{-}Flu)_2Ln]$-[Li(ether) n]+ (Ln = Y, La): Complexes with Unusual Coordination Modes of the Fluorenyl Ligand and the First Examples of Bis-Ansa Lanthanidocenes. *Organometallics* **2003**, *22*, 4038-4046.
32. Kirillov, E.; Kahlal, S.; Roisnel, T.; Georgelin, T.; Saillard, J.; Carpentier, J. Haptotropic rearrangements in sandwich (fluorenyl)(cyclopentadienyl) iron and ruthenium complexes. *Organometallics* **2008**, *27*, 387-393.

33. Chai, Z.; Wang, Y.; Tang, M.; Mu, X.; Hou, J.; Yang, G. Chiral rare-earth metal complexes with a tridentate amido-fluorenyl ligand: Syntheses, structures and catalytic performance. *Journal of Organometallic Chemistry* **2017**, *846*, 236-241.

34. Qian, C.; Nie, W.; Sun, J. Synthesis of diphenylmethylene bridged fluorenyl cyclopentadienyl lanthanocene complexes with Cs symmetry and crystal structures of the ate complexes $[Li(THF)_4][LnCl_2\{(C_{13}H_8)CPh_2(C_5H_4)\}]$ and $[Li(THF)_4][Ln(BH_4)_2\{(C_{13}H_8)CPh_2(C_5H_4)\}]$ (Ln = Nd or La). *Dalton Transactions* **1999**, 3283-3287.

35. Qian, C.; Nie, W.; Sun, J. The first example of a dinuclear anionic lanthanoidocene complex: $[K(18\text{-crown-6})\{(C_{13}H_8)CPh_2(C_5H_4)Nd(BH_4)_2\}]_2 \cdot C_4H_8O_2$. *Journal of Organometallic Chemistry* **2001**, *626*, 171-175.

36. Zaeni, A.; Olbrich, F.; Fischer, A.; Edelmann, F. T. Synthesis and structural characterization of $(COT)Pr(C_{13}H_8CH_2CH_2OMe)(THF)$ containing the chelating 9-(2-methoxyethyl)fluorenyl ligand. *Journal of Organometallic Chemistry* **2008**, *693*, 3791-3796.

37. Wang, H.; Shen, H.; Chan, H.; Xie, Z. Synthesis and Structural Characterization of Group 4 Metal Complexes Bearing Pentavalent Phosphorus-Bridged Ligands $[(C_{13}H_8)(iPr_2N)P(O)(C_2B_{10}H_{10})]^{2-}$ and $[(C_{13}H_9)(iPr_2N)P(O)(C_2B_9H_{10})]_2$. *Organometallics* **2008**, *27*, 3964-3970.

38. Castro-Osma, J. A.; Earlam, A.; Lara-Sánchez, A.; Otero, A.; North, M. Synthesis of Oxazolidinones from Epoxides and Isocyanates Catalysed by Aluminium Heteroscorpionate Complexes. *ChemCatChem* **2016**, *8*, 2100-2108.

39. Clegg, W.; Harrington, R. W.; North, M.; Pasquale, R. Cyclic Carbonate Synthesis Catalysed by Bimetallic Aluminium-Salen Complexes. *Chemistry* **2010**, *16*, 6828-6843.

40. Whiteoak, C. J.; Kielland, N.; Laserna, V.; Escudero-Adán, E. C.; Martin, E.; Kleij, A. W. A Powerful Aluminum Catalyst for the Synthesis of Highly Functional Organic Carbonates. *Journal of the American Chemical Society* **2013**, *135*, 1228-1231.

41. Nuyken, O.; Pask, S. Ring-Opening Polymerization—An Introductory Review. *Polymers* **2013**, *5*, 361-403.

42. Wei, Y.; Wang, S.; Zhou, S. Aluminum alkyl complexes: synthesis, structure, and application in ROP of cyclic esters. *Dalton Transactions* **2016**, *45*, 4471-4485.

43. Gesslbauer, S.; Cheek, H.; White, A. J. P.; Romain, C. Highly active aluminium catalysts for room temperature ring-opening polymerisation of rac-lactide. *Dalton Transactions* **2018**, *47*, 10410-10414.

44. Normand, M.; Dorcet, V.; Kirillov, E.; Carpentier, J. {Phenoxy-imine}aluminum versus -indium Complexes for the Immortal ROP of Lactide: Different Stereocontrol, Different Mechanisms. *Organometallics* **2013**, *32*, 1694-1709.

45. Li, C.; Tsai, C.; Lin, C.; Ko, B. Synthesis, structural characterization and reactivity of aluminium complexes supported by benzotriazole phenoxide ligands: air-stable alumoxane as an efficient catalyst for ring-opening polymerization of l-lactide. *Dalton Transactions* **2011**, *40*, 1880-1887.

46. Schnee, G.; Bolley., A.; Gourlaouen, C.; Welter, R.; Dagorne, S. Synthesis and structural characterization of NHC-stabilized Al(III) and Ga(III) alkyl cations and use

in the ring-opening polymerization of lactide. *Journal of Organometallic Chemistry* **2016**, *820*, 8-13.

47. Schnee, G.; Bolley, A.; Hild, F.; Specklin, D.; Dagorne, S. Group 13 metal (Al, Ga, In) alkyls supported by N-heterocyclic carbenes for use in lactide ring-opening polymerization catalysis. *Catalysis Today* **2017**, *289*, 204-210.
48. Zhang, W.; Wang, Y.; Wang, L.; Redshaw, C.; Sun, W. Dialkylaluminium 2-imidazolylphenolates: Synthesis, characterization and ring-opening polymerization behavior towards lactides. *Journal of Organometallic Chemistry* **2014**, *750*, 65-73.
49. Gaona, M. A.; de la Cruz-Martínez, F.; Fernández-Baeza, J.; Sánchez-Barba, L. F.; Alonso-Moreno, C.; Rodríguez, A. M.; Rodríguez-Diéguez, A.; Castro-Osma, J. A.; Otero, A.; Lara-Sánchez, A. Synthesis of helical aluminium catalysts for cyclic carbonate formation. *Dalton Transactions* **2019**, *48*, 4218-4227.
50. Martínez, J.; Castro-Osma, J. A.; Earlam, A.; Alonso-Moreno, C.; Otero, A.; Lara-Sánchez, A.; North, M.; Rodríguez-Diéguez, A. Synthesis of Cyclic Carbonates Catalysed by Aluminium Heteroscorpionate Complexes. *Chemistry – A European Journal* **2015**, *21*, 9850-9862.
51. Andrea, K. A.; Plommer, H.; Kerton, F. M. Ring-opening polymerizations and copolymerizations of epoxides using aluminum- and boron-centered catalysts. *European Polymer Journal* **2019**, *120*, 109202.
52. North, M.; Pasquale, R.; Young, C. Synthesis of cyclic carbonates from epoxides and CO_2. *Green Chemistry* **2010**, *12*, 1514-1539.

3. Chapter 3: X-Ray Structural Evidence for Monomeric, Dimeric, Polymeric and Octameric Clusters Derived from the Reaction of Molybdenum Trioxide with Ethylene Glycol

3.1 Abstract

A previously reported electrochemical synthesis of MoS_2 nanoflowers at 100 °C in the ionic liquid N-methyl-N-propylpiperidinium bis(trifluoromethane)sulfonimide (PP13-TFSI) from 1,4-butanedithiol and a crude reaction mixture of molybdenum trioxide and ethylene glycol was explored to prepare 2D-MoS_2.[1] The molybdenum precursor (with incomplete workup and characterization) could not be reliably reproduced, resulting in various crude molybdenum precursors of different identity. The only characterization of the prepared molybdenum precursor from reacting molybdenum trioxide with ethylene glycol provided in the reported literature is a description of a "brown, viscous liquid". From eight attempts to synthesize the required "brown oil", most crude solutions were golden in colour, with one successful production of a brown reaction mixture, highlighting reproducibility issues within this original preparation. Four solids crystallized from the crude reaction mixtures, giving insight into the complex nature of the reaction under slightly different conditions. Analysis by Single Crystal X-Ray Diffraction (SC-XRD) offered insight into the wide range of molybdenum to oxygen ratios between four crystalline samples isolated from preparing the molybdenum precursor (1:6 to 1:4 Mo:O ratios).[2,3] Electrochemical studies of the 1,4-butanedithiol, ethylene glycol, and various molybdenum precursors were completed and compared in 0.1 M PP13-TFSI in tetrahydrofuran (THF). In addition to unsuccessful replication of the reported

electrodeposition of MoS_2 from the Mo/S precursors in pure 100 °C PP13-TFSI, the 0.1 M PP13-TFSI supporting electrolyte was also explored to electrochemically deposit MoS_2. All attempts made using these Mo/S precursors resulted in either no deposit, or molybdenum and sulfur containing deposits as indicated by SEM-EDS analysis, however inability to reproduce these deposits via replication on another electrode resulted in no attempts to further characterize these non-reliable deposits.

3.1.1 Graphical Abstract

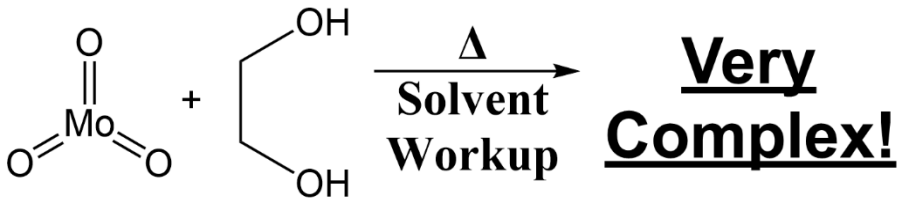

3.2 Introduction

Crystalline molybdenum disulfide (MoS_2), either alone or as a composite involving materials such as ZnO,[4,5] FeS_2,[6-10] Fe_3O_4,[11] and Au,[12,13] have been proven highly effective for an array of diverse applications including use as hardware like supercapacitors and transistors,[6,14,15] solar and hydrogen energy production and storage,[1,9,10,16-20] and environmental remediation.[5,11] Use of 2D-MoS_2 as a substrate for Surface Enhanced Raman Spectroscopy (SERS)[4,12,21-23] has recently emerged, offering the potential of widespread detection of important analytes, including pesticides, biomarkers, or drugs, for the agricultural, biomedical, and forensic industries.[14] Molybdenum disulfide is promising for various applications that usually rely on metals like platinum for performing processes such as the hydrogen evolution reaction (HER), or on metals like gold and silver that dominate SERS.[24,25] Gold and silver are both expensive and come with significant sustainability

issues for the future, resulting in the need to explore and understand materials like MoS_2. Though pure MoS_2 may not be sufficient to compare to noble metals, composites with other materials such as ZnO have been shown to synergize with MoS_2, acting as an alternative substrate to gold and silver for SERS analysis of bisphenol-A (BPA), for example.[4]

Molybdenum disulfide has multiple polymorphs (Tetragonal (D_{3d}) = 1T, Hexagonal (D_{3h}) = 2H, Rhombohedral (C^5_{3v}) = 3R) with conducting (1T) and semiconducting (2H, 3R) properties.[16] The semiconducting forms of MoS_2 highlight a very important property regarding the morphology of MoS_2; monolayers possess a direct band gap despite the bulk material possessing an indirect band gap. This different optical response results in monolayer molybdenum disulfide (2D-MoS_2) promoting the Raman scattering of incident radiation through charge transfer to the molecule upon irradiation with a reported Raman enhancement factor of 3×10^5 which is comparable to the most widely used metals, silver and gold with enhancement factors of ~10^5-10^6.[14,26,27] Techniques of preparing 2D-MoS_2 include chemical vapor deposition,[27,28] sonication,[29] alkali metal exfoliation,[19] electro-ablation of mechanically deposited bulk MoS_2,[15] and thin films of electrochemically deposited amorphous MoS_x ($2 < x < 3$) have commonly required annealing under a sulfur or argon atmosphere at 500 or 550 °C, respectively to attain the desired crystallinity.[30,31] This work seeks to utilize the electrochemical bottom-up approach described by Murugesan et al.[1] to prepare both platinum and glassy carbon working electrodes coated in monolayer molybdenum disulfide for use as a SERS substrate.

Electrochemically depositing thin films of MoS_2 with thickness control is a major goal that has yet to be achieved. Murugesan et al.[1] report thickness control by altering the

duration of chronoamperometric deposition at -2.7 V with no need for high temperature annealing post-treatment.[1] Underpotential deposition of thin films like that of copper casts some doubt on the choice of such a low voltage as well, and the necessity to apply less than -2.0 V has been disputed by later work.[30,32] Other Mo/S sources like ammonium tetra thiomolybdate ($(NH_4)_2MoS_4$)[30,31] and ammonium thiodimolybdate ($(NH_4)_2Mo_2S_{12}$)[33] have led to amorphous thin films upon electroreduction, resulting in the choice to pursue this preparation provided by Murugesan et al.[1] with ionic liquid mediated electrodeposition at 100 °C in order to prepare monolayer 2D-MoS_2 for use as a noble-metal free SERS substrate.

The references[34,35] provided by Murugesan et al.[1] for the reaction of MoO_3 and ethylene glycol had no mention of a reaction between these two materials, and instead focuses on the preparation of similar ammonium and alkali metal salts of a dioxo-molybdenum compound with various acids like glycolic acid in the case of Cuin. et al.[34] The name of glycolic acid ligands is given to the molybdenum precursor in the work by Murugesan et al.[1] ("molybdenum glycolate") despite no glycolic acid present in their reaction. Work by Preiss et al.[35] is slightly more related to the procedure that Murugesan et al. report;[1] however, the focus of the work in this reference is preparation of molybdenum carbide (Mo_2C). The process they use to achieve this involves heating molybdenum oxide (or molybdic acid, the hydrated form in this case) within ethylene glycol; although, a temperature of only 60 °C is used and for an unknown duration until "the odour of ammonia could no longer be detected (the commercial molybdic acid contains ammonium molybdate).". At this point in their Mo_2C preparation, they begin adding saccharose,

deviating from Murugesan et al. One valuable point they noted is that concentration of samples prior to saccharose addition was possible via heating at ~130 °C, which could be the source of the extraction process eluded to within the work by Murugesan et al. The synthesis provided to prepare the MoS_2 molybdenum precursor involves refluxing the mixture of MoO_3 with ethylene glycol under N_2 at 194 °C, and the provided workup stated only to extract the final brown-coloured viscous product, instructions that are not clear enough for a reliable replication. Understanding the identity of the precursors is necessary for understanding the processes underlying a reproducible electrodeposition of crystalline MoS_2 at 100 °C, and this current work sheds light on the complex identity of the molybdenum compounds that form when molybdenum trioxide is heated in ethylene glycol. Multiple reactions resulted in a golden-coloured thick liquid and concentrating the ethylene glycol solution caused the crystallization of $MoO_2(OC_2H_4OH)_2$, giving insight into a literature synthesis[2] and crystal structure[3] related to this preparation. A golden oil or colourless crystal was not used in the electrodeposition of MoS_2,[1] and attempts to replicate the electrochemical synthesis of MoS_2 were not successful, so additional syntheses were undertaken to better understand this complex reagent.

The electrodeposition of morphologically controlled MoS_2 with reproducible, reliable results is of interest to many fields of technology, energy generation (solar, hydrogen), and trace detection of substances when used as a substrate for SERS. It has been a challenging feat for common synthetic methods to produce high quality, uniform coverage, morphologically controlled thin films of MoS_2, and electrodeposition would be an ideal method that could exploit readily available precursors. The purpose of these initial

studies can be broken into three aspects highlighting the need for optimization and further understanding of this specific electrochemical deposition of MoS_2; first to explore the identity of the poorly characterized yet necessary molybdenum precursor via SC-XRD, second to characterize some electrochemical properties of the molybdenum precursors, 1,4-butanedithiol, ethylene glycol, and mixtures of these reagents on platinum or glassy carbon working electrodes in 0.1 M PP13-TFSI in THF along with the electrochemical window of this supporting electrolyte, and finally to attempt to electrochemically produce MoS_2 from either pure PP13-TFSI following the work by Murugesan et al.,[1] or in a solution containing 0.1 M PP13-TFSI in THF using 1,4-butanedithiol as the sulfur source reaction mixtures of MoO_3 and ethylene glycol as the source of molybdenum.

3.3 Results and Discussion

3.3.1 Ionic Liquid Preparation

To prepare the ionic liquid solvent PP13-TFSI, Li-TFSI was used as the anion ($TFSI^-$) precursor while the cation ($PP13^+$) precursor PP13-Br was prepared synthetically from N-methyl piperidine and 1-bromopropane via a modified literature procedure.[36] Briefly, the cation precursors were heated in acetonitrile for a prolonged period, with PP13-Br precipitating as a white solid in the golden liquid upon cooling. Combining PP13-Br and Li-TFSI as aqueous solutions causes precipitation of a dense (> 1 g/mL), mildly viscous colourless liquid within an hour of mixing, and extraction with dichloromethane (DCM), washing with ultrapure water, and drying *in vacuo* results in the PP13-TFSI ionic liquid used for electrochemical experiments (Scheme 3.1).[1]

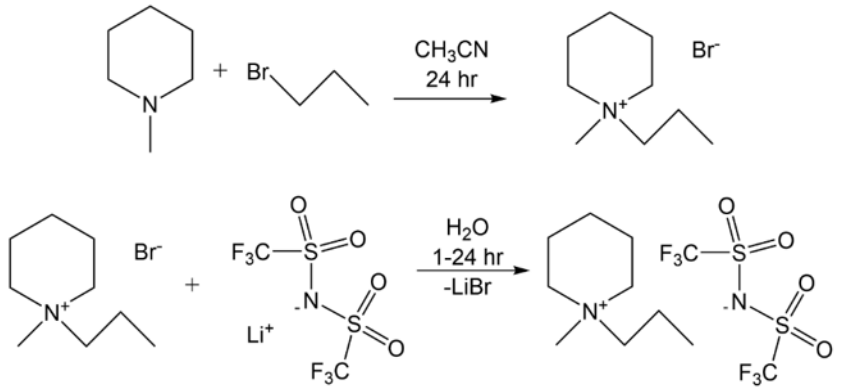

Scheme 3.1 Synthesis of cation precursor PP13-Br and the ionic liquid PP13-TFSI from metathesis with Li-TFSI.

3.3.2 Molybdenum Precursor Synthesis and Studies

The molybdenum precursor was made from MoO_3 and ethylene glycol following a modified literature preparation[1] involving heating the mixture to 194 °C for 1 hr. Extraction was listed as the next step; although, best guess attempts were used to decide on the required extraction process since no procedure or reference was provided for this by Murugesan et al.[1] Eight different syntheses of this molybdenum precursor (Table 3.1 and 3.2) were attempted (**A**(**1**-**8**), **A =** molybdenum precursor reaction, **# 1**-**8** = chronological order of reaction), each with slightly different work up and synthetic conditions, affording four types of product; 1. liquid samples of crude reaction mixtures that have been concentrated and filtered through diatomaceous earth, *"the oil"*. 2. liquid samples resulting from extraction or reaction which have had additional solvents such as THF, hexane, DCM, toluene, or water added to them (**B** = liquid sample). 3. crystalline samples derived directly from either liquid sample (**C** = single crystal sample). 4. Non-crystalline solids (**D** = amorphous solid). Many of these products, although not what was expected or sought after, gave insight into the complex nature of this reaction.

Table 3.1 Reagents and heating conditions associated with the 8 molybdenum precursor syntheses.

Rxn.	MoO_3 mass (g)	Ethylene glycol (EG) volume (mL)	Reaction time (min)	Temperature (± 2 °C)
A1	0.578	75	60	194
A2	0.800	125	60	194
A3	0.345	40	60	194
A4	0.466	50	120	215
A5	0.544	70	60	194
A6	0.286	35	60	194
A7	0.128	20	90	194
A8	0.282	35	150	150

Table 3.2 Synthetic conditions, work up, purification processes, and products isolated from the 8 molybdenum precursor syntheses. Volume in brackets = EG distilled prior to heat.

Rxn.	Pre-distill EG before 194 °C?	N_2 flow? Air exposure?	Solvents for purification or Workup Procedure?	Products isolated
A1	No	Yes, minor	Vacuum distill to green paste, DCM extraction, THF wash	Colourless crystals of $MoO_2(OC_2H_4(OH))_2$ and golden oil
A2	No	Yes, trace	Vacuum distill to green paste, DCM extraction, THF transfer, hexane and toluene insoluble, THF extraction	Green solid, yellow crystals from green oil, Colourless crystals of $MoO_2(OC_2H_4(OH))_2$ upon partial hydrolysis of residue
A3	Yes (~5 mL)	Yes, no	Vacuum distill, filter	Golden oil, Colourless crystals of $MoO_2(OC_2H_4(OH))_2$ after 10 months under N_2
A4	Yes (~6 mL)	Yes, no	Vacuum distill, scrape	Black solid, blue crystal of $Mo_{12}O_{40}X$ upon hydration of residue
A5	No	Yes, no	Vacuum distill, filter, rinse residue into separate container with THF	Golden-brown oil and gold/yellow crystals
A6	No (~10 mL)	Yes, no	Vacuum distill, filter, rinse residue into separate container with THF	Brown oil with black solids, red crystals
A7	No	Yes, no	Vacuum distill to green paste, DCM extraction, THF wash	Yellow crystals, gold oil
A8	No	No, no	Vacuum distill, 95% ethanol, filter, dry	Gold oil turned into blue liquid then dried to blue solid

For discussion, samples will be described by their state, the number reaction they came from, and the sample number (**A#**) referenced to in Table 3.3. Liquid samples will be referred to as (**B**), crystals (**C**), and non-crystalline solids (**D**) from the **1**-**8** molybdenum

precursor reactions. Naming of samples follows the form: Sample Type-Reaction Number-Product, so the sample **B-3-a** refers to the oil sample (**B**) from reaction (**3**) and it is the major liquid product (**a**), while **C2a** and **C2b** refer to the major and minor crystalline products of **A2** isolated from crystallization of the bulk solution (**C2a**) or washing the glassware with water after reaction (**C2b**), respectively.

Table 3.3 Final products derived from **8** reactions of MoO_3 and ethylene glycol with varying chemical workup. These products include liquid samples, crystalline, and amorphous solid samples from the attempts to prepare the Mo precursor. Some solids, residues, and other products created have been discarded and not included such as the green aqueous oil **C2b** was derived from. For more detailed synthesis of **A1**-**8** see experimental (**3.4.3**).

Rxn.	Liquid (**B**#x)	Crystal (**B**#x)	Solid (**D**#x)
A1	**B1a** Gold Oil	**C1a –** Compound **1**	N/A
A2	**B2a** Green Oil (THF)	**C2a** – Compound **2** **C2b** – Compound **1**	**D2a** – Dried Compound **2**
A3	**B3a** Gold Oil*	**C3a –** Compound **1** **C3b –** Compound **5**	N/A
A4	**B4a** Blue Liquid	**C4a –** Compound **6**	**D4a** Black Solid, **D4b** blue solid (**B4a dried**)
A5	**B5a** Golden-brown Oil* **B5b** Golden-brown Oil	**C5a –** Compound **3**	**D5a, D5b**
A6	**B6a** Brown Oil*	**C6a –** Compound **4**	**D6a**
A7	**B7a** gold oil	N/A	N/A
A8	**B8a** gold oil **B8b** blue liquid	N/A	**D8a** Blue Solid (**B8b** dried)
* used within electrochemical experiments as a molybdenum precursor.			

The visual progression during these eight syntheses evolves from mint-green powder (MoO_3) in colourless liquid (ethylene glycol), and upon heating, dissolution begins through a brief vivid turquoise colour change into a golden green hued solution, maintaining a completely transparent, solid-free lighter golden colour if kept below 150 °C (**A8**) and darkening if heat is increased to 194 °C. The darker golden-green solution occurs

with trace black precipitate for **A** (**1-3,7**), and significant amounts for **A** (**4-6**) and heating the mixture to 215 °C formed primarily black precipitate for **A4**. Thick golden (**B1a,3a,7a,8a**), green (**B2a**), golden-brown (**B5a, B5b**) and brown oils (**B6a**) upon *in vacuo* concentration and filtration through diatomaceous earth either neat or dissolved in DCM or THF. The fourth reaction was heated beyond 194 °C, affording a hard black solid rather than an oil upon concentrating *in vacuo*.

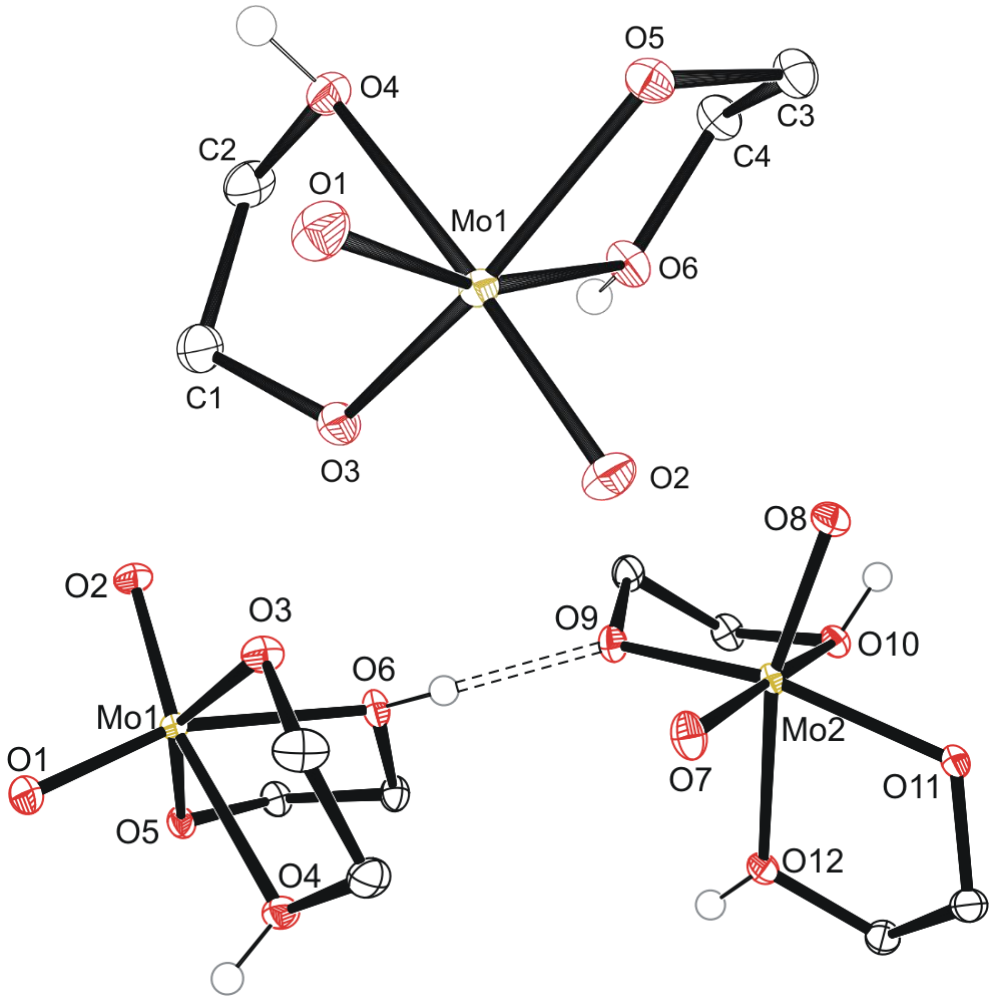

Figure 3.1 Molecular structure of a single molecule of compound **1** (top) and the two molecules in the asymmetric unit cell of compound **1** (bottom) participating in hydrogen bonding with anisotropic displacement ellipsoids projected at the 50% probability level. Methylene CH_2 hydrogen atoms have been omitted for clarity.

The first, second, and third reaction mixtures **A1**-**3** crystallized a known molecular species, compound **1** $MoO_2(OC_2H_4OH)_2$ (Figure 3.1), from an ethylene glycol DCM solution (**C1a**), water (**C2b**), PP13-TFSI (**C1c**), and pure ethylene glycol or acetonitrile mixed with ethylene glycol (**C3a**, **C3b**). Isolating this compound from various mixtures offered insight into the original 1973 preparation[2] and the 1975 X-ray crystallography[3] of this monomeric structure and the relevance of this chemical species within MoO_3 + ethylene glycol reaction (Figure 3.1). All products isolated via attempting this precursor synthesis are detailed in Scheme 3.2. Isolation of compound **1** provided insight into workup of this reaction mixture to isolate this pure crystalline material through giving insight into the work done in the 1970's. The seventh reaction which replicated this alternate literature preparation by heating to 150 °C open to air followed by concentration *in vacuo* and addition of ethanol produced a dark blue solution rather than the expected colourless compound **1**. This blue colour is thought to be due to residual water in the absolute ethanol used since hydrolysis of crude reaction mixtures, the pure $MoO_2(OC_2H_4OH)$ crystals, and the black solid **D4a** all afforded equally rich blue solutions in water. A series of freezing (-18 °C) and thawing (20-25 °C) cycles over the course of a few weeks enabled isolation of a single tiny blue crystal (**C4a –** Compound **6**) that indicates anionic $Mo_{12}O_{40}X$ (X = heteroatom like S, P, Cl) structure by SC-XRD. Poor data and uncertainty regarding co-crystallized species such as the central heteroatom, cations, or water molecules could not be conclusively solved; however, the general $Mo_{12}O_{40}$ structure is visible by SC-XRD (See SI). Any reaction mixture or sample which encountered water and air for prolonged periods of time turned blue seemingly irreversibly. This decomposition via exposure to air and

moisture highlights instability of the proposed molybdenum precursor that was noted by Murugesan et. al.[1]

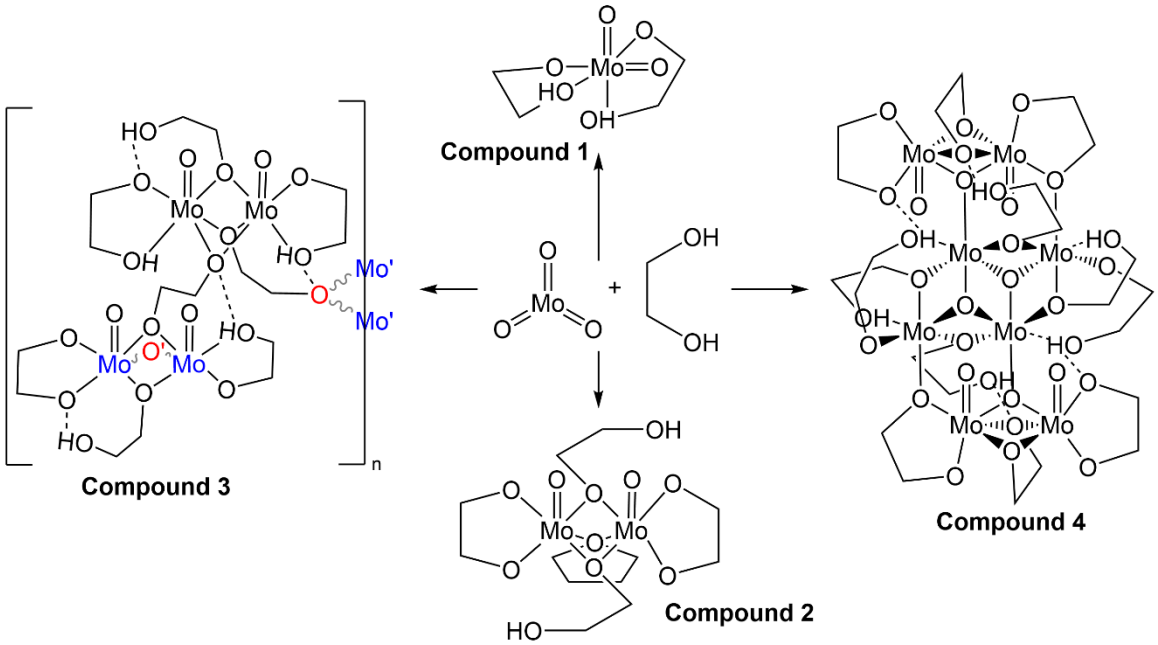

Scheme 3.2 Chemdraw structural representation of compounds **1-4** derived from very similar reactions of MoO_3 and ethylene glycol. Two ethylene glycol units within the single crystal-structure are omitted from the diagram of compound **4.**

Following the identification of compound **1** from this precursor reaction, work up of concentrated reaction mixtures with THF (**A2**, **A5**) revealed unexpected insights into the complexity regarding the reaction of MoO_3 with ethylene glycol via SC-XRD analysis. As replicate attempts were made to create the desired "brown oil" rather than the golden oil of the first reaction. The second reaction resulted in golden oil again upon *in vacuo* concentration of the crude reaction mixture, though extraction with DCM, drying *in vacuo* again and extracting once more with THF afforded a thick green solution upon concentration. Yellow crystals of compound **2** ($(Mo^{V}O(OC_2H_4O)(\mu\text{-}OC_2H_4OH))_2(\mu\text{-}OC_2H_4)$), identified by SC-XRD (figure 3.2), -formed in the green oil, and, upon isolation

and drying, the crystals became opaque. Elemental analysis of this material was incorrect regarding the expected C/H % (~1% above C, ~2% below H) for the formula derived from SC-XRD. This synthesis was the first insight into dimerization, a process seemingly crucial for further clustering observed in reaction mixtures closer in colour to brown.

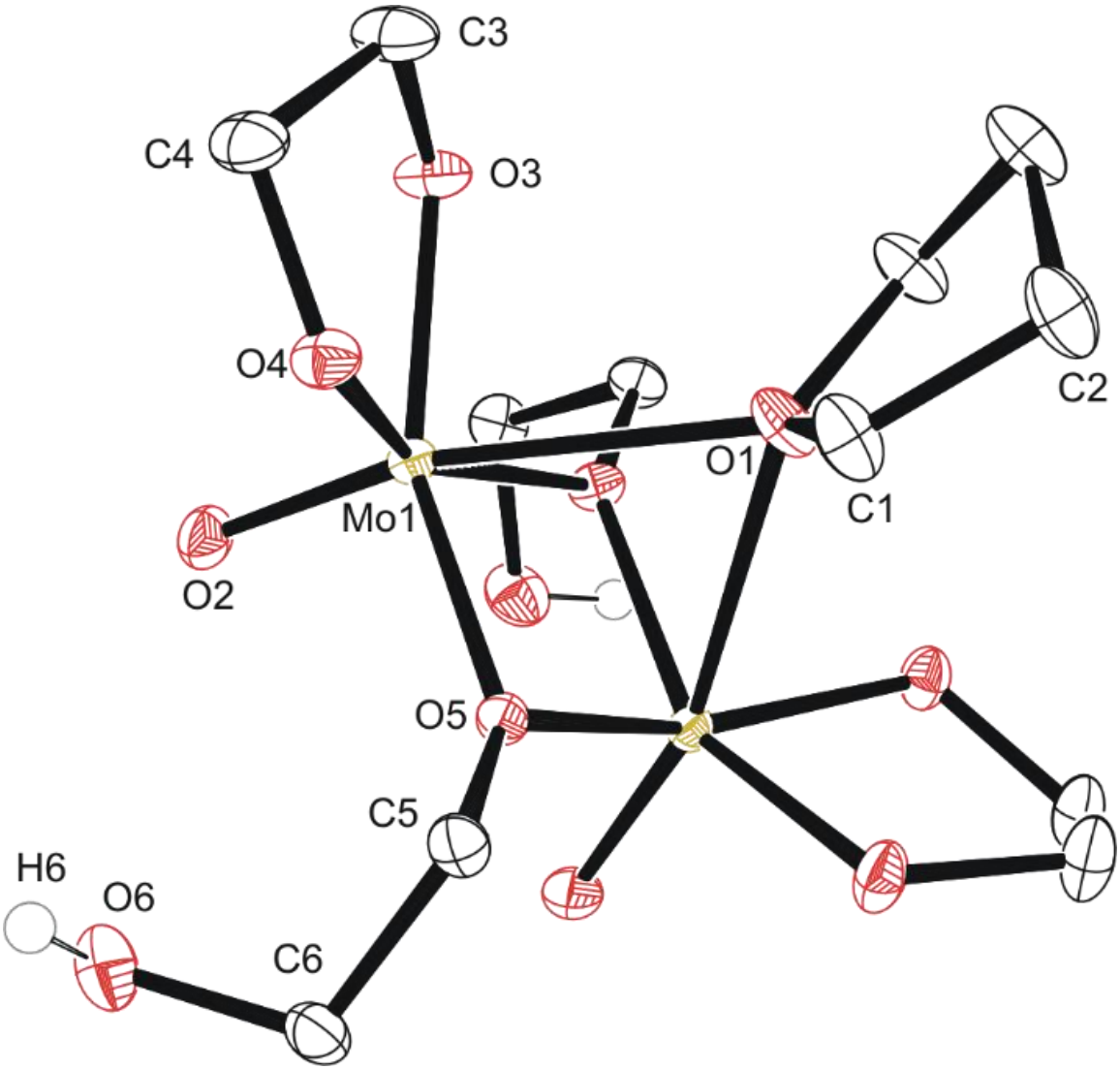

Figure 3.2 Molecular structure of compound **2** with anisotropic displacement ellipsoids projected at the 50% probability level. Methylene CH_2 hydrogen atoms have been omitted for clarity.

This is the first report of crystalline molybdenum dimers with each molybdenum bound to a single oxo group (-2), an ethylene glycoxide ligand (-2), and a bridging ethylene hydroxy glycoxide (-1) based on a Cambridge Structural Database (CSD, version 5.41 (Nov 2019)) search, though similar dimers with different ligands exist with similar bridging of the two Mo atoms by oxygen-based ligands. Few related molybdenum dimers have had their structure reported in the CSD, specifically with each Mo atom in the dimer containing a non-bridging single oxo ligand and a bidentate OC_2O structured ligand. One similar non-anionic dimer features a structurally similar bidentate mono-deprotonated tetramethyl ethylene glycol and two bridging methoxide ligands; however, this dimer is a *cis*-dioxo molybdenum compound rather than mono-oxo like compound **2**, which is also unique in having an additional bridging tetrahydrofuran ligand.[37] Other similar dimeric examples sometimes contain ammonium,[38] phopshonium,[39] alkali,[39] or alkaline earth[40,41] cations, co-crystallized solvents like water,[41,42] ethanol,[43] methanol,[44] toluene[45] or benzene.[46] Coordinating solvents like water,[41] ethanol,[43] or pyridine[38] along with bridging oxo,[38] alkoxide,[44,46] phosphate,[47] hydroxide,[48] oxalato,[38] citrato,[49] or dioxomolybdenum[50] groups either between the Mo dimer atoms or bridging pairs of dimers is also commonly observed. This is similar to the crystal structure observed for the polymeric compound **3**, **C5b** (Figure 3.3). Structure of small molybdenum clusters have direct relevance to the study of biologically important enzymes like nitrogenase, and this literature and work highlights many unique coordination states surrounding molybdenum with respect to small multidentate oxygen containing ligands (Figure 3.2).

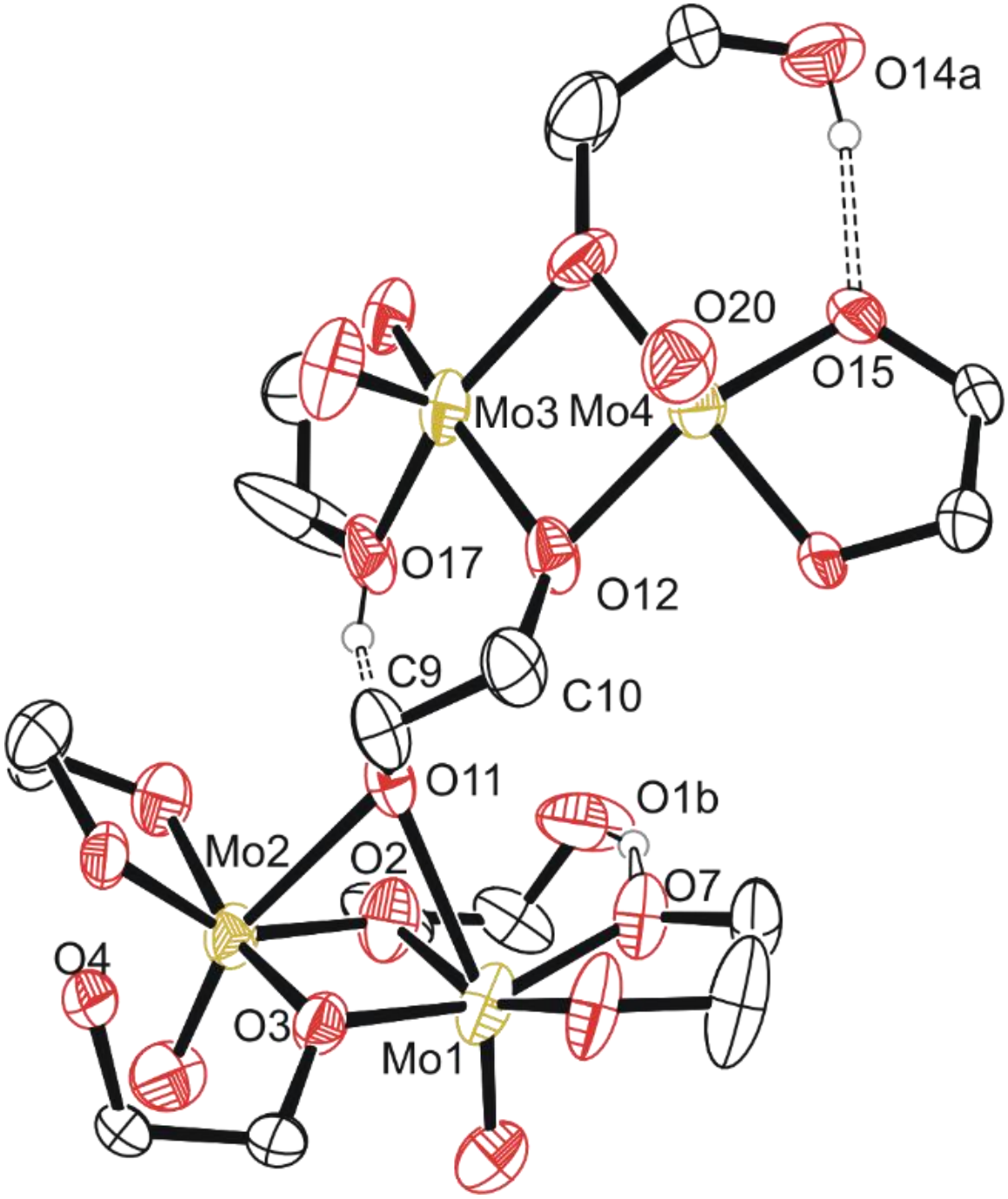

Figure 3.3 Molecular structure of compound **3** with anisotropic displacement ellipsoids projected at the 50% probability level. Methylene CH_2 hydrogen atoms have been omitted for clarity.

The polymeric structure of compound **3** (**C**5a) exhibits two unique bridging interactions with ethylene glycoxide ligands, bridging the molybdenum dimer atoms either parallel O11-(Mo1-Mo2) or perpendicular O12-(Mo3-Mo4) to the molybdenum/oxo double bond (Figure 3.4). An oxalic acid dimer was observed to undergo further dimerization through an oxalic acid bridging ligand; however, the presence of bridging oxo (O^{-2}) ligands may prevent further polymerization as the oxo bridging ligand tends to directly bridge the molybdenum atoms with no spacer like the C_2 backbone of ethylene glycoxides or oxalates resulting in increasingly larger clusters, rather than polymer comprised of the dimer units.[38,51,52] An additional example of an oxalate containing analogous molybdenum dimer polymer exists with R-MoO_2-R bridging units (R = Mo dimer, $(MoO(oxalato)(\mu\text{-}oxo))_2$) and cations; however, for this polymeric structure, the bridging MoO_2 unit is not directly involved in bridging the two Mo atoms in each dimer that was also observed for a phosphate bridged dimer.[47,50] This is not like what's observed for compound **3** with ligands involved in the polymerization coordinating through both molybdenum atoms of the dimer (Figure 3.4) rather than from one molybdenum atom to the second in another dimer molecule.

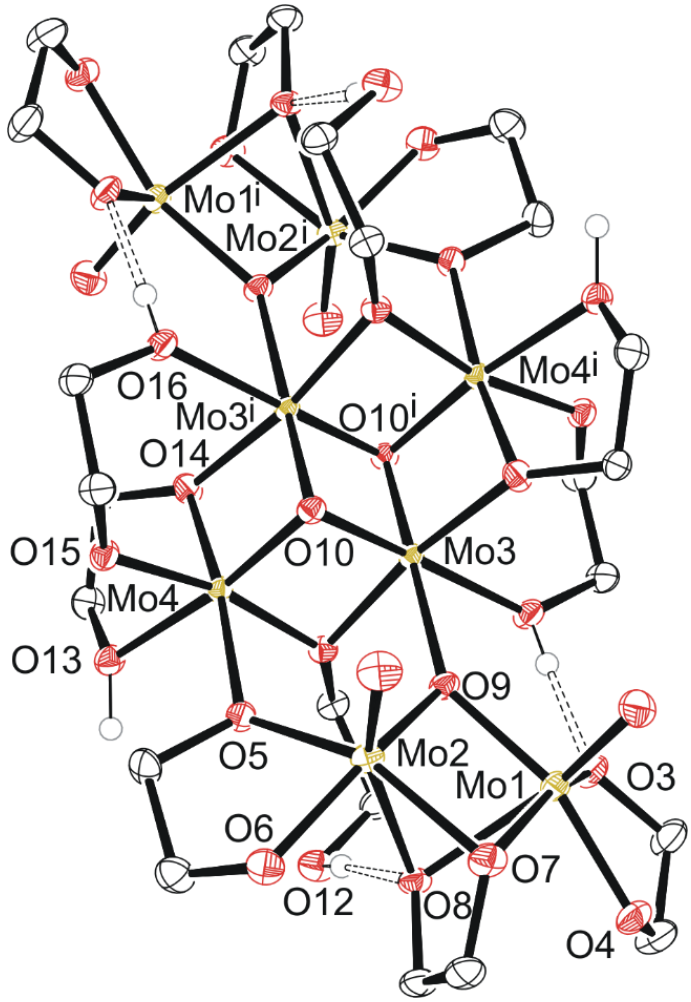

Figure 3.4 Molecular structure of compound **4** with anisotropic displacement ellipsoids projected at the 50% probability level. Methylene CH_2 hydrogen atoms have been omitted for clarity.

Compound **4**, **C6a** (Figure 3.4) exists as a cluster showing the octameric 8 molybdenum atoms consisting of a distinctly different core of four total with two Mo(V) dimers similar to **2** and **3** on each side of the core. Each dimer is equivalent across a symmetry element, and the dimers are held together by a μ-oxo ligand and one of the two oxygen atoms of the bidentate ethylene glycoxide that attaches the dimer to the tetrameric central core. Each dimer also has a bridging ethylene glycoxide ligand bound directly to

both molybdenum atoms. The central tetrameric core has two distinct molybdenum atoms as well, forming a diamond shape. Mo atom #3 and symmetry equivalent Mo#3^{i} (Figure 3.4) exists with three μ_3-oxo ligands, a neutral monodentate ethylene glycol hydroxy ligand, and two μ-ethylene glycoxide ligands.

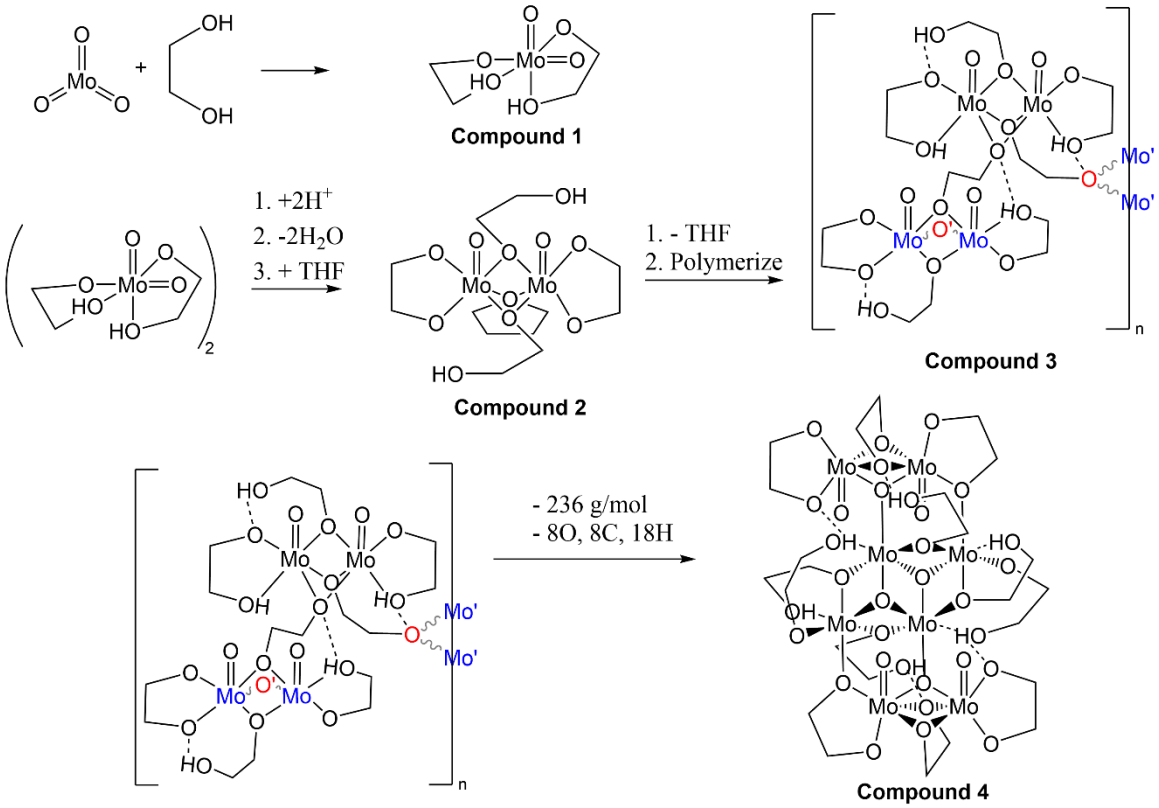

Scheme 3.3 Potential route to each of the compounds produced during the attempted synthesis of the molybdenum precursor.

From Table 3.4, the mass of **1-4** is ~250, 538, 932, and 1766 g/mol, respectively. Assuming **1** turns into **2** then into **3** and finally **4**, one pathway (Scheme 3.3) regarding conservation of mass would be for two molecules of **1** (2×250 g/mol) to be protonated (+ 2×1 g/mol) followed by loss of $2H_2O$ (- 2×18 g/mol) while gaining the THF unit (+ 72 g/mol) to equal 538 g/mol as **2**. Subsequent loss of THF (466 g/mol) and polymerization

through ethylene glycol fragments affords **3** with discreet dimers with a mass equal to twice that of **2**-THF, ~932 g/mol. The final conversion from two molecules of **3** into **4** requires a shift from 932+932 = 1864 g/mol (2×**3**) into 1628 g/mol (excluding 2× ethylene glycol solvent molecules of **4**). This is a net loss of 236 g/mol comprised of 8 oxygen, 8 carbon, and 18 hydrogen atoms, which could equate to the loss of three ethylene glycol and two carbon monoxide molecules. The central cluster contains 2 oxo groups to 4 molybdenum, implying loss of 4 oxygen atoms through loss of oxo groups between a pair of dimers is necessary for creation of the central tetrameric core of **4**. This could be mediated by protonation from hydroxy groups from solvent ethylene glycol, entirely hydrogen-bound ethylene glycol molecules such as that observed in the crystal structure of **4**, or through the singly deprotonated ethylene glycol mono- or bidentate ligand (2-hydroxyethyl-1-oxo) commonly observed hydrogen bonding intramolecularly such as in the crystal structures of 1 and **2** monodentate ligand (Table 3.5). The complexity of this final conversion if this is the route towards formation of **4**, is too great for any degree of certainty for its formation, and more work is needed to determine if this is produced from partial dissolution of MoO_3.

Based on the formula of the Mo1-Mo2 dimer, a doubly bridging bidentate ethylene glycoxide ligand is possible, meaning singly bridging mono-deprotonated ethylene glycol ligands observed in crystal structures of **2-4** could participate in proton transfer. This could result in a variety of observed intramolecular motifs such as the bidentate non-bridging ethylene glycoxide oxygen atoms and oxo groups.

Table 3.4 Crystal data and structure refinement for compounds **1-4**.

Compound	**1**	**2**	**3**	**4**
Crystal	**C1a**	**C2a**	**C5a**	**C6a**
Empirical formula	$C_4H_{10}MoO_6$	$C_{12}H_{26}Mo_2O_{11}$	$C_{16}H_{36}Mo_4O_{20}$	$C_{28}H_{66}Mo_8O_{36}$
Colour	Colourless	Yellow	Yellow	Red
Formula weight	250.06	538.21	932.21	1746.32
Temperature/K	100.0	125.0	125.0	125.0
Crystal system	tetragonal	orthorhombic	orthorhombic	triclinic
Space group	$P4_1$	Fdd2	$Pna2_1$	P-1
a/Å	9.46450(10)	16.7363(3)	34.2851(19)	8.5318(4)
b/Å	9.46450(10)	24.6210(5)	9.7131(5)	11.0284(5)
c/Å	17.3160(4)	8.8062(2)	8.4881(4)	14.5245(7)
α/°	90	90	90	81.706(2)
β/°	90	90	90	77.862(2)
γ/°	90	90	90	69.992(2)
Volume/$Å^3$	1551.11(5)	3628.72(13)	2826.7(3)	1251.55(10)
Z	8	8	4	1
$\rho_{calc}g/cm^3$	2.142	1.970	2.191	2.317
μ/mm^{-1}	1.675	1.436	1.819	2.040
F(000)	992.0	2160.0	1840.0	858.0
Crystal size/mm^3	0.34 × 0.265 × 0.225	0.16 × 0.16 × 0.115	0.24 × 0.12 × 0.12	0.12 × 0.07 × 0.04
Radiation	MoKα (λ = 0.71073)	MoKα (λ = 0.71073)	MoKα (λ = 0.71073)	MoKα (λ = 0.71073)
2Θ range for data collection/°	4.304 to 89.996	5.482 to 90.582	4.358 to 72.67	4.694 to 67.802
Index ranges	$-18 \le h \le 17$, $-15 \le k \le 18$, $-34 \le l \le 34$	$-32 \le h \le 33$, $-49 \le k \le 49$, $-15 \le l \le 17$	$-57 \le h \le 57$, $-16 \le k \le 16$, $-14 \le l \le 14$	$-13 \le h \le 13$, $-17 \le k \le 17$, $-22 \le l \le 22$
Reflections collected	110585	39690	281817	126602
Independent reflections	12760 [R_{int} = 0.0334, R_{sigma} = 0.0174]	7050 [R_{int} = 0.0568, R_{sigma} = 0.0487]	13709 [R_{int} = 0.0390, R_{sigma} = 0.0163]	10104 [R_{int} = 0.0407, R_{sigma} = 0.0176]
Data/restraints/parameters	12760/4/213	7050/1/116	13709/17/428	10104/3/355
Goodness-of-fit on F^2	1.109	1.008	1.092	1.075
Final R indexes [I>=2σ (I)]	R_1 = 0.0206, wR_2 = 0.0511	R_1 = 0.0309, wR_2 = 0.0467	R_1 = 0.0655, wR_2 = 0.1341	R_1 = 0.0219, wR_2 = 0.0528
Final R indexes [all data]	R_1 = 0.0222, wR_2 = 0.0521	R_1 = 0.0485, wR_2 = 0.0508	R_1 = 0.0683, wR_2 = 0.1353	R_1 = 0.0267, wR_2 = 0.0554
Largest diff. peak/hole / e $Å^{-3}$	0.90/-1.55	0.83/-0.67	1.42/-2.23	1.30/-1.21
Flack parameter	0.03(2)	-0.015(16)	0.05(8)	N/A

The protic nature of the solvent and ligands allows for the ability couple molybdenum clusters via protonation of the bridging ethoxide, dissociation or rearrangement of the newly formed hydroxy group, insertion of the newly formed ethoxide

ligand, with the intermediate cationic dimer. The presence of a bridging oxo group between molybdenum atoms of the dimer and the central tetramer of compound **4** could be the result of hydrolysis of the C-O bond of a bridging ethylene glycoxide unit, forming a bridging hydroxy group OH. If this bridging hydroxy group were to encounter a Mo-OH, loss of water and formation of the observed triply bridging oxo groups partially bonding the central tetramer with the outer dimers. Much of this is speculative; however, possible steps are presented by which interconversion from the monomeric $MoO_2(OC_2H_4OH)$ to larger clusters observed in this work may occur. The opposite may be true as well with incomplete dissolution resulting in the clusters, undergoing reduction and extensive hydrolysis, loss of water, and formation of ethylene glycol units.

Table 3.5 Hydrogen bonding interactions observed for compounds **1-4**.

D	H	A	d(D-H)/Å	d(H-A)/Å	d(D-A)/Å	D-H-A/°
Compound **1** – $MoO_6C_4H_{10}$						
O4	H4	O3[1]	0.852(13)	1.851(14)	2.7000(18)	174(4)
O6	H6	O9	0.854(13)	1.836(19)	2.6407(17)	156(4)
O10	H10	O5[2]	0.855(13)	1.808(15)	2.6515(16)	169(4)
O12	H12	O11[3]	0.75(4)	1.76(4)	2.5047(17)	171(4)
Compound **2** – $Mo_2O_{10}C_8H_{18}$•(OC_4H_8, THF)						
O6	H6	O3[4]	0.89	1.93	2.814(2)	174.3
Compound **3** – $Mo_4O_{20}C_{16}H_{36}$						
O1B	H1B	O7	0.84	1.96	2.69(3)	144.8
O5	H5	O4	0.873(13)	1.82(2)	2.582(9)	144(3)
O14A	H14C	O15	0.84	1.86	2.680(13)	166.4
O14B	H14D	O20[5]	0.84	2.18	2.80(3)	130.4
O17	H17	O11	0.874(13)	1.77(2)	2.562(10)	149(3)
Compound **4** – $Mo_8O_{32}C_{24}H_{54}$•2($C_2H_4(OH)_2$, ethylene glycol)						
O12	H12	O8	0.74(3)	1.95(3)	2.686(2)	174(4)
O13	H13	O17	0.94(3)	1.62(3)	2.552(2)	170(3)
O16	H16	O3[6]	0.77(3)	1.73(3)	2.4891(19)	174(4)
O17	H17	O12	0.77(3)	1.89(3)	2.657(2)	171(4)
O18	H18	O4[7]	0.773(17)	1.963(18)	2.720(2)	166(3)

Symmetry operators for relevant hydrogen bonding interactions indicated with superscripts on acceptor atoms. 1: 1+Y,2-X,-1/4+Z; 2: 2-X,1-Y,1/2+Z; 3: +Y,2-X,-1/4+Z; 4: 3/4-X,1/4+Y,-1/4+Z; 5:1-X,1-Y,-1/2+Z; 6: 1-X,1-Y,1-Z; 7: -1+X,1+Y,+Z.

One additional unexpected crystalline material was obtained (compound **5**) through quenching an electrodeposition solution containing 1.5 mL 0.1 M PP13-TFSI in THF with 0.05 mL 1,4-butanedithiol and 0.05 mL **B3a**. Addition of 5% bleach afforded a biphasic solution with a blue and colourless layer, along with and precipitation of ~5-30 mg golden yellow prisms at the interphase. Analysis by SC-XRD indicates the decomposition of the ionic liquid via anion exchange by forming $[PP_{13}]_2[Mo_6O_{19}]$ (Figure 3.5).

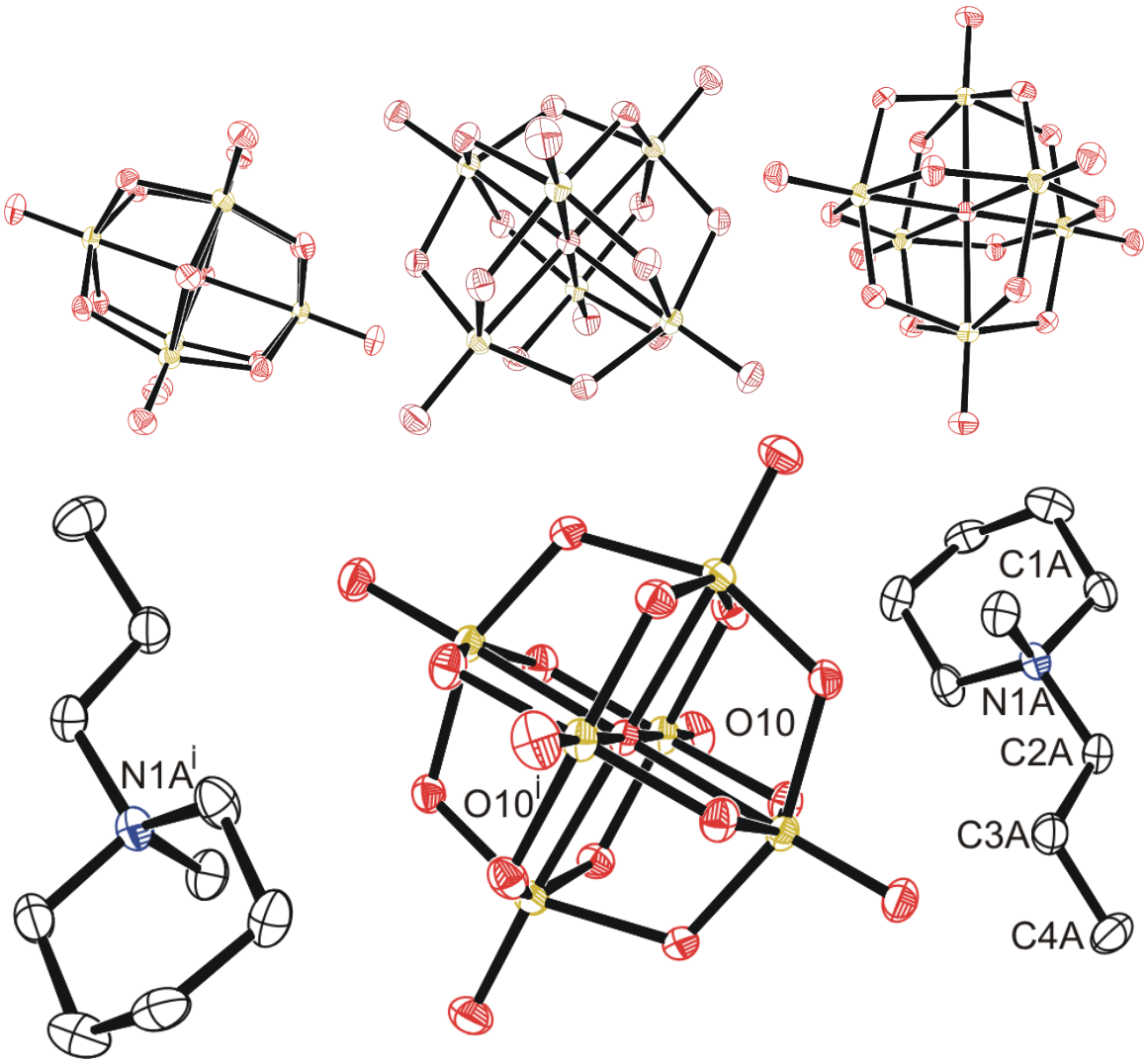

Figure 3.5 Molecular structure of compound **5** with anisotropic displacement ellipsoids projected at the 50% probability level. Hydrogen atoms have been omitted for clarity. From top left to right represent views of the dianion $[Mo_6O_{19}]^{2-}$ down the 100, 010, and 001 axis, respectively. The bottom image represents the complete structure of compound **5**; $[PP13]_2[Mo_6O_{19}]$. Oxygen = red, molybdenum = yellow.

3.3.3 Ratio of Molybdenum and Oxygen

Table 3.6 shows relevant Mo:O ratios observed within six SC-XRD samples showing the ratio of Mo:O drops as the colour of the oil the crystal was isolated from (and the crystal itself) darkens. Compound **1** isolated from **C1a**, **C2b**, and **C3a** has the highest

Mo:O ratio of 1:6, while a drop is observed for the dimeric **2** from **B2a** green oil (1:5.5), the dimer-polymer **3** from **B5a** golden-brown oil (1:5), and the larger cluster **4** observed from **B6a** brown oil with either 1:4 as just the cluster, or 1:4.25 accounting for ethylene glycol solvation. Compounds **5** and **6** feature the lowest Mo:O ratios of 1:3.17 and 1:3.33 for the molybdenum oxide clusters $[Mo_6O_{19}]^{-2}$ and $Mo_{12}O_{40}$, respectively.

Table 3.6 Mo:O ratios for each of the isolated crystalline samples from molybdenum precursor synthesis (**1**-**4**), electrochemical experiments (**5**), and hydrolysis (**6**).

Crystal/solid	Mo:O ratio in crystal, reduced Mo:O ratio
1	1:6
2	2:11, (1:5.5)
3	4:20, (1:5)
4	8:(32 cluster + 4 co-crystallized solvent), (1:4 cluster, 1:4.25 co-crystallized solvent)
5	6:19, (1:3.17)
6	12:40, (1:3.33)

3.3.4 Electrochemistry

Electrochemical studies began with analysis of relevant precursors (1,4-butanedithiol, ethylene glycol, **B3a**, and **B6a**) within an electrolyte solution of 0.1M PP13-TFSI in THF. Various electrodeposition techniques were employed including potentiodynamic (CV), potentiostatic (chronoamperometry (CA), or bulk electrolysis (BE)) in either 0.1 M PP13-TFSI in THF or in the pure PP13-TFSI ionic liquid (with heat).

The glassy carbon electrode was cleaned by polishing with 5 μm alumina on a wet polishing pad, and rinsing with water and then acetone, and drying in a vacuum desiccator overnight. Screen printed platinum electrodes were cleaned by immersion in concentrated sulfuric acid for ~20 minutes, rinsing with deionized water, immersion in 10-20% HNO_3 for ~20 min, and rinsing again with deionized water. This was followed by immersion in a

20 mL scintillation vial in 0.5 M H_2SO_4 made up with Milli-Q water (countered by the internal Pt and referenced to an external Ag/AgCl electrode in sat. KCl Gel). The electrodes were cycled from -0.2 V to +1.0 V at a rate of 250-300 mV/s until a cyclic voltammogram consistent with clean platinum was obtained with significant overlap of multiple cycles (Figure 3.6). Each of the five Pt SPE's used have their clean Pt voltammogram presented to show a rough relative surface area.[53] Pt Screen Printed Electrode (SPE) #5 has the lowest area, followed by Pt SPE #1, and Pt SPE #2-4 have relatively similar real electrochemical surface areas.

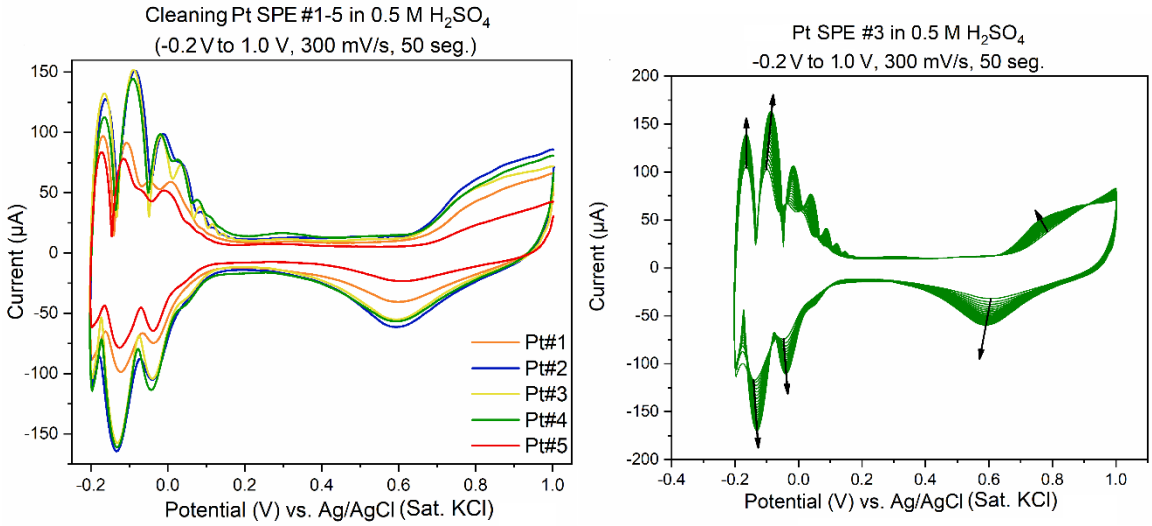

Figure 3.6 Final cyclic voltammogram of Pt SPE #1-5 (left) and 25 cycles of Pt SPE #3 (right) immersed in 0.5 M H_2SO_4 within a window of -200 to 1000 mV vs. Ag/AgCl in sat. KCl gel. Difference in current indicates a difference in available surface area to transfer or receive more electrons, registering as a greater magnitude of total current. Current also increases within increasing scans from cleaning the surface of the electrode, opening up more of the platinum surface to adsorb hydrogen (- V) or oxygen (+ V) atoms.

3.3.5 Electrochemistry of 0.1 M PP13-TFSI in THF

The supporting electrolyte used for electrochemical studies was 0.1 M PP13-TFSI in THF that possesses an electrochemical double layer window of -1.25 to 0.5 V conducted

within a 50-100 ppm O_2 glovebox using a platinum screen-printed electrode (Pt SPE) as a working electrode (WE) along with use of the internal platinum counter electrode (CE), with external reference to an Ag/Ag^+ (0.1 M PP13-TFSI in THF) reference electrode (RE) separated via a small ceramic frit (Figure 3.7). The potentiostat, a laptop, and the electrochemical cell were all present within the glovebox and manipulations were carried out entirely within the open atmosphere of the glovebox that had an oxygen content less than 100 ppm. For these preliminary studies, PP13-TFSI showed significant electrochemical stability far exceeding that of aqueous solutions that readily evolve hydrogen below -0.2 V (in 0.5 M H_2SO_4). This is a key advantage of non-aqueous electrochemistry that allows for very low voltage cathodic reduction, which appears important for reduction of molybdenum precursors directly into crystalline MoS_2 rather than amorphous films of MoS_x. Rather than using an alternate electrolyte solution, PP13-TFSI was used as the electrolyte in case something about it is necessary for the conversion of these precursors to molybdenum disulfide; however, cheaper, more environmentally friendly alternative ionic liquids may be more effective and could also be explored in future work in this area.

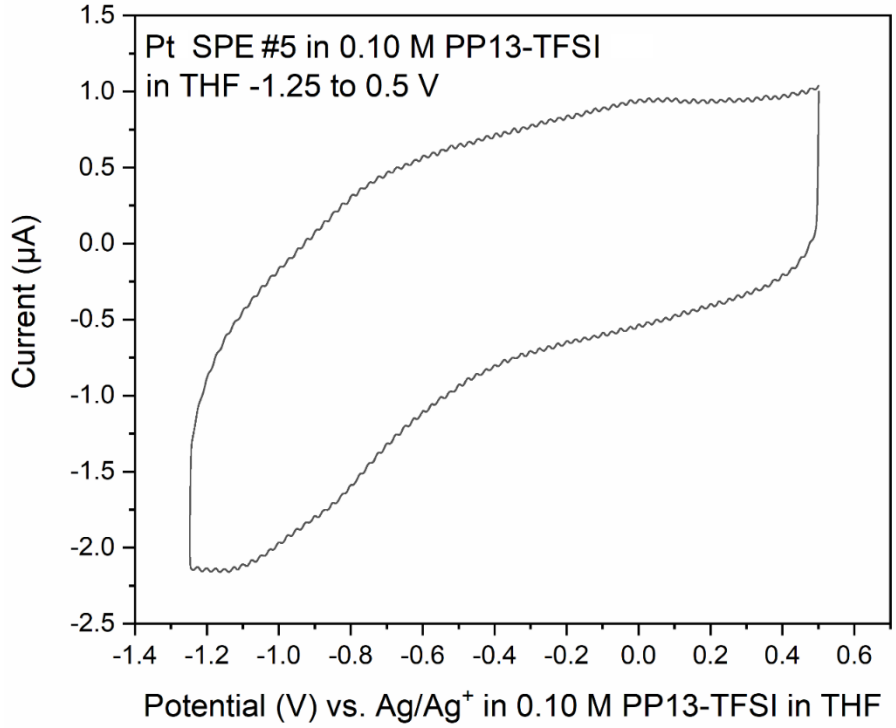

Figure 3.7 Double layer cyclic voltammogram showing the electrochemical window for the Pt SPE (-1.25 to 0.5 V) within the 0.1 M PP13-TFSI in THF supporting electrolyte solution (CE = Pt, RE = Ag/Ag^+ in 0.1 M PP13-TFSI). Sweep rate = 50 mV/s.

Initial exploration of the full electrochemical window of PP13-TFSI in THF (Figure 3.7) exhibited significant oxidation above +0.5 V with subsequent reduction occurring between -0.25 V and 0 V on the cathodic sweep. The first window scanned was -2.7 V to +1.8 V, resulting in significant oxidation occurring above +1.0 V and a reduction event at -0.1 V with very little further activity. When the window was reduced to -1.0 V to +2.0 V, a significant oxidation above +1.0 V was observed with a broad reduction beginning at ~ +0.2 V, peaking at -0.24 V, reaching near baseline around -1.0 V. Changing the window to -1.6 V to +1.0 V results in a similar oxidation behaviour occurring at ~ +0.5 V. The cathodic region for this electrolyte is large, with little current registered to nearly -2.7 V. When the window of -3.0 V to +0.7 V was explored, reduction occurring from -2.0 V to -3.0 V

resulted in an oxidation event on the following anodic sweep at -0.48 V. This work indicates that this ionic liquid is effective for depositions at negative voltages proposed by Murugesan et al.; however, positive voltages above +1.0 V result in oxidation of the ionic liquid or THF on platinum and should thus be avoided.

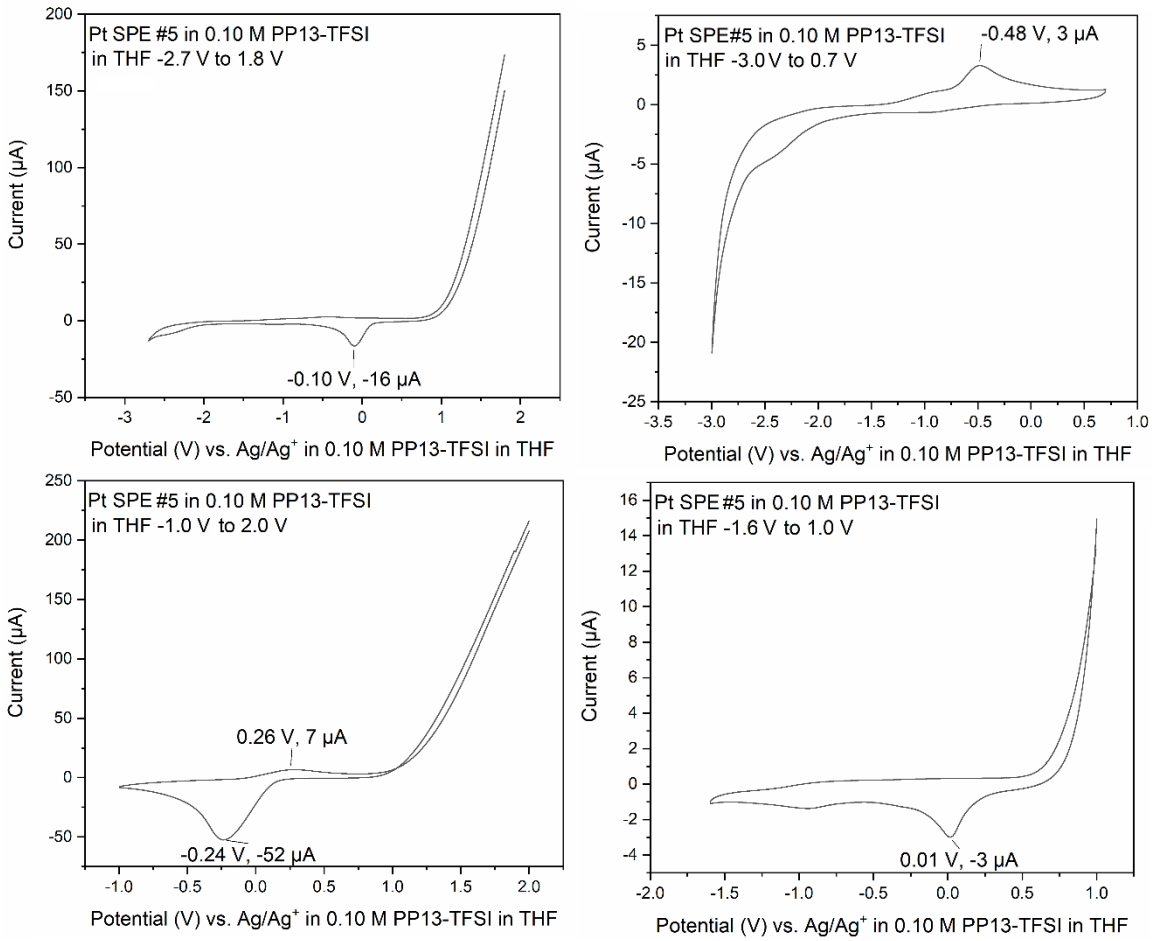

Figure 3.8 Electrochemical window elucidation for the 0.10 M PP13-TFSI in THF solution used for later electrochemical studies. Order of collection on the same electrode in solution follows top left (100 mV/s), top right (50 mV/s), bottom left (50 mV/s), then bottom right (50 mV/s).

On a glassy carbon WE with a platinum wire CE referenced to Ag/Ag^+ (0.1 M PP13-TFSI in THF), the electrochemical window (Figure 3.9) was stable between -0.75 V to

+0.50 V and -1.25 V to +0.50 V. Reduction was observed beginning below roughly -1.6 V; however, a relatively smooth electrochemical window between -2.0 V to +0.5 V was also observed. Altering the electrochemical window to -2.7 V to +0.5 V resulted in a broad reduction with two main features at roughly -2.2 and -2.7 V, respectively, causing a broad asymmetric oxidation signal spanning -1.75 to -0.5 V with a peak at -0.9 V. In general, this shows that both electrode materials within this ionic liquid are suitable for deposition.

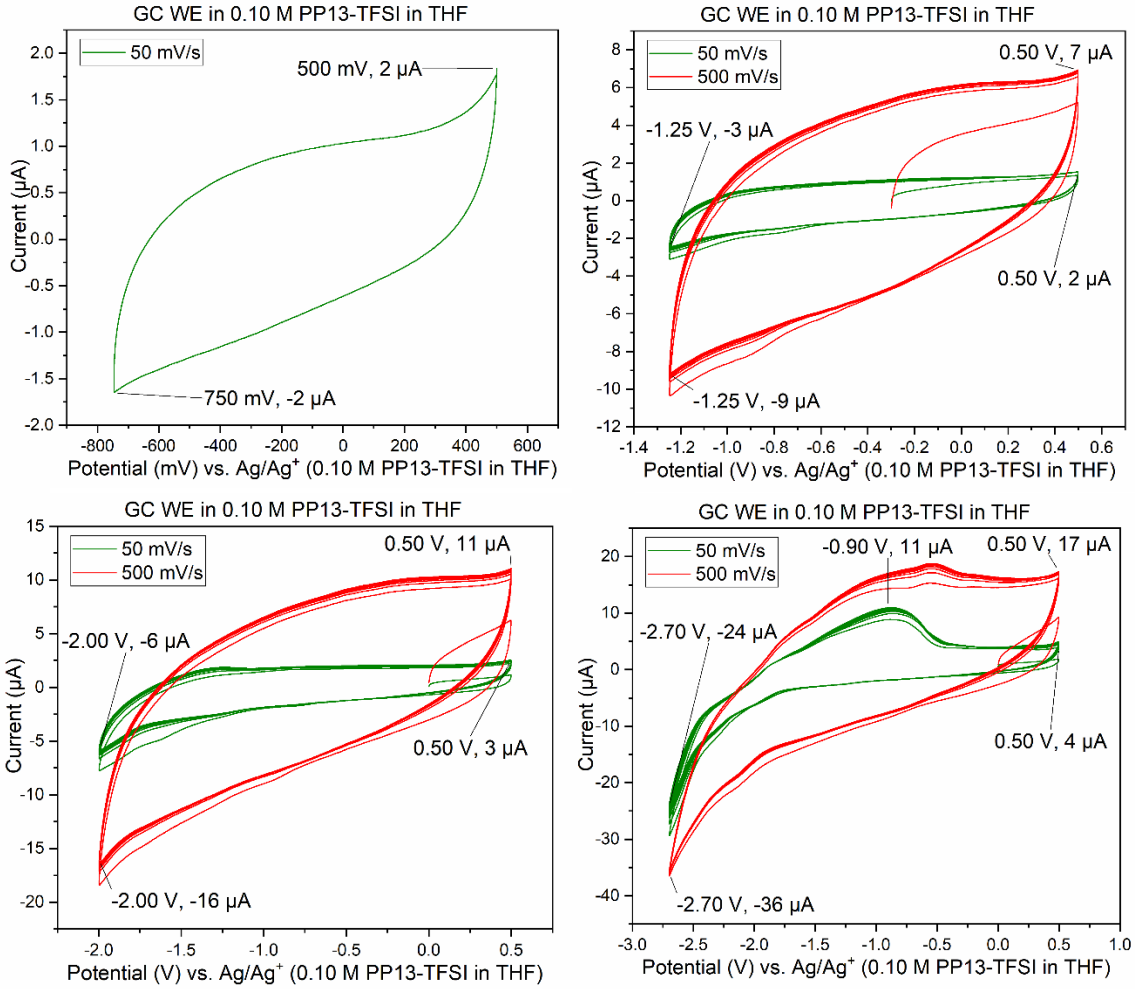

Figure 3.9 Electrochemical window elucidation for the 0.10 M PP13-TFSI in THF solution used for later electrochemical studies. For all but the first chromatogram, 6 cycles are shown for each sweep rate of either 50 (green) or 500 (red) mV/s.

Following the characterization of the electrochemical window of the 0.10 M PP13-TFSI in THF, 1.5 mL of this solution had 0.05 mL of various reagents present during MoS_2 electrodeposition attempts as detailed later. The reagents studied include ethylene glycol, 1,4-butanedithiol, a mixture of ethylene glycol and 1,4-butanedithiol, and molybdenum precursors (**B3a**, **B6a**), the "gold" and "brown" oils, respectively.

3.3.6 Electrochemistry of 1,4-butanedithiol in 0.1 M PP13-TFSI in THF

To better understand the electrochemical behaviour of 1,4-butanedithiol and other reagents under these electrochemical conditions, some control experiments were performed. Cycling between -2.7 V and +1.0 V using Pt SPE #1 at 50 mV/s within a solution containing 1.5 mL of 0.1 M PP13-TFSI in THF and 0.05 mL 1,4-butanedithiol resulted in clearly defined oxidation and reduction peaks with significant separation of peak voltages of roughly 2 V (Figure 3.10).

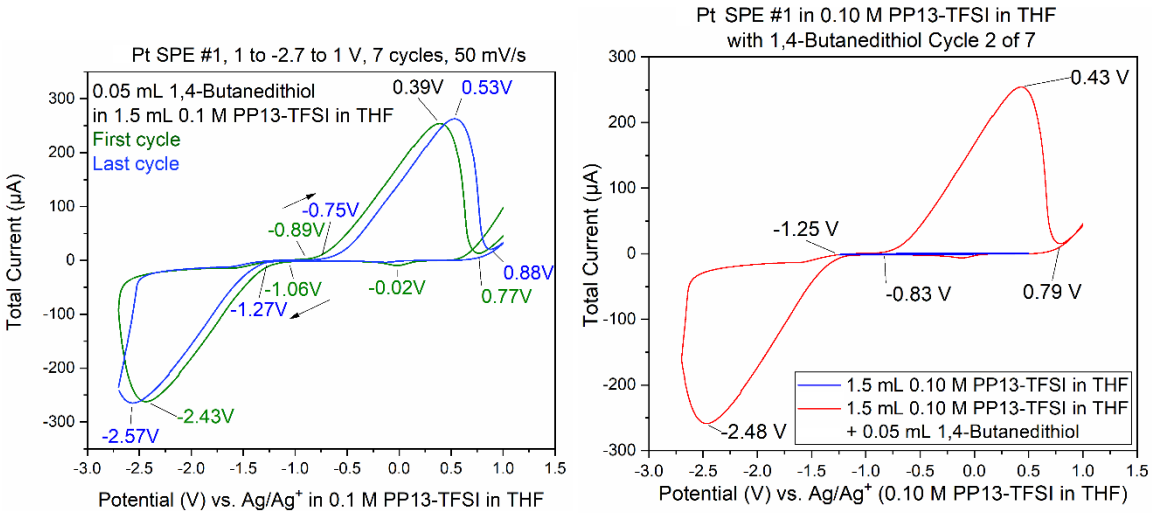

Figure 3.10 CV of 0.05 mL 1,4-butanedithiol added to 1.5 mL of 0.1 M PP13-TFSI in THF cycled between -2.7 V to +1.0 V at 50 mV/s. Left shows the difference between first and last cycles, while right displays the second cycle alongside a cycle in pure 0.1 M PP13-TFSI in THF.

Adsorption onto the platinum surface upon cathodic reduction may occur below roughly -1.2 V, registering current that rapidly dissipates with a maximum current at roughly -2.5 V, decreasing towards -2.7 V. Beginning the anodic sweep from -2.7 V to +1.0 V also occurs with a sharp drop in current. This indicates adsorption of the material to the electrode surface, and desorption is observed above roughly -0.8 V. Support is provided by SEM-EDS analysis of the electrode surface following the proposed desorption process which is free of sulfur (Figure 3.11). This characterization indicates that the 1,4-butanedithiol is electrochemically active within PP13-TFSI in THF and is undergoing an electron transfer process below -1.2 V, and above -0.8 V upon the following anodic sweep.

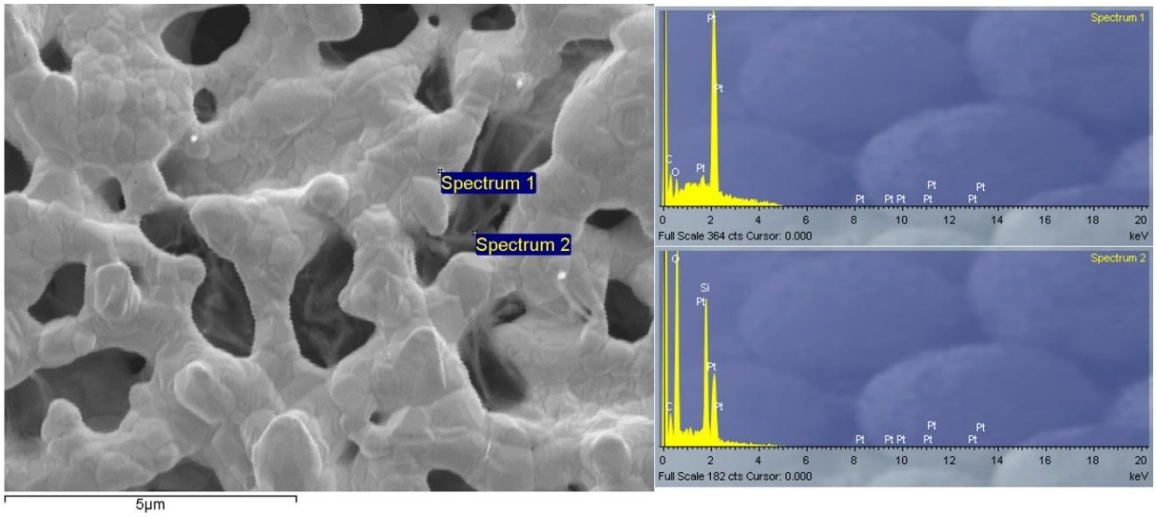

Figure 3.11 SEM-EDS analysis of Pt SPE #1 following electrochemistry within 1.5 mL 0.1 M PP13-TFSI in THF with 0.05 mL 1,4-butanedithiol with the corresponding SE reference image (left).

3.3.7 Electrochemistry of ethylene glycol in 0.1 M PP13-TFSI in THF

Ethylene glycol was chosen as an analyte due to the residual presence of ethylene glycol within the molybdenum precursors so that a comparison between the two could be made. As an additional comparison to the blank 0.1 M PP13-TFSI in THF solution,

ethylene glycol provided a beneficial reference for these products through their distinct difference in electrochemical behaviour upon cathodic reduction. To 1.5 mL PP13-TFSI in THF, 0.05 mL ethylene glycol was added. Cycling potentiodynamically between -2.7 V and +1.0 V at 50 mV/s resulted in the appearance of a significant resistive (diagonal) component in the CV beginning at roughly -1.0 V (Figure 3.12). Appearance of this resistive component in the CV indicates that there is resistance for current flow which may be due to the increased viscosity of the electrolyte after addition of ethylene glycol, which may impede electron flow. Two oxidation events occur during the anodic sweep at roughly -0.9 V and -0.3 V that may correspond with desorption and/or phase reorientation of the ethylene glycol from the WE surface.

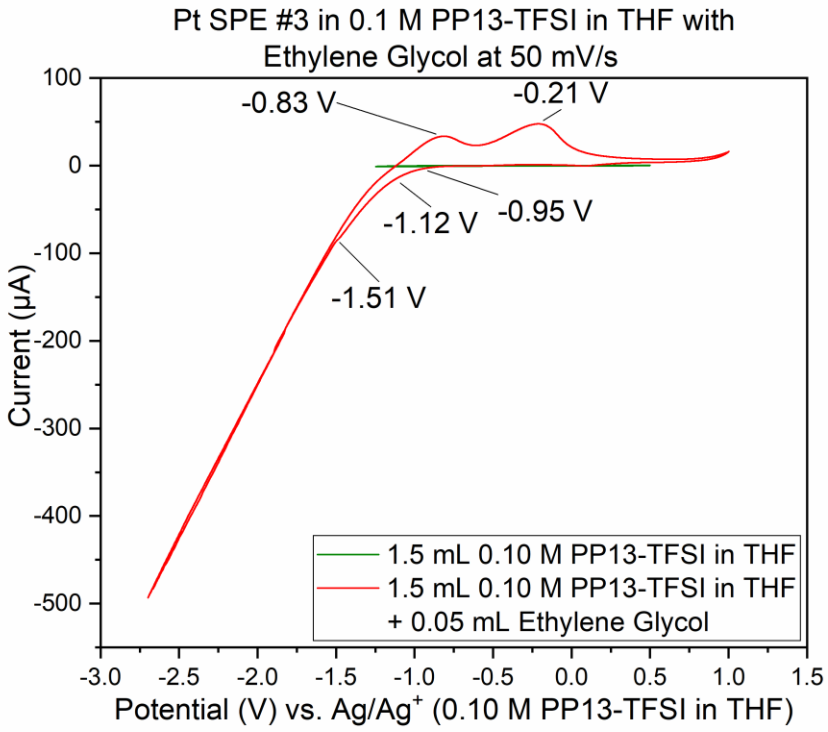

Figure 3.12 CV of 0.05 mL ethylene glycol added to 1.5 mL 0.1 M PP13-TFSI in THF cycled between -2.7 V to +1.0 V.

3.3.8 Ethylene glycol and 1,4-butanedithiol in 0.1 M PP13-TFSI in THF

Following the previous experiments with 1,4-butanedithiol and ethylene glycol, 0.05 mL of both analytes were added to 1.5 mL PP13-TFSI in THF and the cyclic voltammetry was run as before (Figure 3.13). This combination was explored to see if electrochemical behaviour would differ for the two pure compounds for comparison with mixtures of molybdenum and sulfur precursor solutions. A drop in current upon cathodic reduction is observed around -1.0 V, overlapping with the anodic sweep until ~ -1.0 V. Between -1.0 V and -0.5 V nothing occurs on the anodic sweep, and this is where the first of the two ethylene glycol peaks were observed (-0.86 V). Addition of ethylene glycol appears to prohibit the redox chemistry of the pure 1,4-butanedithiol as observed in Figure 3.10.

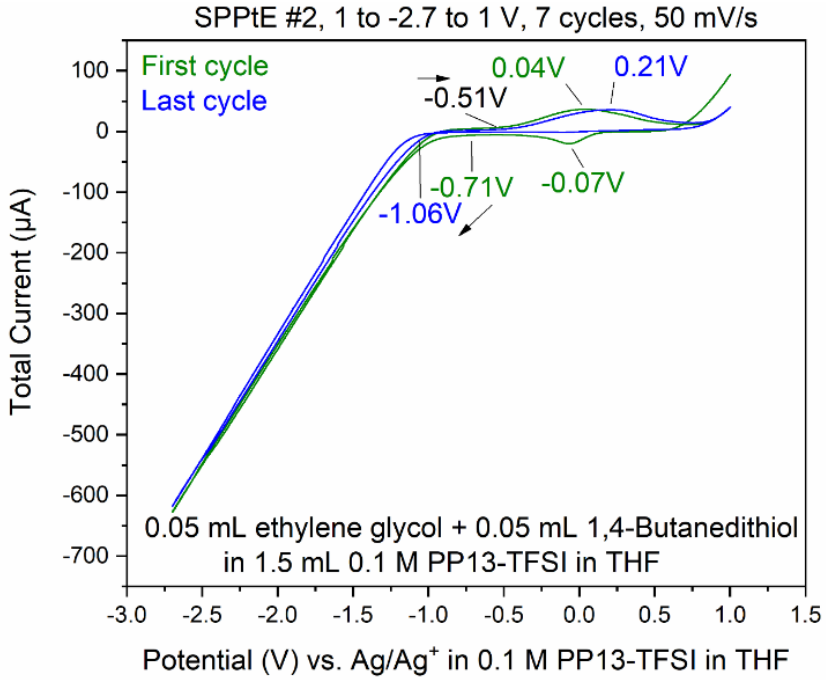

Figure 3.13 CV of a mixture of 0.05 mL ethylene glycol and 0.05 mL 1,4-butanedithiol added to 1.5 mL 0.1 M PP13-TFSI in THF with 7 cycles between -2.7 V to +1.0 V.

3.3.9 Molybdenum Precursors in 0.1 M PP13-TFSI in THF

The molybdenum precursors inevitably contained residual ethylene glycol, resulting in the desire to compare electrochemical behaviour between pure ethylene glycol, the gold-coloured **B3a**, and the brown oil **B6a**. Comparison of 0.05 mL ethylene glycol and 0.05 mL **B3a** within the 1.5 mL PP13-TFSI in THF solution resulted in significant differences between pure ethylene glycol and the molybdenum saturated golden oil **B3a** (Figure 3.14).

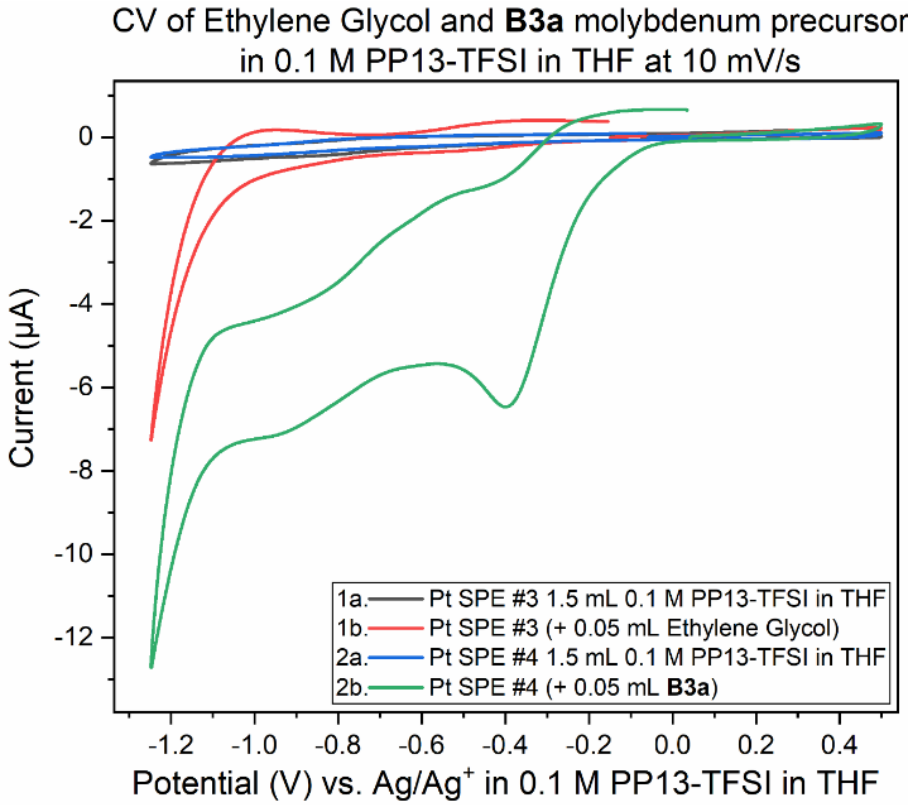

Figure 3.14 Cyclic voltammogram sweep from Open Circuit Potential (OCP) to +0.5 V, then to -1.25 V and back to the starting voltage for solutions of 1.5 mL 0.1 M PP13-TFSI in THF with the addition of 0.05 mL ethylene glycol (left) or B3a (right) at 10 mV/s.

Two Pt SPE (#3 and #4) with similar electrochemical surface area (Figure 3.6, total current very similar in 0.5 M H_2SO_4)[54] were used for this study. Initial cycling from -1.25

V to +0.5 V in the solution pre-analyte resulted in a clean voltammogram (Figure 3.14). Subsequent addition of each analyte and repeat scanning at 10 mV/s from OCP to +0.5 V, down to -1.25 V and back to the original OCP voltage gave rise to a stark difference. The choice to scan from open circuit potential was to avoid initial oxidation or reduction which could occur otherwise. Ethylene glycol alone maintained the same double layer as the blank solution until roughly -0.7 V during the cathodic sweep, with significant reduction beginning around -1.0 V. The **B3a** in contrast had a drop in current beginning at about 0 V, with a peak at -0.4 V. Additional drop in current is observed beginning at -0.7 V with another drop below -1.1 V. The current registered with **B3a** is greater than that of ethylene glycol; however, the initial blank solution scanned with each electrode was very similar. Upon anodic sweeping from -1.25 to +1.0 V, **B3a** gave had a rise in current between -1.25 and -1.1 V, with a very broad rise between -0.8 and -0.4 V. Though a different scan rate was used analyzing the brown oil **B6a**, it is very clear that **B3a** and **B6a** have very different electrochemical features upon cycling once from -1.25 V to +0.5 V (Figure 3.15). The golden-coloured **B3a** displays reduction events at ~ -0.4 V and ~ -0.6 V, beginning a resistive drop in current at ~ -1.0 V (Figure 3.14). In contrast, the brown-coloured oil **B6a** has no reductive event at ~ -0.4 V which is the major distinct feature of the CV containing **B3a**. Unlike ethylene glycol or **B3a**, **B6a** is observed to begin a cathodic reduction beginning at ~ -0.6 V which does match a reduction event of **B3a**; however, there exists no analogous plateau in current like that observed for **B3a** prior to the resistive drop in current below -1.0 V observed for both pure ethylene glycol and **B3a**. A unique observation within the **B6a** sample is a broad oxidation event occurring at ~ -0.6

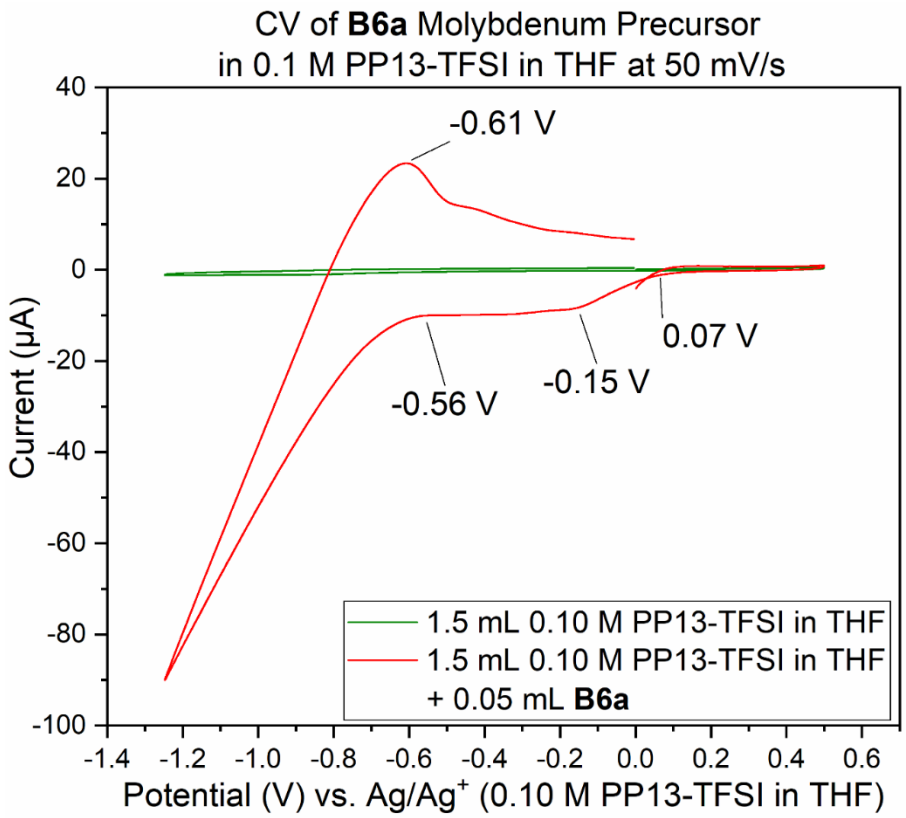

Figure 3.15 Cyclic voltammogram sweep from OCP to +0.5 V, then to -1.25 V and back to the starting voltage for solutions of 1.5 mL 0.1 M PP13-TFSI in THF, followed by addition of 0.05 mL **B6a** at 50 mV/s on Pt SPE #1.

V during the anodic sweep. Analysis by SEM-EDS indicated presence of molybdenum, confirming that the brown-coloured oil **B6a** does deposit onto the platinum working electrode following a single potentiodynamic cycle from 0 V to +0.5 V to -1.25 V and back to 0 V (See SI).

3.3.10 Attempts to Electrodeposit MoS_2 by Literature Optimized Conditions

Following successful synthesis of a MoO_3/ethylene glycol reaction mixture which was "brown" **B6a**, a replication deposition was conducted following the procedure by Murugesan et al. The electrochemical conditions that were successful for their deposition involved a mixture of 1.5 mL pure PP13-TFSI ionic liquid as a single-source non-aqueous

solvent and electrolyte with addition of 100 µL of both 1,4-butanedithiol and the "brown oil" molybdenum precursor. To this mixture at 100 °C, a chronoamperometric deposition at -2.7 V for 600 seconds was conducted and the electrodes rinsed with acetone and dried. In the original work, a 1 x 1 cm piece of glassy carbon was used as the working electrode, mounted on a rotating disc electrode with carbon tape. Platinum was used for both counter and quasi-reference electrodes. Different to this group, Ag/Ag^+ was used as a reference electrode in non-aqueous conditions, and the glassy carbon working electrode of different fabrication was not sonicated following 5 µm alumina polishing.

The ionic liquid was mixed with the molybdenum precursor prior to the heating in a low volume 3 electrode cell within a sand bath on a hotplate. Homogeneity of the mixture wasn't observed until ~50 °C. Addition of 1,4-butanedithiol was done at ~75 °C, which resulted in an immediate dark black precipitate forming which was not mentioned in the work by Murugesan et al.[1] Prior to immersion of the electrodes, majority of the solid was scraped from the solution surface and removed; however, this may be what resulted in crystalline MoS_2 shown by Murugesan et. al. The electrode was immersed at ~80 °C, and upon reaching a steady (5 min) 100 °C, chronoamperometric deposition at -2.7 V for 600 seconds was conducted.

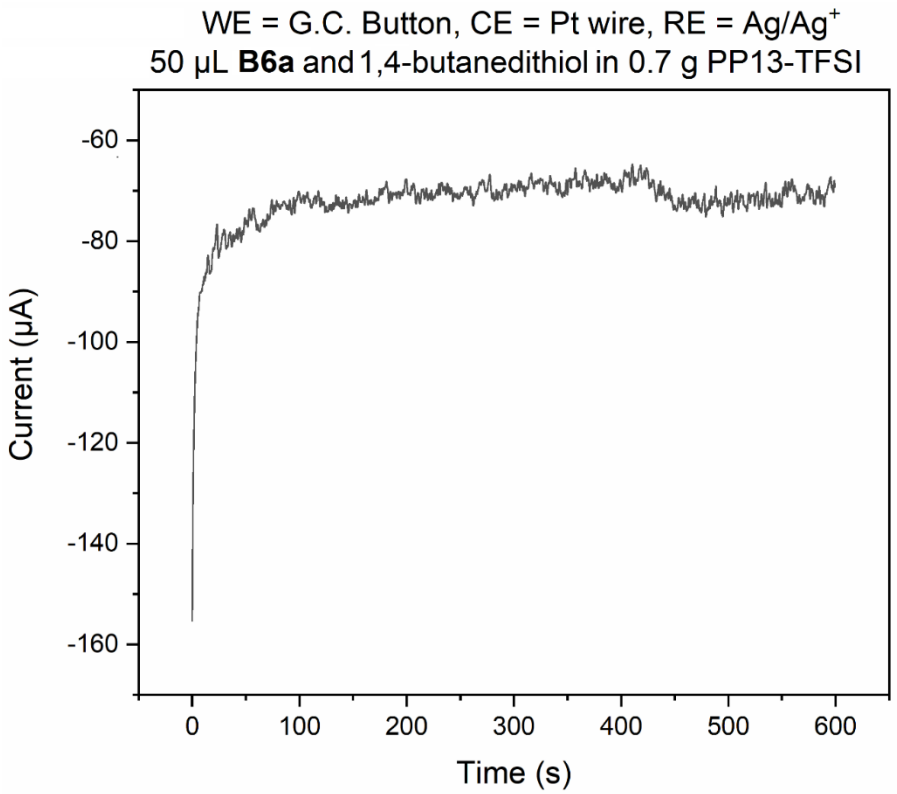

Figure 3.16 Chronoamperometric (CA) deposition attempt at -2.7 V for 600 seconds in a solution of 0.7g PP13-TFSI, 0.05 mL **B6a** and 0.05 mL 1,4-butanedithiol.

Following this electrodeposition, the electrode was rinsed with THF and stored in a desiccator. SEM analysis of the electrode revealed abundant debris, including fragmented material with sharp edges and sparse globular material. Analysis by SEM-EDS revealed the sharp material contains aluminum, indicating residual alumina from polishing. Analysis of the globular material revealed a signal for sulfur; however, in both of these instances signal intensity was mostly carbon (Figure 3.17). The crystalline MoS_2 nanoflowers reported by Murugesan et al.[1] could not be reproduced.

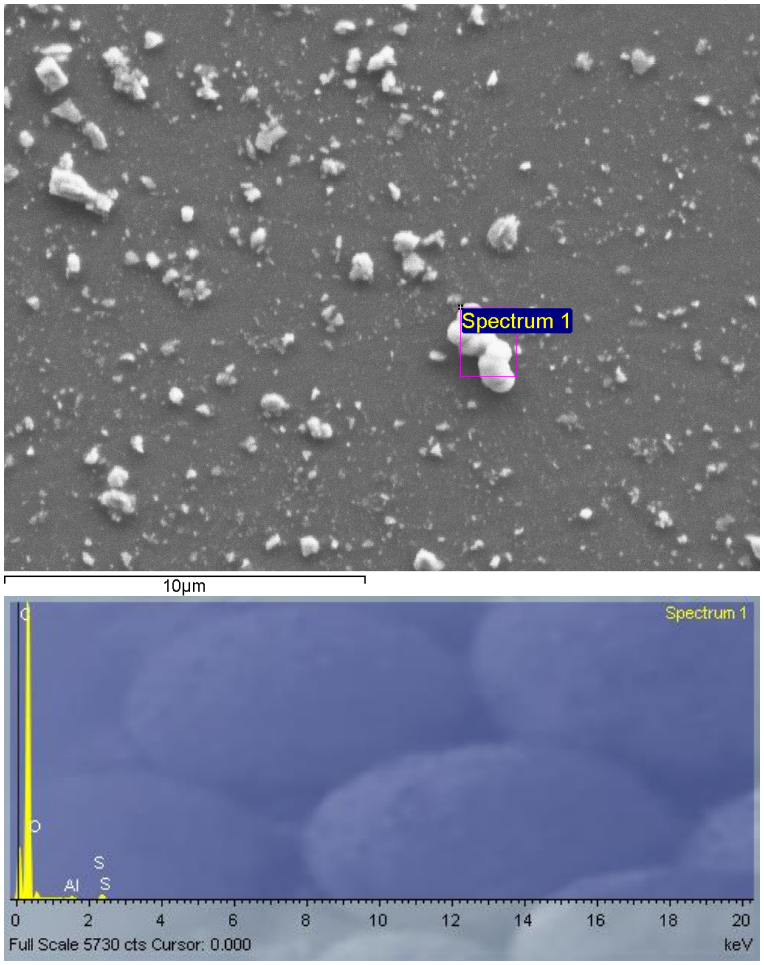

Figure 3.17 SEM-EDS analysis of a glassy carbon electrode following attempted chronoamperometric deposition of MoS_2. Sulfur is present within the brightest globular structures observed.

3.3.11 Attempts to Electrodeposit MoS_2 by Exploratory Methods

Use of the 0.1 M PP13-TFSI in THF supporting electrolyte at room temperature was explored to attempt MoS_2 electrodeposition using a ratio of 1.5 mL 0.1 M PP13-TFSI in THF to 0.05 mL 1,4-butanedithiol and 0.05 mL of **B3a** and **B6a**. In general, these attempts would result in no significant deposit when observed by SEM, while SEM-EDS mostly showed pure platinum, or sulfur, carbon, and oxygen. Aluminum and silicon were also observed as a component of the working electrode fabrication. Amorphous deposits

were achieved in a few instances with either sulfur or molybdenum present; however, the overlap of their signals during SEM-EDS analysis resulted in an inability to discern the composition. The issues associated with the unexpected precipitate material that forms when mixing the molybdenum and sulfur precursors in pure PP13-TFSI was found to be avoided by mixing the precursors in the presence of THF. When solutions were prepared and used right away, no precipitate formed to interfere with electrode-solution contact, and the colour change to a final stable red was similar to that of the pure ionic liquid. Since the "brown oil" **B6a** was not available for early studies, the gold-coloured oil **B3a** was used for majority of the alternative deposition attempts. Use of this solution with screen-printed platinum electrodes in a compact voltammetry low volume cell was explored, though this electrochemical cell could not be heated by manufacturer recommendation. Use of PP13-TFSI as an electrolyte within THF also allowed for increased conservation of this expensive material.

When mixing the gold-coloured **B3a (**0.05 mL) with 0.1 M PP13-TFSI (1.5 mL) a lighter pale yellow is observed. Addition of 0.05 mL 1,4-butanedithiol to this solution causes a colour change to orange, then red over the course of a half hour, with a red precipitate settling over the course of a week. Decanting the red solution and using it for deposition on Pt SPE #3 then Pt SPE #4 back-to-back via first applying -2.7 V for 600 seconds, followed by a single sweep from -0.75 V to -2.7 V (Figure 3.18).

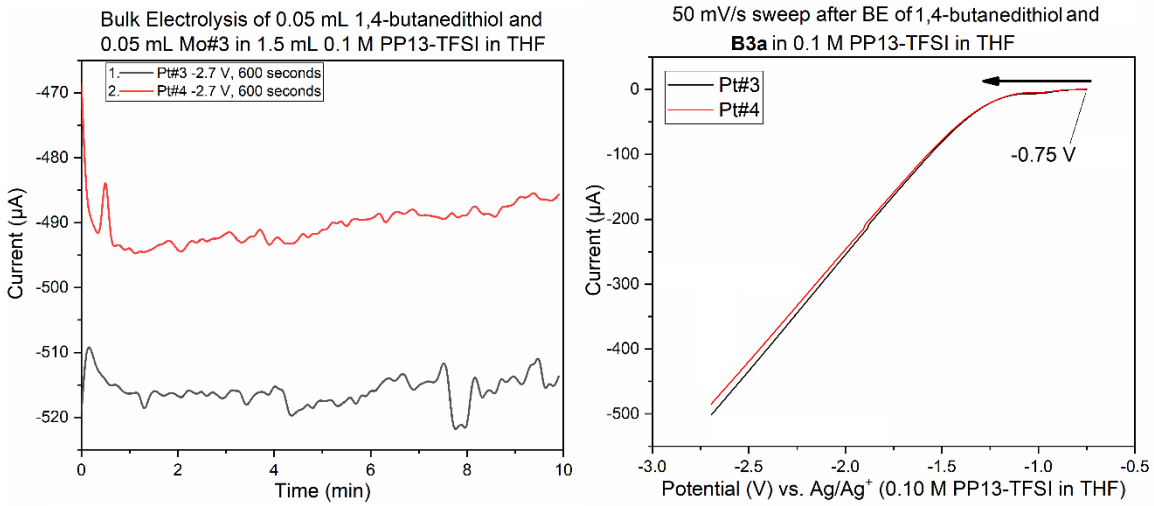

Figure 3.18 Two step electrodeposition attempt involving a single solution of 1.5 mL of 0.1 M PP13-TFSI in THF which had 0.05 mL **B3a**, then 0.05 mL 1,4-butanedithiol added and left to sit for a week. The red solution was put into the electrochemical cell, and Pt SPE #3 followed by Pt SPE #4 had BE conducted at -2.7 V for 600 seconds (left) followed by a single 50 mV/s sweep from -0.75 V to -2.7 V (right).

Both electrodes had a deposit by SEM-analysis (Figure 3.19); however, the morphology presented as a non-homogenous ring around the electrode, with a globular amorphous deposit upon closer examination. Two solutions were prepared containing 50 µL 1,4-butanedithiol, **B3a**, and either 1.5 mL THF, or 1.5 mL 0.1 M PP13-TFSI in THF. The THF solution appeared to have an orange suspended solid, and the 0.1 M PP13-TFSI in THF initially turned clear orange, going a clear red with a red precipitate after sitting for a week. The pure THF solution remained as a solution with an orange solid that did not settle. The clarified reddish orange solution from the 0.1 M PP13-TFSI in THF was decanted and used as the electrochemical solution. SEM-EDS analysis revealed the presence of sulfur and platinum, with other metal signals (Fe, Mg, Co) potentially present as artifacts or as contaminants.

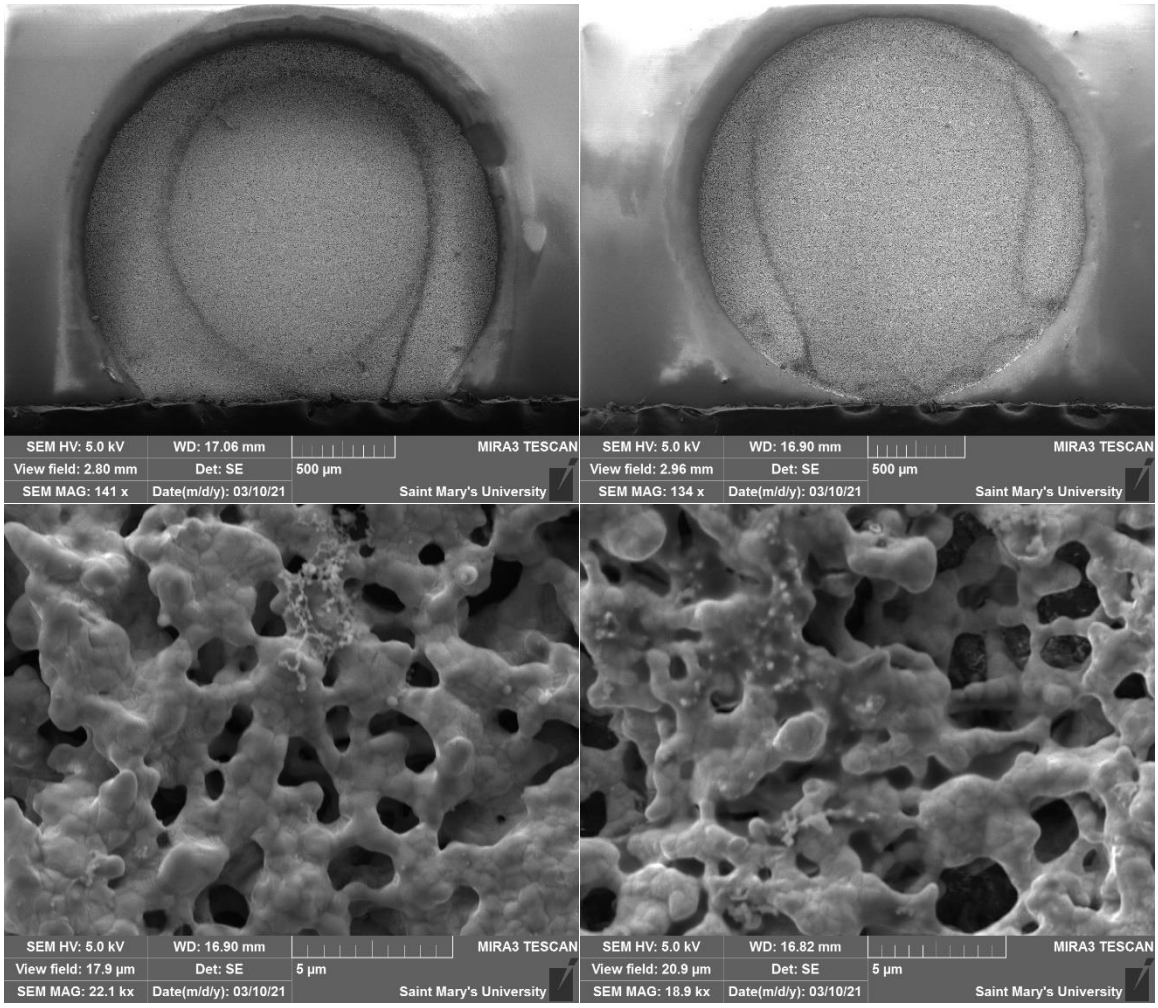

Figure 3.19 SEM SE images of electrodes (left = Pt SPE #3, right = Pt SPE #4) showing amorphous, non-homogenous deposit following a series of bulk electrolysis (-2.7 V for 600 seconds) following by a single sweep from -0.75 V to -2.7 V at 50 mV/s.

An additional deposition attempt was conducted in a solution of 1.5 mL 0.1 M PP13-TFSI in THF had 0.05 mL **B3a** added followed by 0.05 mL 1,4-butanedithiol in a low volume cell had a screen-printed platinum electrode (Pt SPE #5) immersed. The cell was externally referenced to Ag/Ag^+ wire pseudo reference electrode immersed in 0.1 M PP13-TFSI in THF sealed with a small ceramic frit. CV from +1.0 V to -2.7 V for 30 cycles was run to attempt a potentiodynamic deposition. The sweep had reduction at +0.5 V,

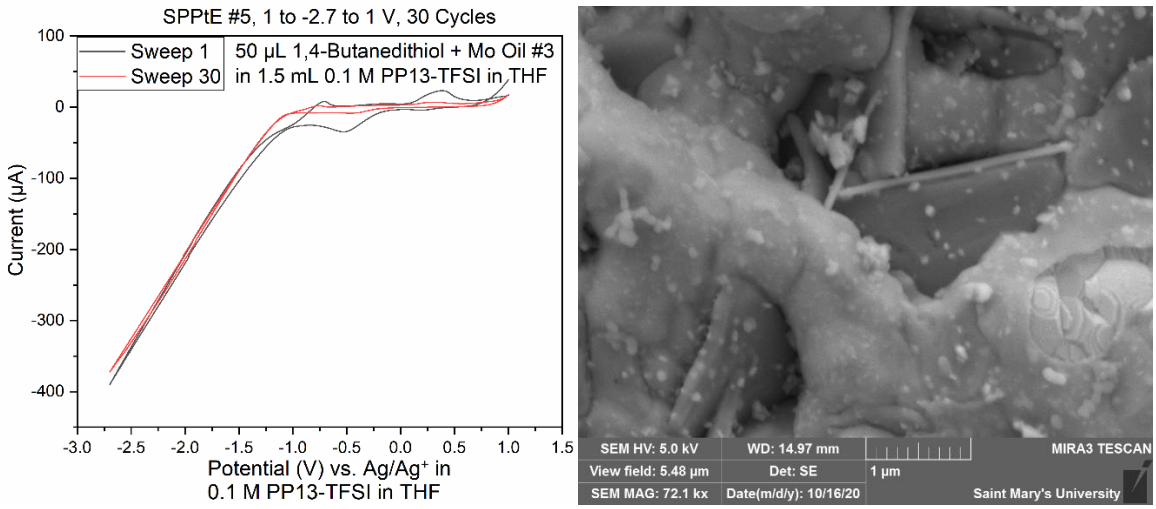

Figure 3.20 Cyclic voltammogram (left) of the attempted electrodeposition of MoS_2 from a mix of 1.5 mL 0.1 M PP13-TFSI in THF, 0.05 mL 1,4-butanedithiol, and 0.05 mL **B3a**. The first and 30th cycle are shown from -1.0 V to -2.7 V with a sweep rate of 50 mV/s. SEM SE image of the surface of the electrode following deposition of a nanoscale material. Long bladed crystals are a mix of Al/Zn/O from electrode fabrication.

dropping from -1.0 V to -2.7 V. The anodic sweep overlaps, indicating a resistive component to the circuit which may be due to the viscosity of residual ethylene glycol at the electrode surface or insufficient electrolyte. There is oxidation at ~ -0.7 V and another at ~ +0.4 V with an incomplete oxidation beginning at ~ +0.8 V increasing towards +1.0 V. After 30 cycles the current observed for the reduction and oxidation events dropped substantially, and the peak voltages shifted +/- 0.1 V with the region between -2.7 V and -1.4 V remaining similar.

This work was not conclusive regarding the state of each deposit; however, various unique morphologies were observed by SEM analysis following electrodeposition by chronoamperometric and potentiodynamic methods within pure PP13-TFSI or 0.1 M PP13-TFSI in THF as a supporting electrolyte solution and 1,4-butanedithiol as a sulfur precursor and concentrated MoO_3 and ethylene glycol reaction solutions. SEM-EDS analysis

indicated the presence of sulfur; however, the overlap with molybdenum signals result in insufficient characterization to conclusively determine the identity of the deposits.

These experiments indicate PP13-TFSI within THF as a supporting electrolyte has a wide electrochemical window in the cathodic region. A solution of 0.1 M PP13-TFSI in THF does display a minor resistive component within -1.25 V to +0.5 V, though a greater concentration of PP13-TFSI may reduce this solution resistance. Electrochemical activity within this solution is very low until voltages below ~ -1.8 V, with oxidation occurring above +0.5 V affording an electrochemical window of greater than +2.0 V. This much wider than what is afforded by aqueous electrolytes, highlighting the value non-aqueous electrochemistry offers for future MoS_2 electrodeposition research. Analysis of ethylene glycol indicated that its presence in solution at the concentrations studied may be problematic, introducing an apparent resistive component to the electrochemical system which impedes current flow. The difficulty associated with complete removal of ethylene glycol (b.p. 194 °C) from the molybdenum precursor proposed by Murugesan et al. without structurally changing the molybdenum precursor is a myriad of irreversible decomposition processes including thermally induced changes (too much heat = black solid), solvent mediated chemical alterations (water irreversibly changes the studied molybdenum precursor, THF coordinates to Mo dimers via μ bridging of the metal center), or a variety of clustering processes (dimerization, polymerization, tetra-/octamerization). SEM-EDS indicates material containing either sulfur or molybdenum has been deposited; however, the complete lack of reproducibility prevented further characterization of these undesirable non-homogenous amorphous films.

3.4 Experimental

3.4.1 Solvents, Reagents, and Materials

Nitrogen (gas and liquid) was supplied by Praxair and Air Liquide. Ethanol (95% and absolute) was purchased from Commercial Alcohols. Toluene, acetone, tetrahydrofuran, hexanes, DCM, and chloroform ($CHCl_3$) were purchased from Fisher Chemical or Fisher Scientific. Anhydrous magnesium sulfate and acetonitrile were purchased from Caledon. Nitric acid was purchased from J.T. Baker and concentrated sulfuric acid was from BDH. $CDCl_3$ (0.05% v/v tetramethyl silane) was purchased from Cambridge Isotope Laboratories Inc. Ethylene glycol (≥ 99%), molybdenum trioxide (99.99%), 1,4-butanedithiol (97%), N-methylpiperidine (99%), 1-bromopropane (99%), 4 Å molecular sieves, pentane, and calcined diatomaceous earth were all purchased from Sigma-Aldrich. Activated alumina used for drying and filtering solvents was purchased from Anachemia and is 80-200 mesh. Heating was performed using a DrySyn aluminum heating block with 50-1000 mL flasks including sealed reaction vessels, round bottom flasks, and Schlenk flasks. Potassium hydride was purchased as a 30% mineral oil dispersion from Sigma-Aldrich and washed four times with an appropriate amount of pentane then dried *in vacuo* to give a free-flowing powder. Alumina, calcined diatomaceous earth, and molecular sieves were pre-dried in a 140 °C oven for a minimum of one week before being dried at 300 °C *in vacuo* in a half-filled round-bottom wrapped in aluminum foil within an aluminum block. Solvents (toluene, pentane, tetrahydrofuran) were purified using an Innovative Technology solvent purification system. Solvents (pentane, toluene, tetrahydrofuran, hexanes, benzene) were then dried using KH for 24-78 hours and

subsequently filtered through dry alumina and stored over 4 Å molecular sieves (~1/10th the volume of solvents).

3.4.2 Equipment, Instruments and Analytical Methods

Electrochemical experiments were performed using a Wavenow USB potentiostat (Pine Research Instrumentation) with Aftermath 1.5.9888 software to control the electrochemical parameters attached to a laptop. Origin 2018 was used for all electrochemical data analysis. All electrodes and electrochemical cells except 20 mL scintillation vials were purchased from Pine Research Instrumentation (Durham, NC, USA). Electrochemical cleaning of screen-printed platinum electrodes (Pt SPE) with built in Pt counter electrode (CE) and Ag/AgCl reference electrode (RE) via cycling rapidly within -0.2 V to +1.0 V in an electrolyte solution containing N_2 purged 0.5 M H_2SO_4 in Milli-Q water in a 20 mL scintillation vial under a N_2 gas blanket using all Pt SPE's prior to use in non-aqueous experiments, with the final cycle fully desorbing all hydrogen atoms by completing the cycles at +0.3 V. All aqueous electrochemistry employed an external LowProfile Ag/AgCl RE sealed within a KCl, glycerol, cellulose gum gel electrolyte, and all non-aqueous electrochemistry utilized the same silver wire inserted in a sealed glass tube with a ceramic frit attached within either pure PP13-TFSI or 0.1 M PP13-TFSI in THF solution as the supporting electrolyte. Electrochemical experiments were performed in dry, low-O_2 (< 100 ppm) conditions under an atmosphere of N_2 within a mBraun Labmaster SP inert atmosphere glovebox in a low volume three electrode cell or compact voltammetry low volume cell kits (Pine Research Instrumentation). All electrochemical equipment and a laptop were used within the glovebox. Two distinct three-electrode set-ups were used for non-aqueous electrochemical experiments for either glassy carbon or platinum working electrodes. The Pt

SPE WE are countered by an internal platinum CE and referenced to Ag/Ag^+ within a compact voltammetry cell low volume kit. When using a 3.0 mm diameter glassy carbon WE a LowProfile 0.5 mm diameter, 65 mm length platinum wire CE shrouded in PTFE within an epoxy tube was used with the same Ag/Ag^+ RE within a low volume three electrode electrochemical cell. Glassware was dried at 140 °C overnight prior to synthetic experimentation. Synthetic reactions were conducted in common glassware and Schlenk flasks using Schlenk techniques if outside the glovebox when listed. Non-air sensitive chemistry was performed in typical glassware such as round bottom flasks or 20 mL scintillation vials open to air. Milli-Q ultra-pure water (≥18.2 MΩ•cm) was used during aqueous electrochemistry and also when polishing the glassy carbon disc electrode.

NMR spectra were recorded on a Bruker Avance 300 MHz NMR spectrometer. Trace amounts of non- or partially deuterated solvent were used as internal references for ^1H and ^{13}C NMR spectra and were referenced relative to tetramethyl silane when present.[55]

Elemental analysis was performed in the Centre for Environmental Analysis and Remediation (CEAR) facility at Saint Mary's University using a Perkin Elmer 2400 II series Elemental Analyzer. Air sensitive samples were prepared within a glovebox, sealed in 20 mL scintillation vials, and rapidly weighed/inserted into the analyzer offering at most ~2 minutes of possible air exposure after opening the vial.

SEM imaging and analysis was performed using a TESCAN MIRA 3 LMU Variable Pressure Schottky Field Emission Scanning Electron Microscope. Brightness difference between SEM-EDS images of some solid products is thought to be caused by

charging during analysis due to poor adhesion between the conductive carbon tape and the amorphous solid sample.

Single crystal X-ray diffraction measurements first involved selection of a suitable single crystal, and mounting it on the tip of a MiTeGen MicroLoop with Paratone-N oil. Measurements were made on a Bruker D8 VENTURE diffractometer equipped with a PHOTON III CMOS detector using monochromated Mo Kα radiation (λ = 0.71073 Å) from an Incoatec micro-focus sealed tube at 100-125 K.[56] The initial orientation and unit cell were indexed using a least-squares analysis of the reflections collected from a complete 180° Φ-scan with 1° per frame. For data collection, a strategy was calculated to maximize data completeness and multiplicity in a reasonable amount of time, and then implemented using the Bruker Apex 3 software suite.[56] The crystal to detector working distance was set to 4 cm. Data collection, unit cell refinement, data processing and multi-scan absorption correction were applied using the APEX3 software package.[56-58] The structures were solved using SHELXT[59] and all non-hydrogen atoms were refined anisotropically with SHELXL[60] using a combination of shelXle[61] and OLEX2[62] graphical user interfaces. Unless otherwise noted, all hydrogen atom positions were idealized and ride on the atom to which they were attached. Molecular structure diagrams we're prepared using Ortep-3 for Windows to colour and label atoms, style bonds, and position the molecule, with the final structure exported as a colour PostScript file. Final refinement of image size, bond style/width, and label size/positioning was done in CorelDRAW 10 using the PostScript file exported from Ortep-3 for Windows.

3.4.3 Synthesis of Ionic Liquid and Molybdenum Precursors

3.4.3.1 Ionic Liquid Synthesis

The ionic liquid PP13-TFSI was prepared following a literature procedure.[36] PP13-TFSI was prepared first by reacting 1-bromopropane and N-methyl piperidine in acetonitrile at 70 °C overnight followed by filtering the white solid PP13-Br and washing 3× with acetonitrile (crop 1 = 16.2 g). Concentration of the filtrate and washings with additional heating caused more precipitate to form which was collected twice more (crop 2, 3 = 8.2, 4.9 g) with matching purity as the first batch by ^{1}H NMR spectroscopy in $CDCl_3$ (See SI). Unexpected peaks at 1.77 and 1.82 ppm within ^{1}H NMR spectra of crops 2 and 3 of PP13-Br were confirmed to be water and acetonitrile as addition of 10 µL of each suspected solvent caused a shift to 1.68 and 1.84 ppm, respectively, showing concentration dependent interactions in $CDCl_3$ solutions with PP13-Br. The first crop contained a peak at 1.94 ppm that was assumed to be acetonitrile based on following the observed trend for increasing concentration of acetonitrile shifting closer to the expected 2.10 ppm within $CDCl_3$ solutions.[55] The PP13-Br was mixed as an aqueous solution into an equimolar solution of Li-TFSI and allowed to stir overnight, followed by multiple washes with water and then extraction with DCM, drying with $MgSO_4$, filtering through a diatomaceous earth pipette filter and drying *in vacuo* to a thick oil, followed by drying overnight at 105 °C. Final analysis revealed three unidentifiable ^{19}F NMR signals (See SI) and a trace of water was observed by ^{1}H NMR spectroscopy.

3.4.3.2 First synthesis of the Molybdenum Precursor – A1

To a 250 mL round bottom flask, 0.578g MoO_3 and ~75 mL ethylene glycol was heated under nitrogen to 194 °C for 1 hour with rapid stirring. The colour progressed from colourless with mint green powder suspended in a dark turquoise solution at 180 °C, to black at 190 °C, then to golden brown after 40 minutes at 194 °C, and finally appearing dark reddish brown with a fine black precipitate after 1 hour at 194 °C. The crude reaction mixture was briefly exposed to air due to not using a Schlenk flask to provide N_2 flow during sampling for solvent compatibility and water exposure tests. This was allowed to sit under nitrogen for four days and then a vacuum distillation at 110 °C for 3 hours was done to remove most of the ethylene glycol leaving a golden green paste that was extracted using 2×30 mL DCM through a coarse glass frit quickly to minimize air exposure. A black paste remained to which ~ 50-100 mL acetone was added to rinse into the waste forming a milky brown fluid with incomplete dissolution, though addition of water greatly increased dissolution, taking on a dark blue/black colour. The combined DCM extracts were reduced *in vacuo* affording a thick golden viscous oil. A valve-less gas adapter was used while concentrating the solution and was swapped with a valved adapter and sealed under vacuum to transfer into the glovebox. The valve-less adapter had some oil residue on it taking on a red colour upon air exposure, turning a rich blue overnight. The sealed flask produced colourless crystals (**C1a**) in a gold oil. 44.5 mg of off-white crystals with a few red blobs were isolated through rinsing the crude mixture with tetrahydrofuran through a glass frit, resulting in a yield of 4.4% of $Mo^{VI}O_2(OC_2H_4OH)_2$ determined by single crystal X-ray

diffraction, supported by E.A. Concentrating the THF/ethylene glycol filtrate *in vacuo* afforded a golden solution (**B1a**)

Analytical Calc. for $C_4H_{10}MoO_6$: C: 19.21% H: 4.03% N: 0.00% Found: C: 19.23% H: 4.09% N: 0.00%

3.4.3.3 Second Synthesis of the Molybdenum Precursor – A2

In a 250 mL Schlenk flask, 0.800 g MoO_3 and 125 mL ethylene glycol was heated to 194 °C for 1 hour under N_2 resulting in the same colour change as TG 77, greenish blue at ~184 °C followed by a golden brown/black. Upon cooling to 80 °C, a vacuum distillation was started while heating to 110-115 °C for 3 hours following the reaction, which was stopped and left to sit under N_2 until the next day and resumed for an additional 5 hours until about 3 mL of golden runny oil was present with a green paste. 1x100 mL DCM was added and left to stir for 1 hour. The filtration utilized a two ended frit with a 1.5 cm pad of diatomaceous earth on the side of the crude extract and was filtered into a second 250 mL Schlenk flask with positive pressure from the reaction flask. The golden-coloured extract was reduced to ~ 3 mL golden oil that was sealed under vacuum and transferred to the glovebox. This was then transferred to a 20 mL vial with THF and the solvent removed *in vacuo*. The residue had hexane added which did not dissolve the solid, so it was removed, and toluene was added with similar insolubility and removal *in vacuo*. THF was used to rinse the solid, affording a filtrate which, upon cooling, was a thick gold-coloured oil with yellow crystals (**C2a**) identified to be $(Mo^{V}O(OC_2H_4OH)(\mu\text{-}OC_2H_4OH))_2(\mu\text{-}OC_2H_4)$ by SC-XRD. Filtering and rinsing the solid with THF 2× and drying *in vacuo* afforded 374 mg of a yellow opaque solid (**D2a**) and removal of THF *in vacuo* from the filtrate left a thick

green oil (**B2a**). The residue on the diatomaceous earth pad from the DCM filtration was rinsed with water and dried *in vacuo* affording crystals of $Mo^{VI}O_2(OC_2H_4OH)_2$ (**C2b**) in a dark green oil, identified by SC-XRD.

Analytical Calc. for $C_{12}H_{28}Mo_2O_{11}$: C: 26.68% H: 5.22% N: 0.00%. Found: C: 27.59% H: 3.19% N: 0.02%.

3.4.3.4 Third synthesis of the Molybdenum Precursor – A3

In a 100 mL round bottom flask 0.345 g MoO_3 and 40 mL ethylene glycol were heated under vacuum to 185 °C with the distillation apparatus attached. ~5 mL colourless runny liquid was removed, presumed to be water. Vacuum was ceased and the reaction continued to warm to 194 °C under N_2. After 10 minutes at 194 °C, a clear green solution was present which persisted for the first 35 minutes of the reaction, and after 1 hour a very clear golden-coloured solution was present with a small amount of black solid. The heat was reduced to 110 °C and the vacuum distillation afforded little ethylene glycol after 2 hours, so the temperature was raised to 120 °C and then 130 °C after 30 minutes. An hour later, ~5 mL of a golden viscous oil remained with a fine black solid. The whole distillation apparatus was cooled and sealed under vacuum and transferred to the glovebox. The reaction flask was taken off the distillation apparatus and the rest were quickly removed from the glovebox. The golden oil with black solid was filtered through a diatomaceous earth pipette filter to remove the black solid that was discarded, and the total mass of the golden oil (**B3a**) was 3.1782 g and was stored at room temperature in a glovebox producing crystals (**C3a**) in 10 months that were identified by SC-XRD to be $Mo^{VI}O_2(OC_2H_4OH)_2$.

Isolation afforded ~0.1 g white crystals. An additional crystalline material from use of **B3a** for attempting electrodeposition was isolated (**C3b**) that is detailed in the SI.

3.4.3.5 Fourth Synthesis of the Molybdenum Precursor – A4

To a 250 mL round bottom flask 0.466 g MoO_3 and 50 mL ethylene glycol were heated in a distillation set up under vacuum to 170 °C removing ~6 mL colourless liquid prior to cooking. Vacuum was stopped and N_2 supplied while heating to 194 °C, with colour changing from greenish blue at 170 °C to golden brown at 194 °. Heat was increased from 194 to 215 °C over 1 hour resulting in a black suspension in brown liquid that was heated for an additional 2 hours, followed by cooling with vacuum distillation at 130 °C, then the black remaining solid was heated under vacuum at 160 °C until dry. The flask was transferred to the glovebox and scraped into a 20 mL scintillation vial yielding 0.491 g of a lustrous metallic black solid (**D4a**). The residue in the flask was dissolved in water and transferred to a 20 mL vial in a -18 °C freezer with atmospheric exposure, resulting in a blue solution (**B4a**) forming very tiny blue crystals (**C4a**) that rapidly melted/dissolved upon warming. By SC-XRD, the blue crystal was identified as a highly hydrated $Mo_{12}O_{40}X$ cluster with an unknown central atom or alkali/alkaline earth cations between the Mo/O/X clusters. Drying the blue solution *in vacuo* afforded a dark blue amorphous solid (**D4b**).

3.4.3.6 Fifth Synthesis of the Molybdenum Precursor – A5

To a 250 mL Schlenk flask 0.544g MoO_3 and 70 mL ethylene glycol were heated to 191-193 °C for 1 hour under nitrogen. By 180 °C, a green solution was present turning to golden greenish black by 190 °C. The reaction was cooled to 100 °C and a 0.5-2 mL sample was taken and placed in a vial with nitrogen flow, then sealed in a 100 ppm O_2

glovebox at room temperature. A vacuum distillation was started following this and was violent until ~5-10 mL was removed. The solution was a dark green at this point, and the temperature was increased to 115 °C for 2 hours until about 5 mL dark greenish brown liquid with black solids was present. This solution was filtered through a diatomaceous earth pipette filter affording 4.347 g of a thick golden-brown oil (**B5a**). The residue in the flask and on the filter were rinsed with 3×1.5 mL THF, then concentrated *in vacuo* to a thick golden-brown oil weighing 0.728g (**B5b**). The pipette filter was broken so the Kim wipe, diatomaceous earth, and black solid within the base of the pipette could be stored in a vial and allowed to dry slowly of THF (**D5a**). were stored at -35 °C with no solids forming in TG 212 B-C. Over time, **s**olutions **B5a** and **B5b** both crystallized very similar golden crystals. A single crystal sample from **B5b** was analyzed by SC-XRD and shown to be $C_{16}H_{36}Mo_4O_{20}$ (**C5a)**. This is not conclusive of being the only compound present, though other crystals had similar colour and morphology.

3.4.3.7 Sixth Synthesis of the Molybdenum Precursor – A6

This was an attempt to repeat the largest scale golden oil synthesis (#3). In a 250 mL Schlenk flask, 0.286 g MoO_3 and 35 mL ethylene glycol and heat to 130 °C under vacuum, removing ~10 mL liquid. Heat was raised to 194 °C for one hour, leading to a brown solution with black solids. The temperature was then reduced to 130 °C to begin vacuum distilling the mixture to ~8 mL thick brown oil with black solids. Sealing and bringing into a glovebox followed by filtration of the solution through a diatomaceous earth pipette filter afforded 6.0383 g of a brown oil (**B6a**) with black solid (**D6a**) remaining on the filter. The reaction flask and the black solid were rinsed with 4×2 mL THF and the

black solid was analyzed by SEM-EDS, yielding a Mo:O ratio of 1:2.8. The combined THF washings were discarded. In 3.5 months at room temperature in a sealed 20 mL scintillation vial in the glovebox, red crystals (**C6a**) formed from **B6a**. The bulk solution was decanted, and the crystals were left to sit in ~1 mL of the crystallization solution since rinsing with ethereal solvents was thought to potentially dissolve or alter the small amount of material. Analysis of a single red crystal by SC-XRD revealed the structure $Mo_8O_{32}C_{24}H_{54}•2(C_2H_4(OH)_2$.

3.4.3.8 Seventh Synthesis of the Molybdenum Precursor – A7

In an apparatus composed of a Schlenk reaction flask and round bottom collection flask with vacuum distillation adaptors, 282 mg of MoO_3 and 35 mL ethylene glycol were heated to 194 °C under nitrogen flow, forming dark golden solution in 1.5 hours after reaching temperature. Vacuum distillation was conducted for ~2 hours at 125 °C on the heating mantle with aide from a heat gun (upper walls of flask not touched by heating mantle) to a green paste. Triplicate extraction with 3×15 mL DCM, filtering through a coarse frit, and removal of solvent *in vacuo* afforded a golden oil (**B7a**). Rinsing with THF afforded 59 mg of a yellow microcrystalline solid.

3.4.3.9 Eighth Synthesis of the Molybdenum Precursor – A8

In an apparatus composed on two Schlenk flasks set up for distillation, 128 mg of MoO_3 and 20 mL ethylene glycol were heated to 150 °C under nitrogen flow, forming a homogenous golden solution in 2.5 hours after reaching temperature. Cooling afforded no precipitate when sealed overnight. Vacuum distillation was conducted for ~4 hours between 100-120 °C on the heating mantle with aide from a heat gun (upper walls of flask

not touched by heating mantle) to a final volume of 1 mL gold-coloured oil (**B8a**). Addition of 10 mL 95 % ethanol afforded a rich blue solution (**B8b**) and filtration followed by rinsing with 10 mL diethyl ether afforded < 5 mg residue on the filter paper. The filtrate was dried *in vacuo* affording a dark blue solid of unknown identity weighing 181 mg (**D8a**).

3.5 Conclusion

A literature procedure for producing MoS_2 via electrodeposition in the ionic liquid N-methyl-N-propylpiperidinium bis(trifluoromethane)sulfonimide at 100 °C from 1,4-butanedithiol as the source of sulfur atoms and crude reaction mixtures of MoO_3 with ethylene glycol as the source of molybdenum was explored in depth. Replication of the proposed ideal -2.7 V, 300 second chronoamperometric electrodeposition conditions using the sixth molybdenum precursor most akin to the required "*brown oil"* was unsuccessful. In the process of replication, four crystals were isolated giving insight into the complexity behind the reaction, representing monomeric (**1**), dimeric (**2**), polymeric composed of dimers (**3**), and a larger cluster containing 8 molybdenum atoms (**4**). In addition, electrochemistry within 0.1 M PP13-TFSI in THF for use as a non-aqueous, polar aprotic electrolyte solution was conducted on both platinum and glassy carbon to then analyze ethylene glycol, 1,4-butanedithiol, a mix of the two and various liquid molybdenum precursor samples. Various attempts were made to produce MoS_2 within this electrolyte solution, and SEM-EDS analysis indicates non-homogenous incomplete coverage of amorphous deposits containing sulfur and molybdenum from room temperature solutions, though overlap of their X-ray signals gave inconclusive results. The variety of diversity

within the MoO_3 ethylene glycol reaction warrants further investigation into the active component that allowed for direct electrodeposition of MoS_2 by Murugesan et al.[1] Though one of these compounds identified may be responsible for the successful direct electrodeposition of molybdenum disulfide, further work would be needed to find reliable procedures to prepare each compound in a pure form to study their efficacy for this electrodeposition process.

3.6 References

1. Murugesan, S.; Akkineni, A.; Chou, B. P.; Glaz, M. S.; Vanden Bout, D. A.; Stevenson, K. J. Room Temperature Electrodeposition of Molybdenum Sulfide for Catalytic and Photoluminescence Applications. *ACS Nano* **2013**, *7*, 8199-8205.

2. Schröder, F. A.; Scherle, J. Beiträge zur Chemie von Molybdän und Wolfram. XI / Contributions to the Chemistry of Molybdenum and Tungsten. XI. *Zeitschrift für Naturforschung* **1973**, *28*, 46-55.

3. Schröder, F. A.; Scherle, J.; Hazell, R. G. The structure of cis-dioxobis-(2-hydroxyethyl-1-oxo)molybdenum(VI). *Acta Crystallographica Section B* **1975**, *31*, 531-536.

4. Quan, Y.; Yao, J.; Yang, S.; Chen, L.; Li, J.; Liu, Y.; Lang, J.; Shen, H.; Wang, Y.; Wang, Y.; Yang, J.; Gao, M. ZnO nanoparticles on MoS_2 microflowers for ultrasensitive SERS detection of bisphenol A. *Microchim Acta* **2019**, *186*, 1-8.

5. Krishnan, U.; Kaur, M.; Kaur, G.; Singh, K.; Dogra, A. R.; Kumar, M.; Kumar, A. MoS_2/ZnO nanocomposites for efficient photocatalytic degradation of industrial pollutants. *Materials Research Bulletin.* **2019**, *111*, 212-221.

6. Wang, Y.; Xie, Y. Electroactive FeS_2-modified MoS_2 nanosheet for high-performance supercapacitor. *Journal of Alloys and Compounds* **2020**, *824*, 153936.

7. Liu, T.; Temprano, I.; King, D. A.; Driver, S. M.; Jenkins, S. J. Epitaxial growth of few-layer MoS_2(0001) on FeS_2{100}. *Chemical Communications* **2015**, *51*, 537-540.

8. Yuvaraj, S.; Veerasubramani, G. K.; Park, M.; Thangavel, P.; Kim, D. Facile synthesis of FeS_2/MoS_2 composite intertwined on rGO nanosheets as a high-performance anode material for sodium-ion battery. *Journal of Alloys and Compounds* **2020**, *821*, 153222.

9. Chen, Y.; Peng, Z.; Guo, Y.; Guan, S.; Fu, X. Novel self-supported MoS_2/FeS_2 nanocomposite as an excellent electrocatalyst for hydrogen evolution. *Solid State Sciences* **2020**, *101*, 106156.

10. Zhao, X.; Ma, X.; Lu, Q.; Li, Q.; Han, C.; Xing, Z.; Yang, X. FeS_2-doped MoS_2 nanoflower with the dominant 1T-MoS_2 phase as an excellent electrocatalyst for high-performance hydrogen evolution. *Electrochimica Acta* **2017**, *249*, 72-78.

11. Wang, Z.; Zhang, J.; Wen, T.; Liu, X.; Wang, Y.; Yang, H.; Sun, J.; Feng, J.; Dong, S.; Sun, J. Highly effective remediation of Pb(II) and Hg(II) contaminated wastewater and soil by flower-like magnetic MoS_2 nanohybrid. *Science of the Total Environment* **2020**, *699*, 134341.

12. Zheng, X.; Guo, Z.; Zhang, G.; Li, H.; Zhang, J.; Xu, Q. Building a lateral/vertical 1T-2H MoS_2/Au heterostructure for enhanced photoelectrocatalysis and surface enhanced Raman scattering. *Journal of Materials Chemistry A* **2019**, *7*, 19922-19928.

13. Milekhin, A. G.; Rahaman, M.; Rodyakina, E. E.; Latyshev, A. V.; Dzhagan, V. M.; Zahn, D. R. T. Giant gap-plasmon tip-enhanced Raman scattering of MoS2monolayers on Au nanocluster arrays. *Nanoscale* **2018**, *10*, 2755-2763.

14. Langer, J.; Jimenez de Aberasturi, D.; Aizpurua, J.; Alvarez-Puebla, R. A.; Auguié, B.; Baumberg, J. J.; Bazan, G. C.; Bell, S. E. J.; Boisen, A.; Brolo, A. G.; Choo, J.; Cialla-May, D.; Deckert, V.; Fabris, L.; Faulds, K.; García de Abajo, F. Javier; Goodacre, R.; Graham, D.; Haes, A. J.; Haynes, C. L.; Huck, C.; Itoh, T.; Käll, M.; Kneipp, J.; Kotov, N. A.; Kuang, H.; Le Ru, E. C.; Lee, H. K.; Li, J.; Ling, X. Y.; Maier, S. A.; Mayerhöfer, T.; Moskovits, M.; Murakoshi, K.; Nam, J.; Nie, S.; Ozaki, Y.; Pastoriza-Santos, I.; Perez-Juste, J.; Popp, J.; Pucci, A.; Reich, S.; Ren, B.; Schatz, G. C.; Shegai, T.; Schlücker, S.; Tay, L.; Thomas, K. G.; Tian, Z.; Van Duyne, R. P.; Vo-Dinh, T.; Wang, Y.; Willets, K. A.; Xu, C.; Xu, H.; Xu, Y.; Yamamoto, Y. S.; Zhao, B.; Liz-Marzán, L. M. Present and Future of Surface-Enhanced Raman Scattering. *ACS Nano* **2020**, *14*, 28-117.

15. Schulman, D. S.; Sebastian, A.; Buzzell, D.; Huang, Y.; Arnold, A. J.; Das, S. Facile Electrochemical Synthesis of 2D Monolayers for High-Performance Thin-Film Transistors. *ACS Applied Materials & Interfaces* **2017**, *9*, 44617-44624.

16. Toh, R. J.; Sofer, Z.; Luxa, J.; Sedmidubský, D.; Pumera, M. 3R phase of MoS_2 and WS_2 outperforms the corresponding 2H phase for hydrogen evolution. *Chemical Communications* **2017**, *53*, 3054-3057.

17. Redman, D. W.; Rose, M. J.; Stevenson, K. J. Electrodeposition of Amorphous Molybdenum Chalcogenides from Ionic Liquids and Their Activity for the Hydrogen Evolution Reaction. *Langmuir* **2017**, *33*, 9354-9360.

18. Patel, M. D.; Zhang, J.; Park, J.; Choudhary, N.; Tour, J. M.; Choi, W. Directly deposited porous two-dimensional MoS_2 films as electrocatalysts for hydrogen evolution reactions. *Materials Letters* **2018**, *225*, 65-68.

19. Jayabal, S.; Wu, J.; Chen, J.; Geng, D.; Meng, X. Metallic 1T-MoS_2 nanosheets and their composite materials: Preparation, properties and emerging applications. *Materials Today Energy* **2018**, *10*, 264-279.

20. Escalera-López, D.; Lou, Z.; Rees, N. V. Benchmarking the Activity, Stability, and Inherent Electrochemistry of Amorphous Molybdenum Sulfide for Hydrogen Production. *Advanced Energy Materials* **2019**, *9*, 1802614.

21. Er, E.; Hou, H.; Criado, A.; Langer, J.; Möller, M.; Erk, N.; Liz-Marzán, L. M.; Prato, M. High-Yield Preparation of Exfoliated 1T-MoS_2 with SERS Activity. *Chemistry of Materials* **2019**, *31*, 5725-5734.

22. Zheng, G.; Zhang, P.; Zhang, S.; Peng, Y.; Huang, L.; Zhang, L.; Jin, Y.; Jiao, Z.; Sun, X. SERS effect of selectively adsorbed dyes by hydrothermally-produced MoS_2 nanosheets. *New Journal of Chemistry* **2018**, *42*, 18906-18912.

23. Kannan, P. K.; Late, D. J.; Morgan, H.; Rout, C. S. Recent developments in 2D layered inorganic nanomaterials for sensing. *Nanoscale* **2015**, *7*, 13293-13312.

24. Zhuang, Z.; Huang, J.; Li, Y.; Zhou, L.; Mai, L. The Holy Grail in Platinum-Free Electrocatalytic Hydrogen Evolution: Molybdenum-Based Catalysts and Recent Advances. *ChemElectroChem* **2019**, *6*, 3570-3589.

25. Vikraman, D.; Hussain, S.; Patil, S. A.; Truong, L.; Arbab, A. A.; Jeong, S. H.; Chun, S.; Jung, J.; Kim, H. Engineering MoSe2/WS2 Hybrids to Replace the Scarce Platinum Electrode for Hydrogen Evolution Reactions and Dye-Sensitized Solar Cells. *ACS Applied Materials & Interfaces* **2021**, *13*, 5061-5072.

26. Yakovkin, I. Dirac Cones in Graphene, Interlayer Interaction in Layered Materials, and the Band Gap in MoS_2. *Crystals* **2016**, *6*, 143.

27. Muehlethaler, C.; Considine, C. R.; Menon, V.; Lin, W.; Lee, Y.; Lombardi, J. R. Ultrahigh Raman Enhancement on Monolayer MoS_2. *ACS Photonics* **2016**, *3*, 1164-1169.

28. Shi, B.; Zhou, D.; Fang, S.; Djebbi, K.; Feng, S.; Zhao, H.; Tlili, C.; Wang, D. Facile and Controllable Synthesis of Large-Area Monolayer WS_2 Flakes Based on WO_3 Precursor Drop-Casted Substrates by Chemical Vapor Deposition. *Nanomaterials* **2019**, *9*, 578.

29. da Fonseca, R. G. M.; Albers, R. F.; Leite, E. R.; de Oliveira, A. J. A. Parallel magnetic anisotropy in few layers MoS_2 films. *Journal of Magnetism and Magnetic Materials* **2020**, *497*, 165985.

30. Thomas, S.; Smith, D. E.; Greenacre, V. K.; Noori, Y. J.; Hector, A. L.; Groot, C. H. (Kees) de; Reid, G.; Bartlett, P. N. Electrodeposition of MoS_2 from Dichloromethane. *Journal of the Electrochemical Society* **2020**, *167*, 106511.

31. Ponomarev, E. A.; Neumann-Spallart, M.; Hodes, G.; Lévy-Clément, C. Electrochemical deposition of MoS_2 thin films by reduction of tetrathiomolybdate. *Thin Solid Films* **1996**, *280*, 86-89.

32. Staikov, G. *Electrochemical Theory: Electrocrystalization;* 2009; Vol. 2, pp 32-40.

33. Mabayoje, O.; Liu, Y.; Wang, M.; Shoola, A.; Ebrahim, A. M.; Frenkel, A. I.; Mullins, C. B. Electrodeposition of MoSx Hydrogen Evolution Catalysts from Sulfur-Rich Precursors. *ACS Applied Materials & Interfaces* **2019**, *11*, 32879-32886.

34. Cuin, A.; Massabni, A. C. Synthesis and characterization of solid molybdenum(VI) complexes with glycolic, mandelic and tartaric acids. Photochemistry behaviour of the glycolate molybdenum complex. *Journal of Coordination Chemistry* **2007**, *60*, 1933-1940.

35. Preiss, H.; Meyer, B.; Olschewski, C. Preparation of molybdenum and tungsten carbides from solution derived precursors. *Journal of Materials Science* **1998**, *33*, 713-722.

36. Sakaebe, H.; Matsumoto, H. N-Methyl- N-propylpiperidinium bis(trifluoromethanesulfonyl)imide (PP13–TFSI) – novel electrolyte base for Li battery. *Electrochemistry Communications* **2003**, *5*, 594-598.

37. Knobler, C. B.; Penfold, B. R.; Robinson, W. T.; Wilkins, C. J. Di-μ-methoxo-bis{[2,3-dimethylbutane-2,3-diolato(1-)]-cis-dioxomolybdenum (VI)}-methanol (1/2). *Acta Crystallographica Section B* **1981**, *37*, 942-944.

38. Modec, B.; Brenčič, J.; Koller, J. A Series of Molybdenum(V) Complexes with the Oxalato Ligand Engaged in Different Binding Roles − An Unusual Staggered Conformation of the μ_4-Oxalate in $[\{Mo_2O_4(\eta^2\text{-}C_2O_4)_2\}_2(\mu_4\text{-}C_2O_4)]_6$. *European Journal of Inorganic Chemistry* **2004**, *2004*, 1611-1620.

39. Modec, B.; Dolenc, D.; Brenčič, J. V.; Koller, J.; Zubieta, J. Dinuclear Oxomolybdate(V) Species with Oxalato and Pyridine Ligands Revisited: cis/trans Isomerization of $[Mo_2O_4(\eta^2\text{-}C_2O_4)_2(R\text{-}Py)_2]_2$- (R-Py = Pyridine, Alkyl-Substituted Pyridine) in Water Evidenced by NMR Spectroscopy. *European Journal of Inorganic Chemistry* **2005**, *2005*, 3224-3237.

40. Lehtonen, A.; Sillanpaa, R. CCDC 141435: Experimental Crystal Structure Determination. **2000**.

41. Cotton, F. A.; Morehouse, S. M. The Molecular Structure of a Diamagnetic, Doubly Oxygen-Bridged, Binuclear Complex of Molybdenum(V) Containing a Metal-Metal Bond. *Inorganic Chemistry* **1965**, *4*, 1377-1381.

42. Sarr, B.; Mbaye, A.; Diop, C. A. K.; Sidibe, M.; Melin, F.; Hellwig, P.; Maury, F.; Senocq, F.; Guionneau, P.; Giorgi, M.; Gautier, R. One pot-synthesis of the fourth category of dinuclear molybdenum(VI) oxalate series: Structure and study of thermal and redox properties. *Inorganica Chimica Acta* **2019**, *491*, 84-92.

43. Takekuma Shin-ichi; Tomoda Kengo; Sasaki Masato; Minematsu Toshie; Takekuma Hideko Preparation of a Binuclear Oxo(tropolonato)molybdenum(V) Complex and Its Spectroscopic Properties and Crystal Structure. *Bulletin of the Chemical Society of Japan* **2004**, *77*, 1935-1936.

44. Lehtonen, A.; Sillanpää, R. Synthesis and crystal structures of bis(2,3-dimethyl-2,3-butanediolato) (1,2-ethanediolato)tungsten(VI) and tris(2,3-dimethyl-2,3-butanediolato)tungsten(VI). *Polyhedron* **1994**, *13*, 2519-2524.

45. Buchanan, R. M.; Pierpont, C. G. Synthesis, structure, and properties of the oxygen-deficient bis(3,5-di-tert-butylcatecholato)oxomolybdenum(VI) dimer, $[MoO(O_2C_6H_2(^t\text{-}Bu)_2)_2]_2$. *Inorganic Chemistry* **1979**, *18*, 1616-1620.

46. Shekar, S.; Brown, S. N. Mixed amidophenolate-catecholates of molybdenum(VI). *Dalton Transactions* **2014**, *43*, 3601-3611.

47. Lee, M.; Wang, S. Syntheses and Characterizations of Four Organically Templated One-Dimensional Molybdenum Compounds including the First Inorganic−Organic Mixed-Anion Structures in the Mo/X/O (X = As, P) System. *Chemistry of Materials* **1999**, *11*, 3588-3594.

48. Bayot, D.; Tinant, B.; Devillers, M. Spectroscopic and structural characterizations of ammonium peroxo–carboxylato molybdate(VI) complexes. *Inorganica Chimica Acta* **2004**, *357*, 809-816.

49. Zhou, Z.; Deng, Y.; Cao, Z.; Zhang, R.; Chow, Y. L. Dimeric Dioxomolybdenum(VI) and Oxomolybdenum(V) Complexes with Citrate at Very Low pH and Neutral Conditions. *Inorganic Chemistry* **2005**, *44*, 6912-6914.

50. Liu, D.; Zhang, P.; Xu, J.; Feng, S.; Shi, Z. Solvothermal synthesis and crystal structure of the Mo(VI)-bridged helical chain containing Mo_2(V) dimers: $(C_4H_{12}N_2)_2[(Mo(V)_2O_4)(Mo(VI)O_4)(C_2O_4)_2]\cdot 2H_2O$. *Solid State Sciences* **2007**, *9*, 16-20.

51. Mialane, P.; Dolbecq, A.; Costaz, G.; Lisnard, L.; Marrot, J.; Sécheresse, F. Synthesis and structure of the first dinuclear lanthanide oxalato complexes $[\{Mo(V)_2O_4(C_2O_4)_2(H_2O)_2\}_2\{(Ln_2(H_2O)_4)_2(C_2O_4)\}]\cdot 7H_2O$ ($Ln=La^{3+},Ce^{3+}$). *Inorganic Chemistry Communications* **2002**, *5*, 702-705.

52. Wang, S.; Jin, W.; Chen, H.; Zhou, Z. Comparison of hydroxycarboxylato imidazole molybdenum(iv) complexes and nitrogenase protein structures: indirect evidence for the protonation of homocitrato FeMo-cofactors. *Dalton Transactions* **2018**, *47*, 7412-7421.

53. Łukaszewski, M. Electrochemical Methods of Real Surface Area Determination of Noble Metal Electrodes – an Overview. *International Journal of Electrochemical Science* **2016**, 4442-4469.

54. Doña Rodríguez, J. M.; Herrera Melián, J. A.; Pérez Peña, J. Determination of the Real Surface Area of Pt Electrodes by Hydrogen Adsorption Using Cyclic Voltammetry. *Journal of Chemical Education* **2000**, *77*, 1195.

55. Fulmer, G. R.; Miller, A. J. M.; Sherden, N. H.; Gottlieb, H. E.; Nudelman, A.; Stoltz, B. M.; Bercaw, J. E.; Goldberg, K. I. NMR Chemical Shifts of Trace Impurities: Common Laboratory Solvents, Organics, and Gases in Deuterated Solvents Relevant to the Organometallic Chemist. *Organometallics* **2010**, *29*, 2176-2179.

56. APEX 3 (Bruker, 2018) Bruker AXS Inc., Madison, Wisconsin, USA.

57. SAINT (Bruker, 2016) Bruker AXS Inc., Madison, Wisconsin, USA.

58. SADABS (Bruker, 2016) Bruker AXS Inc., Madison, Wisconsin, USA.

59. Sheldrick, G. M. SHELXT– Integrated space-group and crystal-structure determination. *Acta Crystallographica. Section A* **2015**, *71*, 3-8.

60. Sheldrick, G. M. Crystal structure refinement with SHELXL. *Acta Crystallographica. Section C* **2015**, *71*, 3-8.

61. Hübschle, C. B.; Sheldrick, G. M.; Dittrich, B. ShelXle: a Qt graphical user interface for SHELXL. *Journal of Applied Crystallography* **2011**, *44*, 1281-1284.

62. Dolomanov, O. V.; Bourhis, L. J.; Gildea, R. J.; Howard, J. A. K.; Puschmann, H. OLEX2: a complete structure solution, refinement and analysis program. *Journal of Applied Crystallography* **2009**, *42*, 339-341.

4. Chapter 4: Alkali Metal Amide Salts of a Bulky Nitrogen Tethered Phosphonium Fluorenide Ligand

4.1 Abstract

The reaction of a previously reported phosphine-imine ligand with 9-bromofluorene afforded a phosphonium bromide (E)-enamine that, upon deprotonation, affords an enamine tethered to a phosphonium fluorenide. Isolation of various crystals of this enamine and subsequent analysis by single-crystal X-ray diffraction (SC-XRD) showed that both (E)- and (Z)-isomers occur, which is supported by three dynamic isomers in C_6D_6 solution that led to this isomerization. Within solution-state NMR spectroscopy the enamine phosphonium fluorenide is the dominant isomer and is also observed within all four solid-state crystal structures. The un-solvated and 0.5(THF, n-hexane) solvate occur as the (Z)-enamine, while co-crystallization of either diethyl ether or 3 molecules of THF resulted in the (E)-enamine. The ability to participate in two types of hydrogen bonds between either the methyne or amine protons with THF was observed from the 0.5(THF, n-hexane) and 3(THF) solvates, respectively. Subsequent deprotonation of the secondary amine with lithium-, sodium-, and potassium-containing bases yielded metal amides that were isolated as various THF, Et_2O, C_6H_6 and C_6H_{14} containing crystals, forming mostly monomeric structures. Each alkali metal is chelated by one ligand with a coordinating solvent molecule (Et_2O or THF), with the only exception being a potassium complex that lacked a coordinating solvent. Instead of a solvent donor, this potassium complex has this vacancy filled by a 6-membered fluorenide ring from an adjacent ligand, forming an oligomer with non-coordinating n-hexane within the lattice that readily de-solvates upon storage or further drying. The single crystal X-ray structure of these complexes as various solvates with

diethyl ether (Li, K), THF (Li, Na) and non-coordinating n-hexane and benzene (Li, K) revealed the highly dynamic donor properties of the electron-delocalized phosphonium fluorenide undergoing $\eta^{1\text{-}6}$ interactions with the different alkali metals. Increasing atomic size was correlated with an unexpected significant decrease (>21°) in the angle between the alkali metal and the *ipso*-position of the 2,6-Diisopropylphenyl (Dipp) substituent bound to nitrogen with the M-N-(*ipso*-Dipp) angle for Li equal to 114.87(6) ° (Et_2O), 111.51(14) ° (THF)), Na equal to 100.66(10) ° (THF), and K equal to 95.13(11) ° (Et_2O) and 94.37(8) ° (η^6-flourenide')), respectively.

4.1.1 Graphical Abstract

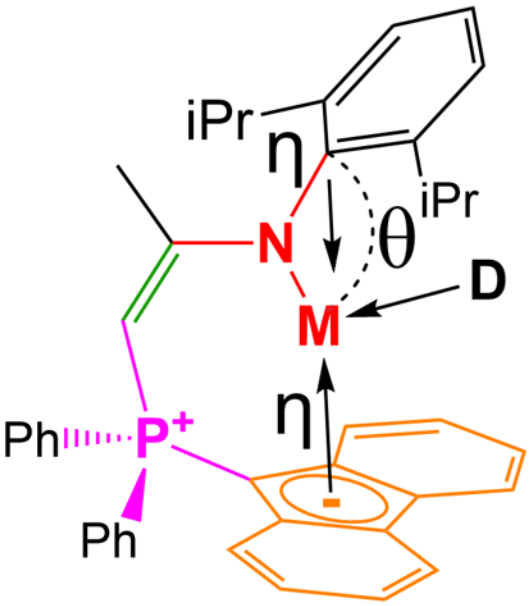

Alkali Metal (M)
Amide (NR_2-M)
Tether
Phosphonium $[PR_4]^+$
Fluorenide $[C_{13}H_8]^-$

M	D	θ (°)	η (Flu-M, Dipp-M)
Li	Et_2O	114.87(6)	2, 0
Li	THF	111.51(14)	3, 0
Na	THF	100.66(10)	4, 1
K	Et_2O	95.13(11)	6, 2
K	η^6-Flu'	94.37(8)	4, 2

4.2 Introduction

Aromatic hydrocarbons like cyclopentadiene (Cp, Figure 4.1 **A**) and sterically bulkier derivatives such as pentamethylcyclopentadiene (Cp*) have proven to be effective ligands when bound to metals like titanium and zirconium, enabling controllable alkene

polymerization.[1,2] Ligands like Cp and related derivatives, once deprotonated, are monoanionic ligands that can donate more electron density through the conjugated 5-membered 6-e^- π system of the ring via an η^5-interaction, offering-steric bulk that can shield and satisfy a stable electron count at a variety of electron rich (Ni, Zn) or poor (Y, Zr) d-block metal centers. The dibenzo-substituted Cp known as fluorene (Figure 4.1 **B**) is most relevant to this work; when bound to a phosphorus atom at the C9 position (Figure 4.1 **C**), delocalization of electrons from the double bond results in a cationic phosphonium and anionic fluorenide.

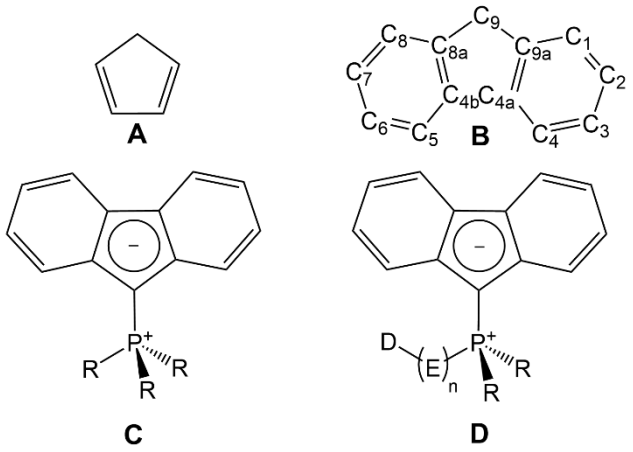

Figure 4.1 Various molecular structures prefacing the focus of this work. (**A**) Cyclopentadiene (**B**) Fluorene (standard numbering scheme) (**C**) Phosphonium fluorenide (**D**) Tethered phosphonium fluorenide.

When the phosphonium fluorenide is coupled with an additional donor atom and used as a bidentate ligand (Figure 4.1 **D**) it is suspected that the additional donor bound to a metal will encourage stabilization of low-energy dynamic interactions between the fluorenide donor and metal via haptotropic shifting (ring slipping) between with the central 5-membered Cp ring and both of the 6-membered benzene rings (Figure 4.2). The extended

conjugation of fluorene allows for low energy ring slipping from different types of η-interactions between fluorene and a metal (ex: η^5 6-e^- π-donor or η^1 2-e^- σ-donor). Due to this, it is suspected that low energy catalytic transformations may be possible for metal complexes containing Flu based ligands through substrate induced haptotropic shifting that could maintain stable electron count surrounding the metal center through the fluorene ligands variable electron donation.[3] These low-energy intramolecular haptotropic rearrangements between Flu-containing ligands and metal atoms allow for reversible electron donation (ex: $\eta^3 \rightarrow \eta^5$ *shift to more donation*, $\eta^5 \rightarrow \eta^3$ *shift to less donation*) enabling non-oxidative addition of ligands such as phosphines resulting in no net change in a metals electron count as the Flu-containing ligands electron donation changes.[4,5] Steric interactions with additional ligands may also be accommodated via lower η-interactions. Ligands of the donor-tethered phosphonium fluorenide type are expected to allow for a dynamic donor process that may be beneficial during catalytic processes.

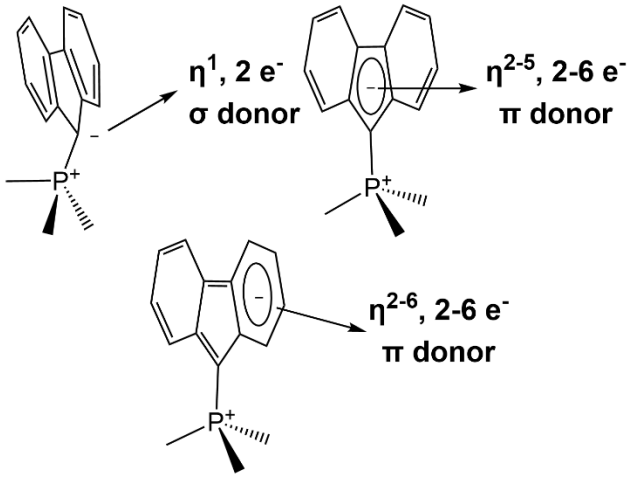

Figure 4.2 Neutral donor-metal bonding interactions expected from a phosphonium fluorenide with trimethyl phosphonium fluorenide as an example.

Recent work into tethered fluorenide alkali metal complexes shows a variety of η-interactions with all three rings of fluorene, along with the ability to form bimetallic alkali metal complexes when coupled with additional equivalents of alkali metal amide reagents.[6] Differences in ligand coordination of Li vs. Na and K was also shown and thought to be due to increasing atomic radius tending to favor polymeric complexes rather than the commonly monomeric or dimeric Li-complexes observed for N-heterocyclic carbene tethered fluorenide ligands and amide bridged bimetallic. In either case, fluorenide tends to interact with the alkali metal except when solvated.[6,7]

Fluorene as either a neutral or anionic donor has been observed to donate electron density to many metal atoms through different spatial positions encompassing η^1 through η^6 depending on the specific metal, oxidation state, other ligands present, fluorene substitution, and solvents/complexing agents within the crystal being analyzed. Directly bonding fluorene through the 9-positions to phosphines forms phosphonium ylides (P=Flu), and electron delocalization results in zwitterionic character, forming a charge separated phosphonium fluorenide (P^+-Flu^-). Fluorenide with no additional tether can be readily displaced from a metal, and the higher denticity ligands utilizing fluorene are expected to chelate more strongly to the metal atom through the chelate effect. Additional fluorene functionalization has been explored to create multidentate ligands with fluorenide functional groups, showing efficacy for many metal ions that benefit from the large steric bulk and extensive electron donation offered by fluorenide. Plenty of work exploring fluorene and substituted derivatives with and without tethered donors have uncovered a wide variety of organometallic complexes of alkali,[6-15] alkaline earth,[12,16] transition,[4,15,17-

[23] main group,[24] and lanthanide metals.[17,24-28] These organometallic complexes containing neutral or anionic fluorene with different substitutions provide insight into the ability for these ligands to form η-interactions from η^1 to η^6 with a variety of metals including K, Ca, Sn, Y, Ti, V, Mo, Fe, Ni, Cu, Co, and La. In the following work, a phosphonium bromide salt was made that could then be deprotonated forming either an enamine-fluorenylide, or further deprotonated forming a variety of alkali metals complexes for later use as organometallic precursors (Figure 4.3).

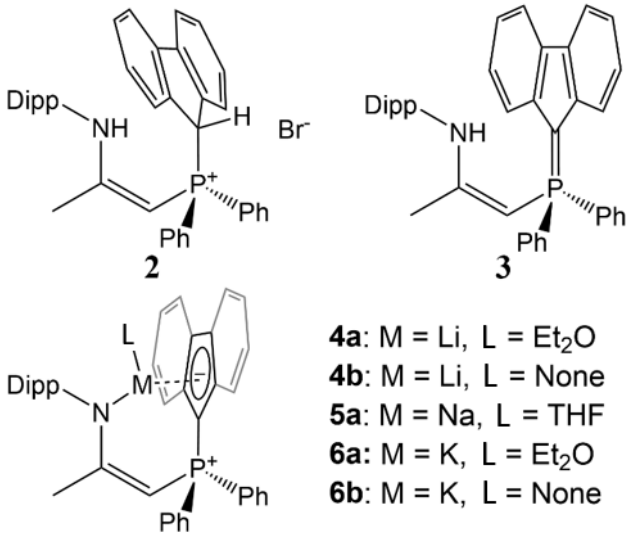

Figure 4.3 Compounds produced include a hydro bromide salt **2**, the corresponding free ligand **3** that occurs upon reaction of **2** with 1 eq. strong base, and alkali metal complexes **4**-**6** produced from **2** or **3** with either 2 or 1 eq. n-BuLi, NaH, or KH, respectively.

4.3 Results and Discussion

4.3.1 Synthesis and Reactivity

Compound **1** was synthesized according to a modified literature procedure via condensation reaction of 2,6-diisopropylphenyl aniline with acetone (~95% conversion)

facilitated by a mixture of molecular sieves, anhydrous $MgSO_4$, and $CaSO_4$ within acetone and toluene. The resulting imine was reacted first with n-BuLi in the presence of tetramethylethylenediamine (TMEDA) in pentane, forming an intermediate lithium complex that was then reacted with PPh_2Cl forming **1**. Recrystallization of the isolated product from ethanol affords colourless or slightly yellow crystals commonly contaminated with the phosphine oxide. Compound **2** could be produced from the reaction of **1** with 9-bromofluorene by stirring at room temperature in either toluene or THF for 2.5 weeks or a day, respectively in moderate yield (~67%) in the first crop of precipitate. To isolate the product, brief centrifugation (~3×3 min, < 10000 rpm) and washing three times with toluene enabled removal of the residual oxide of **1** formed during synthesis, without much loss of **2** due to low solubility in nonpolar aromatic or alkane solvents. Concentration of the filtrate allowed for additional **2** to be collected via the same method. Crystals of **2** could be obtained from chlorinated solvents like DCM, pentane layered chloroform ($CHCl_3$), acetone (low solubility), or ethanol (monohydrate). Other than non-solvated crystals from evaporation of concentrated acetone solutions, solvent co-crystallization was not favorable in all later reactions due to their own reactions with alkali reagents, so these forms of **2** were avoided in favor of the fine powder that precipitates from the reaction. From compound **2**, compounds **3**-**6** were produced using a variety of methods involving different solvents and bases. Of the bases and solvents tested (n-BuLi, LiHMDS, NaH, and KH in either toluene, benzene, pentane, hexane, heptane or THF), NaH in THF enabled a rapid reaction rate forming **3** with minimal conversion to **5** if only allowed to react for less than 4 hours at room temperature. Several days after filtration, elution of the red/orange/yellow

non-homogenous coloured material from the column with THF containing a mixture of **3** and **5a** that could be fully converted to **3** by brief stirring with excess **2**, filtering, and removing the solvent. Since compound **2** has a molecular weight exceeding ~20x that of the solid bases chosen, reliable stoichiometry was difficult to achieve without large amounts of **2** being used. Non-polar solvents offer low solubility for **2** and both metal hydrides, resulting in slow, low yielding reactions. Nonpolar aromatic solvents were favorable compared to alkane chains because **3** is much more soluble in the former and could be more easily recovered without clogging a filter or requiring a lot of solvent to elute through the necessary diatomaceous earth filtration step. While attempting to create a reliable procedure for compound **3**, many unique solid-state structures were discovered by SC-XRD (0.5 THF and 0.5 hexane, 3-THF and 0.5 diethyl ether solvates or no solvent). As such, stoichiometry with compound **3** was difficult to measure during synthesis because overlap of ^{1}H NMR spectroscopic signals from the multiple tautomers occurred where alkane chain CH_2 and CH_3, THF and diethyl ether backbone CH_2 or toluene or benzene CH signals occurred. Attempts to achieve an isolated sample of completely solvent free **3** was not achieved, and as a result the elemental analysis of this sample occurred with a lower carbon % than expected for the pure compound due to residual solvents. Of the various solvates, the 0.5 diethyl ether solvate was found to form large, easy to handle crystalline solids. Similar to **3** showing a variety of solvated structures, **4-6** also occurred in a variety of solid states with unique properties attributed to the presence or lack of coordinating and co-crystallized solvents. Once coordinating solvents were present in the lattice of the solid, it was difficult to remove them entirely with heat and vacuum though it was possible to

remove diethyl ether from **6a** by stirring in hexane all night, forming a fine powder suspension of **6b**. Upon melting, crystals of **6a** did appear to de-solvate beyond 120 °C prior to completely melting by 245 °C in contrast to **6b** melting completely by 120 °C. This preliminary result may imply that de-solvation results in a more thermally resistant crystal structure more analogous to **2** (decomposes above 295 °C) with stronger intermolecular fluorene interactions that could result in the observed thermal stability. Future studies will explore the SC-XRD of **6a** after heating beyond the suspected de-solvation temperature.

Preliminary small-scale reactions of **6** with metal halides in organic aromatic or ethereal solvents afforded precipitation of halide salts analogous to **2** containing the chloride or triiodide anions from reactions with $ZrCl_4$ and AlI_3, respectively determined by SC-XRD (See SI). A reaction of **6** with $(RhCl(COE)_2)_2$ afforded an immediate conversion of some **6** to **3** in C_6D_6 by ^{31}P NMR spectroscopy, and heating produced 6 new ^{31}P signals with significant **6** and **3** remaining, eventually fully converting to **3** in the NMR tube. Reaction conditions have yet to be optimized for production of isolable products containing the ligand and these metals of significant yield and purity. A reaction of In(I)I and **6** in THF resulted in non-homogenous micro and nano-particles depositing onto the vial at the rim of the solvent line; however, no analysis beyond imaging with SEM and a camera was conducted (Figure 4.4). The deposited nanomaterial may serve a function for other purposes; however, the focus of this work is the preparation of organometallic compounds, so this was not studied further. By ^{1}H and ^{31}P NMR spectroscopy, the products in the liquid mixture after filtration and drying *in vacuo* included four previously unobserved ^{31}P signals, though majority of the sample was **3**. Dissolution of the remaining residue in 2 mL THF

and storing at -35 °C for several months resulted in evaporation and co-crystallization of all the THF forming a single ~30 mg crystal of **3•(3 THF**). Future work will follow once attempts to produce organometallic complexes are successful.

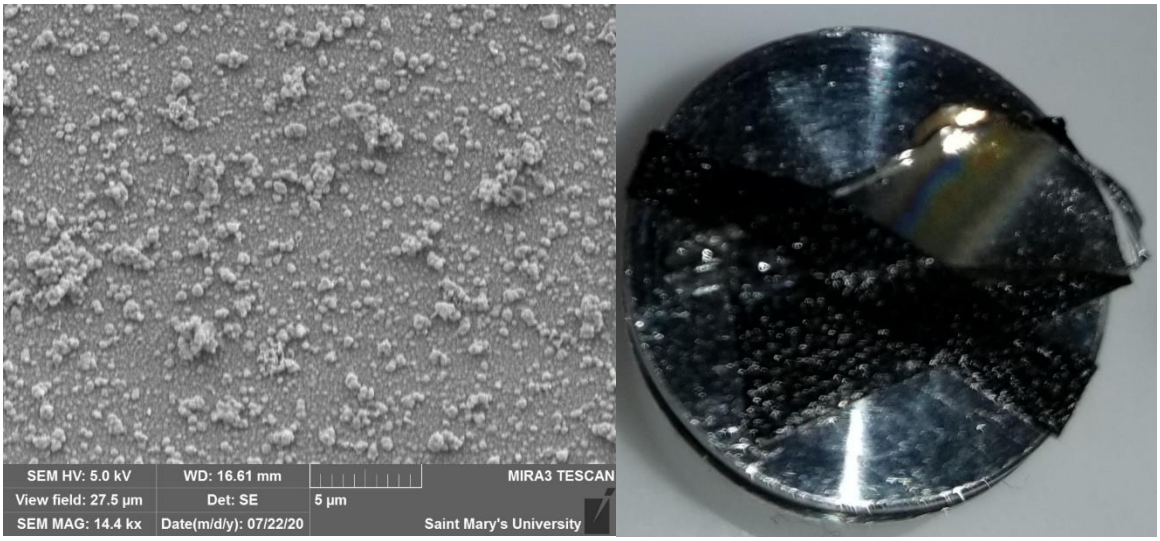

Figure 4.4 SEM SE image of micro- and nano-particulate deposited on the walls of a glass vial following a reaction between In(I)I and compound **6** (left) and photograph of the analyzed shard of the vial showing thin film interference from the deposit (right). EDX analysis revealed In, I, and K present.

4.3.2 NMR spectroscopy

The combined washes from the use of toluene for synthesis of **2** had no unknown signals in the ^{31}P NMR spectrum and only **1** was present, but use of THF as a solvent led to many unidentified signals with no residual **1**. In $CDCl_3$ solution, compound **2** is present as a mixture of tautomers, predominantly forming as the phosphonium bromide with a methyne backbone carbon and protons on both the nitrogen. The alternate tautomers could not be explicitly identified as many trace ^{1}H NMR signals were present appearing to resemble the backbone and fluorenyl $^{2}J_{P\text{-}H}$ split doublets, amine (s, 9-11 ppm) and CH_3 (s, 1.8-2.4 ppm) signals. Similar work observed the presence of a 1:1 tautomer within a similar

tethered fluorenyl ligand with the acidic proton found on either the 9-Flu position or on a carbene carbon.[29] The major isomer is clear due to a 1:1:2 integration of the NH, CH-P, and C*H*$(CH_3)_2$ protons. The NH signal is resolved within the ^{1}H NMR spectra, slightly overlapping *o*-phenyl aromatic protons and integrating to 1.

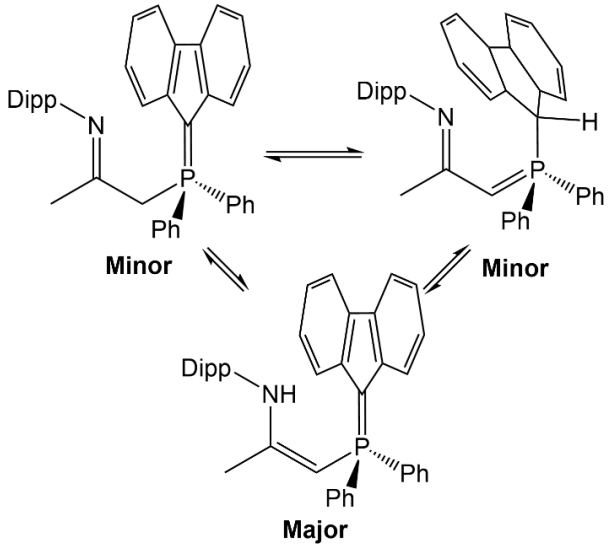

Scheme 4.1 Observed tautomers of **3** with ratios derived from ^{1}H NMR spectra taken at 25 °C in C_6D_6. Top left is the imine-fluorenide, top right is the imine-fluorenyl, and the bottom is the dominant enamine-fluorenylide/fluorenide tautomer.

In C_6D_6 solution of both **3** and the diethyl ether solvate, the different isomers were able to be distinguished based on a slow rate of (hours up to a day) equilibration to the imine-fluorenylide tautomer (Scheme 4.1 Top left). The ratios of the three tautomers were observed to differ under different circumstances, and this was used to help with assignment of the two minor isomers in the ^{1}H, ^{13}C, and ^{31}P NMR spectra.

Compounds **6** and **6•(Et$_2$O)** each give rise to the same NMR spectroscopic signals once dissolved in C_6D_6 thought to be due to rapid dissociation of the Et_2O ligand. This is in contrast to complex **4a** that display interactions between the alkali metal and coordinating solvents indicated by a shift in the typical solvent's ^{1}H NMR spectroscopic signals (**4a** Et_2O

= 2.31 and 0.31 ppm for CH_2 and CH_3, respectively, typically 3.26 and 1.11 ppm in C_6D_6).[30] Compound **5** also displays similar (but less) shifting of coordinated solvent signals compared to **4a**, with THF signals of 3.57 and 1.40 ppm in C_6D_6 shifting to ~2.81 and ~1.08 ppm, respectively. As the alkali metals size increases, solutions of **4**-**6** containing ethereal solvents such as Et_2O and THF in C_6D_6 tend to have weaker solvent donor/alkali metal interactions. This is based on both the more rapid loss of coordinated solvent by potassium salt **6a**, while **4a** and **5**, which both experience significant shifts in their coordinated solvent ^{1}H NMR spectroscopic signal, appear to be more resistant to loss of coordinated solvent in C_6D_6 solution. Notably, C_6D_6 solutions containing **4** with a coordinating solvent changed over time affording different ^{1}H, ^{7}Li, and ^{31}P NMR spectroscopic signals, most importantly a restoration of the expected solvent signal over time, accompanied by colour changes to green, yellow, or red solutions.

4.3.3 X-ray Crystallography

Compound **2** is best crystallized from acetone (Figure 4.5); however, solvates can be formed from water, DCM and chloroform. Crystals of **2** exhibit hydrogen bonding between the secondary amine and the bromide anion. Compound **3** was found to form solvent free or as three solvates, each of which is either present as (Z)- or (E)-isomers, respectively (Figure 4.6).

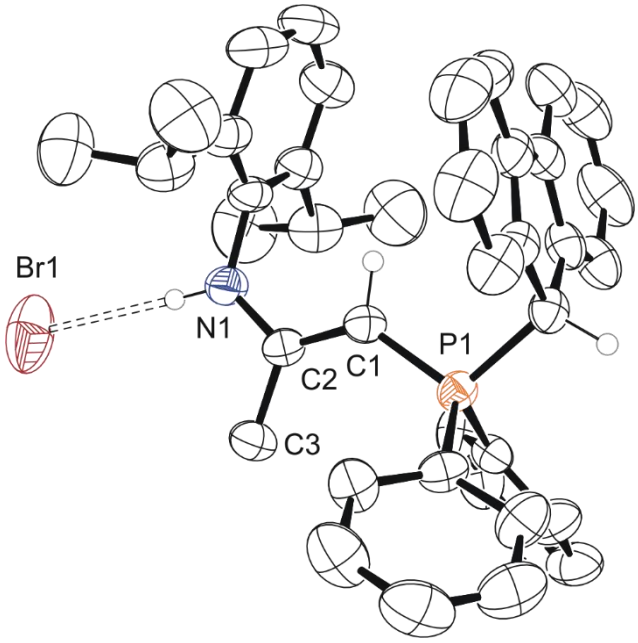

Figure 4.5 Molecular structure of compound **2** with anisotropic displacement ellipsoids projected at the 50% probability level. Hydrogen atoms except for 9-Flu-H, N1-H, and C1-H have been omitted for clarity.

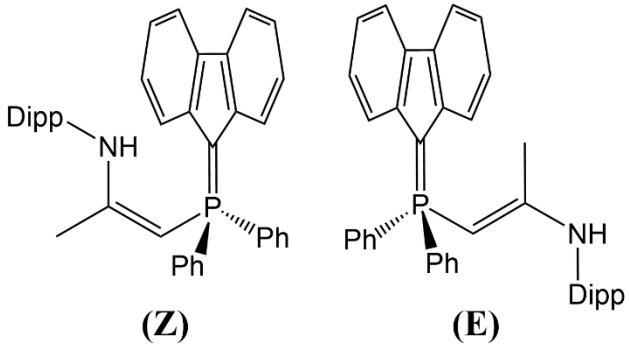

Figure 4.6 (E)- and (Z)-conformations of **3** as an enamine that occur in solution due to tautomerization of acidic protons resulting in the two rotational isomers observed in various solid-state crystal structures.

Atomic numbering specific to all compounds prepared is provided overlaid on the ligand **3** as both a structure drawing (Figure 4.7) or single crystal structure (Figure 4.8).

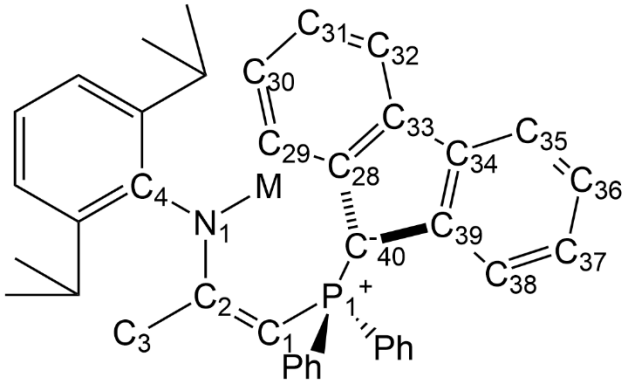

Figure 4.7 Numbering scheme for selected bond angles and lengths within discussion for crystal structures **2-6**.

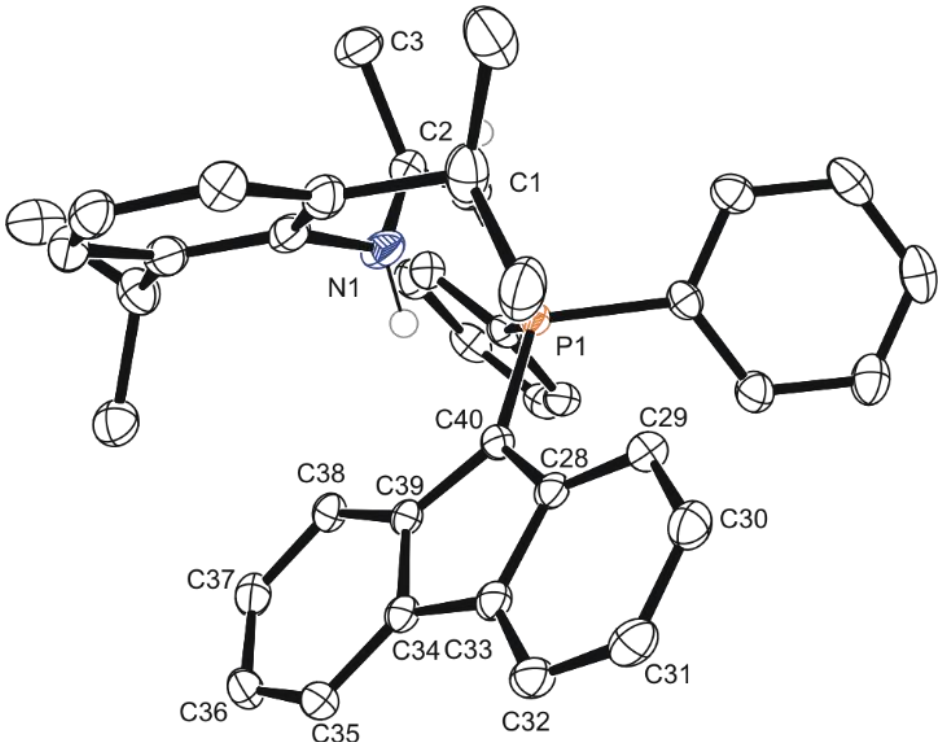

Figure 4.8 Molecular structure of compound 3 with anisotropic displacement ellipsoids projected at the 50% probability level. Hydrogen atoms except for N1-H and C1-H have been omitted for clarity. The equivalence between the labels provided in the structure and IUPAC fluorene labelling equates as: C40 = C9, C28 = C9a, C29 = C1, C30 = C2, C31 = C3, C32= 42, C33 = C4a, C34 = C4a, C35 = C5, C36 = C6, C37 = C7, C38 = C8, C39 = C8a.

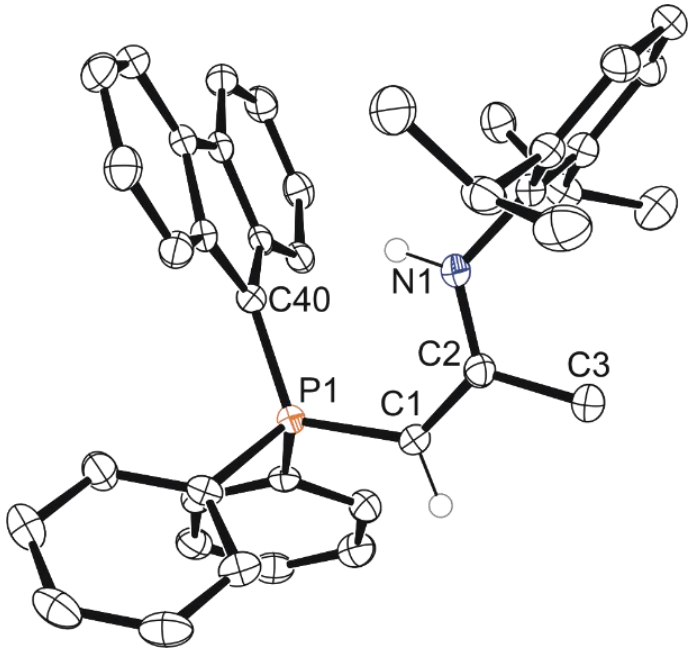

Figure 4.9 Molecular structure of compound **3** with anisotropic displacement ellipsoids projected at the 50% probability level. Hydrogen atoms except for N1-H and C1-H have been omitted for clarity.

The four structures isolated for compound **3** include solvent free (Figure 4.9), three solvates with either 0.5 diethyl ether (Figure 4.10), both 0.5 THF/ 0.5 n-hexane (Figure 4.11), and 3-THF (Figure 4.12). The various structures of **3** had two major rotational conformations with the amine pointing towards (Z)- or away (E) from the phosphonium fluorenide. The solvent free and 3-THF solvate occurred as the (Z)-isomer (along with **4a-b**, **5a**, **6a-b**), while the 0.5 diethyl ether and the 0.5 THF/n-hexane solvates both occur as the (E)-isomer (along with all halide salts that occur analogous to **2** including the chloride and triiodide). Both solvates containing **3** and THF show hydrogen bonding (CH…O_{THF} or NH…O_{THF}) depending on the (Z)- or (E)-isomers of **3**, respectively. The (Z)-isomer solvate of **3** (**0.5 THF, 0.5 n-hexane**) where the fluorenyl ring is closest to the amine through space, occurs with the methine proton participating in hydrogen bonding. On the contrary, the (E)-isomer

solvate of **3** (**3 THF**) occurs with a hydrogen bonding interaction between the amine and a single THF molecule, while the other two THF molecules reside next to the fluorenyl rings with no distinct hydrogen bonding interactions.

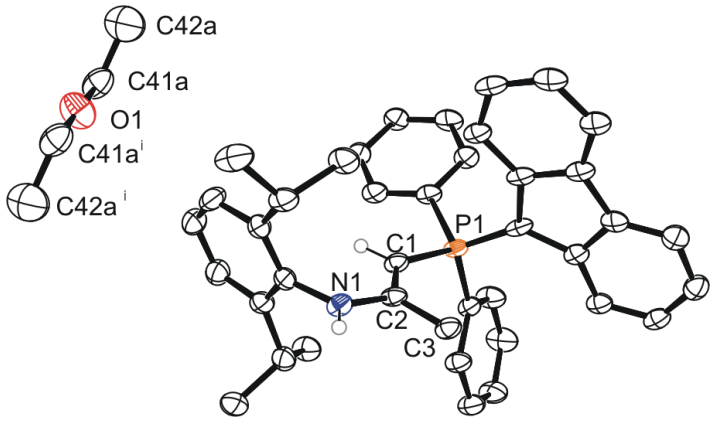

Figure 4.10 Molecular structure of compound **3•(0.5 Et_2O)** with anisotropic displacement ellipsoids projected at the 50% probability level. Hydrogen atoms except for N1-H and C1-H have been omitted for clarity.

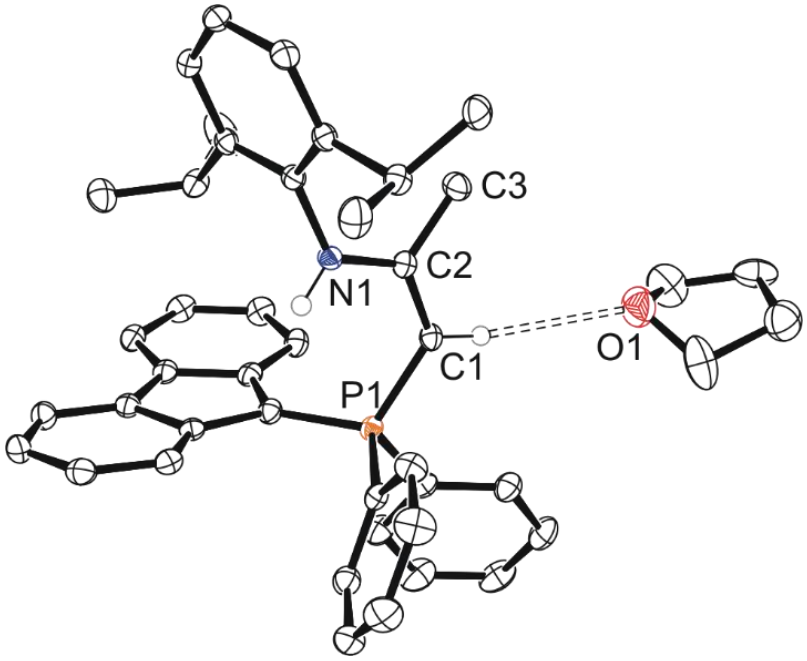

Figure 4.11 Molecular structure of compound **3•(THF, 0.5 n-hexane)** with anisotropic displacement ellipsoids projected at the 50% probability level. Hydrogen atoms except for N1-H and C1-H have been omitted for clarity.

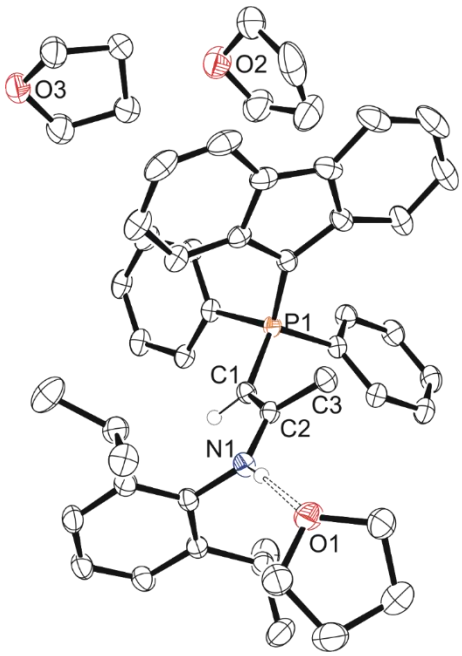

Figure 4.12 Molecular structure of compound **3•(3 THF)** with anisotropic displacement ellipsoids projected at the 50% probability level. Hydrogen atoms except for N1-H and C1-H have been omitted for clarity.

Crystal structures of **4-6** contain a range of η-interactions, with **4a•(Et$_2$O)** (Figure 4.13) and **4•(THF, 0.5 C$_6$H$_6$)** (Figure 4.14) displaying the lowest η^2 and η^3 interactions, respectively while **5a•(THF)** (Figure 4.15), **6a•(Et$_2$O)** (Figure 4.16) and **6•(0.5 n-C$_6$H$_{14}$)** (Figure 4.17) display η^4, η^5, and both $\eta^4 + \eta^6$ interactions with the fluorenide ring system, respectively. Compounds of sodium and potassium **5a•(THF)**, **6a•(Et$_2$O)**, and **6•(0.5 n-C$_6$H$_{14}$)** display *ipso*-Dipp (C4) η-interactions, while **6•(Et$_2$O)** has η-interacts with both *ipso*- and *ortho*- (C5) positions of the Dipp ring. **6•(0.5 n-C$_6$H$_{14}$)** had no coordinating donor solvent present that opened a vacancy in the coordination sphere of potassium. In the solid state, this vacancy is instead filled by an adjacent molecule through potassium-fluorene η^6 interactions due to oligomerization, with oligomer chains also held together via π-stacking interactions between phenyl rings (C22-27) across the symmetry operator (3/2-X, 3/2-Y,

1-Z) with a centroid distance and shift of 3.963 Å apart and 1.656 Å off center. When present as **4a•(Et$_2$O)**, lithium interacts with the 9 and 9a of the fluorenyl ring system via a highly asymmetric η^2 interaction with Li1-C distances of 2.2284(16) Å and 2.4837(16) Å to C40 (9-Flu) and C28 (9a-Flu), respectively (Figure 4.14). This asymmetry favors the Li1-C40 interaction, bordering on the σ-donor character of a sp^3 hybridized C40 noted within the IUCr checkcif via PLAT343_ALERT_2_G: "Unusual sp^3 angle range in main residue for C40", also observed for **4•(THF, 0.5 C$_6$H$_6$)**, highlighting the distortion of the P-Flu plane. The angle difference between Li1-C40-(C28, C39 (8a-Flu)) is ~23.4°, favoring the Li1-C40-C28 interaction, resulting in the Li1-C28 bond length of 2.4837(16) Å, significantly shorter than 2.970(14) Å for Li1-C38. A single isolated crystal of **4•(THF, 0.5 C$_6$H$_6$)** exhibits an η^3-Flu interaction with Li-(C40/C28/C39) that begins to distort the planarity of the P-Flu plane with C40 taking on a very mild tetrahedral shape. The difference between the angles Li1-C40-C28 (88.35(13) °) and Li1-C40-C39 (94.96(14) °) is ~6.6°, with lithium closer to C28 compared to C39 similar to the Li1-C28/C40 η^2 interactions observed for **4a•(Et$_2$O)** with a closer proximity to C28 due to the Li1-C40-C28 (81.77(6) °) and Li1-C40-C39 (105.17(6) °) difference of ~23.4° favoring Li-C28 interaction over Li-C39. Comparing the bond lengths Li1-C28 = 2.625(3) Å and Li1-C39 = 2.763(4) Å, C39 is farther from Li1 than the symmetry equivalent C28, participating within an asymmetric η^3 Li-Flu interaction. The angle difference between Li1-C40-C28 and Li1-C40-C39 is significant for both η^2 and η^3 structures observed for **4a•(Et$_2$O)** and **4•(THF, 0.5 C$_6$H$_6$)**, respectively. This shows the way the fluorenide ring is twisted towards lithium favors the same side, though the ligand and donor solvent orientation changing

between the two structures. A similar η^3 Li-Flu interaction is observed for the diethyl ether adduct of unsubstituted fluorene.[31] There exists a smaller bond length difference for **4a**(**Et$_2$O**) vs. **4•**(**THF**, **0.5-C$_6$H$_6$**) with respect to the Li1-C40, Li1-N1, and Li-O1 bond lengths of 2.2284(16) Å vs. 2.2226(36) Å, 1.9813(15) Å vs. 1.9595(34) Å, and 1.9536(15) Å vs. 1.8947(33) Å, respectively in order of structures (A vs. B) and specific bond length. Single crystals of **4•**(**THF**) and **4b** (solvent-free) suitable for SC-XRD were not made; however, one isolated polymorph of **4b** possessed highly radial morphology from a concentrated pentane solution that were unsuitable for SC-XRD. Similar to **4•**(**THF**, **0.5-C$_6$H$_6$**), **5a•**(**THF**) contains a THF adduct coordinated to the alkali metal. The sodium-fluorenide interaction resembles **4a•**(**Et$_2$O**); however, the larger size of Na also allows for interactions with C33 and C39 resulting in the observed η^4 interaction with the fluorenide ring system.

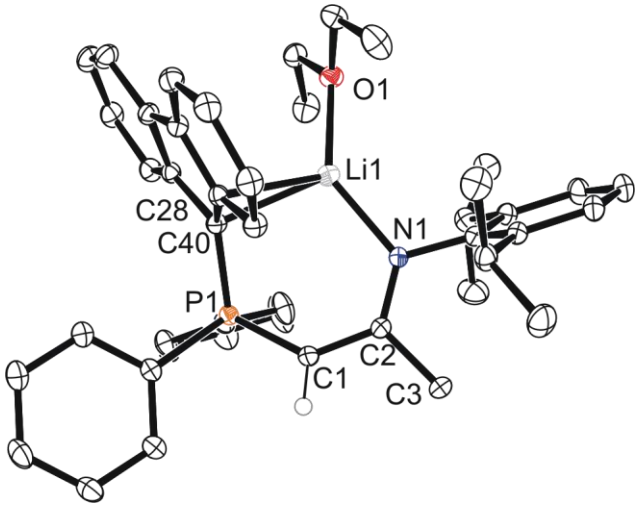

Figure 4.13 Molecular structure of compound **4a•(Et$_2$O)** with anisotropic displacement ellipsoids projected at the 50% probability level. Hydrogen atoms except for C1-H have been omitted for clarity.

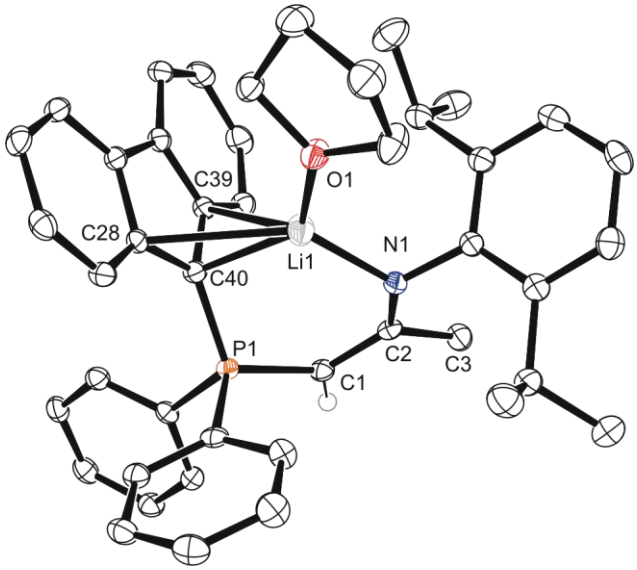

Figure 4.14 Molecular structure of compound **4•(THF, 0.5 benzene)** with anisotropic displacement ellipsoids projected at the 50% probability level. ½ Benzene and hydrogen atoms except for C1-H have been omitted for clarity.

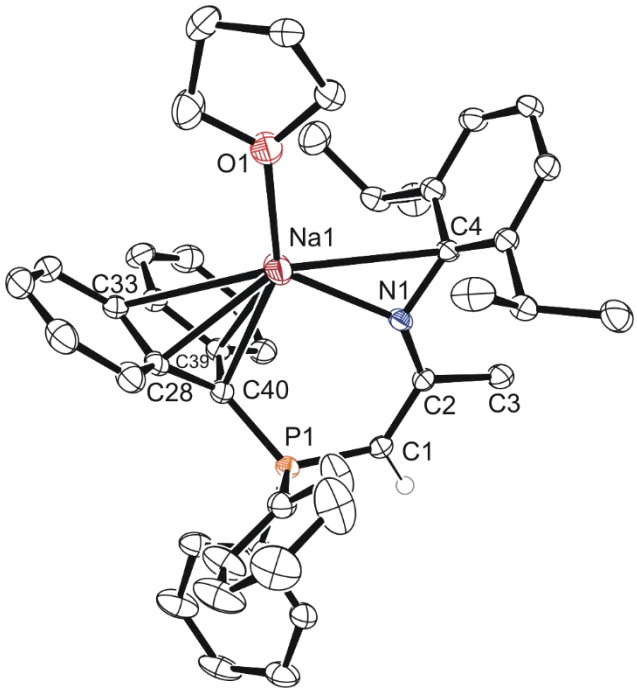

Figure 4.15 Molecular structure of compound **5a•(THF)** with anisotropic displacement ellipsoids projected at the 50% probability level. Hydrogen atoms except for C1-H have been omitted for clarity.

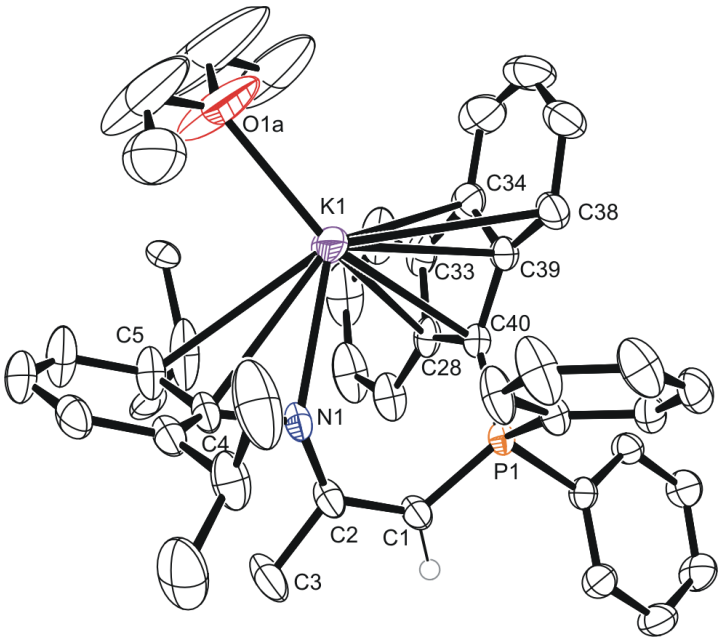

Figure 4.16 Molecular structure of compound **6a•(Et$_2$O)** with anisotropic displacement ellipsoids projected at the 50% probability level. Hydrogen atoms except for C1-H have been omitted for clarity and only one diethyl ether is shown due to 38:62 two component disorder. There is also a disordered isopropyl group attached to C5 in a 31:69 ratio.

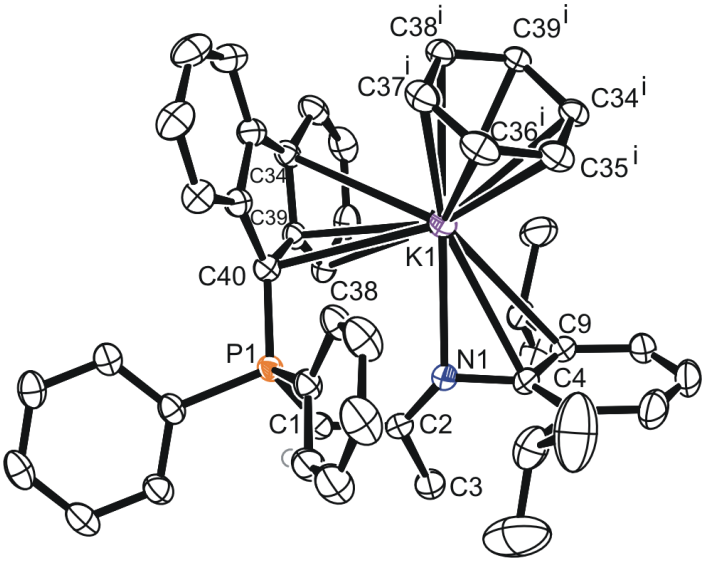

Figure 4.17 Molecular structure of compound **6•(0.5 n-hexane)** with anisotropic displacement ellipsoids projected at the 50% probability level. Hydrogen atoms except for C1-H and the disordered ½ hexane has been omitted for clarity. The structure has been grown to illustrate the η^6 interaction between potassium and an adjacent backside of a fluorenide ring.

The crystal structure of each alkali metal complex gave rise to a wide range of M-N-C4 bond angles, highlighting an unexpected aryl interaction with the larger alkali metals Na and K. A nitrogen atom with a trigonal planar configuration would ideally possess 120-degree bond angles; however, angles significantly lower were observed with increasing alkali metal mass from roughly 114.87(6) ° and 111.51(14) ° for lithium complexes **4a•(Et$_2$O)** and **4•(THF, 0.5 C$_6$H$_6$)**, 100.66(10) ° for sodium complex **5a•(THF)**, and 95.13(11) ° or 94.37(8) ° for potassium complexes **6a•(Et$_2$O)** and **6•(0.5 n-C$_6$H$_{14}$)** (Table 4.1).

Table 4.1 Angle between the ipso-Dipp (C4), nitrogen (N1), and alkali metals (M1) for each of the isolated crystal structures of **4**-**6**.

Compound	**4•(Et$_2$O)**	**4•(THF, 0.5 C$_6$H$_6$)**	**5•(THF)**	**6•(Et$_2$O)**	**6•(0.5 n-C$_6$H$_{14}$)**
C4-N1-M1 (°)	114.87(6)	111.51(14)	100.66(10)	95.13(11)	94.37(8)

The small angle between C4-N1-K1 (Figure 4.18) for the potassium complex **6** is different when compared with two similar bidentate potassium complexes containing a NacNac ligand (two N-Dipp groups instead of one N-Dipp and a P-Flu group present in **6**).[16,32] While **6** shows very low C4-N1-K1 angles of 95.13(11) ° (Et$_2$O) and 94.37(8) ° (η^6-flourenide'), the solvent free NacNacK shows a larger analogous angle of 101.05(17) ° and 103.96(17) °, while the NacNacK(DME)$_2$ has even larger angles of 107.34(15) ° and 108.96(15) ° (Figure 4.19). The NacNacK angle is similar to the sodium complex **5** (100.66(10) °), while the angle for the solvated NacNacK(DME)$_2$ is closer to but smaller than **4** (114.87(6) ° Et$_2$O, 111.51(14) ° THF). This comparison indicates the angle between

the Dipp group and the nitrogen atom bound to potassium is quite low, which could be due to the labile nature of the phosphonium fluorenide allowing for this increased π-interaction between the larger sodium or potassium ion and the conjugated Dipp *ipso*- and *ortho*-positions.

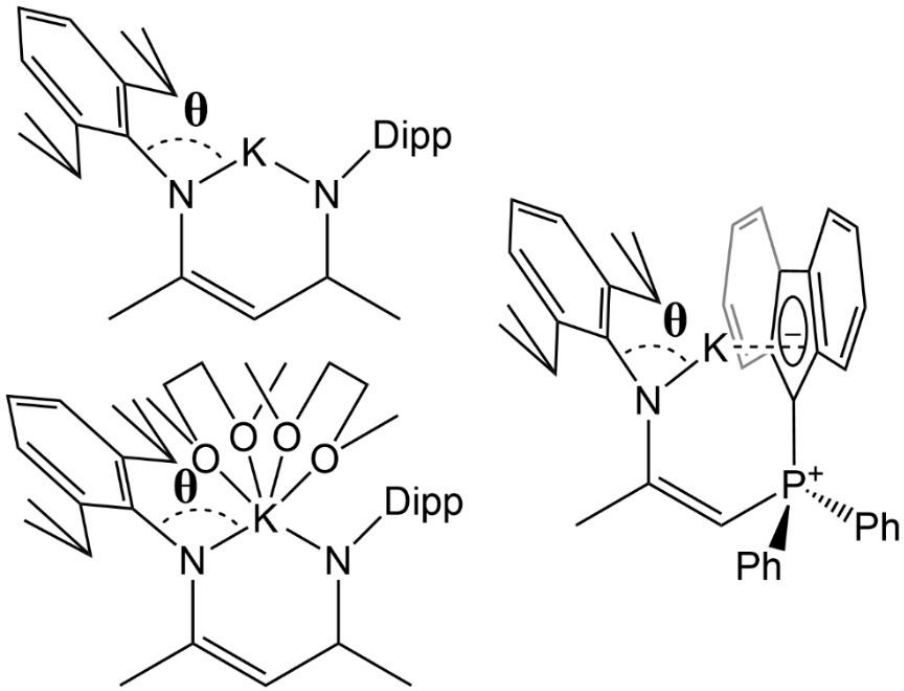

Figure 4.18 Comparison between NacNacK (top left),[16] NacNacK(DME)$_2$ (bottom left),[32] and compound **6** (right, 94.37(8) ° = **6a** and 95.13(11) ° = **6•(0.5 n-C$_6$H$_{14}$)**. The highlighted angle θ for NacNacK is 101.05(17) ° and 103.96(17) ° while for NacNacK(DME)$_2$ this angle is 107.34(15) ° and 108.96(15) °.

4.4 Experimental

4.4.1 Solvents, Reagents, and Materials

Nitrogen gas and liquid was supplied by Praxair and Air Liquide. 95% ethanol was purchased from Commercial Alcohols. Toluene, acetone, tetrahydrofuran (BHT stabilized), diethyl ether, hexanes and 85% phosphoric acid used as an external reference for ^{31}P NMR were purchased from Fisher Chemical or Fisher Scientific. Pentane, benzene and heptane

were purchased from Sigma-Aldrich. All deuterated solvents including $CDCl_3$ (0.05% v/v tetramethyl silane), C_6D_6, and CD_3CN were purchased from Cambridge Isotope Laboratories Inc. 2,6-diisopropyl aniline (90%), chlorodiphenylphosphine (96%), 2.5 M n-BuLi in hexanes, N,N,N',N'-tetramethylethylenediamine (99%), 9-bromofluorene, 4 Å molecular sieves, calcined diatomaceous earth, and 2.0 M trimethylaluminum in heptane were all purchased from Sigma-Aldrich. Trimethyl indium (99.9+%) was purchased from Strem Chemicals Incorporated. Anhydrous magnesium sulfate was purchased from Caledon Laboratories. Activated alumina used for drying and filtering solvents was purchased from Anachemia and is 80-200 mesh. Heating was performed using a DrySyn aluminum heating block with 50-1000 mL flasks. Potassium and sodium hydride were purchased as 30% and 60% mineral oil dispersions from Sigma-Aldrich and washed four times with ~8x v/v pentane, then dried *in vacuo* to give a free-flowing powder. Alumina, calcined diatomaceous earth, and molecular sieves were pre-dried in a 140 °C oven for a minimum of one week before being dried at 300 °C *in vacuo* in a half-filled round-bottom wrapped in aluminum foil within an aluminum block. Solvents (toluene, pentane, tetrahydrofuran) were purified using an Innovative Technology solvent purification system. Solvents (pentane, toluene, tetrahydrofuran, hexanes, benzene) were then dried using KH for 24-78 hours and subsequently filtered through dry alumina and stored over 4 Å molecular sieves (~$1/10^{th}$ the volume of solvents).

4.4.2 Equipment, Instruments and Analytical Methods

All reactions were performed in dry, O_2-free (< 10 ppm) conditions under an atmosphere of N_2 within a mBraun Labmaster SP inert atmosphere glovebox in 20 mL scintillation vials or

using Schlenk flasks sealed with rubber or glass stoppers with standard Schlenk techniques. Glassware was dried at 140 °C overnight prior to experimentation. NMR spectra were recorded on a Bruker Avance 300 MHz NMR spectrometer. Trace amounts of non- or partially deuterated solvent or tetramethyl silane were used as internal references for ^{1}H and ^{13}C NMR spectra. ^{31}P and ^{7}Li nuclei were referenced to 85% phosphoric acid or 1.0 M LiCl in D_2O, respectively. Melting points were recorded on an Electrothermal MEL-Temp 3.0 using glass capillaries sealed under inert conditions for air sensitive compounds (**3**-**6**) or open to air for air and moisture stable compound **2**. Elemental analysis was performed within the Centre for Environmental Analysis and Remediation (CEAR) facility at Saint Mary's University using a Perkin Elmer 2400 II series Elemental Analyzer.

Single crystal X-ray diffraction measurements first involved selection of a suitable single crystal, and mounting it on the tip of a MiTeGen MicroLoop with Paratone-N oil. Measurements were made on a Bruker D8 VENTURE diffractometer equipped with a PHOTON III CMOS detector using monochromated Mo Kα radiation (λ = 0.71073 Å) from an Incoatec micro-focus sealed tube at 100-125 K.[33] The initial orientation and unit cell were indexed using a least-squares analysis of the reflections collected from a complete 180° phi-scan with 1° per frame. For data collection, a strategy was calculated to maximize data completeness and multiplicity in a reasonable amount of time, and then implemented using the Bruker Apex 3 software suite.[33] The crystal to detector working distance was set to 4 cm. Data collection, unit cell refinement, data processing and multi-scan absorption correction were applied using the APEX3 software package.[33-35] The structures were solved using SHELXT[36] and all non-hydrogen atoms were refined anisotropically with SHELXL[37]

using a combination of shelXle[38] and Olex2[39] graphical user interfaces. Unless otherwise noted, all hydrogen atom positions were idealized and ride on the atom to that they were attached. Alkali metal/aromatic η-Interactions were based on the default bond (bond radius 1 + bond radius 2 + 0.5 Å) provided within Olex 2 version 1.3, with bonds to hydrogen or sp^3 carbon atoms omitted to only allow for η-interactions with π-conjugated carbon atoms. Molecular structure diagrams were prepared using the cif file generated by Olex2 within Ortep-3 to colour and label atoms, style bonds, and position the molecule, with the final structure exported as a colour PostScript file. Final refinement of image size, bond style/width, and label size/positioning was done in CorelDRAW 10 using the Ortep-3 file.

4.4.3 Synthesis of Precursors, Ligands, and Dimethyl Aluminum and Indium Complexes

4.4.3.1 Synthesis of Compound 1 - Dipp-N=C(CH_3)-(CH_2)-P(C_6H_5)$_2$

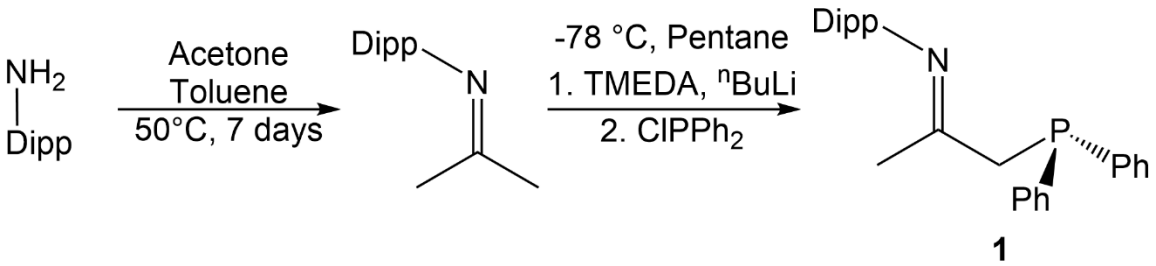

1

Part 1: Following a modified previously established synthesis,[40] a solution of 100 mL (0.5 mol) 2,6-diisopropylaniline in 200 mL (2.7 mol) acetone was refluxed for one week with ~40 mL anhydrous $MgSO_4$ to encourage condensation, producing N-isopropyl-N-2,6-diisopropylphenylimine with incomplete conversion possibly due to acid catalyzed hydrolysis of the imine. The resulting solution was filtered through diatomaceous earth, acetone removed, and the mixture was distilled *in vacuo* affording a 1:2 ratio of the amine

to imine. Toluene, molecular sieves, and anhydrous calcium sulfate with refluxing over the course of a few weeks caused a 1:10 ratio of reagent to product. Distillation afforded 3 fractions with the purest being the first, 9 grams of a 1:11 ratio of amine to imine.

Part 2: In a 500 mL round bottom flask 8.6 g of the previously made imine was used directly in a -78 °C reaction in 230 mL pentane with first 0.5 g TMEDA (43 mmol) followed by addition of 17.7 mL of a 2.4 M n-BuLi solution (42 mmol, conc. determined by titration) with slow warming to room temperature over 2 hours. Cooling back to -78 °C is followed by addition of 8.7 g chlorodiphenylphosphine (39 mmol) with warming to room temperature and stirring under nitrogen for two days. Filtration through diatomaceous earth and removal of pentane *in vacuo* affords a yellowish white solid. Dissolution in minimal hot ethanol creates s a golden solution, which, upon cooling, crystallizes **1** as white crystals that can be isolated by filtration with 3×5 mL ethanol rinses. Concentration of the filtrate *in vacuo* can give additional crops of crystals, and three were harvested with masses of 12.97 g, 0.77 g, and 0.05 g in order of collection. Purity decreased in later crops, with the first to third crop occurring at 91, 86, and 84% purity with an impurity of the oxide of **2**. The third crop presented as more suitable distinct single crystals for X-ray analysis compared to the first two crops that both occurred as highly radial spherical crystalline clumps.

Yield (if pure): Crop 1 = 82% Crop 2 = 5% Crop 3 = 0.32%

Yield (adjusted for purity): Crop 1 = 75% Crop 2 = 4% Crop 3 = 0.27%

I.e.: Crop 1 = 12.97 g, 91% purity, so 82%*0.91 = ~75%. This is a rough estimation of yield owing to difference in molecular weight of product **1** and impurity **2** of ~4%.

4.4.3.2 Synthesis of Compound 2 – [Dipp-NH-C(CH_3)=(CH)-P^+(C_6H_5)$_2$($C_{13}H_9$)][Br^-]

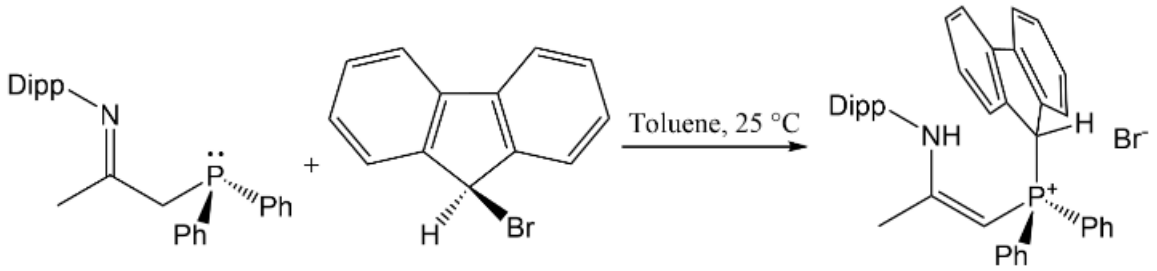

1 **2**

To a 50 mL sealed reaction vessel, **1** (0.9245 g, 2.30 mmol) and 9-bromofluorene (0.5664 g, 2.30 mmol) were combined with 12 mL toluene resulting in a very faintly yellow solution. After stirring for 1 week, compound **2** precipitates a fine white powder. This solid was separated from the yellow supernatant via centrifugation, and was washed with fresh toluene until the supernatant was clear and colourless (2×5 mL times). The solid was then rinsed into a vial with minimal toluene and dried *in vacuo* yielding a white solid (0.688 g, 1.06 mmol). A second crop was obtained (0.248 g, 0.38 mmol) after stirring the concentrated supernatant and washings an additional week with the same workup.

Note: Longer stirring (2.5 weeks) afforded 67% in the first crop using toluene. Use of THF as a solvent results in a similar yield in less than 24 hr; however, it was noted by ^{31}P NMR spectroscopy that the supernatant had more unidentified side products when using THF. Crystals suitable for X-ray crystallography were grown from evaporation of concentrated solutions of **2** in acetone (solvent free), ethanol (monohydrate), chloroform (trisolvate) or DCM (monosolvate).

Yield: 46% (Crop 1), 16% (Crop 2).

m.p. (°C): > 295 decomposes.

Analytical Calc. for $C_{40}H_{40}NP$•HBr: C: 74.30% H: 6.39% N: 2.17% Found: C: 74.10% H: 6.28% N: 2.23%.

^{1}H ($CDCl_3$, 300 MHz, 25 °C): δ 9.98 (d, 1H, *J* = 4.9 Hz, N*H*), 7.72-7.76(m, 2H, *p*-Ph), 7.55-7.66 (m, 8H, *m*-Ph, *o*-Ph), 7.43 (d, 2H, $^{3}J_{H-H}$ = 7.8 Hz, (4,5)-Flu), 7.27 (t, 4H, $^{3}J_{H-H}$ = 7.8 Hz, (3,6)-Flu), 7.16 (m, 1H, *p*-Dipp), 7.07 (d, 2H, $^{3}J_{H-H}$ = 7.8 Hz, *m*-Dipp), 6.97 (t, 2H, $^{3}J_{H-H}$ = 7.8 Hz, (2,7)-Flu), 6.29 (dd, 2H, $^{3}J_{H-H}$ = 7.8 Hz, $^{4}J_{P-H}$ = 1.2 Hz, (1,8)-Flu), 5.01 (d, 2H, $^{2}J_{P-H}$ = 16.6 Hz, P-(9)-Flu), 2.94 (sept, 2H,$^{3}J_{H-H}$ = 6.8 Hz, C*H*(CH_3)$_2$), 2.68 (d, 2H, $^{2}J_{P-H}$ = 15.9 Hz, PC*H*), 1.94 (s, 3H, N-C(C*H*$_3$)), 1.15 (d, 6H, $^{3}J_{H-H}$ = 6.8 Hz, CH(C*H*$_3$)$_2$), 0.85 (d, 6H, $^{3}J_{H-H}$ = 6.8 Hz, CH(C*H*$_3$)$_2$) ppm.

^{13}C{^{1}H} ($CDCl_3$, 75 MHz, 25 °C): δ 168.42 (d, $^{2}J_{P-C}$ = 14.9 Hz, N-*C*(CH_3)=(CH)), 146.47 (*o*-Dipp), 142.10 (d, $^{3}J_{P-C}$ = 4.3 Hz, (4a,4b)-Flu), 136.17 (d, $^{2}J_{P-C}$ = 5.4 Hz, (8a,9a)-Flu), 134.39 (d, $^{4}J_{P-C}$ = 2.8 Hz, *p*-PPh_2), 133.49 (d, $^{3}J_{P-C}$ = 9.8 Hz, *m*-PPh_2), 132.72 (*ipso*-Dipp), 129.87 (d, $^{2}J_{P-C}$ = 12.5 Hz, *o*-PPh_2), 129.37 (d, $^{4}J_{P-C}$ = 2.4 Hz, (2,7)-Flu), 127.25 (d, $^{5}J_{P-C}$ = 2.4Hz, (3,6)-Flu), 125.65 (d, $^{3}J_{P-C}$ = 3.3 Hz, (1,8)-Flu), 128.62 (*p*-Dipp), 123.87 (*m*-Dipp), 121.46 (d, $^{1}J_{P-C}$ = 84.6 Hz, *ipso*-PPh_2), 120.70 ((4,5)-Flu), 52.77 (d, $^{1}J_{P-C}$ = 123.7 Hz, P*C*H), 46.04 (d, $^{1}J_{P-C}$ = 53.4 Hz, (9)-Flu), 28.52 (*C*H(CH_3)$_2$), 25.27 (CH(*C*H$_3$)$_2$), 23.43 (CH(*C*H$_3$)$_2$), 21.67 (d, $^{3}J_{P-C}$ = 16.9 Hz, CH(*C*H$_3$)$_2$) ppm.

^{31}P{^{1}H} ($CDCl_3$, 121 MHz, 25 °C): δ 20.70 ppm.

4.4.3.3 Synthesis of Compound 3 - Dipp-NH-C(CH_3)=(CH)-P(C_6H_5)$_2$=($C_{13}H_9$)

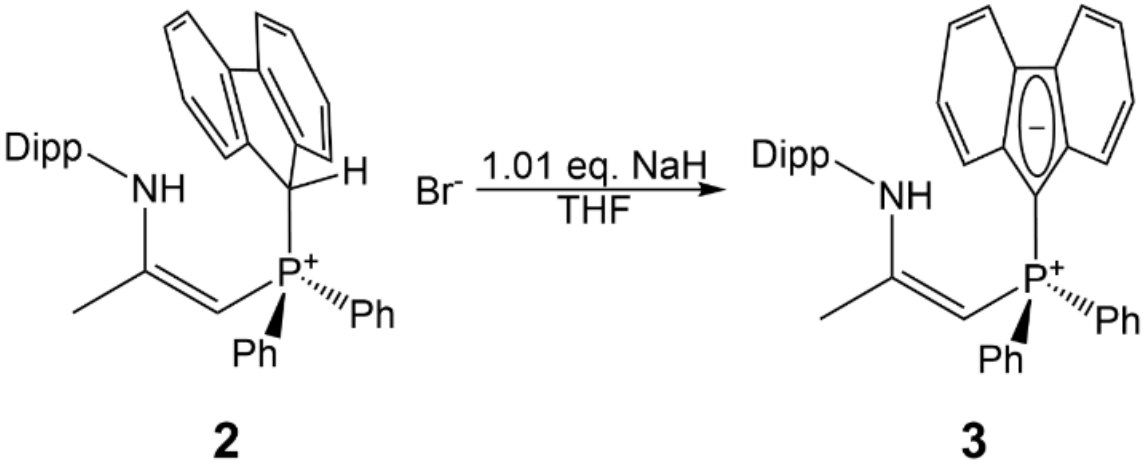

2 **3**

To a 20 mL scintillation vial, **2** (0.5166 g, 0.80 mmol) and NaH (0.0194 g, 0.81 mmol) were combined with 15 mL THF affording a white suspension that was stirred for 20 hours. The gold-coloured suspension was filtered through a pipette containing diatomaceous earth, and the solvent volume was concentrated to 1 mL. Slow addition of heptane (5 mL) with rapid stirring precipitates **3** as a canary yellow solid. This mixture was stirred 10 min, and the solvent was removed *in vacuo* resulting in a yellow paste. To this, 1 mL pentane was added and stirred for 10 min, and the solvent was decanted after the solid had settled. Drying *in vacuo* afforded 0.269 g (0.50 mmol) of an analytically pure yellow free flowing powder. Four crystal structures were obtained from cooling saturated solutions of **3** in hexane ((Z)-**3**), diethyl ether ((E)-**3**•(0.5 Et_2O)), THF ((E)-**3**•(3 THF)), and a mixture of THF and hexane ((Z)-**3**•(0.5 THF/0.5 hexane)).

Yield: 60%.

m.p. (°C): 160.1-161.5 (solvent free), 192.0 - 194.0 ((E)-**3**•(0.5 Et_2O))

Analytical Calc. for $C_{40}H_{40}NP$: C: 84.92% H: 7.13% N: 2.48% Found: C: 84.48% H: 7.20% N: 2.50%.

Major isomer: Enamine-fluorenylide 60%:

^{1}H (C_6D_6, 300 MHz, 25 °C): δ 8.33-8.36 (m, 2H, (1,8)-Flu), 7.64-7.71 (m, 4H, *o*-Ph), 7.61 (1H, s, N*H*), 7.19-7.27 (m, 4H, (2,3,6,7)-Flu), 6.96-7.11 (m, 9H, (*m*-,*p*-(Dipp, Ph)), 6.98 (d, 2H, $^{3}J_{H\text{-}H}$ = 7.5 Hz, (4,5)-Flu), 4.33 (d, 1H, $^{2}J_{P\text{-}H}$ = 16.2 Hz, PC*H*), 2.61 (2H, sept, $^{3}J_{H\text{-}H}$ = 6.9 Hz, C*H*(CH_3)$_2$), 1.48 (3H, s, N-C(C*H*$_3$)), 1.01 (d, 6H, $^{3}J_{H\text{-}H}$ = 6.9 Hz, CH(C*H*$_3$)$_2$), 0.61 (d, 6H, $^{3}J_{H\text{-}H}$ = 6.9 Hz, CH(C*H*$_3$)$_2$) ppm.

^{13}C{^{1}H} (C_6D_6, 75 MHz, 25 °C): δ 164.05 (N-*C*(CH_3)=(CH)), 146.86 (*o*-Dipp), 144.62 (4a,4b)-Flu), 141.40 (d, $^{2}J_{P\text{-}C}$ = 14.5 Hz, (8a,9a)-Flu), 136.49 (*ipso*-Dipp), 135.82 (d, $^{2}J_{P\text{-}C}$ = 120.2 Hz, *ipso*-PPh_2), 132.87 (d, $^{2}J_{P\text{-}C}$ = 10.6 Hz, *o*-PPh_2), 131.92 (d, $^{4}J_{P\text{-}C}$ = 2.5 Hz, *p*-PPh_2), 129.20 (d, $^{3}J_{P\text{-}C}$ = 12.2 Hz, *m*-PPh_2), 123.70 (*m*-Dipp), 123.62 (4,5-Flu), 123.52 (2,7-Flu), 120.37 (1,8-Flu), 117.07-117.24 (m, *p*-Dipp, 3,6-Flu), 68.39 (d, $^{1}J_{P\text{-}C}$ = 104.4 Hz, P*C*H), 55.58 (d, $^{1}J_{P\text{-}C}$ = 120.6 Hz, 9-Flu), 28.41 (*C*H(CH_3)$_2$), 22.68 (N-C-*C*H_3), 24.45 (CH(*C*H_3)$_2$), 22.87 (CH(*C*H_3)$_2$) ppm.

^{31}P{^{1}H} (C_6D_6, 121 MHz, 25 °C): δ -7.24 ppm.

Minor isomer: Imine-fluorenyl 20%:

^{1}H (C_6D_6, 300 MHz, 25 °C): δ 8.54-8.56 (m, 2H, (1,8)-Flu), 7.50-7.57 (m, 4H, *o*-PPh_2), 7.30-7.37 (m, 4H, (2,3,6,7)-Flu), 6.96-7.11 (m, 9H, *m*-,*p*-Ph, *m*-,*p*-Dipp), 6.91-6.96 (m, 2H, (4,5)-Flu), 4.49 (d, 1H, $^{2}J_{P\text{-}H}$ = 3.9 Hz, 9-Flu), 4.23 (d, 1H, $^{2}J_{P\text{-}H}$ = 14.3 Hz, PC*H*), 3.04 (2H, sept, $^{3}J_{H\text{-}H}$ = 6.9 Hz, C*H*(CH_3)$_2$), 1.36 (3H, d, $^{4}J_{P\text{-}H}$ = 2.1 Hz, N-C(C*H*$_3$)), 1.20 (d, 6H, $^{3}J_{H\text{-}H}$ = 6.9 Hz, CH(C*H*$_3$)$_2$), 1.06 (d, 6H, $^{3}J_{H\text{-}H}$ = 6.9 Hz, CH(C*H*$_3$)$_2$) ppm.

^{13}C{^{1}H} (C_6D_6, 75 MHz, 25 °C): δ 165.03 ($^{2}J_{P\text{-}C}$ = 7.5 Hz, N=*C*(CH_3)-(CH_2)), 145.50 (*o*-Dipp), 142.19 ((4a,4b)-Flu), 142.04 (d, $^{2}J_{P\text{-}C}$ = 15.3 Hz, (8a,9a)-Flu), 136.99 (*ipso*-Dipp),

between 130-135 (*ipso*-PPh_2), 132.90 (d, $^2J_{P-C}$ = 10.6 Hz, *o*-PPh_2), 132.57 (d, $^4J_{P-C}$ = 2.5 Hz, *p*-PPh_2), 128.97 (d, $^3J_{P-C}$ = 12.1 Hz, *m*-PPh_2), 124.56 (2,7-Flu), 123.23 (*m*-Dipp), 120.22 (1,8-Flu), 116.35 (3,6-Flu), 117.07-117.24 (m, *p*-Dipp, 4,5-Flu), 70.87 (d, $^1J_{P-C}$ = 119.8 Hz, P*C*H), 55.16 (d, $^1J_{P-C}$ = 129.9 Hz, 9-Flu), 28.26 (*C*H(CH_3)$_2$), 24.15 (CH(*C*H_3)$_2$), 22.99 (CH(*C*H_3)$_2$), 18.28 (d, $^3J_{P-C}$ = 4.4 Hz, N-C-*C*H_3) ppm.

$^{31}P\{^1H\}$ (C_6D_6, 121 MHz, 25 °C): δ -0.40 ppm.

Minor isomer: Imine-fluorenylide 20%:

^1H (C_6D_6, 300 MHz, 25 °C): δ 8.37-8.40 (m, 2H, (1,8)-Flu), 7.77-7.84 (m, 4H, *o*-PPh_2), 7.19-7.27 (m, 4H, (2,3,6,7)-Flu), 6.86-6.94 (m, 9H, *m*-,*p*-(Dipp, Ph), 6.69-6.72 (m, 2H, (4,5)-Flu), 3.83 (d, 2H, $^2J_{P-H}$ = 15.3 Hz, PC*H*$_2$), 2.61 (2H, sept, $^3J_{H-H}$ = 6.9 Hz, C*H*(CH_3)$_2$), 1.04 (3H, d, $^4J_{P-H}$ = 1.3 Hz, N-C(C*H*$_3$)), 1.12 (d, 6H, $^3J_{H-H}$ = 6.9 Hz, CH(C*H*$_3$)$_2$), 0.78 (d, 6H, $^3J_{H-H}$ = 6.9 Hz, CH(C*H*$_3$)$_2$) ppm.

$^{13}C\{^1H\}$ (C_6D_6, 75 MHz, 25 °C): δ 193.09 (N=*C*(CH_3)-(CH_2)), 147.56 (*o*-Dipp), 143.56 ((4a,4b)-Flu), 142.45 (d, $^3J_{P-C}$ = 15.0 Hz, (8a,9a)-Flu), 136.62 (*ipso*-Dipp), between 130-135 (*ipso*-PPh_2), 133.67 (d, $^2J_{P-C}$ = 10.5 Hz, *o*-PPh_2), 131.65 (d, $^4J_{P-C}$ = 2.4 Hz, *p*-PPh_2), 124.37 (2,7-Flu), 124.23 (*m*-Dipp), 120.22 (1,8-Flu), 117.07 – 117.24 (m, *p*-Dipp, (4,5)-Flu, (3,6)-Flu), 50.74 (d, $^1J_{P-C}$ = 123.6 Hz, 9-Flu), 39.36 (d, $^1J_{P-C}$ = 48.64 Hz, P*C*H_2), 28.55 (*C*H(CH_3)$_2$), 22.48 (N-C-*C*H_3), 24.75 (CH(*C*H_3)$_2$), 23.96 (CH(*C*H_3)$_2$) ppm.

$^{31}P\{^1H\}$ (C_6D_6, 121 MHz, 25 °C): δ -0.38 ppm.

4.4.3.4 Synthesis of Compound 4a – $[Li^+][Dipp\text{-}N^-\text{-}C(CH_3)=(CH)\text{-}P(C_6H_5)_2(\eta^2\text{-}C_{13}H_9)]$ • Et_2O

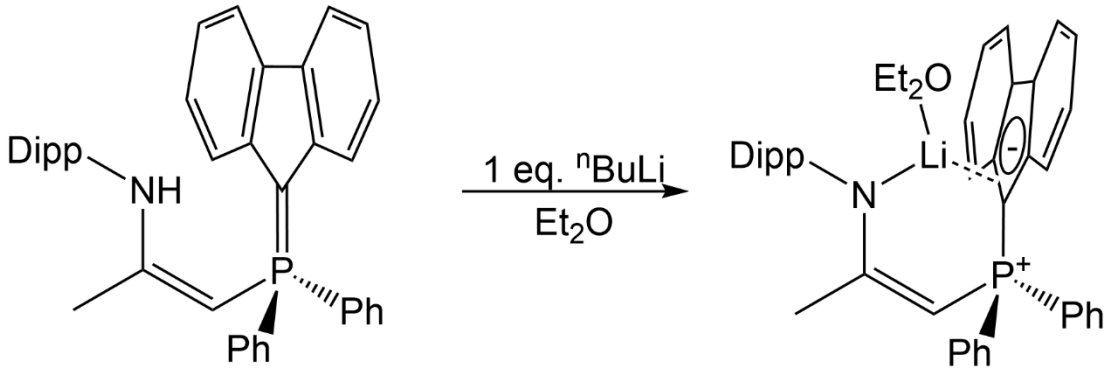

3 **4a**

To a 20 mL scintillation vial 223.2 mg (0.40 mmol) of yellow **3** was suspended in 6 mL diethyl ether, and to this golden yellow suspension 0.16 mL 2.5 M n-BuLi (0.40 mmol) in hexane were added rapidly at room temperature followed by an additional 2 mL diethyl ether. The solution became orange with yellow suspended solid within 2 hr, and stirring for 24 hr afforded a red, clear solution. Filtration through a medium frit removed a trace of dark red solid that was discarded (turned green overnight) after eluting hot toluene through it afforded nothing. The filtrate was heated gently to a reflux and reduced to 1 mL until solid began forming and was sealed and placed in -35 °C overnight forming a microcrystalline solid. Decanting the diethyl ether and drying the solid *in vacuo* afforded 202 mg (0.32 mmol) of a yellow microcrystalline solid that was analytically pure and suitable for X-ray analysis.

Yield: 79%

m.p. (°C): 135.5 – 136.3

Analytical Calc. for $C_{44}H_{49}NPLiO$: C: 81.83% H: 7.65% N: 2.17%. Found: C: 82.06% H: 7.63% N: 2.14%.

^{1}H (C_6D_6, 300 MHz, 25 °C): δ 8.25-8.28 (m, 2H, (1,8)-Flu), 7.79 (d, 2H, J_{P-H} = 7.1 Hz, (3,6)-Flu), 7.64-7.70 (m, 4H, (2,4,5,7)-Flu), 7.25 (m, 4H, *o*-Ph), 6.94-7.08 (m, 9H, *m*-,*p*-Ph, *m*-,*p*-Dipp), 3.66 (d, 1H, $^{2}J_{P-H}$ = 19.4 Hz, PC*H*), 3.27 (2H, sept, $^{3}J_{H-H}$ = 6.9 Hz, C*H*$(CH_3)_2$), 2.31 (quart, 4H, $^{3}J_{H-H}$ = 7.1 Hz, $Et_2O(CH_2)$, 1.89 (3H, d, $^{4}J_{P-H}$ = 2.1 Hz, N-C(C*H*$_3$)), 1.28 (d, 6H, $^{3}J_{H-H}$ = 6.9 Hz, CH(C*H*$_3)_2$), 0.97 (d, 6H, $^{3}J_{H-H}$ = 6.9 Hz, CH(C*H*$_3)_2$), 0.31 (t, 6H, $^{3}J_{H-H}$ = 7.1 Hz, Et_2O-C*H*$_3$) ppm.

$^{13}C\{^{1}H\}$ (C_6D_6, 75 MHz, 25 °C): δ 171.70 (d, $^{2}J_{P-C}$ = 3.4 Hz, N-*C*(CH_3)=(CH)), 149.25 (*ipso*-Dipp), 142.43 (*o*-Dipp), 141.36 (d, $^{2}J_{P-C}$ = 10.9 Hz, (4a,4b)-Flu), 134.76 (d, $^{1}J_{P-C}$ = 86.7 Hz, *ipso*-PPh_2), 132.43 (d, $^{2}J_{P-C}$ = 10.0 Hz, *o*-PPh_2), 132.00 (d, $^{2}J_{P-C}$ = 11.5 Hz, (8a,9a)-Flu), 130.9 (d, $^{4}J_{P-C}$ = 2.5 Hz, *p*-PPh_2), 128.74 (d, $^{3}J_{P-C}$ = 11.5 Hz, *m*-PPh_2), 124.57 (3,6-Flu), 123.49 (*p*-Dipp), 123.42 (*m*-Dipp), 120.00 (4,5-Flu), 119.00 (1,8-Flu), 118.30 (2,7-Flu), 63.76 (Et_2O-*C*H_3), 54.72 (d, $^{1}J_{P-C}$ = 113.8 Hz, P*C*H), 27.91 (*C*H$(CH_3)_2$), 25.12 (d, $^{3}J_{P-C}$ = 17.0 Hz, N-C-*C*H_3), 24.63 (CH(*C*$H_3)_2$), 24.42 (CH(*C*$H_3)_2$), 13.90 (Et_2O-*C*H_3) ppm.

$^{31}P\{^{1}H\}$ (C_6D_6, 121 MHz, 25 °C): δ -2.39 ppm.

^{7}Li (C_6D_6, 117 MHz, 25 °C): δ -0.58 ppm.

4.4.3.5 Synthesis of Compound 4b - [Li^+][Dipp-N^--C(CH_3)=(CH)-P(C_6H_5)$_2$($C_{13}H_9$)]

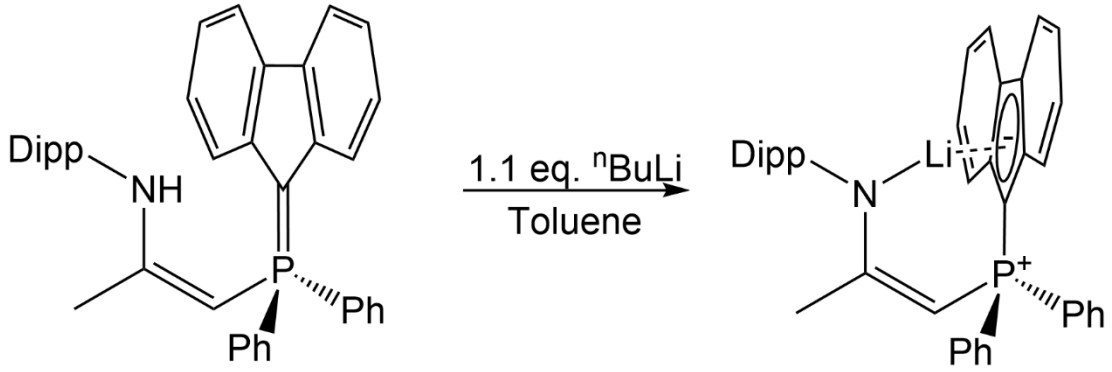

3 **4b**

To a 20 mL scintillation vial 114 mg **3** (0.20 mmol) dissolved in 4 mL toluene had 0.09 mL 2.5 M n-BuLi (0.23 mmol) in hexane added. The initial gold solution became more orange over 30 minutes and the solvent was concentrated *in vacuo* to ~2 mL, filtered and rinsed through a lint free wipe, concentrated again to ~2 mL and dried *in vacuo* affording 210 mg of a red crystalline paste. This was triturated with pentane (4 mL) and filtered through a medium porosity glass frit resulting in an orange powder that turned green upon drying (28 mg) that was discarded. The dark red filtrate was dried as a red microcrystalline paste (99 mg) and 4×0.5 mL rinses with pentane followed by decanting the solvent afforded 46 mg of a peach-coloured powder upon drying *in vacuo* (0.08 mmol).

Yield: 40%

Analytical Calc. for $C_{40}H_{39}NPLi$: C: 84.04% H: 6.88% N: 2.45%. Found: C: 82.47% H: 7.59% N: 2.14%.

^1H (C_6D_6, 300 MHz, 25 °C): δ 8.26-8.29 (m, 2H, (1,8)-Flu), 7.56-7.65 (m, 6H, *o*-PPh_2, (3,6)-Flu), 7.22-7.29 (m, 4H, (2,4,5,7)-Flu), 6.94-7.08 (m, 9H, *m*-,*p*-Ph, *m*-,*p*-Dipp), 3.58 (d, 1H, $^2J_{P\text{-}H}$ = 19.4 Hz, PC*H*), 2.98 (2H, sept, $^3J_{H\text{-}H}$ = 6.8 Hz, C*H*(CH_3)$_2$), 1.78 (3H, d, $^4J_{P\text{-}}$

$_H$ = 2.1 Hz, N-C(CH_3)), 1.17 (d, 6H, $^3J_{H-H}$ = 6.8 Hz, CH(CH_3)$_2$), 0.88 (d, 6H, $^3J_{H-H}$ = 6.8 Hz, CH(CH_3)$_2$) ppm.

$^{13}C\{^1H\}$ (C_6D_6, 75 MHz, 25 °C): δ 171.84 (N-*C*(CH_3)=(CH)), 148.85 (*ipso*-Dipp), 142.15 (*o*-Dipp), 140.57 (d, $^2J_{P-C}$ = 10.9 Hz, (4a,4b)-Flu), 130.20 (d, $^1J_{P-C}$ = 87.1 Hz, *ipso*-PPh_2), 132.20 (d, $^2J_{P-C}$ = 10.0 Hz, *o*-PPh_2), 131.81 (d, $^2J_{P-C}$ = 11.5 Hz, (8a,9a)-Flu), 130.03 (d, $^4J_{P-C}$ = 2.5 Hz, *p*-PPh_2), 128.78 (d, $^3J_{P-C}$ = 11.5 Hz, *m*-PPh_2), 124.82 (2,7-Flu), 123.57 (*p*-, *m*-Dipp), 120.27 (1,8-Flu), 118.86 (4,5-Flu), 118.76 (3,6-Flu), 55.08 (d, $^1J_{P-C}$ = 113.5 Hz, P*C*H), 27.90 (*C*H(CH_3)$_2$), 25.01 (d, $^3J_{P-C}$ = 17.0 Hz, N-C-*C*H_3), 24.57 (CH(*C*H_3)$_2$), 24.29 (CH(*C*H_3)$_2$) ppm.

$^{31}P\{^1H\}$ (C_6D_6, 121 MHz, 25 °C): δ -2.35 ppm.

^{7}Li (C_6D_6, 117 MHz, 25 °C): δ -2.19 ppm.

4.4.3.6 Synthesis of Compound 5 - [Na^+][(η^1-Dipp)-N^--C(CH_3)=(CH)-P(C_6H_5)$_2$(η^4-$C_{13}H_9$)] • THF

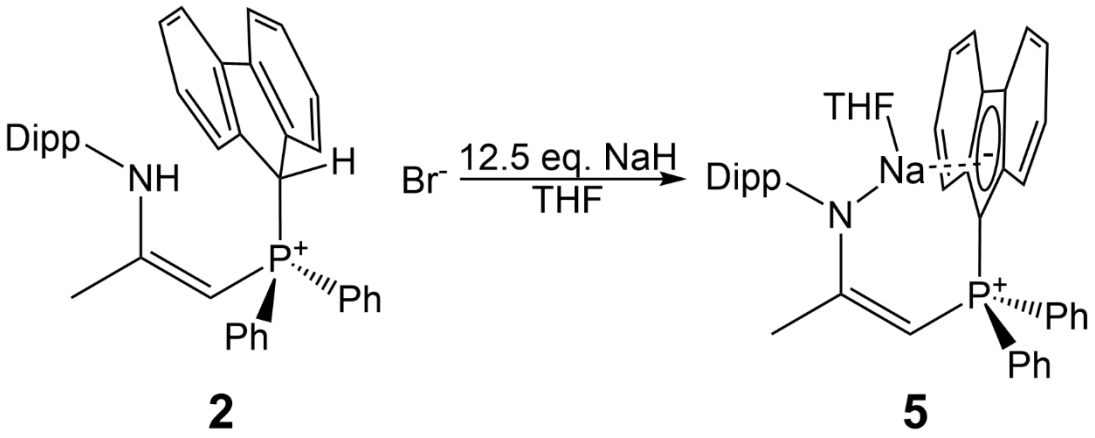

2 **5**

In a 20 mL scintillation vial, 350 mg (0.50 mmol) **2** and 162 mg (6.80 mmol) NaH were suspended in 14 mL hexane for 3 days, with minimal changes (slight yellowing). 1 mL

toluene were added followed by removal of most of the solvent *in vacuo*, with addition of 11 mL THF following removal of hexane progressing to a yellow, then orange, and finally a red with light-coloured precipitate the next day. A ~1 mL aliquot was taken, and removal of solvent *in vacuo* followed by dissolution into C_6D_6 showed complete conversion to **5**. Removing the solvent *in vacuo* and adding the C_6D_6 solution to the red solid was followed with swirling the 0.5 mL solution around the vial leading to spontaneous crystallization. The solid was washed with 2×1 mL hexane resulting in immediate precipitation as the crystals went opaque. The solids were initially a non-uniform beige, yellow, orange and red, but drying *in vacuo* afforded 364 mg (0.50 mmol) of a homogenous beige solid. Final analysis using ^{1}H NMR spectroscopy showed residual hexanes (~1/4 hexane to **5** ratio) resulting in an adjusted final yield of 0.35 g (0.48 mmol) for the ~96% dry solid.

Yield: 96%

m.p. (°C): 168.1-170.2

Analytical Calc. for $C_{44}H_{47}NPONa$: C: 80.09% H: 7.18% N: 2.12% Found: C: 79.47% H: 6.95% N: 2.22%.

^{1}H (C_6D_6, 300 MHz, 25 °C): δ 8.32 (d, 2H, $^3J_{H\text{-}H}$ = 7.8 Hz, (1,8)-Flu), 7.84 (dd, 4H, $^3J_{H\text{-}H}$ = 7.5 Hz, $^3J_{P\text{-}H}$ = 12.0 Hz, *o*-PPh_2), 7.54 (d, 2H, $^3J_{H\text{-}H}$ = 7.8 Hz, (4,5)-Flu), 7.03-7.26 (m, 10H, *m*-Ph, *p*-Ph, (2,3,6,7)-Flu), 6.89-6.97 (m, 3H, *m*-,*p*-Dipp), 3.51 (d, 1H, $^2J_{P\text{-}H}$ = 21.3 Hz, PC*H*), 3.02 (2H, sept, $^3J_{H\text{-}H}$ = 6.9 Hz, C*H*(CH_3)$_2$), 2.75-2.87 (m, 4H, O(C*H*$_2$)$_2$), 1.84 (3H, d, $^4J_{P\text{-}H}$ = 2.2 Hz, N-C(C*H*$_3$)), 1.21 (d, 6H, $^3J_{H\text{-}H}$ = 6.9 Hz, CH(C*H*$_3$)$_2$), 1.04-1.12 (m, 4H, O(CH_2)$_2$(C*H*$_2$)$_2$), 0.74 (d, 6H, $^3J_{H\text{-}H}$ = 6.9 Hz, CH(C*H*$_3$)$_2$) ppm.

$^{13}C\{^{1}H\}$ (C_6D_6, 75 MHz, 25 °C): δ 169.95 (N-*C*(CH_3)=(CH)), 150.02 (*ipso*-Dipp), 141.34 (*o*-Dipp), 140.07 (d, $^{2}J_{P\text{-}C}$ = 13.7 Hz, 8a,9a-Flu), 135.46 (d, $^{1}J_{P\text{-}C}$ = 88.0 Hz, *ipso*-PPh_2), 132.73 (d, $^{2}J_{P\text{-}C}$ = 10.4 Hz, *o*-PPh_2), 130.88 (d, $^{4}J_{P\text{-}C}$ = 2.2 Hz, *p*-PPh_2), 128.83 (d, $^{3}J_{P\text{-}C}$ = 11.7 Hz, *m*-PPh_2), 127.6-128.4 (4a,5a-Flu), 123.97 (2,7-Flu), 123.57 (*m*-Dipp), 122.54 (*p*-Dipp), 120.16 (1,8-Flu), 118.16 (4,5-Flu), 116.80 (3,6-Flu), 67.54 (O(*C*H_2)$_2$), 52.33 (d, $^{1}J_{P\text{-}C}$ = 115.0 Hz, P*C*H), 27.44 (*C*H(CH_3)$_2$), 25.30 (O(CH_2)$_2$(*C*H_2)$_2$), 24.3-24.7 (N-C-*C*H_3), 24.36 (CH(*C*H_3)$_2$), 24.15 (CH(*C*H_3)$_2$) ppm.

$^{31}P\{^{1}H\}$ (C_6D_6, 121 MHz, 25 °C): δ -4.28 ppm.

4.4.3.7 Synthesis of Compound 6a - [K^+][(η^2-Dipp)-N^--C(CH_3)=(CH)-P(C_6H_5)$_2$(η^5-$C_{13}H_9$)] • Et_2O

2 **6a**

To a 20 mL scintillation vial, 0.3630 g (0.56 mmol) compound **2** and 0.0470 g (1.17 mmol) KH were suspended in 10 mL diethyl ether as a white suspension with stirring overnight at room temperature. The solution became dark red, and filtration through a medium glass frit afforded a small amount of red solid that was discarded, and the golden filtrate was concentrated *in vacuo* to 5 mL that gave no solid upon cooling to -35 °C. Further concentration to 2 mL *in vacuo*, sealing the vial while boiling, and cooling to -35 °C gave

0.336 g (0.49 mmol) of **6a** as analytically pure, X-ray quality yellow crystals upon decanting the solution and drying *in vacuo*.

Yield: 88%

m.p. (°C): Condensation at 120, non-homogenous melt from 135-230, fully molten at 245

Analytical Calc. for $C_{44}H_{49}NPKO$: C: 77.95% H: 7.29% N: 2.07%. Found: C: 78.21% H: 7.20% N: 2.08%.

^{1}H (C_6D_6, 300 MHz, 25 °C): δ 8.26 (d, 2H, $^{3}J_{H\text{-}H}$ = 7.8 Hz, (1,8)-Flu), 7.85 (dd, 4H, $^{3}J_{H\text{-}H}$ = 7.0 Hz, $^{3}J_{P\text{-}H}$ = 11.8 Hz, *o*-PPh_2) (d, 2H, $^{3}J_{H\text{-}H}$ = 7.8 Hz, (4,5)-Flu), 7.04-7.20 (m, 10H, *m*-Ph, *p*-Ph, (2,3,6,7)-Flu), 6.88-6.97 (m, 3H, *m*-,*p*-Dipp), 3.43 (d, 1H, $^{2}J_{P\text{-}H}$ = 22.2 Hz, PC*H*), 2.84 (2H, sept, $^{3}J_{H\text{-}H}$ = 6.8 Hz, C*H*$(CH_3)_2$), 1.85 (3H, d, $^{4}J_{P\text{-}H}$ = 2.2 Hz, N-C(C*H*$_3$)), 1.17 (d, 6H, $^{3}J_{H\text{-}H}$ = 6.8 Hz, CH(C*H*$_3$)$_2$), 0.69 (d, 6H, $^{3}J_{H\text{-}H}$ = 6.8 Hz, CH(C*H*$_3$)$_2$) ppm.

^{13}C{^{1}H} (C_6D_6, 75 MHz, 25 °C): δ 168.02 (N-*C*(CH_3)=(CH)), 149.95 (*ipso*-Dipp), 141.06 (d, $^{2}J_{P\text{-}C}$ = 14.0 Hz, 8a,9a-Flu), 140.89 (*o*-Dipp), 136.05 (d, $^{1}J_{P\text{-}C}$ = 88.1 Hz, *ipso*-PPh_2), 132.81 (d, $^{2}J_{P\text{-}C}$ = 10.3 Hz, *o*-PPh_2), 130.67 (d, $^{4}J_{P\text{-}C}$ = 2.4 Hz, *p*-PPh_2), 128.72 (d, $^{3}J_{P\text{-}C}$ = 11.8 Hz, *m*-PPh_2), 127.59 (4a,5a-Flu), 123.84 (*m*-Dipp), 123.58 (2,7-Flu), 121.96 (*p*-Dipp), 119.67 (1,8-Flu), 118.04 (4,5-Flu), 115.85 (3,6-Flu), 51.7 (d, $^{1}J_{P\text{-}C}$ = 115.7 Hz, P*C*H), 27.20 (*C*H$(CH_3)_2$), 24.64 (CH(*C*H$_3$)$_2$), 24.26 (CH(*C*H$_3$)$_2$), 24.26 (d, $^{3}J_{P\text{-}C}$ = 17.8 Hz, N-C-*C*H$_3$) ppm.

^{31}P{^{1}H} (C_6D_6, 121 MHz, 25 °C): δ -3.33 ppm.

4.4.3.8 Synthesis of Compound 6b - [K^+][(Dipp)--N^--C(CH_3)=(CH)P(C_6H_5)$_2$($C_{13}H_9$)]

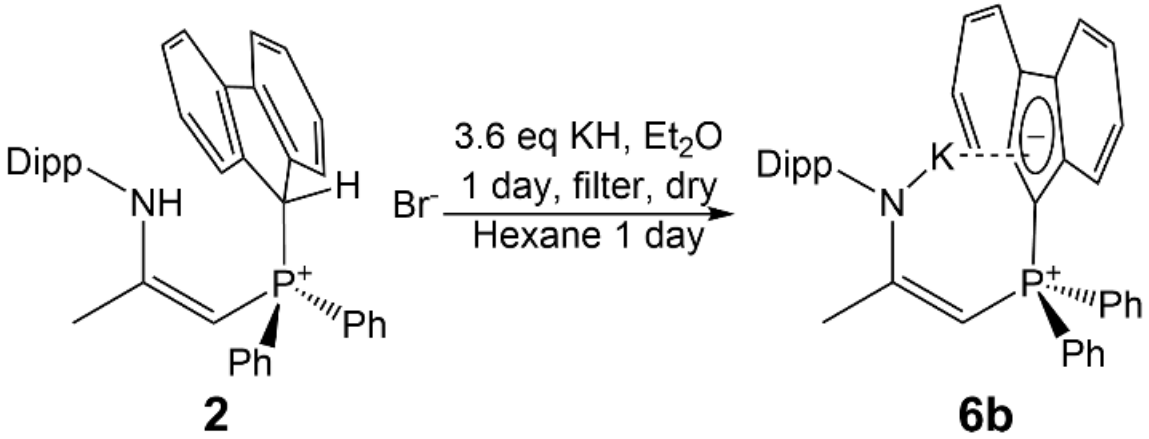

2 **6b**

A white suspension of 165 mg (0.26 mmol) **2** and 37 mg (0.92 mmol) KH in 12 mL diethyl ether were stirred for one day at room temperature in a 20 mL scintillation vial. The resulting yellow solution with yellow solids was dried *in vacuo* and extracted with hot hexane using 6x1.5 mL aliquots through a diatomaceous earth pipette filter leaving yellow solid. The solid was eluted from the filter with 3×2 mL diethyl ether, dried *in vacuo* forming a glassy greenish yellow foam. 8 mL hexanes were added and allowed to stir with the suspended yellow solid for 3 days. The yellow solids were allowed to settle out of the faintly yellow hexane solution that was mostly removed via a pipette. Drying the remaining solution and yellow solid *in vacuo* for 8 hours over 2 days gave 0.050 g of a free-flowing yellow powder. NMR spectroscopy including ^{1}H, ^{31}P, and ^{31}P HMBC indicated the solids were primarily **6** with a small amount of THF absorbed from the glovebox atmosphere, residual hexanes, and a trace of **3**. Compound **6** was found to form yellow crystals upon cooling or slow evaporation of a concentrated diethyl ether solution containing a single diethyl ether adduct on potassium. Crystals with half a molecule of hexane and oligomeric **6** were also found to form from slow evaporation of a concentrated hexane solution. Loss

of co-crystallized solvent does occur with prolonged drying *in vacuo*, though coordinating solvents were not able to be easily removed via dissolution in C_6D_6. Degradation into **3** via either hydrolysis or other unexplored reactivity occurred readily while working within the glovebox.

Yield: 32%

m.p. (°C): 116.0 – 118.1

Analytical Calc. for $C_{40}H_{39}NPK$: C: 79.57% H: 6.51% N: 2.32% Found: C: 79.55% H: 6.58% N: 2.32%.

^{1}H (C_6D_6, 300 MHz, 25 °C): δ 8.26 (d, 2H, $^3J_{H\text{-}H}$ = 7.8 Hz, (1,8)-Flu), 7.85 (dd, 4H, $^3J_{H\text{-}H}$ = 7.0 Hz, $^3J_{P\text{-}H}$ = 11.8 Hz, *o*-PPh_2), 7.39 (d, 2H, $^3J_{H\text{-}H}$ = 7.8 Hz, (4,5)-Flu), 7.04-7.20 (m, 10H, *m*-Ph, *p*-Ph, (2,3,6,7)-Flu), 6.88-6.97 (m, 3H, *m*-,*p*-Dipp), 3.43 (d, 1H, $^2J_{P\text{-}H}$ = 22.2 Hz, PC*H*), 2.84 (2H, sept, $^3J_{H\text{-}H}$ = 6.8 Hz, C*H*$(CH_3)_2$), 1.85 (3H, d, $^4J_{P\text{-}H}$ = 2.2 Hz, N-C(C*H*$_3$)), 1.17 (d, 6H, $^3J_{H\text{-}H}$ = 6.8 Hz, CH(C*H*$_3$)$_2$), 0.69 (d, 6H, $^3J_{H\text{-}H}$ = 6.8 Hz, CH(C*H*$_3$)$_2$) ppm.

^{13}C{^{1}H} (C_6D_6, 75 MHz, 25 °C): δ 168.02 (N-*C*(CH_3)=(CH)), 149.95 (*ipso*-Dipp), 141.06 (d, $^2J_{P\text{-}C}$ = 14.0 Hz, 8a,9a-Flu), 140.89 (*o*-Dipp), 136.05 (d, $^1J_{P\text{-}C}$ = 88.1 Hz, *ipso*-PPh_2), 132.81 (d, $^2J_{P\text{-}C}$ = 10.3 Hz, *o*-PPh_2), 130.67 (d, $^4J_{P\text{-}C}$ = 2.4 Hz, *p*-PPh_2), 128.72 (d, $^3J_{P\text{-}C}$ = 11.8 Hz, *m*-PPh_2), 127.59 (4a,5a-Flu), 123.84 (*m*-Dipp), 123.58 (2,7-Flu), 121.96 (*p*-Dipp), 119.67 (1,8-Flu), 118.04 (4,5-Flu), 115.85 (3,6-Flu), 63.24 (d, $^1J_{P\text{-}C}$ = 121.2 Hz, P*C*H), 51.66 (d, $^1J_{P\text{-}C}$ = 115.7 Hz, P*C*H), 27.20 (*C*H$(CH_3)_2$), 24.64 (CH(*C*H$_3)_2$), 24.26 (CH(*C*H$_3)_2$), 24.26 (d, $^3J_{P\text{-}C}$ = 17.8 Hz, N-C-*C*H$_3$) ppm, 15.55 (Et_2O-*C*H$_3$).

^{31}P{^{1}H} (C_6D_6, 121 MHz, 25 °C): δ -3.33 ppm.

4.5 Conclusion

Reacting a previously reported[40] bulky phosphine-imine **1** with 9-bromofluorene results in a hydrobromide salt **2** that upon deprotonation forms a phosphonium fluorenylide/Enamine bidentate ligand precursor **3**, along with alkali metal complexes of Li (**4**), Na (**5**), and K (**6**). Analysis of various solvates provided additional information about the η-interactions that occur within the solid state. Following the work presented in this paper, future work seeks to form other metal complexes including aluminum, rhodium, bismuth, and other transition and alkaline earth metal complexes using the free ligand **3** and alkali metal complexes **4**-**6** as precursors to explore the bonding motifs and efficacy of forming other non-alkali metal complexes for further understanding their bonding and structure. Two small-scale reactions with metal halides (AlI_3, $ZrCl_4$) have resulted in multiple unidentifiable ^{31}P NMR spectroscopy signals each, though attempts to isolate a single product only gave crystals of the hydrochloride and hydro triiodide salts. Though a literature gap exists for amide tethered phosphonium fluorenide ligands, we suspect the bidentate monoanionic [**3**]$^-$ will be good at stabilizing metal centers through the bulky amide tether that will hold the metal center directly adjacent the highly variable phosphonium fluorenide donor. Further studies will utilize **3**-**6** as precursors for preparing a variety of potential organometallic catalysts utilizing alkaline earth, transition, main-group and lanthanide metals, with initial sights set on structural characterization to further understand how metals with higher oxidation states behave when bound with this ligand. One suspected avenue of decomposition expected is cleavage of the phosphonium fluorenide. Phosphonium ylides tend towards formation of phosphine oxides and alkene

products via Wittig reactions, implying instability of these complexes to carbonyl-containing organic functional groups such as ketones and aldehydes; however, this decomposition may be beneficial resulting in a monoanionic (or neutral) bidentate phosphine-amide/imine ligand **1** and a 9-fluoreneylidene ligand on the metal similar to a Ru(II) complex baring a tridentate neutral ligand alongside two chloride ligands.[41]

4.6 References

1. Shamiri, A.; Chakrabarti, M. H.; Jahan, S.; Hussain, M. A.; Kaminsky, W.; Aravind, P. V.; Yehye, W. A. The Influence of Ziegler-Natta and Metallocene Catalysts on Polyolefin Structure, Properties, and Processing Ability. *Materials* **2014**, *7*, 5069-5108.

2. Cohen, S. A.; Auburn, P. R.; Bercaw, J. E. Structure and reactivity of bis(pentamethylcyclopentadienyl)(ethylene)titanium(II), a simple olefin adduct of titanium. *Journal of the American Chemical Society* **1983**, *105*, 1136-1143.

3. Veiros, L. F. Haptotropic shifts in organometallic complexes with eta(5)-coordinated pi ligands. *Journal of Organometallic Chemistry* **1999**, *587*, 221-232.

4. Kirillov, E.; Kahlal, S.; Roisnel, T.; Georgelin, T.; Saillard, J.; Carpentier, J. Haptotropic rearrangements in sandwich (fluorenyl)(cyclopentadienyl) iron and ruthenium complexes. *Organometallics* **2008**, *27*, 387-393.

5. Veiros, L. F. The Role of Haptotropic Shifts in Phosphine Addition to Tricarbonylmanganese Organometallic Complexes: The Indenyl Effect Revisited. *Organometallics* **2000**, *19*, 3127-3136.

6. Evans, K. J.; Campbell, C. L.; Haddow, M. F.; Luz, C.; Morton, P. A.; Mansell, S. M. Lithium Complexes with Bridging and Terminal NHC ligands: The Decisive Influence

of an Anionic Tether. *European Journal of Inorganic Chemistry* **2019**, *2019*, 4894-4901.

7. Evans, K. J.; Mansell, S. M. Synergic Deprotonation Generates Alkali-Metal Salts of Tethered Fluorenide-NHC Ligands Co-Complexed to Alkali-Metal Amides. *Chemistry* **2019**, *25*, 3766-3769.

8. Downing, S. P.; Danopoulos, A. A. Indenyl- and Fluorenyl-Functionalized N-Heterocyclic Carbene Complexes of Titanium and Vanadium. *Organometallics* **2006**, *25*, 1337-1340.

9. Geitner, R.; Kosygin, I.; Görls, H.; Pahl, J.; Harder, S.; Westerhausen, M.; Langer, J.; Langer, J. An unsymmetrical phosphonium diylide with a fluorenylidene subunit and its lithium complexes. *Journal of Coordination Chemistry* **2015**, *68*, 3302-3316.

10. Neander, S.; Tio, F. E.; Buschmann, R.; Behrens, U.; Olbrich, F. Cyclopentadienyl, indenyl, fluorenyl, and pentamethylcyclopentadienyl complexes of potassium with 18-crown-6. *Journal of Organometallic Chemistry* **1999**, *582*, 58-65.

11. Neander, S.; Körnich, J.; Olbrich, F. Novel fluorenyl alkali metal Diglyme complexes: synthesis and solid state structures. *Journal of Organometallic Chemistry* **2002**, *656*, 89-96.

12. Harder, S.; Lutz, M.; Straub, A. W. G. Silicon-Bridged Alkali-Metal and Alkaline-Earth-Metal Metallocene Complexes. *Organometallics* **1997**, *16*, 107-113.

13. Üffing, C.; Köppe, R.; Schnöckel, H. Molecular Structure of Fluorenyllithium. *Organometallics* **1998**, *17*, 3512-3515.

14. Neander, S.; Behrens, U.; Olbrich, F. Novel 18-crown-6 organometallic rubidium and cesium complexes containing cyclopentadienyl, indenyl, pentamethylcyclopentadienyl, and fluorenyl as carbanions. *Journal of Organometallic Chemistry* **2000**, *604*, 59-67.

15. Arce, A.; De Sanctis, Y.; Galarza, E.; Garland, M. T.; Baggio, R. Two complexes derived from the reaction of M3(CO)12 clusters (M = Ru, Os) with the 9-(triphenylphosphonio)fluorenide ylide: tricarbonyl[9-(triphenylphosphonio)fluorenylidene]ruthenium and nonacarbonyl-μ3-fluorenylidene-μ2-hydrido-triangulo-triosmium(III). *Acta Crystallographica, Section C* **2013**, *69*, 363-366.

16. Avent, A. G.; Crimmin, M. R.; Hill, M. S.; Hitchcock, P. B. Reactivity of [HC{(C(Me)N(Dipp))}(2)-Ca{N(SiMe$_3$)(2)}(THF)] (Dipp = (C$_6$H$_3$Pr$_2$)-Pr-i-2,6) with C-H acids: Synthesis of heteroleptic calcium eta(5)-organometallics. *Journal of Organometallic Chemistry* **2006**, *691*, 1242-1250.

17. Kirillov, E.; Toupet, L.; Lehmann, C. W.; Razavi, A.; Kahlal, S.; Saillard, J.; Carpentier, J. [(Cp−CMe$_2$−Flu)$_2$Ln]-[Li(ether) n]+ (Ln = Y, La): Complexes with Unusual Coordination Modes of the Fluorenyl Ligand and the First Examples of Bis-Ansa Lanthanidocenes. *Organometallics* **2003**, *22*, 4038-4046.

18. Werle, C.; Bailly, C.; Karmazin-Brelot, L.; Le Goff, X.; Pfeffer, M.; Djukic, J. First Stabilization of 14-Electron Rhodium(I) Complexes by Hemichelation. *Angewandte Chemie-International Edition* **2014**, *53*, 9827-9831.

19. Freund, C.; Barros, N.; Gornitzka, H.; Martin-Vaca, B.; Maron, L.; Bourissou, D. Enforced η^1-Fluorenyl Coordination to Rhodium(I) with the [FluPPh_2NPh]- Ligand. *Organometallics* **2006**, *25*, 4927-4930.

20. Schulte, P.; Behrens, U. Organometallic compounds of copper. XX - On the reaction of the alkyne copper(I) complexes [CuCl(S-alkyne)] and [Cu_2Br_2(S-alkyne)(dms)] (S-alkyne=3,3,6,6-tetramethyl-1-thiacyclohept-4-yne; dms = dimethylsulfide) with the lithiumorganyls phenyllithium and fluorenyllithium. *Zeitschrift Fur Anorganische Und Allgemeine Chemie* **2000**, *626*, 1692-1696.

21. Mutseneck, E. V.; Loginov, D. A.; Perekalin, D. S.; Starikova, Z. A.; Golovanov, D. G.; Petrovskii, P. V.; Zanello, P.; Corsini, M.; Laschi, F.; Kudinov, A. R. (Tetramethylcyclobutadiene)cobalt complexes with five-electron carbo- and heterocyclic ligands. *Organometallics* **2004**, *23*, 5944-5957.

22. Kozioł, A.; Jerzykiewicz, L. B.; Justyniak, I.; Lis, T.; Pasynkiewicz, S.; Pietrzykowski, A. New ionic fluorenylnickel complexes: Synthesis and solid state structure. *Journal of Organometallic Chemistry* **2014**, *767*, 22-26.

23. Edwards, A. J.; Paver, M. A.; Raithby, P. R.; Rennie, M. A.; Russell, C. A.; Wright, D. S. Preparation of copper organometallics via nucleophilic substitution of Cp$CuPPh_3$:

syntheses and X-ray structure determinations of $[Li(THF)_4]^+[(fluorenyl)_2CuPPh_3]^-$ and $[Cy_3PCu(\mu\text{-}C{\equiv}CtBu)_2Cu(PPh_3)_2]$ (THF = tetrahydrofuran, fluorenyl = $C_{13}H_9$). *Organometallics* **1994**, *13*, 4967-4972.

24. Roselló-Merino, M.; Mansell, S. M. Synthesis and reactivity of fluorenyl-tethered N-heterocyclic stannylenes. *Dalton Transactions* **2016**, *45*, 6282-6293.

25. Chai, Z.; Wang, Y.; Tang, M.; Mu, X.; Hou, J.; Yang, G. Chiral rare-earth metal complexes with a tridentate amido-fluorenyl ligand: Syntheses, structures and catalytic performance. *Journal of Organometallic Chemistry* **2017**, *846*, 236-241.

26. Qian, C.; Nie, W.; Sun, J. Synthesis of diphenylmethylene bridged fluorenyl cyclopentadienyl lanthanocene complexes with Cs symmetry and crystal structures of the ate complexes $[Li(THF)_4][LnCl_2\{(C_{13}H_8)CPh_2(C_5H_4)\}]$ and $[Li(THF)_4][Ln(BH_4)_2\{(C_{13}H_8)CPh_2(C_5H_4)\}]$ (Ln = Nd or La). *Dalton Transactions* **1999**, 3283-3287.

27. Wang, C.; Xiang, L.; Leng, X.; Chen, Y. Synthesis and Structure of Silicon-Bridged Boratabenzene Fluorenyl Rare-Earth Metal Complexes. *Organometallics* **2016**, *35*, 1995-2002.

28. Zaeni, A.; Olbrich, F.; Fischer, A.; Edelmann, F. T. Synthesis and structural characterization of $(COT)Pr(C_{13}H_8CH_2CH_2OMe)(THF)$ containing the chelating 9-(2-methoxyethyl)fluorenyl ligand. *Journal of Organometallic Chemistry* **2008**, *693*, 3791-3796.

29. Downing, S. P.; Danopoulos, A. A. Indenyl- and Fluorenyl-Functionalized N-Heterocyclic Carbene Complexes of Titanium and Vanadium. *Organometallics* **2006**, *25*, 1337-1340.

30. Fulmer, G. R.; Miller, A. J. M.; Sherden, N. H.; Gottlieb, H. E.; Nudelman, A.; Stoltz, B. M.; Bercaw, J. E.; Goldberg, K. I. NMR Chemical Shifts of Trace Impurities: Common Laboratory Solvents, Organics, and Gases in Deuterated Solvents Relevant to the Organometallic Chemist. *Organometallics* **2010**, *29*, 2176-2179.

31. Könemann, M.; Erker, G.; Fröhlich, R.; Würthwein, E. Structure and Chemical Behavior of an η5-(1-Azapentadienyl)lithium Derivative Generated by Deprotonation Reactions Starting from 9-(N-tert-Butylaminomethyl)fluorene or 6-(tert-Butylamino)dibenzofulvene. *Journal of the American Chemical Society* **1997**, *119*, 11155-11164.

32. Liddle, S. T.; Arnold, P. L. CCDC 649167: Experimental Crystal Structure Determination. **2008**.

33. APEX 3 (Bruker, 2018) Bruker AXS Inc., Madison, Wisconsin, USA.

34. SAINT (Bruker, 2016) Bruker AXS Inc., Madison, Wisconsin, USA.

35. SADABS (Bruker, 2016) Bruker AXS Inc., Madison, Wisconsin, USA.

36. Sheldrick, G. M. SHELXT– Integrated space-group and crystal-structure determination. *Acta Crystallographica, Section A* **2015**, *71*, 3-8.

37. Sheldrick, G. M. Crystal structure refinement with SHELXL. *Acta Crystallographica, Section C* **2015**, *71*, 3-8.

38. Hübschle, C. B.; Sheldrick, G. M.; Dittrich, B. ShelXle: a Qt graphical user interface for SHELXL. *Journal of Applied Crystallography* **2011**, *44*, 1281-1284.

39. Dolomanov, O. V.; Bourhis, L. J.; Gildea, R. J.; Howard, J. A. K.; Puschmann, H. OLEX2: a complete structure solution, refinement and analysis program. *Journal of Applied Crystallography* **2009**, *42*, 339-341.

40. Masuda, J. D.; Wei, P.; Stephan, D. W. Nickel and palladium phosphinimine-imine ligand complexes. *Dalton Transactions* **2003**, 35-355.

41. Zhang, J.; Gandelman, M.; Shimon, L. J. W.; Milstein, D. Stable Carbene and Diazoalkane Complexes of the Same Complex System. Synthesis, Structure, and Reactivity of PNP−Ru(II) Fluorenylidene and Diazofluorene Complexes. *Organometallics* **2008**, *27*, 3526-3533.

5. Chapter 5: Dimethyl Aluminum and Indium Complexes of Oxygen, Sulfur, and Selenium Substituted Phosphine-Imine Ligands

5.1 Abstract

A previously reported bidentate phosphine-imine[1] **1** was reacted with 30% hydrogen peroxide, sulfur powder, or gray selenium metal in toluene forming chalcogen substituted phosphine-imines **2**, **3**, and **4**. Although **1**, **3**, and **4** have only been observed as the chalcogen substituted phosphine-imine, **2** was observed to crystallize as both the imine and (E)-enamine isomers since in solution, **1**-**4** undergo dynamic tautomerization. The acidic proton within C_6D_6, $CDCl_3$, and CD_3CN solutions dominantly resides on the backbone sp^3 CH_2 as the imine; however, minor tautomers exist with a sp^2 CH backbone carbon while the acidic proton exists as either (E)- or (Z)-enamine isomers, with a possible fourth/fifth ylide tautomer with the proton residing as OH/SH/SeH, supported by gas-phase DFT calculations of compound **2**. Reactions with trimethyl aluminum or trimethyl indium in toluene with **1**-**4** results in the loss of 1 eq. methane gas and cyclization into 5- (**1-AlMe$_2$**), 6-, and 12-membered dimethyl group 13 complexes. These monoanionic ligands chelate the metal atoms through the chalcogen and nitrogen for 6-membered complexes **5-10**, with compound **8** containing the phosphine-oxide donor with dimethyl indium dimerizing and forming a 12-membered metallacycle with nitrogen from one ligand and the phosphine oxide of another coordinated to the distorted tetrahedral indium center. The corresponding infrared spectroscopy, nuclear magnetic resonance spectroscopy, single crystal X-ray diffraction, and physical properties are described herein for the three ligands **2**-**4** and the dimethyl aluminum and indium complexes **5**-**7** and **8**-**10**.

5.1.1 Graphical Abstract

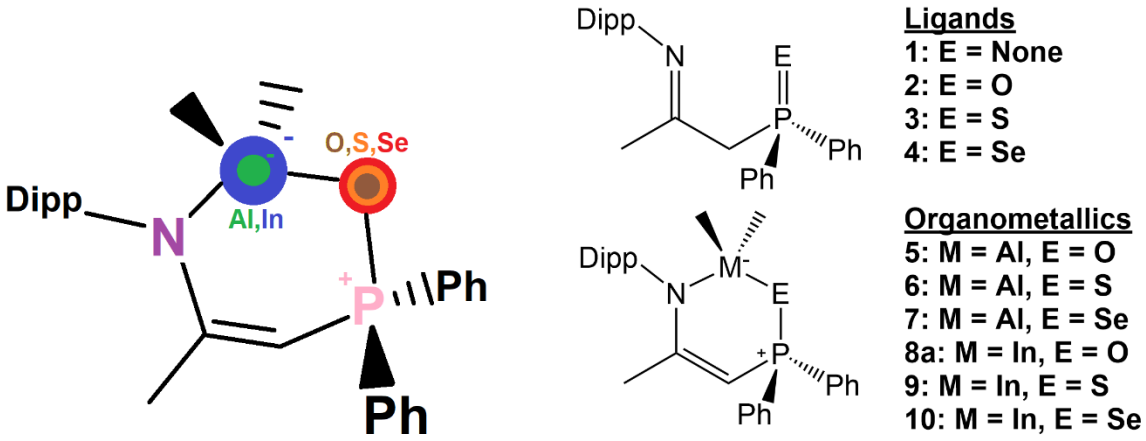

5.2 Introduction

Multidentate ligands are useful for organometallic chemistry of reactive metals offering greater steric bulk and tunable electronic properties for metal centers that can help prevent rapid decomposition upon exposure to air or moisture or stabilize reactive and uncommon metal environments. Ligands such as the bulky nitrogen-based bidentate ß-diketimine family ("NacNacH" Figure 5.1 **A**)), once deprotonated, form ß-diketiminate ligands ("NacNac") (Figure 5.1 **B**) that have proven capable of supporting uncommon and reactive metal environments such as Ni(I) nitrogen adducts and Ni(II) hydrides,[2] stable aluminum(I) and gallium(I) complexes,[3,4] and alkylation of benzene via an alkyl calcium dimer resulting in a calcium hydride dimer that is readily re-alkylated via insertion of a variety of alkenes (general structure of metal complexes, Figure 5.1 **C**).[5] The NacNac ligand is monoanionic, yet spatially encompasses a significant area around the metal atom, while dimers are essentially fully protected with a reactive core shrouded in bulky N-substituents like the commonly used 2,6-diisopropylphenyl (Dipp) group. NacNac ligands can offer significant steric bulk and have ubiquitous value as a general-purpose tunable

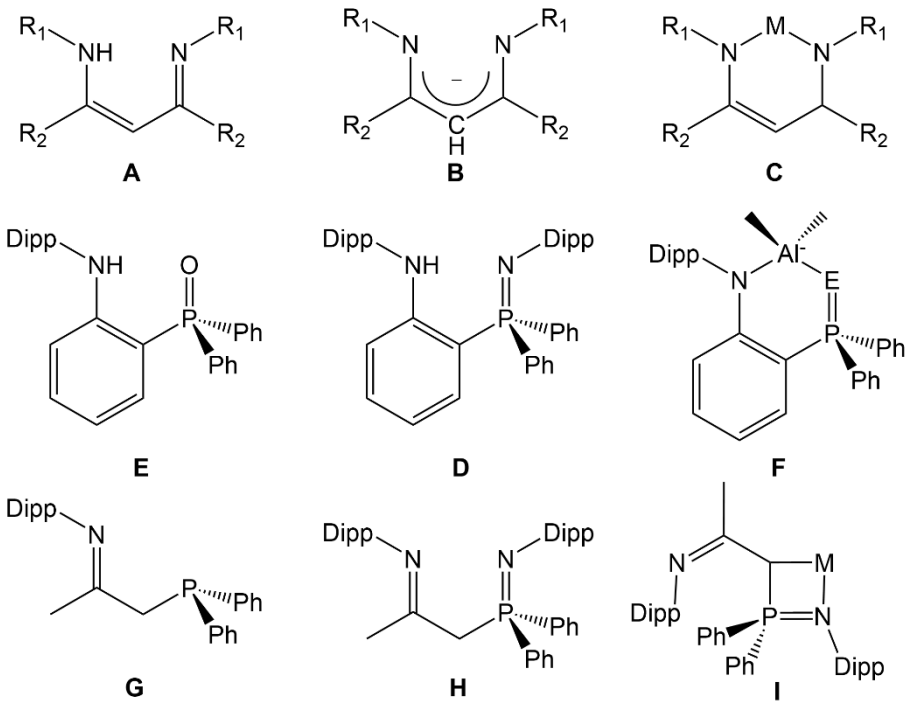

Figure 5.1 A: General structure of ß-diketimine (NacNacH) ligand precursors with R groups commonly R_1 = alkyl, aryl, 2-6-diisopropylphenyl and R_2 = methyl, t-butyl, aromatic. **B**: deprotonation of **A** affords **B**, the ß-diketiminate (NacNac) ligand. **C**: Typical chelation of the NacNac ligand where M = metal with varying ligands. **D**: A literature phosphine-oxide amine ligand precursor **E**: a phosphinimine amine bidentate ligand precursor to produce **F**: dimethyl aluminum complexes with E = O, or N-Dipp. **G**: Precursor **1** used to prepare **2-4** within this work, which was also used in the past to create **H**: a phosphinimine – imine bidentate ligand that then resulted in **I**: Pd and Ni complexes with no imine-metal interaction.

ligand structure, ligands with similar groups directly bound to the metal center are suspected to have similar beneficial donor properties. The natural diversity of unique metallic elements that can be stabilized by bulky monoanionic bidentate ligands like the NacNac ligands encourages exploration into similar ligands to better understand their interaction with various metals to enable similar stabilization of reactive, catalytically active metal centers. One group explored a bidentate ligand similar to NacNac with one imine group replaced by either a phosphine oxide (Figure 5.1 **D**) or a phosphinimine (Figure

5.1 **E**) leading to alkyl aluminum complexes with a similar 6-membered chelation of these bidentate ligands when compared to dimethyl aluminum complexes of NacNac (Figure 5.1 **F**).[6,7] Exploration into an altered NacNac-type of analogue ligand with similar substitution of the phosphine imine (Figure 5.1 **G** = Compound **1**) was used to prepare the ligands within the present work. This diphenylphosphinimine-imine ligand (Figure 5.1 **H**) was previously found to form both Ni and Pd complexes with a four membered ring, differing from the 6-membered ring structure of similar NacNac nickel complexes (Figure 5.1 **I**) owing to increasing the reactivity of the α-carbon when a phosphinimine replaces one of the imine groups present within NacNac ligands.[1,2]

Aluminum and other group 13 metal complexes are able to initiate ring-opening polymerization of monomers such as cyclic esters,[8,9] and perform regioselective[10] or functional group tolerant[11] catalytic coupling of epoxides with environmentally and industrially important small molecules like carbon dioxide (CO_2) or isocyanates (RNCO) forming cyclic carbonates and oxazolidinones, respectively. Therefore, the group 13 metals aluminum and indium were chosen for synthesis and characterization within this work. Aluminum complexes can enantioselectively couple epoxides with isocyanates with high yield conversions to the oxazolidinone products depending on the amount of metal atoms present in the complex (mono, bi, tri metallic species), the electronic effects of the donor atoms bound to the metal, and the steric bulk shielding the active metal center.[10] In addition, functional group tolerance was shown for aluminum complexes within coupling reactions of epoxides (alcohol and halocarbon) with isocyanates (ether and halocarbon). Cyclic carbonate formation is also possible using epoxides, and it has been shown to possess even

greater functional group tolerance including alcohols, esters, halocarbons, alkynes, alkenes, amides, silyl ethers, and cyclic tertiary amines.[11] Mechanisms have been suggested for chemical processes performed by mono- or bi-metallic aluminum complexes relying on aluminum acting as the active site for initial coordination of oxygen prior to ring opening polymerization or copolymerization processes.[8,12] Some ligands have resulted in properties and applications including air stability,[13,14] and the ability to completely fixate carbon dioxide with styrene oxide forming styrene carbonate at room temperature without extreme pressure using a tetrabutylammonium bromide cocatalyst, showing promise for utilization of carbon dioxide sequestered within capture technology to produce value added products.[15,16] Active aluminum catalysts are often in the +3-oxidation state, or cationic with an associated borate anion.[12] Catalysts often possess bulky group 15-16 based multi-dentate monoanionic donor ligands with coordinated solvent, alkyl chains, halogens, or lone pair electrons in the carbene-like group 13(I) heterocycles.[3,8] Despite promising preliminary reactivity and catalytic performance, it remains uncertain that ligands enable group 13 elements to achieve optimal performance for the currently known applications, and further exploration into unstudied group 13 ligand interactions may show significant improvement over current highly promising ligands.

The following research into chalcogen substituted derivatives of a previously reported phosphine-imine bidentate ligand **1**,[1] resulted in ligands **2**-**4** bearing a phosphine oxide, sulfide, or selenide that undergo tautomerization in C_6D_6, $CDCl_3$ and CD_3CN solutions to at least 3 isomers. An unsuccessful attempt was made to form the phosphine telluride derivative, though complete conversion to a single product was not achieved.

From these three ligands, three dimethyl aluminum and three dimethyl indium complexes were prepared. The corresponding IR spectroscopy, nuclear magnetic resonance spectroscopy, single crystal X-ray diffraction, and general physical properties like stability and appearance follow.

5.3 Results and Discussion

5.3.1 Synthesis - Ligands

From a previously reported phosphine-imine **1**,[1] compounds **2-4** were prepared from a toluene mixture of either 30 % H_2O_2 at room temperature for **2**, or elemental sulfur powder or grey selenium metal heated to 100 °C for **3** and **4**, respectively (Scheme 5.1). Compound **2** crystallized as both imine (**2a**) and (E)-enamine (**2b**) isomers depending on crystallization conditions. Compound **4** was observed to degrade in solution exposed to air, noted by precipitation of a red solid. Attempts to make the tellurium substituted phosphine were unsuccessful using tellurium metal powder heated in toluene or mesitylene at 100 and 160 °C, respectively. Te-P chemistry is known to differ from patterns observed with other chalcogens through the weaker non-polar covalent interactions leading to instability, owing to the use of phosphine tellurides as tellurium transfer agents.[17] Reaction of elemental Te was not as straightforward as the first phosphine telluride, tributyl phosphine telluride, which was successfully produced from the phosphine and powdered tellurium refluxed in toluene.[18] Rather than attempting alternate Te sources such as Ph_2Te_2(Ph2Te2 -> Ph2Te + Te), this chemistry was not explored further. Compound **1** is crystallized from ethanol, and multiple impure (~70-90%) batches were harvested despite slow oxidation in air into **2** resulting in a mixture that could not be separated. **3** was sometimes contaminated with

excess sulfur when **1** was the limiting reagent and could be cleaned using a column with an 80:20 pentane-acetone mobile phase and silica gel stationary phase affording flaky white crystals (second UV-active fraction) upon removal of solvent after initial elution of S_8 with pentane as an eluent.

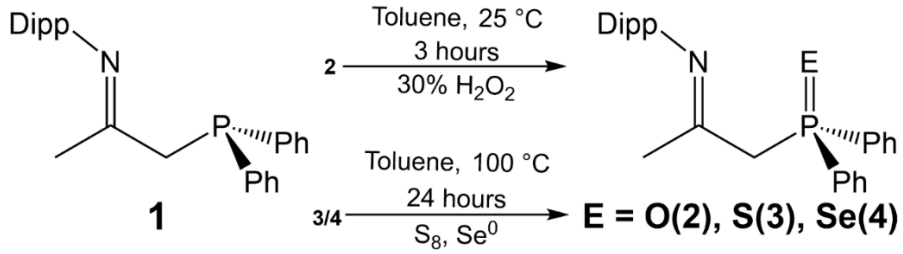

Scheme 5.1 Synthesis of three bidentate chalcogen substituted phosphine-imine ligands **2-4** from compound **1**. In the center a resonance conformation of the imine is shown highlighting the ability of neutral phosphine-chalcogenides to act as strong donors through the chalcogen substituent.

5.3.2 NMR Spectroscopy and Computational Analysis - Ligands

The ^{1}H NMR spectra of compounds **2-4** is different across various deuterated solvents ($CDCl_3$, CD_3CN, C_6D_6) for the ratio of tautomeric imine/enamine/ylide and trace unknown isomers occurring in solution (Table 5.1, Scheme 5.2).

Table 5.1 Ratio's of observed isomers (imine:(E)-enamine:(Z)-enamine:ylide (E)- or (Z)-isomers) in different deuterated solvents at 298 K based on ^{1}H NMR integration.

Compound	solvent = $CDCl_3$	solvent = C_6D_6	solvent = CD_3CN
2 (Oxygen)	84:11:5:0	80:20:<1:0	75:19:6:0
3 (Sulfur)	75:6:19:<1	84:16:0:0	78:4:10:4
4 (Selenium)	63:33:4:0	74:24:2:0	72:14:13:1

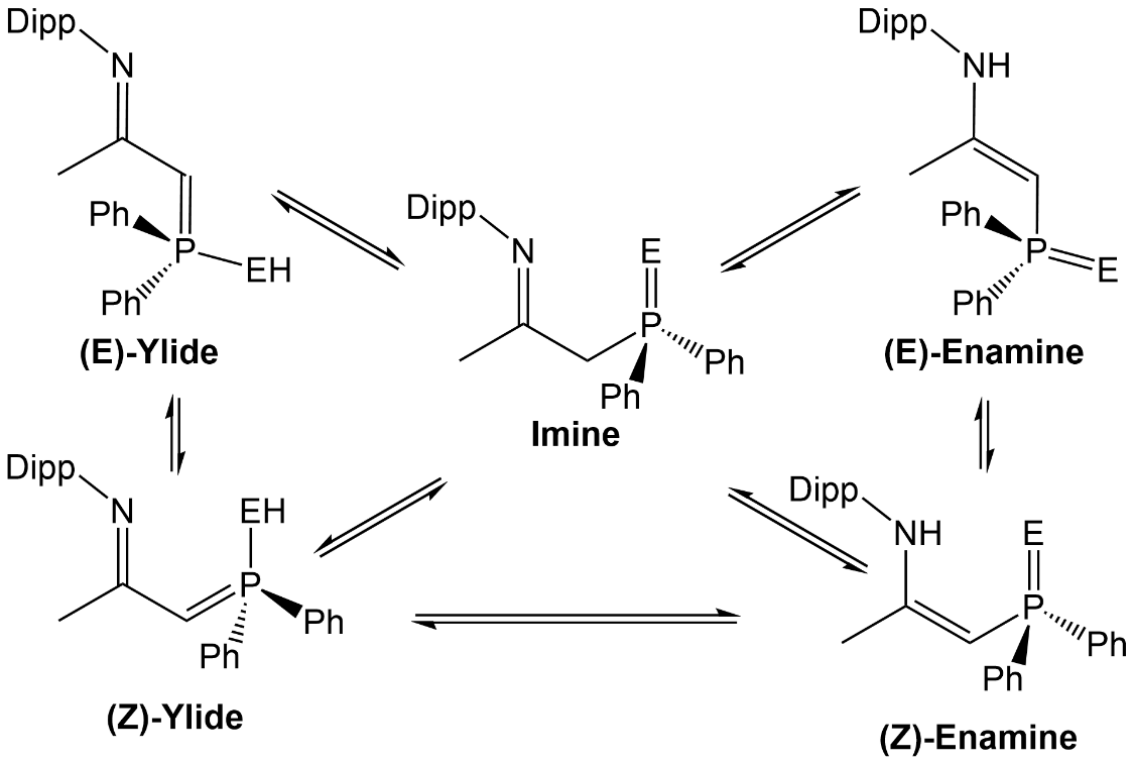

Scheme 5.2 Possible conformations expected to occur through solution-state isomerization processes. The (E)- and (Z)-isomers of the ylide may arise from rotation about the P=C bond following electron delocalization into a phosphonium carbanion (P^+-C^-). Low concentration or absence of the suspected fourth and fifth ylide isomers in various solutions at room temperature may afford different results at different temperatures, allowing for calculation of bond rotation activation energies.[19]

Across all solvents, the imine is favored by 59-85 %, clear based on ^{1}H NMR integration showing a 2:2 ratio for the P-C*H*$_2$ with the two isopropyl (CH_3)$_2$C*H*. Compounds **2** and **3** both maintained >75 % imine in all solvents with enamine the second most abundant isomer in $CDCl_3$ and C_6D_6 solutions. In the ^{1}H NMR spectra of **2-4** in CD_3CN solutions, a sharp NH singlet from 7-10 ppm is observed along with a broad singlet between 4-6 ppm attributed to either an NH or a P-EH (E = O, S, Se) proton. Determination of the identity of each tautomer is conflicting based on a combination of inconclusive ^{1}H NMR spectroscopy (very similar signals expected for (E)- and (Z)-enamine or P-EH tautomers), SC-XRD

analysis of **2** as the imine isomer and the (E)- enamine isomer, and gas phase calculations showing **2** as the (Z)-isomer is most stable. Each isomer is expected to potentially occur in solution via dynamic proton migration processes; however, in the (Z)-conformation the proton may migrate back and forth from nitrogen to oxygen or vice versa as a high energy intermediate state that rapidly rearranges to the more stable imine. When present in solution as the imine, both the bonds of the methylene bridge may rotate allowing for many different arrangements in solution, and with the abundance of heteroatoms, aromatic Dipp/Ph, along with a highly acidic proton, solution interactions such as hydrogen bonding ($CDCl_3$ donor, CD_3CN acceptor) or π-interactions (C_6D_6) are expected to influence the isomerization processes. For the sake of assignment, calculations were performed on compound **2** as the imine, enamine (Z and E), and with the acidic proton as P-OH. A fourth tautomer in very low concentrations was observed for compound **3** in CD_3CN solution, thought to be a high energy P-SH tautomer that rapidly rearranges to either the enamine or imine tautomer.

For NMR spectroscopy of all ligands and dialkyl metal complexes, asymmetry down the possible centrosymmetric structure is clear by differences in the isopropyl CH_3 (Figure 5.2) ^1H and ^{13}C NMR spectra. By ^{13}C NMR spectroscopy, the 2,6-diisopropyl symmetry is split either down the middle as unique "left and right of the plane" isopropyl NMR signals, or across the plane of the ring with one signal indicative of the "above" methyl groups of the isopropyl groups and the other to the "below". The symmetric origin of this splitting of resonance in the ^1H and ^{13}C NMR spectra of the Dipp group methyl signals for compounds **2-10** was not further studied and remains unknown and both signals are simply indicated as $CH(CH_3)_2$ signals.

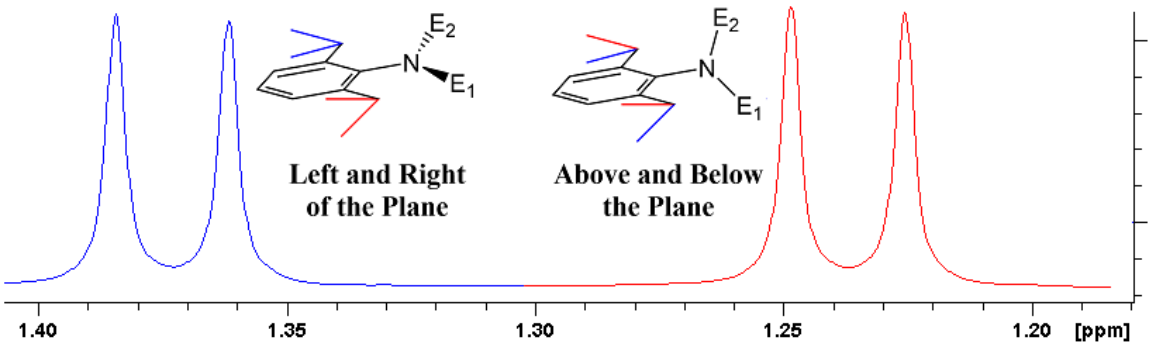

Figure 5.2 Asymmetry of the isopropyl groups within ^{1}H NMR spectroscopy. This is observed to a different degree for all of compounds **1**-**10**.

To get an idea of the relative energy of each suspected isomer of **2**, a series of calculations (Figure 5.3) were performed to guide NMR spectroscopic assignments since the non-imine isomers were not the major isomer in solution and the expected NMR signals of each minor isomer are very similar (doublet for CH backbone, singlet for NH or OH). Initial geometries were calculated at the B3LYP/6-31G(d) level of theory, followed by optimization at the PBEPBE/TZVP level of theory, with all stationary points verified using frequency calculations. These calculations were conducted by Dr. Masuda as a means of supporting the identification of various isomers within this work; however, it is important to note that gas phase calculations do not directly translate to solution state systems. Likewise, crystallography presented later is all solid state and does not correlate directly with solution state systems, resulting in the inability to identify between (E)- and (Z)-isomers of the enamine or ylide.

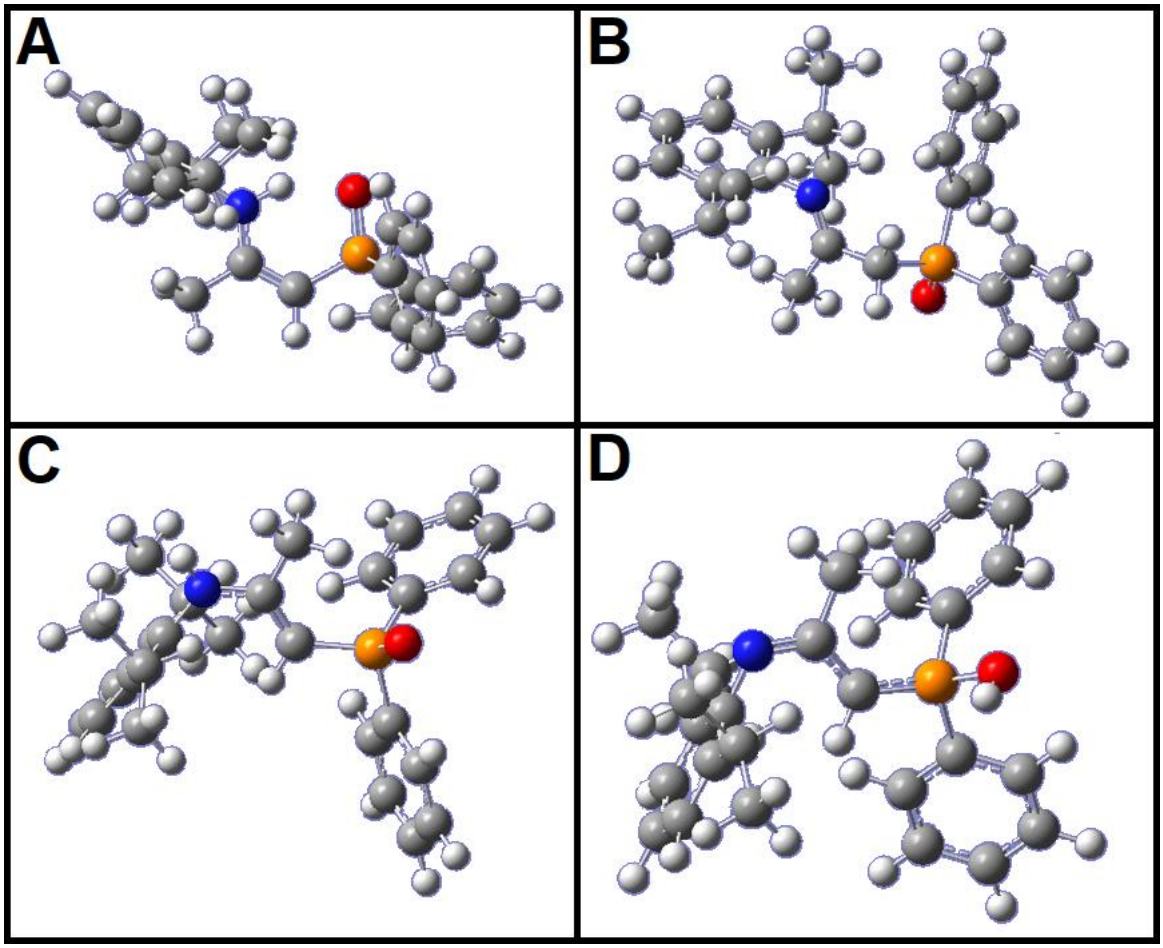

Figure 5.3 Structural isomers of compound **2** in the gas phase. Initial geometries and later optimization were calculated at the B3LYP/6-31G(d) at PBEPBE/TZVP levels of theory. **A** shows the lowest energy (0 kcal/mol) for the chelating (Z)-enamine (OH in this conformation rearranges to enamine). **B** is the imine isomer that is most stable in solution, calculated with an energy of +1.4 kcal/mol in the gas phase. **C** is the (E)-conformation of the enamine that appears less stable at +3.8 kcal/mol, while the (E)-conformation with P-OH (**D**) displays the highest energy at +23.5 kcal/mol.

While gas phase calculations show the (Z)-enamine is the most stable followed by the imine and then (E)-enamine, solution-based NMR spectroscopy indicates the imine is most stable followed by the two enamine isomers. For the sake of assignment, the (E)-isomer was treated as the second most abundant minor isomer followed by the (Z)-isomers, except for when the most abundant N-*H* signal occurs as a broad singlet between 4-6 ppm by ^{1}H NMR

spectroscopy that is thought to be broadened due to proximity to phosphorus since the (Z)-isomer = $^{2}J_{P\text{-}H}$ while (E)-isomer would be $^{4}J_{P\text{-}H}$ coupling due to the possible proton transfer between adjacent heteroatoms (N, O, S, Se) as the (Z)-isomer.

5.3.3 X-ray crystallography - Ligands

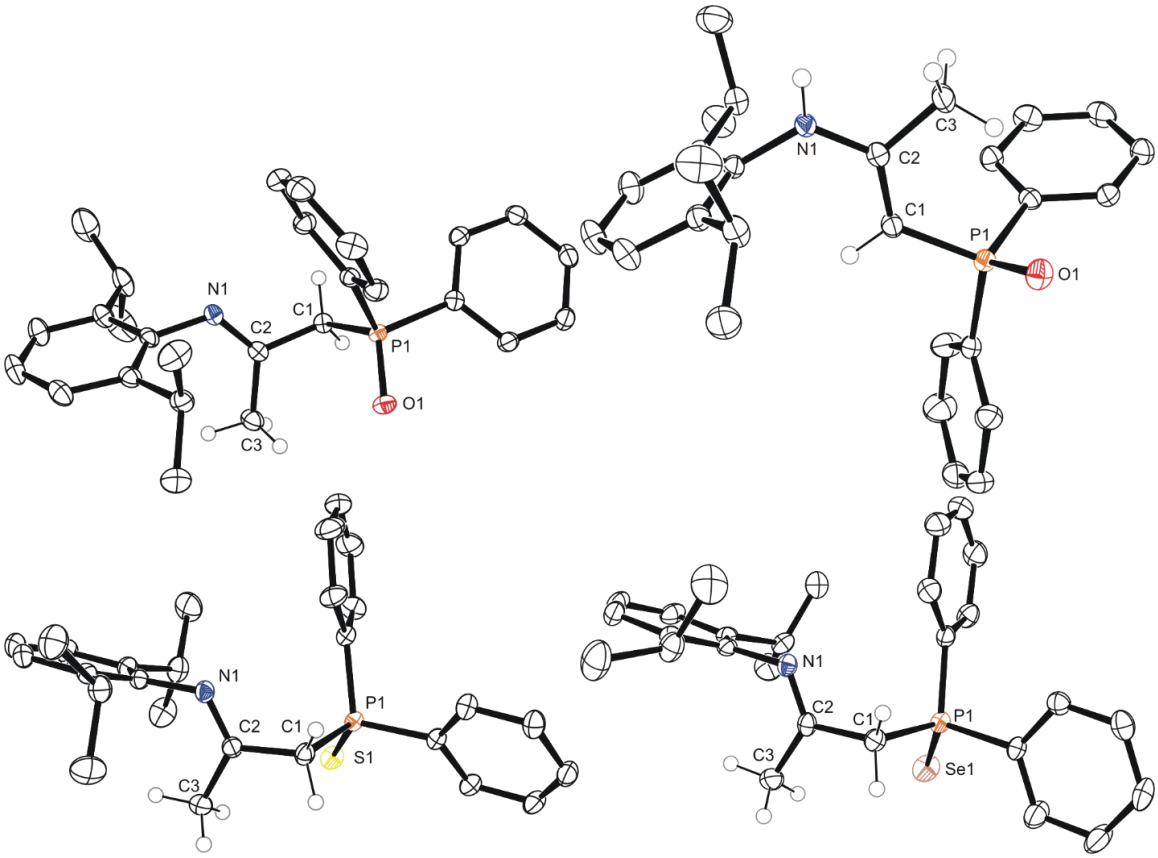

Figure 5.4 Single crystal structures of **2-4** in the solid state. Anisotropic displacement ellipsoids are set to 50 % probability and hydrogen atoms are omitted for clarity except when present on a heteroatom or the central C1-C3 backbone. Top left and right (**2a**, **2b**), bottom left and right (**3**, **4**). See Supporting Information for details.

In crystal structures of compound **2** both the imine **2a** and enamine **2b** tautomers were observed as colourless rhombohedral plates from pentane and radial colourless needles from acetone, respectively. Compounds **3** and **4** both crystallized as the imine from pentane as colourless rhombohedral plates and large prismatic shards, respectively. Figure

5.4 displays the four crystal structures obtained for these three ligands and Table 5.2 contains relevant bond angles and lengths.

Table 5.2 Bond lengths and angles of interest for ligands **2-4**.

Compound	N1-C2 (Å)	C2-C1 (Å)	C1-P1 (Å)	P1-E1 (Å)
2a	1.2724(18)	1.5145(18)	1.8219(14)	1.4905(10)
2b	1.3486(17)	1.3661(19)	1.7540(14)	1.4949(10)
3	1.2767(10)	1.5151(10)	1.8350(8)	1.9552(3)
4	1.2660(28)	1.5164(31)	1.8303(23)	2.1069(6)

5.3.4 Synthesis - Organometallics

Despite **2** crystallizing as both imine (**2a**) and (E)-enamine (**2b**) isomers, the solids were used indiscriminately for synthesis of dimethyl aluminum and indium complexes **5** and **8** due to solution state tautomerism occurring upon dissolution of **2**, regardless of it being the enamine or imine in the solid state. All compounds were prepared and isolated via combining an excess of trimethyl aluminum or indium ($M(Me)_3$, M = Al, In) and **2-4** in toluene and heating for the day or stirring at room temperature for extended periods of time under inert conditions. The heavier chalcogens tended to require longer reaction times to fully convert into the corresponding metal complex. Removal of toluene *in vacuo* and crystallization from cooled/evaporated pentane solutions precipitated crystalline **5-10** with isolated yields above 70% (Scheme 5.3). If a catalytic process is finished via quenching the reaction mixture, extracting the ligand and re-complexing the alkyl-metals may be a possibility. Alternately, these complexes could pose as a source of very small and dispersed group-13 metal oxides or hydroxides via air or moisture exposure.

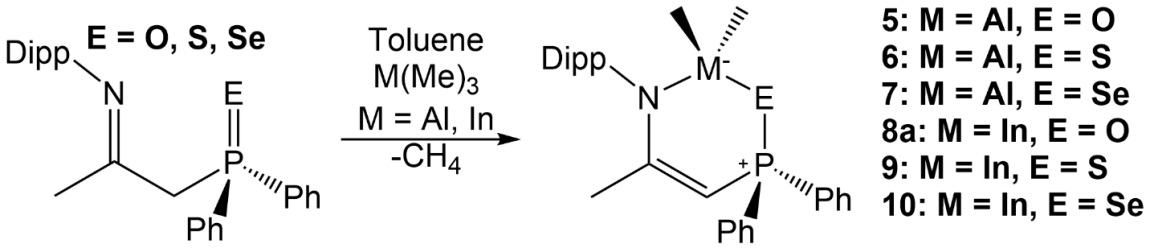

Scheme 5.3 General synthetic procedure for preparation of **5-10** from **2-4**. Heating the ligand in the presence of trimethyl aluminum within toluene causes the loss of methane and subsequent cyclization of the bidentate ligand around the tetrahedral metal center.

5.3.5 NMR Spectroscopy - Organometallics

Table 5.3 ^{1}H NMR spectroscopy signals for organometallic complexes **5-10** with associated ^{31}P-(^{77}Se, ^{1}H) coupling constants.

NMR Nuclei	**5**	**6**	**7**	**8**	**9**	**10**
PC*H* (ppm, d)	3.84	3.92	4.03	3.84	3.70	3.76
C*H*-(CH_3)$_2$ (ppm, sept)	3.40	3.67	3.70	3.23	3.56	3.61
CH(C*H*$_3$)$_2$ (ppm, d)	1.24	1.37	1.38	1.03-1.07 (m)	1.27	1.31
CH(C*H*$_3$)$_2$ (ppm, d)	1.05	1.24	1.25	1.03-1.07 (m)	1.22	1.25
M(C*H*$_3$)$_2$ (ppm, M = Al, In, broad s.)	-0.29	-0.48	-0.49	0.11	-0.22	-0.27
^{27}Al (ppm)	67	73	71	-	-	-
^{31}P (ppm)	41.45	25.8	10.14	36.54	26.27	9.01
^{77}Se (ppm)	-	-	-275	-	-	-294
^{77}Se ($^{1}J_{Se-P}$, Hz)	-	-	496	-	-	502
PC*H* ($^{2}J_{P-H}$, Hz)	26.3	18.7	16.2	24.1	18.8	17.4
P-C=C-C*H*$_3$ ($^{4}J_{P-H}$, Hz)	1.3	1.7	1.8	2.1	1.9	2.2
C*H*(C*H*$_3$)$_2$ ($^{3}J_{H-H}$, Hz)	7.0	6.9	6.9	6.9 from sept	6.9	6.9

All NMR samples of compounds **5-10** contained 5-40 mg material dissolved in 0.4-1.0 mL C_6D_6. Compounds **5-10** possess protons that couple to phosphorus, most notably the backbone P-C*H* and P-C=C-C*H*$_3$ protons with $^{2}J_{P-H}$ and $^{4}J_{P-H}$ coupling, respectively. Some periodic trends exist for various coupling constants and NMR signals within complexes **5-10** (Table 5.3, Figure 5.5). For the PC*H* ^{1}H NMR signal, the coupling constant is largest when oxygen is present, and lowest for selenium for both series of aluminum and indium complexes. For aluminum complexes **5-7**, the ^{1}H NMR signal in ppm for the PC*H*

proton increases from oxygen (3.84 ppm) to selenium (4.03 ppm), though the same trend isn't followed when indium is present. For both series of metal complexes, the P-C=C-CH_3 ^{1}H NMR signal in ppm gets more positive from oxygen to selenium. The magnitude of the coupling constant of $^4J_{P\text{-}H}$ for this P-C=C-CH_3 interaction becomes larger from oxygen to selenium for aluminum complexes, but no trend is followed for the indium complexes.

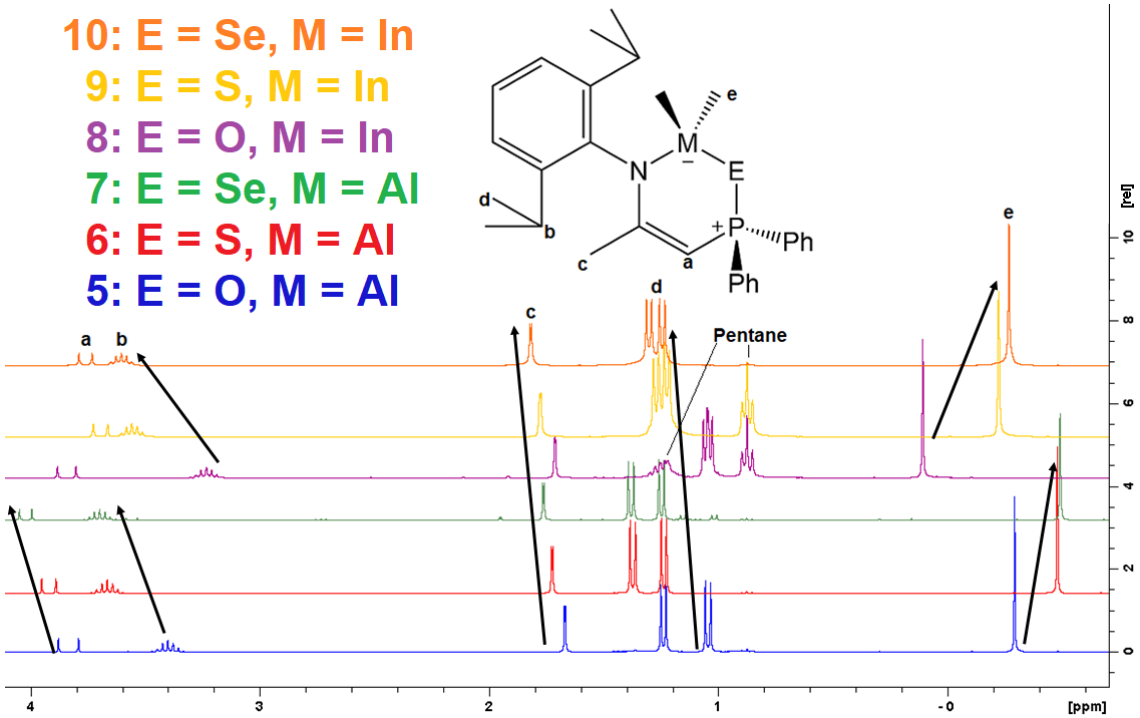

Figure 5.5 Diagram of ^{1}H NMR spectra from 4 to -1 ppm of compounds **5**-**10** in C_6D_6. Arrows illustrate trends from O→S→Se.

The ^{27}Al NMR spectroscopy of compounds **5**, **6,** and **7** presents as broad single peaks at 67, 73, and 71 ppm with a full width at half height of 1600, 2340, and 1550 Hz, respectively. The ^{31}P NMR signal is most positive when oxygen is present (41.45 or 36.54 ppm for **5** and **8**), second largest for sulfur (25.80 or 26.27 ppm for **6** and **9**), and lowest for selenium (10.14 or 9.01 ppm for **7** and **10**) containing complexes. Oxygen and selenium had a shift to a lower ppm in the ^{31}P NMR spectrum when indium was present, but sulfur

had the opposite with a lower ppm signal for the aluminum complex. The difference in ^{31}P NMR spectroscopic signal between aluminum and indium complexes was greatest for oxygen (4.91 ppm), then selenium (1.13 ppm), and sulfur had the smallest difference (0.47 ppm). Compared to isomers of the ligands **2-4**, the ^{31}P NMR chemical shifts for compounds **5-10** were closest to the enamine isomer, which based on the single crystal structure of **2b,** occur in solid state as the (E)-conformation, implying that in solution the expected solid state zwitterionic tetrahedral 6-membered rings may lose the donation from the phosphine chalcogenide in solution forming the non-cyclic trigonal structure (Figure 5.6) or dimers such as **8b**.

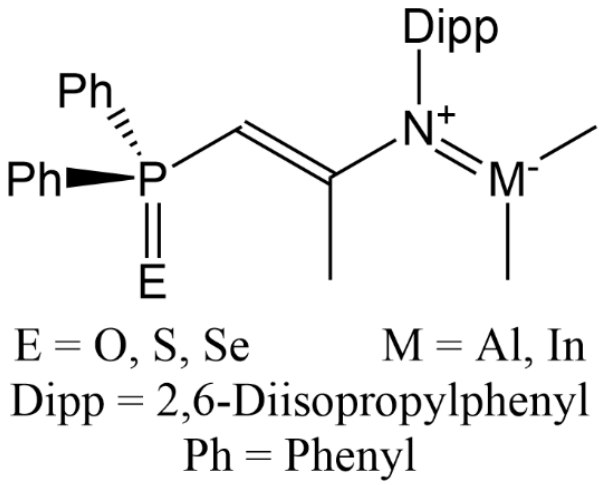

Figure 5.6 Hypothetical non-chelated structure of neutral dimethyl group-13 metal complexes that may occur in solution.

Correlations between solid/liquid/gas states as mentioned before do not conclusively indicate anything about one another; i.e. observation of the (E)-enamine and not the (Z)-enamine in the solid-state structure of compound **2b** does not imply that the (E)-isomer is most stable in solution. Considering the evidence observed for the solid state of

2b as the (E)-enamine, most abundant minor isomer in each instance is associated with the isomer with N-H ^{1}H NMR peaks above 7 ppm, and (Z)-enamine below 7 ppm.

5.3.6 X-ray crystallography – Dimethyl Group 13 Complexes

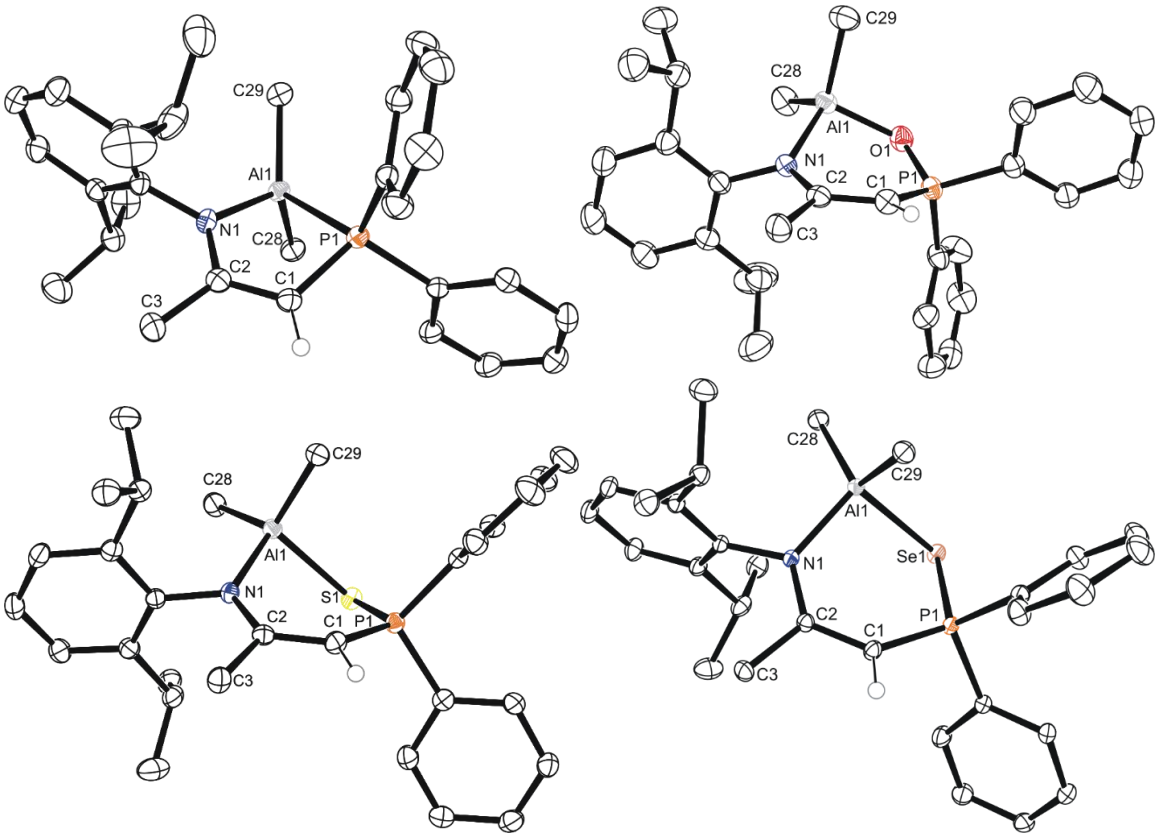

Figure 5.7 Single crystal structure of **5**-**7** in the solid state. Anisotropic displacement ellipsoids are set to 50 % probability and hydrogen atoms except for H1 are omitted for clarity. Top left and right (**1•AlMe$_2$, 5**), and bottom left and right (**6**,**7**). See Supporting Information for details.

Compound **5** formed radial needle crystals and plates, **6**-**7** formed prismatic rhombohedral crystals, **8a**, **9**, and **10** formed radial prismatic crystals and **8b** formed as prismatic blocks, all from cooled pentane solutions. Compounds **6**-**7** and **9**-**10** represent the first reported instances of 6-membered metallacycles (Figure 5.7) of the structure -

NC_2PEM- (E = S, Se M = Al, In) within the CSD. One study looked at a variety of tetrahedral dialkyl aluminum complexes with bidentate monoanionic N/O, N/N, or N/S donors forming both mono-, bi-, and trimetallic 6-membered chelates, which resemble **5** and **6**.[10] Table 5.4 lists some key bond lengths and angles corresponding to some similar 6-membered tetrahedral dimethyl aluminum and indium compounds. In this work, compound **8** formed two solid state structures from -35 °C pentane solutions; a 6-membered monomer (**8a**) when grown from a concentrated solution, and a 12-membered dimer (**8b**) when grown from a dilute solution. Similar crystallization of both **9** and **10** form 6-membered rings like **8a** from concentrated pentane solutions. Dimers of **9** and **10** were not observed (or sought after) and may form under different conditions. (Figure 5.8).

Table 5.4 Bond lengths and angles surrounding the active aluminum and indium centers of similar bidentate chelates.

Reference	M1-E1 (M = Al, In and E = O,S,Se)	M-N (Å)	M1-C29 (Å)	M1-C28 (Å)	N1-M1-E1 (°)	C-M1-C (°)
SNAl [20]	2.285(3)	1.964(6)	1.957(8)	1.972(7)	94.8(2)	117.6(3)
ONAl[21]	1.795(5)	1.954(6)	1.949(6)	1.955(7)	93.9(3)	118.6(4)
SeNAl[22]	2.3953(13)	2.042(3)	1.950(5)	1.961(5)	99.21(11)	117.1(3)
ONIn[23]	2.1010(13)	2.2685(16)	2.139(2)	2.140(2)	85.33(5)	142.33(9)
2(ONIn)[23]	2.1404(13)	2.5745(16)	2.1673(18)	2.1710(18)	73.83(5)	128.41(8)

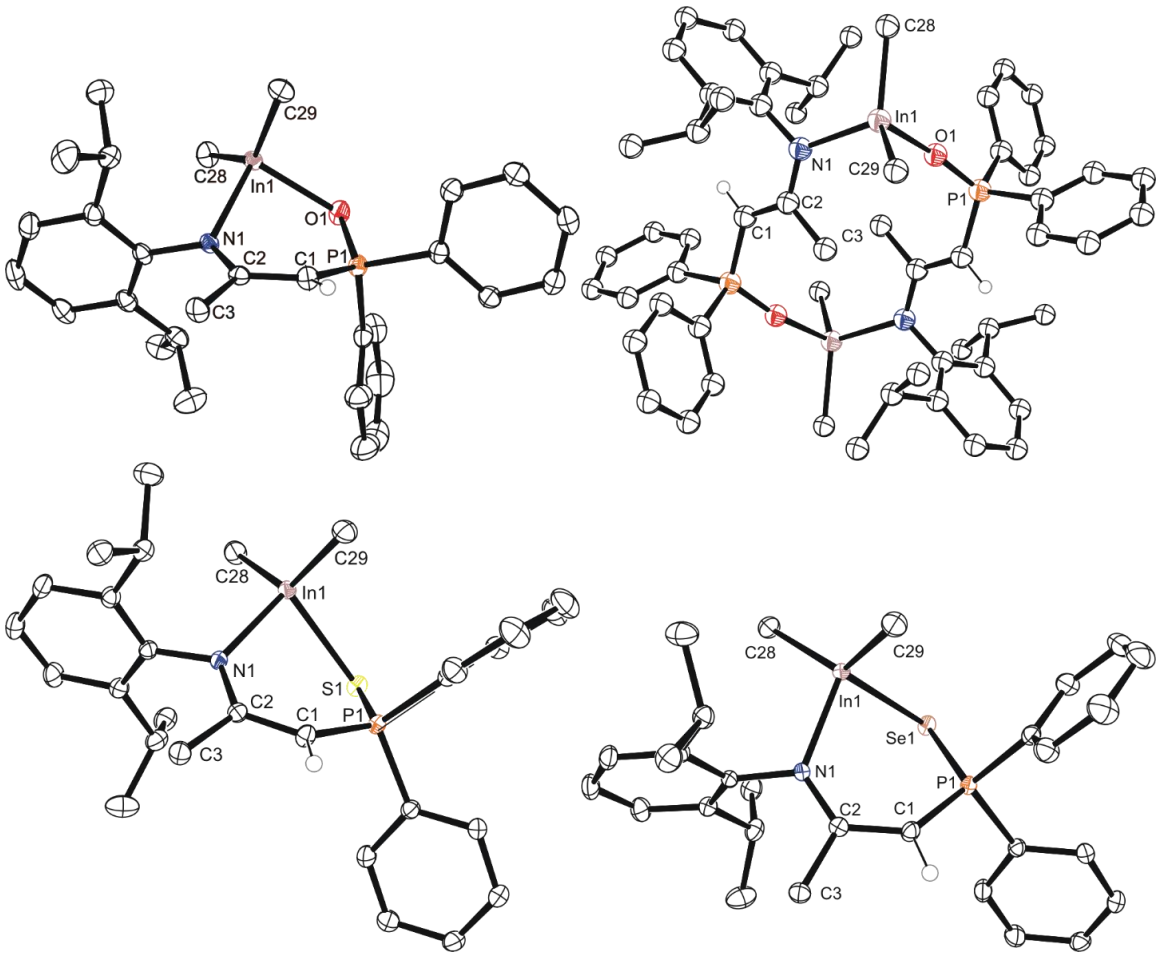

Figure 5.8 Single crystal structure of **8-10** in the solid state. Anisotropic displacement ellipsoids are set to 50 % probability and hydrogen atoms except for H1 are omitted for clarity. Top left and right (**8a**, **8b**), bottom left and right (**9**, **10**). See Supporting Information for details.

Literature based on a Cambridge Structural Database (CSD, version 5.41 (Nov 2019))[24] search for tetrahedral dialkyl indium species "N-In(R_2)-E" (R = C, E = O, S, Se) for comparison to compounds **8-10** is somewhat limited, with compound **10** appearing to be the first nitrogen/selenium chelate of dialkyl indium to our knowledge (Based on CSD and SciFinder searches). N/O chelates of dialkyl indium appear commonly dimerized like

8b, though instead of forming large single cyclic structures, multicyclic species with central In-O-In'-O' 4-membered rings tend to be common.

Table 5.5 Bond lengths and angles of interest for organoaluminum and indium complexes **5-10**.

Compound	P1-E1 (Å)	M1-N1 (Å)	M1-E1 (Å) (M = Al, In and E = O,S,Se)	M1-C29 (Å)	M1-C28 (Å)	N1-M1-E1 (°)	C28-M1-C29 (°)
5	1.5233(59)	1.9220(69)	1.8292(61)	1.9811(95)	1.9536(88)	98.92 (28)	118.14 (43)
6	2.0244(6)	1.8985(14)	2.3635(7)	1.9658(18)	1.9656(18)	98.22 (5)	117.78 (8)
7	2.1735(2)	1.8996(7)	2.4955(3)	1.9689(9)	1.9655(9)	98.42 (2)	118.17 (4)
8a	1.5249(16)	2.1899(18)	2.1660(15)	2.1479(23)	2.1524(25)	91.02 (7)	134.28 (10)
8b	1.5173(8)	2.1883(9)	2.1625(8)	2.1493(14)	2.1605(14)	95.60 (3)	125.46 (6)
9	2.0218(5)	2.1772(12)	2.5821(4)	2.1574(16)	2.1521(16)	90.70 (3)	127.40 (7)
10	2.1765(3)	2.1782(9)	2.6808(1)	2.1590(12)	2.1535(12)	91.32 (2)	127.16 (5)

One example of a dimethyl indium complex with a bidentate N/O ligand formed a 6-membered ring like **8a**,[23] however no known 6-membered chelates exist and E = O, S, Se) to tetrahedral dialkyl indium complexes **8a**, **9**, and **10** was found during a CSD search. No similar example of a 12-membered ring analogous to **8b** was observed during these searches; however, dialkyl N-InR_2-O based complexes appear to have a tendency towards dimerization through additional In-O' interactions (O' being from the second ligand in the dimer), resulting in penta-coordinate complexes in the solid state.

5.3.7 IR spectroscopy

Infrared spectra of compounds **2-10** is available in the SI; however, absolute assignments could not be completed conclusively for each compound. Oxygen substituted

ligand **2a** as the imine displays the strongest signal at 1185 cm^{-1}, suspected to be the P=O stretching vibration. The sulfur **3** and selenium **4** ligands display no single sharp dominant peak such as is seen with **2**, though they do have one of their strong signals at 1101 and 1097 cm^{-1}, respectively, which may correlate with. For these two ligands, signals in the lower wave numbers for **3** include three strong peaks at 612, 700 and 735 cm^{-1} and **4** contains four strong peaks at 527, 693, 727, and 751 cm^{-1}. The aluminum complexes displayed significant differences with the oxygen containing **5** absorbing strongest between 1050-1250 cm^{-1} with broad signals with a largest peak at 1118 cm^{-1}. The sulfur analogue **6** had far less absorption in the region below 1320 cm^{-1}, with a large strong peak at 1504 cm^{-1} and a broad medium signal at 692 cm^{-1}. The selenium analogue **7** featured absorption patterns similar to **5**, with the major absorbing region and largest single peak of 480-880 cm^{-1} and 691 cm^{-1}, respectively. For the indium complexes **8b**-**10**, all three analogues possess strong absorption between 1320 – 1580 cm^{-1} with additional strong absorption between 480 – 880 cm^{-1}. The dimeric oxygen analogue **8b** has strong peaks at 1437 and 695 cm^{-1}, and both the sulfur and selenium analogues **9** and **10** display the same set of two strong peaks at 1500 and 1420 cm^{-1} along with medium broad peaks at 701 and 694 cm^{-1}, respectively. Each IR spectra is available within the SI.

5.4 Experimental

5.4.1 Solvents, Reagents, and Materials

Nitrogen (gas and liquid) was supplied by Praxair and Air Liquide. Ethanol (95%) was purchased from Commercial Alcohols. Toluene, acetone, tetrahydrofuran, hexanes and 85% phosphoric acid used as an external reference for ^{31}P NMR were purchased from

Fisher Chemical or Fisher Scientific. Pentane was purchased from Sigma-Aldrich. All deuterated solvents including $CDCl_3$ (0.05% v/v tetramethyl silane), C_6D_6, and CD_3CN were purchased from Cambridge Isotope Laboratories Inc. 2,6-diisopropyl aniline (90%), chlorodiphenylphosphine (96%), 2.5 M n-BuLi in hexanes, N,N,N',N'-tetramethyl-ethylenediamine (99%), sulfur powder, selenium metal, 4 Å molecular sieves, calcined diatomaceous earth, and 2.0 M trimethylaluminum in heptane were all purchased from Sigma-Aldrich. Trimethyl indium (99.99%) was purchased from Strem Chemical Incorporated. Anhydrous magnesium sulfate was purchased from Caledon Laboratories. Activated alumina used for drying and filtering solvents was purchased from Anachemia and is 80-200 mesh. Heating was performed using a DrySyn aluminum heating block with 50-1000 mL flasks. Potassium hydride was purchased as a 30% mineral oil dispersion from Sigma-Aldrich and washed four times with an appropriate amount of pentane then dried *in vacuo* to give a free-flowing powder. Alumina, calcined diatomaceous earth, and molecular sieves were pre-dried in a 140 °C oven for a minimum of one week before being dried at 300 °C *in vacuo* in a half-filled round-bottom wrapped in aluminum foil within an aluminum block. Solvents (toluene, pentane, tetrahydrofuran) were purified using an Innovative Technology solvent purification system. Solvents (pentane, toluene, tetrahydrofuran, hexanes, benzene) were then dried using KH for 24-78 hours and subsequently filtered through dry alumina and stored over 4 Å molecular sieves (~$1/10^{th}$ the volume of solvents). Potassium bromide used for producing KBr pellets for infrared spectroscopic analysis was purchased from ACP Chemicals and dried at 140 °C and stored in a glovebox.

5.4.2 Equipment, Instruments and Analytical Methods

All reactions were performed in dry, O_2-free (< 10 ppm) conditions under an atmosphere of N_2 within a mBraun Labmaster SP inert atmosphere glovebox in 20 mL scintillation vials or using Schlenk flasks sealed with rubber or glass stoppers with standard Schlenk techniques. Glassware was dried at 140 °C overnight prior to experimentation. NMR spectra were recorded on a Bruker Avance 300 MHz NMR spectrometer. Trace amounts of non- or partially deuterated solvent or tetramethyl silane were used as internal references for ^{1}H and ^{13}C NMR spectra. ^{31}P NMR spectra were referenced to 85% phosphoric acid. Melting points were recorded on an Electrothermal MEL-Temp 3.0 using glass capillaries sealed under inert conditions for air sensitive compounds (**5-10**) or open to air for air and moisture stable compounds **2-4**. Elemental analysis was performed within the Centre for Environmental Analysis and Remediation (CEAR) facility at Saint Mary's University using a Perkin Elmer 2400 II series Elemental Analyzer. Single crystal X-ray diffraction measurements first involved selection of a suitable single crystal, and mounting it on the tip of a MiTeGen MicroLoop with Paratone-N oil. Measurements were made on a Bruker D8 VENTURE diffractometer equipped with a PHOTON III CMOS detector using monochromated Mo Kα radiation (λ = 0.71073 Å) from an Incoatec micro-focus sealed tube at 100-125 K.[25] The initial orientation and unit cell were indexed using a least-squares analysis of the reflections collected from a complete 180° phi-scan with 1° per frame. For data collection, a strategy was calculated to maximize data completeness and multiplicity in a reasonable amount of time, and then implemented using the Bruker Apex 3 software suite.[25] The crystal to detector working distance was set to 4 cm. Data collection, unit cell

refinement, data processing and multi-scan absorption correction were applied using the APEX3 software package.[25-27] The structures were solved using SHELXT[28] and all non-hydrogen atoms were refined anisotropically with SHELXL[29] using a combination of shelXle[30] and Olex2[31] graphical user interfaces. Unless otherwise noted, all hydrogen atom positions were idealized and ride on the atom to that they were attached. For comparison to literature examples of related crystalline materials, the Cambridge Structural Database was used.[24] General bond lengths for elucidation of bond order were used from the following reference.[32] Infrared spectroscopy was conducted using Bruker OPUS 7.5 software with all samples analyzed as pressed KBr pellets using roughly 2-5 mg sample finely powdered in an agate mortar with 40-50 mg KBr.

5.4.3 Synthesis of Precursors, Ligands, and Alkali Metal Complexes

5.4.3.1 Synthesis of Compound 1 - Dipp-N=C(CH_3)-(CH_2)P(C_6H_5)$_2$

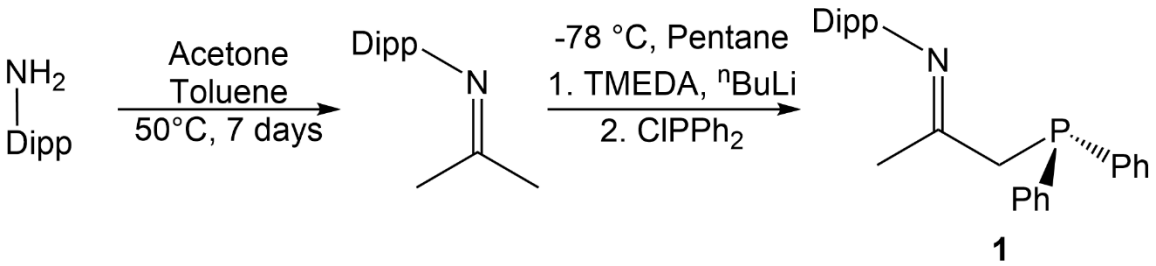

1

Part 1: Following a modified previously established synthesis,[1] a solution of 100 mL (0.5 mol) 2,6-diisopropylaniline in 200 mL (2.7 mol) acetone was refluxed for one week with ~40 mL anhydrous $MgSO_4$ to encourage condensation, producing N-isopropyl-N-2,6-diisopropylphenylimine with incomplete conversion possibly due to acid catalyzed hydrolysis of the imine. The resulting solution was filtered through calcined diatomaceous earth, acetone removed, and the mixture was distilled *in vacuo* affording a 1:2 ratio of the

amine to imine. Toluene, molecular sieves, and anhydrous calcium sulfate with refluxing over the course of a few weeks caused a 1:10 ratio of reagent to product. Distillation resulted in 3 fractions with the purest being the first, 9 grams of a 1:11 ratio of reagent amine to product imine.

Part 2: In a 500 mL round bottom flask 8.6 g was used directly in a -78 °C reaction in 230 mL pentane with first 0.5 g TMEDA (43 mmol) followed by addition of 17.7 mL of a 2.4 M n-BuLi solution (42 mmol) with slow warming to room temperature over 2 hours. Cooling back to -78 °C is followed by addition of 8.7 g chlorodiphenylphosphine (39 mmol) with warming to room temperature and stirring under nitrogen for two days. Filtration through calcined diatomaceous earth and removal of pentane *in vacuo* affords a yellowish white solid. Dissolution in minimal hot ethanol affords a golden solution which, upon cooling, crystallizes **1** as white crystals that can be isolated by filtration with 3×5 mL ethanol rinses. Concentration of the filtrate *in vacuo* can afford additional crops of crystals, and three were harvested with masses of 12.97 g, 0.77 g, and 0.05 g in order of collection. Purity decreased in later crops, with the first to third crop occurring at 91, 86, and 84% purity with an impurity of the oxide of **2**. The third crop presented as more suitable distinct single crystals for X-ray analysis compared to the first two crops that both occurred as highly radial spherical crystalline clumps.

Yield (if pure): Crop 1 = 82% Crop 2 = 5% Crop 3 = 0.32%

Yield (adjusted purity): Crop 1 = 75% Crop 2 = 4% Crop 3 = 0.27%

I.e.: Crop 1 = 12.97 g, 91% purity, so 82%*0.91 = ~75%. This is a rough estimation of yield owing to difference in molecular weight of product **1** and impurity **2** of ~4%.

5.4.3.2 Synthesis of Compound 2 - Dipp-N=C(CH_3)-(CH_2)P(C_6H_5)$_2$O

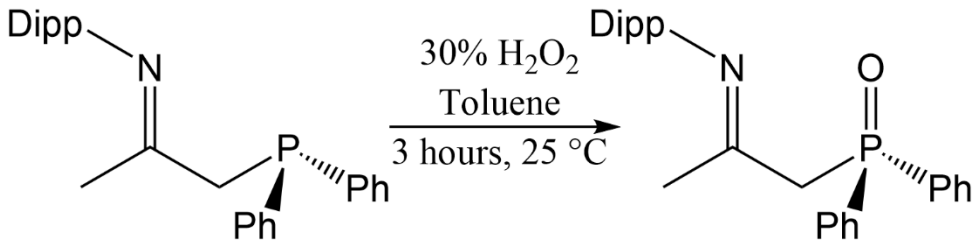

1 **2**

In a 20 mL scintillation vial, a biphasic solution containing 5 mL toluene, 135 mg (0.34 mmol) **1**, and 1.5 mL 30% H_2O_2 (15 mmol) was mixed thoroughly for 3 hours. The layers were left to settle, and the organic layer was removed with a pipette. The aqueous layer was washed with 3×2 mL toluene and the organic fraction dried with $MgSO_4$. Filtering through calcined diatomaceous earth and evaporation *in vacuo* gave 140 mg (0.34 mmol, 99%) of an analytically pure white powder. Layering a toluene solution with pentane formed white radial needles, recrystallization from hot pentane gave colourless thin X-ray quality platy crystals, and acetone affords both plates and needles. The plate morphology from hot pentane form as the imine isomer, while the needles from acetone present as the enamine isomer.

Yield: 99%

m.p. (°C): 141.5 - 143.4 (Plate, imine).

Analytical Calc. for $C_{27}H_{32}NOP$: C: 77.67% H: 7.73% N: 3.35 P: 7.42% O: 3.83%. Found: C: 77.49% H: 7.63% N: 3.22%.

Major isomer $CDCl_3$: imine, 84%:

^{1}H NMR ($CDCl_3$, 300 MHz, 25 °C): δ 7.87 – 7.94 (4H, m, *m*-PPh_2), 7.46 – 7.58 (6H, m, *o*-, *p*-PPh_2), 7.01 (3H, m, *m*-Dipp, *p*-Dipp) 3.71 (2H, d, $^{2}J_{P\text{-}H}$ = 14.2 Hz, PCH_2), 2.30 (2H, sept, $^{3}J_{H\text{-}H}$ = 6.9 Hz, CH(CH_3)$_2$), 1.92 (3H, d, $^{4}J_{P\text{-}H}$ = 1.6 Hz, N=C(CH_3)), 0.93 (d, 6H, $^{3}J_{H\text{-}H}$ = 6.9 Hz, CH(CH_3)$_2$), 0.92 (d, 6H, $^{3}J_{H\text{-}H}$ = 6.9 Hz, CH(CH_3)$_2$) ppm.

^{13}C{^{1}H} NMR ($CDCl_3$, 75 MHz, 25 °C): δ 164.93 (d, $^{2}J_{P\text{-}C}$ = 7.0 Hz, N=C), 145.39 (*ipso*-Dipp), 136.34 (*o*-Dipp), 132.89 (d, $^{1}J_{P\text{-}C}$ = 100.7 Hz, *ipso*-PPh_2), 131.95 (d, $^{4}J_{P\text{-}C}$ = 2.8 Hz, *p*-PPh_2), 130.94 (d, $^{3}J_{P\text{-}C}$ = 9.8 Hz, *m*-PPh_2), 128.73 (d, $^{2}J_{P\text{-}C}$ = 12.8 Hz, *o*-PPh_2), 123.65 (*p*-Dipp), 122.90 (*m*-Dipp), 44.16 (d, $^{1}J_{P\text{-}C}$ = 60.6 Hz, PCH$_2$), 27.73 (CH(CH_3)$_2$), 23.42 (CH(CH$_3$)$_2$), 23.25 (CH(CH$_3$)$_2$), 22.81 (s, N=C(CH$_3$)) ppm.

^{31}P{^{1}H} NMR ($CDCl_3$, 121 MHz, 25 °C): δ 28.34 ppm.

Minor isomer $CDCl_3$: (E)-enamine, 11%:

^{1}H NMR ($CDCl_3$, 300 MHz, 25 °C): δ 8.80 (1H, s, NH), 7.76 - 7.83 (4H, m, *m*-PPh_2), 4.27 (1H, d, $^{2}J_{P\text{-}H}$ = 20.8 Hz, PCH), 3.17 (septet, 2H, $^{3}J_{H\text{-}H}$ = 6.8 Hz, CH(CH_3)$_2$), 1.63 (3H, s, N=C(CH_3)), 1.18 (d, 6H, $^{3}J_{H\text{-}H}$ = 6.8 Hz, CH(CH_3)$_2$), 1.04 (d, 6H, $^{3}J_{H\text{-}H}$ = 6.8 Hz, CH(CH_3)$_2$) ppm.

^{13}C{^{1}H} NMR ($CDCl_3$, 75 MHz, 25 °C): δ 162.37 (N=C), 147.56 (*ipso*-Dipp), 136.67 (d, $^{1}J_{P\text{-}C}$ = 103.5 Hz, *ipso*-PPh_2), 135.00 (*o*-Dipp), 130.86 (m, *m*-PPh_2), 128.38 (d, $^{2}J_{P\text{-}C}$ = 12.8 Hz, *o*-PPh_2), 123.86 (*p*-Dipp), 123.25 (*m*-Dipp), 76.26 (d, $^{1}J_{P\text{-}C}$ = 114.8 Hz, PCH), 28.29 (CH(CH_3)$_2$), 24.62 (CH(CH$_3$)$_2$), 21.81 (d, $^{2}J_{P\text{-}C}$ = 7.6 Hz, N=C(CH$_3$)) ppm.

^{31}P{^{1}H} NMR ($CDCl_3$, 121 MHz, 25 °C): δ 29.72 ppm.

Minor isomer $CDCl_3$: (Z)-enamine, 5%:

^{1}H NMR ($CDCl_3$, 300 MHz, 25 °C): δ 5.27 (1H, s, N*H*), 4.04 (1H, d, $^{2}J_{P\text{-}H}$ = 20.2 Hz, PC*H*), 3.17 (2H, sept, $^{3}J_{H\text{-}H}$ = 6.9 Hz, C*H*(CH_3)$_2$), 1.27 (d, 6H, $^{3}J_{H\text{-}H}$ = 6.8 Hz, CH(C*H*$_3$)$_2$) ppm.

^{31}P{^{1}H} NMR ($CDCl_3$, 121 MHz, 25 °C): δ 26.17 ppm.

Major isomer C_6D_6: imine, 80%:

^{1}H NMR (C_6D_6, 300 MHz, 25 °C): δ 7.82-7.89 (4H, m, *m*-PPh_2), 7.03-7.13 (9H, m, *o*-, *p*-PPh_2, *m*-Dipp, *p*-Dipp), 3.25 (2H, d, $^{2}J_{P\text{-}H}$ = 14.5 Hz, PC*H*$_2$), 2.55 (2H, sept, $^{3}J_{H\text{-}H}$ = 6.9 Hz, C*H*(CH_3)$_2$), 1.93 (3H, d, $^{4}J_{P\text{-}H}$ = 1.6 Hz, N=C(C*H*$_3$)), 1.06 (d, 6H, $^{3}J_{H\text{-}H}$ = 6.9 Hz, CH(C*H*$_3$)$_2$), 1.02 (d, 6H, $^{3}J_{H\text{-}H}$ = 6.9 Hz, CH(C*H*$_3$)$_2$) ppm.

^{13}C{^{1}H} NMR (C_6D_6, 75 MHz, 25 °C): δ 165.18 (d, $^{2}J_{P\text{-}C}$ = 7.7 Hz, N=C), 146.49 (*ipso*-Dipp), 136.53 (*o*-Dipp), 134.67 (d, $^{1}J_{P\text{-}C}$ = 99.5 Hz, *ipso*-PPh_2), 131.58 (d, $^{4}J_{P\text{-}C}$ = 2.7 Hz, *p*-PPh_2), 131.32 (d, $^{3}J_{P\text{-}C}$ = 9.6 Hz, *m*-PPh_2), 128.67 (d, $^{2}J_{P\text{-}C}$ = 11.6 Hz, *o*-PPh_2), 124.11 (*p*-Dipp), 123.37 (*m*-Dipp), 43.98 (d, $^{1}J_{P\text{-}C}$ = 61.8 Hz, P*C*H$_2$), 28.18 (*C*H(CH_3)$_2$), 23.74 (CH(*C*H$_3$)$_2$), 23.41 (CH(*C*H$_3$)$_2$), 21.72 (d, $^{3}J_{P\text{-}C}$ = 14.4 Hz, N=C(C*H*$_3$)) ppm.

^{31}P{^{1}H} NMR (C_6D_6, 121 MHz, 25 °C): δ 25.39 ppm.

Minor isomer C_6D_6: (E)-enamine, 20%:

^{1}H NMR (C_6D_6, 300 MHz, 25 °C): δ 9.91 (1H, s, N*H*), 7.89 – 7.94 (m, 4H, *m*-PPh_2), 7.03-7.13 (9H, m, *o*-, *p*-PPh_2, *m*-Dipp, *p*-Dipp), 4.27 (d, 1H, $^{2}J_{P\text{-}H}$ = 22.5 Hz, PC*H*), 3.36 (septet, 2H, $^{3}J_{H\text{-}H}$ = 6.9 Hz, C*H*(CH_3)$_2$), 1.56 (3H, d, $^{4}J_{P\text{-}H}$ = 1.9 Hz, N=C(C*H*$_3$)), 1.13 (d, 6H, $^{3}J_{H\text{-}H}$ = 6.9 Hz, CH(C*H*$_3$)$_2$), 1.06 (d, 6H, $^{3}J_{H\text{-}H}$ = 6.9 Hz, CH(C*H*$_3$)$_2$) ppm.

^{13}C{^{1}H} NMR (C_6D_6, 75 MHz, 25 °C): δ 162.47 (N=C), 147.93 (*o*-Dipp), 137.95 (d, $^{1}J_{P\text{-}C}$ = 102.7 Hz, *ipso*-Ph), 123.67 (*m*-Dipp), 77.22 (d, $^{1}J_{P\text{-}C}$ = 113.3 Hz, P*C*H), 28.80 (*C*H(CH_3)$_2$), 24.65 (CH(*C*H$_3$)$_2$), 22.67 (CH(*C*H$_3$)$_2$), 21.63 (N=C(*C*H$_3$)) ppm.

$^{31}P\{^{1}H\}$ NMR (C_6D_6, 121 MHz, 25 °C): δ 28.56 ppm.

Trace isomer C_6D_6: (Z)-enamine, <1%:

^{1}H NMR (C_6D_6, 300 MHz, 25 °C): δ 5.18 (1H, bs, N*H*)

Major isomer CD_3CN: imine, 75%:

^{1}H NMR (C_6D_6, 300 MHz, 25 °C): δ 7.84-7.91 (4H, m, *m*-PPh_2), 7.50-7.61 (6H, m, *o*-, *p*-PPh_2), 6.93-7.04 (3H, m, *m*-Dipp, *p*-Dipp) 3.75 (2H, d, $^{2}J_{P-H}$ = 14.2 Hz, PCH_2), 2.35 (2H, sept, $^{3}J_{H-H}$ = 6.9 Hz, C$H(CH_3)_2$), 1.80 (3H, d, $^{4}J_{P-H}$ = 1.4 Hz, N=C(CH_3)), 0.96 (d, 6H, $^{3}J_{H-H}$ = 6.9 Hz, CH(C$H_3)_2$), 0.85 (d, 6H, $^{3}J_{H-H}$ = 6.9 Hz, CH(C$H_3)_2$) ppm.

$^{31}P\{^{1}H\}$ NMR (C_6D_6, 121 MHz, 25 °C): δ 26.82 ppm.

Minor isomer CD_3CN: (Z)-enamine 19%:

^{1}H NMR (CD_3CN, 300 MHz, 25 °C): δ 6.47 (1H, s, N*H*), 3.80 (m, 1H, PC*H*), 3.16 (septet, 2H, C$H(CH_3)_2$), 2.20 (3H, s, N=C(CH_3)), 1.14-1.21 (12H, m, CH(C$H_3)_2$) ppm.

$^{31}P\{^{1}H\}$ NMR (CD_3CN, 121 MHz, 25 °C): δ 28.61 ppm.

Minor isomer CD_3CN: (E)-enamine, 6%:

^{1}H NMR (C_6D_6, 300 MHz, 25 °C): δ 9.05 (1H, s, N*H*), 7.76 – 7.83 (m, 4H, *m*-PPh_2), 4.27 (d, 1H, $^{2}J_{P-H}$ = 20.8 Hz, PC*H*), 3.16 (septet, 2H, C$H(CH_3)_2$), 1.64 (3H, s, N=C(CH_3)), 1.14-1.21 (6H, m, CH(C$H_3)_2$), 1.02 (d, 6H, $^{3}J_{H-H}$ = 6.9 Hz, CH(C$H_3)_2$) ppm.

$^{31}P\{^{1}H\}$ NMR (CD_3CN, 121 MHz, 25 °C): δ 22.74 ppm.

5.4.3.3 Synthesis of Compound 3 - Dipp-N=C(CH_3)CP(C_6H_5)$_2$S

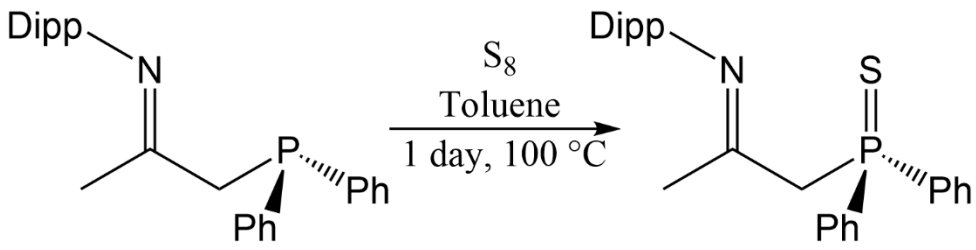

1 **3**

To a 50 mL sealed reaction vessel under nitrogen, a solution containing ~10 mL toluene, 162 mg (0.40 mmol) **1** and 13 mg (0.40 mmol) S_8 were heated for 3.5 hr at 100 °C. Reduction to ~5 mL *in vacuo* and filtering through calcined diatomaceous earth gave a colourless solution. Evaporation of toluene *in vacuo* yields ~0.5 mL of a colourless oil turning to an analytically pure white crystalline solid after the addition of 10 mL pentane and removal *in vacuo* with gentle swirling and heating from a heat gun. Dissolution in minimal boiling pentane, slowly cooling to room temperature, cooling overnight at -18 °C followed by decanting and washing with minimal cold pentane twice and drying *in vacuo* produced X-ray quality thin rhombohedral prismatic colourless crystals. One large single rhombohedral monohydrate crystal was grown from slow evaporation of ethanol at room temperature open to air.

Yield: 97%.

m.p. (°C): 98.1 - 99.4.

Analytical Calc. for $C_{27}H_{32}NSP$: C: 74.79% H: 7.44% N: 3.23% P: 7.14% S: 7.40%. Found: C: 74.53%, H: 7.68%, N: 3.59%

Major isomer $CDCl_3$: imine, 75%:

^{1}H NMR ($CDCl_3$, 300 MHz, 25 °C): δ 8.00 – 8.05 (4H, m, *m*-PPh_2), 7.43 – 7.53 (6H, m, *o*-, *p*-PPh_2), 6.96 – 7.11 (3H, m, *m*-Dipp, *p*-Dipp), 3.90 (2H, d, $^{2}J_{P\text{-}H}$ = 15.0 Hz, PCH_2), 2.43 (2H, sept, $^{3}J_{H\text{-}H}$ = 6.9 Hz, CH(CH_3)$_2$), 1.92 (3H, d, $^{4}J_{P\text{-}H}$ = 1.6 Hz, N=C(CH_3)), 0.98 (d, 6H, $^{3}J_{H\text{-}H}$ = 6.9 Hz, CH(CH_3)$_2$), 0.92 (d, 6H, $^{3}J_{H\text{-}H}$ = 6.9 Hz, CH(CH_3)$_2$) ppm.

^{13}C{^{1}H} NMR ($CDCl_3$, 75 MHz, 25 °C): δ 164.56 (d, $^{2}J_{P\text{-}C}$ = 6.5 Hz, N=C), 145.60 (*ipso*-Dipp), 136.35 (*o*-Dipp), 132.94 (d, $^{1}J_{P\text{-}C}$ = 81.8 Hz, *ipso*-PPh_2), 131.70 (d, $^{4}J_{P\text{-}C}$ = 2.7 Hz, *p*-PPh_2), 131.53 (d, $^{3}J_{P\text{-}C}$ = 10.6 Hz, *m*-PPh_2), 128.68 (d, $^{2}J_{P\text{-}C}$ = 12.5 Hz, *o*-PPh_2), 123.69 (*p*-Dipp), 123.01 (*m*-Dipp), 46.16 (d, $^{1}J_{P\text{-}C}$ = 49.5 Hz, PCH$_2$), 27.83 (CH(CH_3)$_2$), 23.53 (CH(CH$_3$)$_2$), 23.37 (CH(CH$_3$)$_2$), 22.64 (N=C(CH_3)),) ppm.

^{31}P{^{1}H} NMR ($CDCl_3$, 121 MHz, 25 °C): δ 38.10 ppm.

Minor isomer $CDCl_3$: (E)-enamine, 19%:

^{1}H NMR ($CDCl_3$, 300 MHz, 25 °C): δ 8.55 (1H, s, N-H), 7.90 – 7.97 (4H, m, *m*-PPh_2), 4.43 (1H, d, $^{2}J_{P\text{-}H}$ = 18.9 Hz, PCH), 3.09 (2H, sept, $^{3}J_{H\text{-}H}$ = 6.9 Hz, CH(CH_3)$_2$), 1.70 (3H, s, N=C(CH_3)), 1.19 (d, 6H, $^{3}J_{H\text{-}H}$ = 6.9 Hz, CH(CH_3)$_2$) ppm.

^{13}C{^{1}H} NMR ($CDCl_3$, 75 MHz, 25 °C): δ 160.81 (N=C), 147.3 (*ipso*-Dipp), 136.69 (*o*-Dipp), 135.10 (d, $^{1}J_{P\text{-}C}$ = 70.0 Hz), 130.98 (*p*-Ph), 124.05 (*p*-Dipp), 123.40 (*m*-Dipp), 76.29 (d, $^{1}J_{P\text{-}C}$ = 97.7 Hz, PCH), 28.47 (CH(CH_3)$_2$), 24.90 (CH(CH$_3$)$_2$), 23.73 (CH(CH$_3$)$_2$), 21.81 (d, $^{2}J_{P\text{-}C}$ = 14.4 Hz, N=C(CH$_3$)) ppm.

^{31}P{^{1}H} NMR ($CDCl_3$, 121 MHz, 25 °C): δ 27.96 ppm.

Minor isomer $CDCl_3$: (Z)-enamine, 6%:

^{1}H NMR ($CDCl_3$, 300 MHz, 25 °C): δ 5.25 (1H, s, N-H), 3.72 (1H, d, $^{2}J_{P\text{-}H}$ = 14.3 Hz, PC*H*), 2.31 (2H, sept, $^{3}J_{H\text{-}H}$ = 6.9 Hz, C*H*(CH_3)$_2$), 1.62 (3H, s, N=C(C*H*$_3$)), 0.91 – 1.00 (m, 12H, CH(C*H*$_3$)$_2$) ppm.

^{31}P{^{1}H} NMR ($CDCl_3$, 121 MHz, 25 °C): δ 28.34 ppm.

Trace isomer $CDCl_3$: ylide, <1%:

^{31}P{^{1}H} NMR ($CDCl_3$, 121 MHz, 25 °C): δ 34.50 ppm.

Major isomer C_6D_6: imine, 84%:

^{1}H NMR (C_6D_6, 300 MHz, 25 °C): δ 7.93 – 8.01 (4H, m, *m*-PPh_2), 6.98-7.12 (9H, m, *o*-, *p*-PPh_2, *m*-Dipp, *p*-Dipp), 3.42 (2H, d, $^{2}J_{P\text{-}H}$ = 14.9 Hz, PC*H*$_2$), 2.69 (2H, sept, $^{3}J_{H\text{-}H}$ = 6.9 Hz, C*H*(CH_3)$_2$), 1.92 (3H, d, $^{4}J_{P\text{-}H}$ = 1.8 Hz, N=C(C*H*$_3$)), 1.13 (d, 6H, $^{3}J_{H\text{-}H}$ = 6.9 Hz, CH(C*H*$_3$)$_2$), 1.01 (d, 6H, $^{3}J_{H\text{-}H}$ = 6.9 Hz, CH(C*H*$_3$)$_2$) ppm.

^{31}P{^{1}H} NMR (C_6D_6, 121 MHz, 25 °C): δ 37.46 ppm.

Minor isomer C_6D_6: (E)-enamine, 16%:

^{1}H NMR (C_6D_6, 300 MHz, 25 °C): δ 9.37 (1H, s, N-H), 8.01-8.09 (4H, m, *m*-PPh_2), 6.98-7.12 (9H, m, *o*-, *p*-PPh_2, *m*-Dipp, *p*-Dipp), 4.28 (1H, d, $^{2}J_{P\text{-}H}$ = 18.5 Hz, PC*H*), 3.26 (2H, sept, $^{3}J_{H\text{-}H}$ = 6.9 Hz, C*H*(CH_3)$_2$), 1.50 (3H, s, N=C(C*H*$_3$)), 1.22 (d, 6H, $^{3}J_{H\text{-}H}$ = 6.9 Hz, CH(C*H*$_3$)$_2$) ppm.

^{31}P{^{1}H} NMR (C_6D_6, 121 MHz, 25 °C): δ 28.13 ppm.

Major isomer CD_3CN: imine, 78%:

^{1}H NMR (CD_3CN, 300 MHz, 25 °C): δ 7.97 – 8.05 (4H, m, *m*-PPh_2), 7.48 – 7.57 (6H, m, *o*-, *p*-PPh_2), 6.94 – 7.05 (3H, m, *m*-Dipp, *p*-Dipp), 3.99 (2H, d, $^{2}J_{P\text{-}H}$ = 14.7 Hz, PC*H*$_2$), 2.51

(2H, sept, $^{3}J_{H\text{-}H}$ = 6.9 Hz, C*H*(CH_3)$_2$), 1.83 (3H, d, $^{4}J_{P\text{-}H}$ = 1.4 Hz, N=C(C*H*$_3$)), 1.01 (d, 6H, $^{3}J_{H\text{-}H}$ = 6.9 Hz, CH(C*H*$_3$)$_2$), 0.86 (d, 6H, $^{3}J_{H\text{-}H}$ = 6.9 Hz, CH(C*H*$_3$)$_2$) ppm.

$^{31}P\{^{1}H\}$ NMR (CD_3CN, 121 MHz, 25 °C): δ 38.10 ppm.

Minor isomer CD_3CN: (Z)-enamine, 10%:

^{1}H NMR (CD_3CN, 300 MHz, 25 °C): δ 3.80 (d, 1H, $^{2}J_{P\text{-}H}$ = 17.3 Hz, PC*H*), 3.07 (2H, sept, $^{3}J_{H\text{-}H}$ = 6.8 Hz, C*H*(CH_3)$_2$), 1.80 (3H, d, $^{3}J_{P\text{-}H}$ = 1.5 Hz, N=C(C*H*$_3$)), 1.23 (d, 6H, $^{3}J_{H\text{-}H}$ = 6.8 Hz, CH(C*H*$_3$)$_2$), 1.17 (d, 6H, $^{3}J_{H\text{-}H}$ = 6.8 Hz, CH(C*H*$_3$)$_2$) ppm.

$^{31}P\{^{1}H\}$ NMR (CD_3CN, 121 MHz, 25 °C): δ 27.39 ppm.

Minor isomer CD_3CN: (E)-enamine, 8%:

^{1}H NMR (CD_3CN, 300 MHz, 25 °C): δ 8.55 (1H, s, N-H), 7.90 – 7.97 (4H, m, *m*-PPh_2), 4.43 (1H, d, $^{2}J_{P\text{-}H}$ = 18.9 Hz, PC*H*), 3.18 (2H, sept, $^{3}J_{H\text{-}H}$ = 6.9 Hz, C*H*(CH_3)$_2$), 1.67 (3H, s, N=C(C*H*$_3$)), 1.20 (6H, d, $^{3}J_{H\text{-}H}$ = 6.9 Hz, CH(C*H*$_3$)$_2$), 0.93 (6H, d, $^{3}J_{H\text{-}H}$ = 6.9 Hz, CH(C*H*$_3$)$_2$) ppm.

$^{31}P\{^{1}H\}$ NMR (CD_3CN, 121 MHz, 25 °C): δ 33.93 ppm.

Trace isomer CD_3CN: ylide, 4%:

^{1}H NMR (CD_3CN, 300 MHz, 25 °C): δ 3.75 (1H, d, $^{2}J_{P\text{-}H}$ = 14.3 Hz, PC*H*), 2.36 (2H, sept, $^{3}J_{H\text{-}H}$ = 6.8 Hz, C*H*(CH_3)$_2$) ppm.

$^{31}P\{^{1}H\}$ NMR (CD_3CN, 121 MHz, 25 °C): δ 26.91 ppm.

5.4.3.4 Synthesis of Compound 4 - Dipp-N=C(CH_3)CP(C_6H_5)$_2$Se

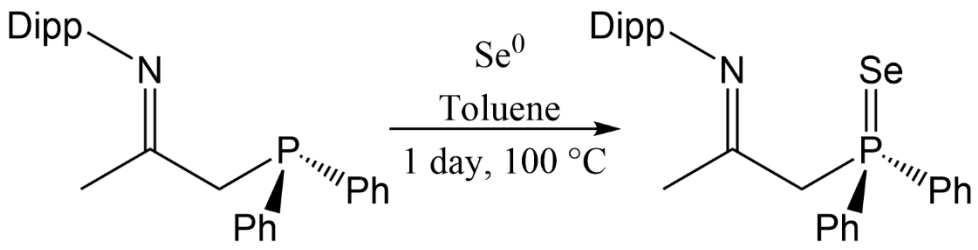

1 **4**

In a 50 mL sealed reaction vessel a solution containing ~20 mL toluene, 105 mg (0.26 mmol) **1** and 25 mg (0.32 mmol) grey selenium metal powder was prepared under nitrogen, sealed, and heated overnight at 100 °C. Filtering through calcined diatomaceous earth in open air and evaporation of toluene results in a yellowish white, finely crystalline pure powder with a 95% yield. Dissolution in minimal boiling pentane and cooling to -18 °C for 24hr produced radial tabular pale-yellow crystals affording 119 mg **4** (0.25 mmol). An unknown pink impurity was observed during some smaller scale reaction that may result from poor filtration of the fine selenium metal. A garlic odor attributed to selenium compounds was observed with prolonged storage under air.

Yield: 95%.

m.p. (°C): 81.8 - 83.4.

Analytical Calc. for $C_{27}H_{32}NSeP$: C: 67.49% H: 6.71% N: 2.92% P: 6.45% Se: 16.43%. Found: C: 67.53%, H: 6.74%, N: 2.87%

Major isomer $CDCl_3$: imine, 63%:

^{1}H NMR ($CDCl_3$, 300 MHz, 25 °C): δ 8.02 – 8.10 (4H, m, *m*-PPh_2), 7.45 – 7.53 (6H, m, *o*-, *p*-PPh_2), 7.00 – 7.10 (3H, m, *m*-Dipp, *p*-Dipp), 4.10 (2H, d, $^2J_{P\text{-}H}$ = 15.1 Hz, PCH_2), 2.51

(2H, sept, $^{3}J_{H\text{-}H}$ = 6.9 Hz, C*H*(CH_3)$_2$), 1.98 (3H, d, $^{4}J_{P\text{-}H}$ = 1.5 Hz, N=C(C*H*$_3$)), 1.04 (d, 6H, $^{3}J_{H\text{-}H}$ = 6.9 Hz, CH(C*H*$_3$)$_2$), 0.96 (d, 6H, $^{3}J_{H\text{-}H}$ = 6.9 Hz, CH(C*H*$_3$)$_2$) ppm.

^{13}C{^{1}H} NMR ($CDCl_3$, 75 MHz, 25 °C): δ 164.51 (d, $^{2}J_{P\text{-}C}$ = 6.7 Hz, N=C), 145.56 (ipso-Dipp), 136.28 (*o*-Dipp), 132.07 (d, $^{3}J_{P\text{-}C}$ = 10.7 Hz, *m*-PPh_2), 131.77 (d, $^{4}J_{P\text{-}C}$ = 2.8 Hz, *p*-PPh_2), 131.73 (d, $^{1}J_{P\text{-}C}$ = 73.0 Hz, *ipso*-PPh_2), 128.69 (d, $^{2}J_{P\text{-}C}$ = 12.4 Hz, *o*-PPh_2), 123.44 (*p*-Dipp), 123.03 (*m*-Dipp), 45.78 (d, $^{1}J_{P\text{-}C}$ = 42.8 Hz, P*C*H_2), 27.85 (*C*H(CH_3)$_2$), 23.97 (N=C(*C*H_3)), 23.58 (CH(*C*H_3)$_2$), 23.36 (CH(*C*H_3)$_2$) ppm.

^{31}P{^{1}H} NMR ($CDCl_3$, 121 MHz, 25 °C): δ 27.64 ($^{1}J_{Se\text{-}P}$ = 760 Hz) ppm.

^{77}Se NMR ($CDCl_3$, 57 MHz, 25 °C): δ -333.46 ($^{1}J_{Se\text{-}P}$ = 760 Hz) ppm.

Minor isomer $CDCl_3$: (E)-enamine, 33%:

^{1}H NMR ($CDCl_3$, 300 MHz, 25 °C): δ 8.43 (1H, s, N-H), 7.97 – 8.01 (4H, m, *m*-PPh_2), 7.11 – 7.23 (3H, m, *m*-Dipp, *p*-Dipp), 4.51 (1H, d, $^{2}J_{P\text{-}H}$ = 17.6 Hz, PC*H*), 3.14 (2H, sept, $^{3}J_{H\text{-}H}$ = 6.9 Hz, C*H*(CH_3)$_2$), 1.76 (3H, s, N=C(C*H*$_3$)), 1.24 (d, 6H, $^{3}J_{H\text{-}H}$ = 6.9 Hz, CH(C*H*$_3$)$_2$), 1.01 (d, 6H, $^{3}J_{H\text{-}H}$ = 6.9 Hz, CH(C*H*$_3$)$_2$) ppm.

^{13}C{^{1}H} NMR ($CDCl_3$, 75 MHz, 25 °C): δ 160.61 (N=*C*), 147.42 (*ipso*-Dipp), 134.70 (d, $^{1}J_{P\text{-}C}$ = 78.2 Hz, *ipso*-PPh_2), 134.52 (*o*-Dipp), 131.60 (d, $^{3}J_{P\text{-}C}$ = 11.3 Hz, *m*-PPh_2), 131.07 (d, $^{4}J_{P\text{-}C}$ = 2.9 Hz, *p*-PPh_2), 128.46 (d, $^{2}J_{P\text{-}C}$ = 12.7 Hz, *o*-PPh_2), 124.09 (*p*-Dipp), 123.71 (*m*-Dipp), 74.88 (d, $^{1}J_{P\text{-}C}$ = 89.9 Hz, P*C*H), 28.50 (*C*H(CH_3)$_2$), 25.10 (CH(*C*H_3)$_2$), 22.70 (CH(*C*H_3)$_2$), 22.42 (d, $^{3}J_{P\text{-}C}$ = 14.5 Hz, N=C(*C*H_3)) ppm.

^{31}P{^{1}H} NMR ($CDCl_3$, 121 MHz, 25 °C): δ 13.14 ($^{1}J_{Se\text{-}P}$ = 669 Hz) ppm.

^{77}Se NMR ($CDCl_3$, 57 MHz, 25 °C): δ -272 (d, $^{1}J_{Se\text{-}P}$ = 669 Hz) ppm.

Minor isomer $CDCl_3$: (Z)-enamine, 4%:

^{1}H NMR ($CDCl_3$, 300 MHz, 25 °C): δ 5.35 (1H, bs, N*H*), 3.76 (1H, d, $^{2}J_{P-H}$ = 17.6 Hz, PC*H*), 3.20 (2H, sept, $^{3}J_{H-H}$ = 6.9 Hz, C*H*(CH_3)$_2$), 1.67 (3H, s, N=C(C*H*$_3$)), 1.31 (d, 6H, $^{3}J_{H-H}$ = 6.9 Hz, CH(C*H*$_3$)$_2$) ppm.

^{31}P{^{1}H} NMR ($CDCl_3$, 121 MHz, 25 °C): δ 22.51 ppm.

Major isomer C_6D_6: imine, 74%:

^{1}H NMR (C_6D_6, 300 MHz, 25 °C): δ 7.95 – 8.02 (4H, m, *m*-PPh_2), 6.97 – 7.13 (9H, m, *o*-, *p*-PPh_2, *m*-Dipp, *p*-Dipp), 3.57 (2H, d, $^{2}J_{P-H}$ = 15.1 Hz, PC*H*$_2$), 2.73 (2H, sept, $^{3}J_{H-H}$ = 6.9 Hz, C*H*(CH_3)$_2$), 1.95 (3H, d, $^{4}J_{P-H}$ = 1.7 Hz, N=C(C*H*$_3$)), 1.15 (d, 6H, $^{3}J_{H-H}$ = 6.9 Hz, CH(C*H*$_3$)$_2$), 1.01 (d, 6H, $^{3}J_{H-H}$ = 6.9 Hz, CH(C*H*$_3$)$_2$) ppm.

^{31}P{^{1}H} NMR (C_6D_6, 121 MHz, 25 °C): δ 27.13 ($^{1}J_{Se-P}$ = 760 Hz) ppm.

^{77}Se NMR (C_6D_6, 57 MHz, 25 °C): δ -333 ($^{1}J_{Se-P}$ = 760 Hz) ppm.

Minor isomer C_6D_6: (E)-enamine, 24%:

^{1}H NMR (C_6D_6, 300 MHz, 25 °C): δ 9.23 (1H, s, N*H*), 8.02 – 8.11 (4H, m, *m*-PPh_2), 6.97 – 7.13 (9H, m, *o*-, *p*-PPh_2, *m*-Dipp, *p*-Dipp), 4.39 (1H, d, $^{2}J_{P-H}$ = 16.9 Hz, PC*H*), 3.26 (2H, sept, $^{3}J_{H-H}$ = 6.9 Hz, C*H*(CH_3)$_2$), 1.50 (3H, s, N=C(C*H*$_3$)), 1.13 (d, 6H, $^{3}J_{H-H}$ = 6.9 Hz, CH(C*H*$_3$)$_2$), 1.01 (d, 6H, $^{3}J_{H-H}$ = 6.9 Hz, CH(C*H*$_3$)$_2$) ppm.

^{31}P{^{1}H} NMR (C_6D_6, 121 MHz, 25 °C): δ 12.87 ($^{1}J_{Se-P}$ = 677 Hz) ppm.

^{77}Se NMR (C_6D_6, 57 MHz, 25 °C): δ -272 ($^{1}J_{Se-P}$ = 677 Hz) ppm.

Trace isomer C_6D_6: (Z)-enamine, 2%:

^{1}H NMR (C_6D_6, 300 MHz, 25 °C): δ 4.57 (1H, bs, N*H*), 3.79 (1H, s, $^{2}J_{P\text{-}H}$ = 15.8 Hz, PC*H*), 3.10 (2H, sept, $^{3}J_{H\text{-}H}$ = 6.8 Hz, C*H*(CH_3)$_2$), 2.08 (3H, s, N=C(C*H*$_3$)), 1.36 (d, 6H, $^{3}J_{H\text{-}H}$ = 6.8 Hz, CH(C*H*$_3$)$_2$), 0.80 (d, 6H, $^{3}J_{H\text{-}H}$ = 6.8 Hz, CH(C*H*$_3$)$_2$) ppm.

^{31}P{^{1}H} NMR (C_6D_6, 121 MHz, 25 °C): δ 21.91 ppm.

Major isomer CD_3CN: imine, 72%:

^{1}H NMR (CD_3CN, 300 MHz, 25 °C): δ 7.97 – 8.04 (4H, m, *m*-PPh_2), 7.48 – 7.56 (6H, m, *o*-, *p*-PPh_2), 6.94 – 7.05 (3H, m, *m*-Dipp, *p*-Dipp), 4.15 (2H, d, $^{2}J_{P\text{-}H}$ = 15.0 Hz, PC*H*$_2$), 2.55 (2H, sept, $^{3}J_{H\text{-}H}$ = 6.9 Hz, C*H*(CH_3)$_2$), 1.85 (3H, d, $^{4}J_{P\text{-}H}$ = 1.2 Hz, N=C(C*H*$_3$)), 1.02 (d, 6H, $^{3}J_{H\text{-}H}$ = 6.9 Hz, CH(C*H*$_3$)$_2$), 0.86 (d, 6H, $^{3}J_{H\text{-}H}$ = 6.9 Hz, CH(C*H*$_3$)$_2$) ppm.

^{31}P{^{1}H} NMR (CD_3CN, 121 MHz, 25 °C): δ 27.99 ($^{1}J_{Se\text{-}P}$ = 743 Hz) ppm.

Minor isomer CD_3CN: (E)-enamine, 14%:

^{1}H NMR (CD_3CN, 300 MHz, 25 °C): δ 8.63 (1H, s, N*H*), 7.73 – 7.79 (6H, m, *o*-, *p*-PPh_2), 7.15 – 7.32 (3H, m, *m*-Dipp, *p*-Dipp), 3.78 (1H, d, $^{2}J_{P\text{-}H}$ = 17.2 Hz, PC*H*), 3.19 (2H, sept, $^{3}J_{H\text{-}H}$ = 6.9 Hz, C*H*(CH_3)$_2$), 2.15 (3H, s, N=C(C*H*$_3$)), 1.19 (d, 6H, $^{3}J_{H\text{-}H}$ = 6.9 Hz, CH(C*H*$_3$)$_2$), 0.92 (d, 6H, $^{3}J_{H\text{-}H}$ = 6.9 Hz, CH(C*H*$_3$)$_2$) ppm.

^{31}P{^{1}H} NMR (CD_3CN, 121 MHz, 25 °C): δ 12.56 ($^{1}J_{Se\text{-}P}$ = 661 Hz) ppm.

Minor isomer CD_3CN: (Z)-enamine, 13%:

^{1}H NMR (CD_3CN, 300 MHz, 25 °C): δ 7.89 – 7.97 (m, 4H, *m*-PPh_2), 7.48 – 7.56 (6H, m, *o*-, *p*-PPh_2), 7.15 – 7.32 (3H, m, *m*-Dipp, *p*-Dipp), 6.54 (1H, s, N*H*), 4.60 (d, 1H, $^{2}J_{P\text{-}H}$ = 17.8 Hz, PC*H*), 3.07 (2H, sept, $^{3}J_{H\text{-}H}$ = 6.8 Hz, C*H*(CH_3)$_2$), 2.15 (3H, s, N=C(C*H*$_3$)), 1.24 (d, 6H, $^{3}J_{H\text{-}H}$ = 6.8 Hz, CH(C*H*$_3$)$_2$), 1.17 (d, 6H, $^{3}J_{H\text{-}H}$ = 6.8 Hz, CH(C*H*$_3$)$_2$) ppm.

$^{31}P\{^{1}H\}$ NMR (CD_3CN, 121 MHz, 25 °C): δ 22.42 ppm.

Trace isomer CD_3CN: ylide, 1%:

^{1}H NMR (CD_3CN, 300 MHz, 25 °C): δ 3.75 (d, 1H, $^{2}J_{P\text{-}H}$ = 17.8 Hz, PC*H*), 2.36 (2H, sept, $^{3}J_{H\text{-}H}$ = 6.8 Hz, C*H*$(CH_3)_2$), 1.81 (3H, s, N=C(C*H*$_3$)), 0.96 (d, 6H, $^{3}J_{H\text{-}H}$ = 6.8 Hz, CH(C*H*$_3)_2$), 0.65 (d, 6H, $^{3}J_{H\text{-}H}$ = 6.8 Hz, CH(C*H*$_3)_2$) ppm.

5.4.3.5 Synthesis of Compound 5 - Dipp-N($Al^{-}Me_2$)=C(CH_3)$CP^{+}(C_6H_5)_2O$

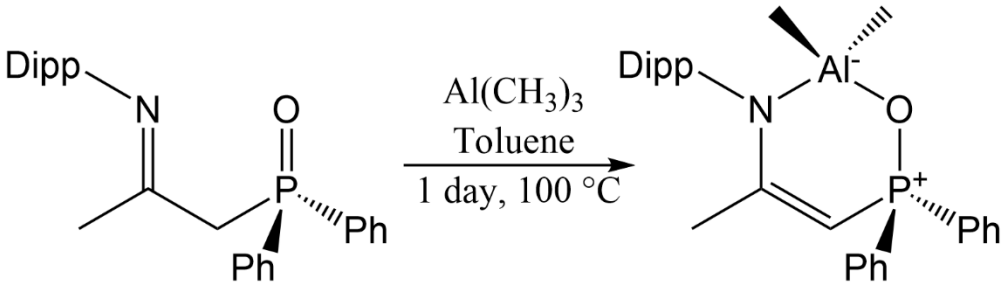

2 **5**

In the glovebox within a 20 mL scintillation vial, 73 mg (0.17 mmol) **2** was dissolved in ~4 mL benzene, followed by addition of two aliquots of 0.45 mL for a total of 0.90 mL $AlMe_3$ (2.0 M, heptane, 1.80 mmol) using 2 insulin syringes, dispensing directly into the benzene solution. This was left to stir for 5 days, pumped mostly dry *in vacuo*, and transferred to an NMR tube using triplicate benzene-d_6 aliquots. The sample was put back into the dry box having shown complete PNMR conversion, transferred to a 20 mL vial and the solvent stripped *in vacuo*. The white residue with hints of beige was dissolved entirely into ~8 mL pentane with stirring and was then filtered into a pre-weighed vial through a calcined diatomaceous earth pipette filter with triplicate pentane washings totalling ~12 mL. Placing this in the freezer caused crystals to form that were re-dissolved into the bulk solution with gentle low heat from a heat gun. Once re dissolved, the solution

was reduced to ~8 mL *in vacuo* with frequent observation until crystallization began. Redissolution with low heat and placing into the freezer similarly caused radial fine white needles to form. Decanting the bulk solution and rinsing the crystals with ~1 mL cold pentane and drying *in vacuo* gave 63 mg (0.13 mmol) when dry.

Yield: 76%.

m.p. (°C): 166.3 – 167.0.

Analytical Calc. for $C_{29}H_{37}NAlOP$: C: 73.55% H: 7.88% N: 2.96% Found: C: 73.55% H: 7.95% N: 3.08%.

^{1}H NMR (C_6D_6, 300 MHz, 25 °C): δ 7.63 – 7.70 (4H, m, *m*-PPh_2), 6.98 – 7.16 (9H, m, *m*-,*p*-Dipp, *o*-, *p*-PPh_2), 3.84 (1H, d, $^{2}J_{P\text{-}H}$ = 26.3 Hz, PC*H*), 3.40 (2H, sept, $^{3}J_{H\text{-}H}$ = 7.0 Hz, C*H*(CH_3)$_2$), 1.67 (3H, d, $^{4}J_{P\text{-}H}$ = 1.3 Hz, N=C(C*H*$_3$)), 1.24 (d, 6H, $^{3}J_{H\text{-}H}$ = 7.0 Hz, CH(C*H*$_3$)$_2$), 1.05 (d, 6H, $^{3}J_{H\text{-}H}$ = 7.0 Hz, CH(C*H*$_3$)$_2$), -0.29 (6H, s, Al(C*H*$_3$)$_2$) ppm.

^{13}C{^{1}H} NMR (C_6D_6, 75MHz, 25 °C): δ 175.2 (s, N=*C*), 145.6 (s, *o*-Dipp), 142.6 (s, *ipso*-Dipp), 133.45 (d, $^{1}J_{P\text{-}C}$ = 111.0 Hz, *ipso*-PPh_2), 132.11 (d, $^{4}J_{P\text{-}C}$ = 2.4 Hz, *p*-PPh_2), 131.74 (d, $^{3}J_{P\text{-}C}$ = 10.6 Hz, *m*-PPh_2), 128.6 (d, $^{2}J_{P\text{-}C}$ = 12.5 Hz, *o*-PPh_2), 126.46 (s, *p*-Dipp), 124.04 (s, *m*-Dipp), 66.31 (d, $^{1}J_{P\text{-}C}$ = 103.3 Hz, P*C*H), 28.2 (s, *C*H(CH_3)$_2$), 25.67 (d, $^{3}J_{P\text{-}C}$ = 15.6 Hz, N=C(*C*H$_3$)), 25.01 (s, CH(*C*H$_3$)$_2$), 24.46 (s, CH(*C*H$_3$)$_2$), -9.38 (s, Al(*C*H$_3$)$_2$) ppm.

^{27}Al NMR (C_6D_6, 78 MHz, 25 °C): δ 67 ppm +/- 1600 Hz.

^{31}P{^{1}H} NMR (C_6D_6, 121 MHz, 25 °C): δ 41.45 ppm.

5.4.3.6 Synthesis of Compound 6 - Dipp-N($Al^{-}Me_2$)-C(CH_3)=(CH)$P^{+}(C_6H_5)_2S$

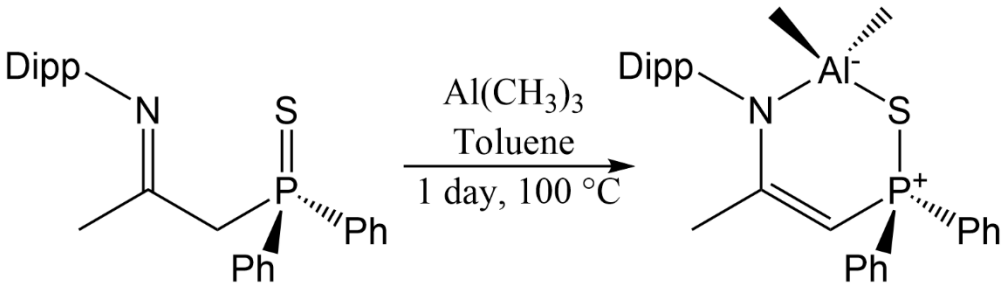

3 **6**

In a 20 mL scintillation vial 66 mg (0.15 mmol) **3** was dissolved in 2 mL toluene and added to a 50 mL sealed reaction vessel with a PTFE stopper followed by addition of 0.087 mL $AlMe_3$ (2.0 M, heptane, 0.17 mmol) added to 2 mL toluene prior with 3×2 mL rinsing totalling 10 mL toluene. Heating at 100 °C for 1.5 hours, cooling, and filtration through a calcined diatomaceous earth pipette filter in the glovebox with triplicate rinsing into a pre-weighed 20 mL scintillation vial. Drying *in vacuo* and rinsing with 2×1 mL pentane gave 62 mg (0.13 mmol) of an analytically pure crystalline white solid. Colourless prismatic crystals were grown from cooling a pentane solution of **6**.

Yield: 83%

m.p. (°C): 149.9-151.3

Analytical Calc. for $C_{29}H_{37}NAlSP$: C: 71.14% H: 7.62% N: 2.85% Found: C: 71.22% H: 7.63% N: 2.92%

^{1}H NMR (C_6D_6, 300 MHz, 25 °C): δ 7.68 – 7.75 (4H, m, *m*-PPh_2), 7.10 – 7.19 (3H, m, *m*-,*p*-Dipp), 6.98 – 7.05 (6H, m, *o*-,*p*-PPh_2), 3.92 (1H, d, $^{2}J_{P\text{-}H}$ = 18.7 Hz, PC*H*), 3.67 (2H, sept, $^{3}J_{H\text{-}H}$ = 6.9 Hz, C*H*(CH_3)$_2$), 1.72 (3H, d, $^{4}J_{P\text{-}H}$ = 1.7 Hz, N=C(C*H*$_3$)), 1.37 (d, 6H, $^{3}J_{H\text{-}}$

$_H$ = 6.9 Hz, CH(CH_3)$_2$), 1.24 (d, 6H, $^3J_{H-H}$ = 6.9 Hz, CH(CH_3)$_2$), -0.48 (6H, s, Al(CH_3)$_2$) ppm.

$^{13}C\{^1H\}$ NMR (C_6D_6, 75 MHz, 25 °C): δ 170.3 (s, N=C), 145.8 (*o*-Dipp), 142.8 (*ipso*-Dipp), 134.9 (d, $^1J_{P-C}$ = 90.2 Hz, *ipso*-PPh$_2$), 131.5 – 131.7 (m, *m*-,*p*-PPh$_2$), 128.6 (d, $^2J_{P-C}$ = 12.5 Hz, *o*-PPh$_2$), 126.6 (*p*-Dipp), 124.1 (*m*-Dipp), 66.1 (d, $^1J_{P-C}$ = 103.3 Hz, P*C*H), 28.2 (*C*H(CH$_3$)$_2$), 27.2 (d, $^3J_{P-C}$ = 15.6 Hz, N=C(*C*H$_3$)), 25.1 (CH(*C*H$_3$)$_2$), 24.6 (CH(*C*H$_3$)$_2$), -7.8 (Al(*C*H$_3$)$_2$) ppm.

^{27}Al NMR (C_6D_6, 78 MHz, 25 °C): δ 73 ppm +/- 2340 Hz.

$^{31}P\{^1H\}$ NMR (C_6D_6, 121 MHz, 25 °C): δ 25.80 ppm.

5.4.3.7 Synthesis of Compound 7 - Dipp-N(Al$^-$Me$_2$)-C(CH$_3$)=(CH)P$^+$(C$_6$H$_5$)$_2$Se

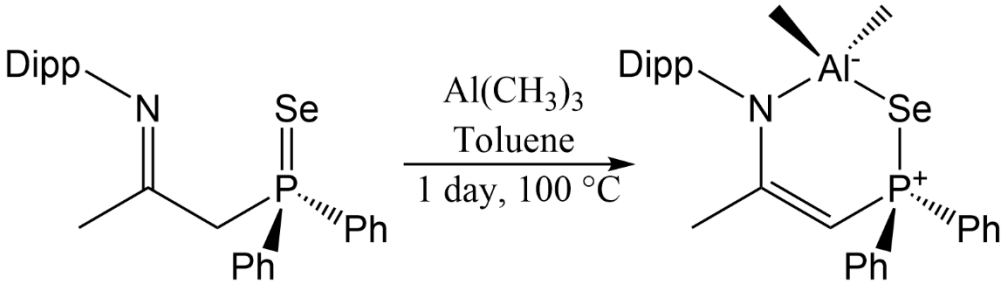

4 **7**

In a 20 mL scintillation vial 33 mg (0.07 mmol) **4** was dissolved in 1 mL toluene followed by addition of 0.040 mL AlMe$_3$ (2.0 M, heptane, 0.08 mmol) below the liquid level to avoid decomposition. Triplicate rinsing followed mixing with an additional 5mL toluene into a 50 mL sealed reaction vessel with heating at 100 °C for 4 hours. The toluene was stripped *in vacuo* and the solids rinsed twice with 1 mL pentane. Dissolution in 2 mL toluene, filtering through calcined diatomaceous earth, and rinsing the flask and filter three times with 1 mL aliquots of toluene was followed by drying *in vacuo* giving 28 mg (0.05

mmol) of an analytically pure crystalline white solid. Colourless prismatic crystals were grown from cooling a pentane solution of **7**.

Yield: 77%

m.p. (°C): - 168.3-171.3.

Analytical Calc. for $C_{29}H_{37}NAlSeP$: C: 64.92% H: 6.95% N: 2.61% Found: C: 65.13% H: 6.95% N: 2.55%

^{1}H NMR (C_6D_6, 300 MHz, 25 °C): δ 7.69 – 7.77 (4H, m, *m*-PPh_2, $^{5}J_{Se-H}$ = 80 Hz) , 7.10 – 7.19 (3H, m, *p*-Dipp, *m*-Dipp), 6.98 – 7.03 (6H, m, *o*-, *p*-PPh_2), 4.03 (H, d, $^{2}J_{P-H}$ = 16.2 Hz, PC*H*), 3.70 (2H, sept, $^{3}J_{H-H}$ = 6.9 Hz, C*H*$(CH_3)_2$), 1.76 (3H, d, $^{4}J_{P-H}$ = 1.8 Hz, N=C(C*H*$_3$)), 1.38 (d, 6H, $^{3}J_{H-H}$ = 6.9 Hz, CH(C*H*$_3)_2$), 1.25 (d, 6H, $^{3}J_{H-H}$ = 6.9 Hz, CH(C*H*$_3)_2$), -0.49 (6H, s, Al(C*H*$_3)_2$) ppm.

^{13}C{^{1}H} NMR (C_6D_6, 75 MHz, 25 °C): δ 170.1 (d, $^{3}J_{P-C}$ = 2.2 Hz, N=C), 145.9 (*o*-Dipp), 142.9 (*ipso*-Dipp), 134.3 (d, $^{1}J_{P-C}$ = 83.0 Hz, *ipso*-PPh_2), 132.0 (d, $^{3}J_{P-C}$ = 11.2 Hz, *m*-PPh_2), 131.6 (d, $^{4}J_{P-C}$ = 3.1 Hz, *p*-PPh_2), 128.7 (d, $^{2}J_{P-C}$ = 12.8 Hz, *o*-PPh_2), 126.7 (*p*-Dipp), 124.1 (*m*-Dipp), 65.7 (d, $^{1}J_{P-C}$ = 96.6 Hz, P*C*H), 28.2 (*C*H$(CH_3)_2$), 27.7 (d, $^{3}J_{P-C}$ = 15.8 Hz, N=C(*C*H$_3$)), 25.2 (CH(*C*H$_3)_2$), 24.6 (CH(*C*H$_3)_2$), -7.2 (Al(*C*H$_3)_2$) ppm.

^{27}Al NMR (C_6D_6, 78 MHz, 25 °C): δ 71 ppm +/- 1550 Hz.

^{31}P{^{1}H} NMR (C_6D_6, 121 MHz, 25 °C): δ 10.14 ppm ($^{1}J_{Se-P}$ = 496 Hz).

^{77}Se NMR (C_6D_6, 57 MHz, 25 °C): δ -274.8 ppm ($^{1}J_{Se-P}$ = 496 Hz).

5.4.3.8 Synthesis of Compound 8 -Dipp-N(In^-Me_2)-C(CH_3)(CH)$P^+(C_6H_5)_2O$

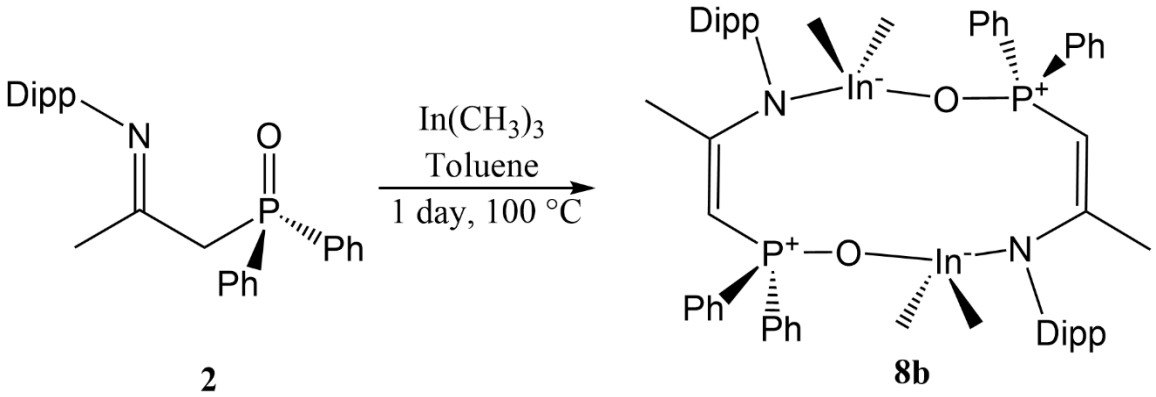

2 **8b**

Both 0.2250 g (0.54 mmol) **3** and 0.0881 g (0.55 mmol) $InMe_3$ were transferred to a 50 mL sealed reaction vessel along with 10 mL toluene. The reaction mixture was heated for 3 hours at 110 °C, cooled to room temperature and transferred into a glovebox. The solution was concentrated *in vacuo* to 5 mL, filtered through a pipette filter (3×2 mL toluene rinses) into a pre-weighed 20 mL scintillation vial and concentrated to a thick oil. Addition and removal *in vacuo* of 3×1 mL pentane to the oil resulted in a white solid forming that was dissolved in minimal pentane (4 mL) with heat in the sealed flask, followed by cooling to -35 °C overnight. The following day small white radial crystals had formed, and the solution was allowed to slowly evaporate to 2 mL and warm to room temperature causing growth of pink-hued larger bladed crystals growing from the central white core determined to be a 6-membered chelate by SC-XRD. The solids were rinsed once with 1 mL pentane and dried *in vacuo* totaling 0.2592 g. ^{1}H NMR analysis of one clump of crystals after drying showed 1.1 equivalents of pentane remained within the radial crystal, so prior to elemental analysis the sample was crushed. Assuming the whole sample to have the same pentane ratio of 1.1 eq. within the crystals, the adjusted yield is 0.227 g

(0.40 mmol) of **8**. A much more dilute solution in pentane cooled to -35 °C formed small colourless blocks that formed as dimers.

Yield: 75%

m.p. (°C): 90.1 - 92.3

Analytical Calc. for: $C_{29}H_{37}NInOP$: 62.04% H: 6.64% N: 2.49% Found: C: 62.43% H: 6.77% N: 2.37%

^{1}H NMR (C_6D_6, 300 MHz, 25 °C): δ 7.77 – 7.84 (4H, m, *m*-PPh_2), 7.02-7.11 (9H, m, *m*-Dipp, *p*-Dipp, *o*-, *p*-PPh_2), 3.84 (2H, d, $^{2}J_{P\text{-}H}$ = 24.1 Hz, PC*H*), 3.23 (2H, sept, $^{3}J_{H\text{-}H}$ = 6.9 Hz, C*H*$(CH_3)_2$), 1.71 (3H, d, $^{4}J_{P\text{-}H}$ = 2.1 Hz,), 1.03-1.07 (12H, m, CH(C*H*$_3)_2$), 0.11 (6H, s, In(C*H*$_3)_2$) ppm.

^{13}C{^{1}H} NMR (C_6D_6, 75 MHz, 25 °C): δ 175.3 (N=C), 144.7 (*ipso*-Dipp), 144.5 (*o*-Dipp), 136.4 (d, $^{1}J_{P\text{-}C}$ = 109.2 Hz, *ipso*-PPh_2), 132.0 (d, $^{3}J_{P\text{-}C}$ = 11.3 Hz, *m*-PPh_2), 131.4 (d, $^{4}J_{P\text{-}C}$ = 2.9 Hz, *p*-PPh_2), 128.5 (d, $^{2}J_{P\text{-}C}$ = 12.6 Hz, *o*-PPh_2), 125.6 (*p*-Dipp), 123.8 (*m*-Dipp), 66.9 (d, $^{1}J_{P\text{-}C}$ = 123.4 Hz, P*C*H), 28.0 (*C*H$(CH_3)_2$), 27.4 (d, N=C(*C*H_3)), 25.2 (CH(*C*$H_3)_2$), 24.5 (CH(*C*$H_3)_2$), -6.7 (In(*C*$H_3)_2$ ppm.

^{31}P{^{1}H} NMR (C_6D_6, 121 MHz, 25 °C): δ 36.54 ppm.

5.4.3.9 Synthesis of Compound 9 - Dipp-N(In^{-}Me$_2$)-C(CH$_3$)(CH)P^{+}(C$_6$H$_5$)$_2$S

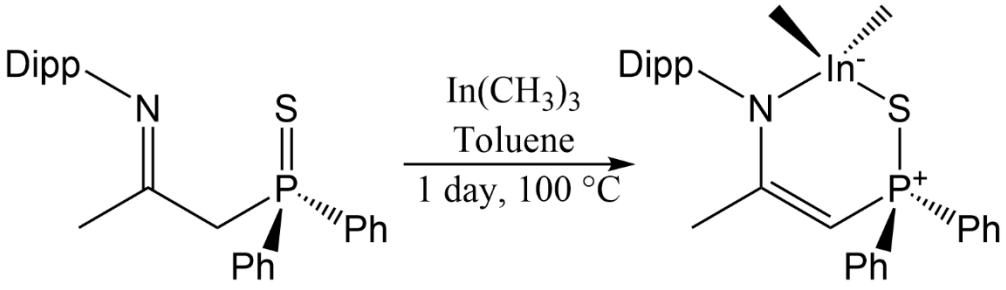

3 **9**

Both 0.1842 g (0.42 mmol) **3** and 0.0694 g (0.43 mmol) combined in a 50 mL sealed reaction vessel along with 10 mL toluene and subsequent heating to 100 °C for 5.5 hours. The mixture was left to stand for 4 days, and ^{31}P NMR analysis of the bulk solution with a few drops of C_6D_6 showed incomplete conversion of **3** to **9** and the mixture appeared to have a small amount of fine white precipitate, assumed to be $InMe_3$ hydrolysis products. To the reaction mixture an additional 0.0018 g (0.01 mmol) $InMe_3$ was added along with the NMR sample and 3 mL toluene to rinse, followed by ~10 minutes of heating with a heat gun until bubbling occurred. The toluene was then removed *in vacuo* resulting in a thick oil that solidified into a white solid upon addition and *in vacuo* removal of 2×1 mL pentane. 3 mL pentane was then added to the flask with the solid and sealed, fully dissolving with mild heat until boiling occurred. The solution was transferred to a pre-weighed 20 mL scintillation vial with 3×1 mL pentane rinses through a lint free wipe plug in a pipette. The vial was heated and sealed once boiling began and then placed in a -35 °C freezer over night. The bulk solution was removed with a pipette, 1 mL pentane used to rinse, and subsequent drying *in vacuo* gave 0.1830 mg of large radial white crystals. ^{1}H NMR analysis of one radial clump of crystals after drying showed 1.3 equivalents of pentane remained within the crystal clump, so prior to elemental analysis the sample was crushed. Assuming the whole sample to have the same pentane ratio of 1.3 eq. within the crystals, the adjusted yield is 0.157 g of **9**.

Yield: 72%

m.p. (°C): 120.6-121.7

Analytical Calc. for $C_{29}H_{37}NInSP$: C: 60.32% H: 6.46% N: 2.43% Found: C: 60.43% H: 6.50% N: 2.37%.

^{1}H NMR (C_6D_6, 300 MHz, 25 °C): δ 7.79 – 7.86 (4H, m, *m*-PPh_2), 7.10 (3H, s, *m*-Dipp, *p*-Dipp), 7.03-7.06 (6H, m, *o*-, *p*-PPh_2), 3.70 (2H, d, $^{2}J_{P\text{-}H}$ = 18.8 Hz, PC*H*), 3.56 (2H, sept, $^{3}J_{H\text{-}H}$ = 6.9 Hz, C*H*(CH_3)$_2$), 1.78 (3H, d, $^{4}J_{P\text{-}H}$ = 1.9 Hz, N=C(C*H*$_3$)), 1.27 (d, 6H, $^{3}J_{H\text{-}H}$ = 6.9 Hz, CH(C*H*$_3$)$_2$), 1.22 (d, 6H, $^{3}J_{H\text{-}H}$ = 6.9 Hz, CH(C*H*$_3$)$_2$), -0.22 (6H, s, In(C*H*$_3$)$_2$) ppm.

^{13}C{^{1}H} (C_6D_6, 75 MHz, 25 °C): δ 171.02 (N=C), 145.09 (*ipso*-Dipp), 144.47 (*o*-Dipp), 136.80 (d, $^{1}J_{P\text{-}C}$ = 89.1 Hz, *ipso*-PPh_2), 131.63 (d, $^{3}J_{P\text{-}C}$ = 11.1 Hz, *m*-PPh_2), 136.80 (d, $^{4}J_{P\text{-}C}$ = 2.8 Hz, *p*-PPh_2), 128.56 (d, $^{2}J_{P\text{-}C}$ = 12.9 Hz, *o*-PPh_2), 125.70 (*p*-Dipp), 123.94 (*m*-Dipp), 62.70 (d, $^{1}J_{P\text{-}C}$ = 107.0 Hz, P*C*H), 34.45 (*C*H(CH_3)$_2$), 27.98 (CH(*C*H$_3$)$_2$), 26.97 (d, $^{3}J_{P\text{-}C}$ = 15.1 Hz, N=C(*C*H$_3$)), 25.10 (CH(*C*H$_3$)$_2$), -6.67 (In(*C*H$_3$)$_2$ ppm.

^{31}P{^{1}H} (C_6D_6, 121 MHz, 25 °C): δ 26.27 ppm.

^{1}H NMR (C_7D_8, 300 MHz, 25 °C): δ 7.75 – 7.83 (m, 4H, *m*-PPh_2), 6.97 – 7.09 (m, 9H, *m*-,*p*-Dipp, *o*-, *p*-PPh_2), 3.66 (d, 1H, $^{2}J_{P\text{-}H}$ = 18.8 Hz, PC*H*), 3.50 (2H, sept, $^{3}J_{H\text{-}H}$ = 7.0 Hz, C(CH_3)$_2$*H*), 1.75 (d, 3H, $^{4}J_{P\text{-}H}$ = 2.0 Hz, N=C(C*H*$_3$)), 1.24 (d, 6H, $^{3}J_{H\text{-}H}$ = 7.0 Hz, C(C*H*$_3$)$_2$H), 1.20 (d, 6H, $^{3}J_{H\text{-}H}$ = 7.0 Hz, C(C*H*$_3$)$_2$H), -0.29 (s, 6H, In(C*H*$_3$)$_2$). ppm.

5.4.3.10 Synthesis of Compound 10 - Dipp-N($In^{-}Me_2$)-C(CH_3)(CH)$P^{+}(C_6H_5)_2$Se

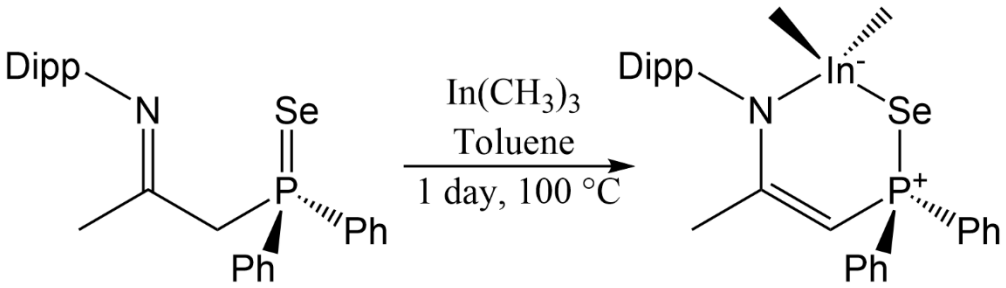

4 **10**

Both 0.2050 g (0.43 mmol) **4** and 0.0712 g (0.45 mmol) $InMe_3$ were added to a 50 mL sealed reaction vessel using 10 mL toluene. The solution was heated to 110 °C for 1.5 hr then cooled and left overnight. Heating the next day for an additional 2 hours was followed by cooling, transferring to the glovebox, and removing the toluene and methane *in vacuo* resulting in a thick gold oil. Addition and subsequent *in vacuo* removal of 3×1 mL of pentane gave a white solid precipitate and golden oil. 2 mL pentane was used to wash the solid, which crystallized upon slow evaporation. The remaining white solid was transferred to a 20 mL scintillation vial with pentane (5x2 mL), sealed, and warmed until the solid had completely dissolved. The vial was vented, heated until bubbling occurred, and sealed again and placed in -35 °C for 4 days. Decanting the pentane into the previous washings, rinsing with 1 mL cold pentane, and drying for 30 minutes prior to drying *in vacuo* left 0.1948 g slightly yellow radial prismatic crystals. ^{1}H NMR analysis of one radial clump of crystals after drying showed 0.06 equivalents of pentane remained within the crystal clump, so prior to elemental analysis the sample was crushed. Assuming the whole sample to have the same pentane ratio of 0.06 within the crystals, the adjusted yield is 0.193 g (0.31 mmol) of **10**.

Yield: 73%

m.p. (°C): 141.7-143.0

Analytical Calc. for $C_{29}H_{37}NInSeP$: C: 55.79% H: 5.97% N: 2.24% Found: C: 55.40% H: 6.12% N: 2.15%.

^{1}H (C_6D_6, 300 MHz, 25 °C): δ 7.79 – 7.87 (4H, m, *m*-PPh_2), 7.11 (3H, s, *m*-Dipp, *p*-Dipp), 7.01 – 7.05 (6H, m, *o*-, *p*-PPh_2), 3.76 (2H, d, $^{2}J_{P\text{-}H}$ = 17.4 Hz, PC*H*), 3.61 (2H, sept, $^{3}J_{H\text{-}H}$ = 6.9 Hz, C*H*$(CH_3)_2$), 1.82 (3H, d, $^{4}J_{P\text{-}H}$ = 2.2 Hz, N=C(C*H*$_3$)), 1.31 (d, 6H, $^{3}J_{H\text{-}H}$ = 6.9 Hz, CH(C*H*$_3)_2$), 1.25 (d, 6H, $^{3}J_{H\text{-}H}$ = 6.9 Hz, CH(C*H*$_3)_2$), -0.27 (6H, s, In(C*H*$_3)_2$) ppm.

$^{13}C\{^{1}H\}$ (C_6D_6, 75 MHz, 25 °C): δ 170.7 (d, $^{2}J_{P\text{-}C}$ = 2.3 Hz, N=C), 145.3 (*ipso*-Dipp), 144.4 (*o*-Dipp), 136.0 (d, $^{1}J_{P\text{-}C}$ = 82.3 Hz, *ipso*-PPh_2), 132.0 (d, $^{3}J_{P\text{-}C}$ = 11.3 Hz, *m*-PPh_2), 131.4 (d, $^{4}J_{P\text{-}C}$ = 2.9 Hz, *p*-PPh_2), 128.6 (d, $^{2}J_{P\text{-}C}$ = 12.6 Hz, *o*-PPh_2), 125.7 (*p*-Dipp), 124.0 (*m*-Dipp), 61.0 (d, $^{1}J_{P\text{-}C}$ = 100.0 Hz, P*C*H), 28.0 (*C*H$(CH_3)_2$), 27.4 (d, $^{3}J_{P\text{-}C}$ = 15.8 Hz, N=C(*C*H$_3$)), 25.2 (CH(*C*H$_3)_2$), 24.5 (CH(*C*H$_3)_2$), -6.5 (In(*C*H$_3)_2$ ppm.

$^{31}P\{^{1}H\}$ (C_6D_6, 121 MHz, 25 °C): δ 9.01 ($^{1}J_{Se\text{-}P}$ = 502 Hz) ppm.

^{77}Se (C_6D_6, 57 MHz, 25 °C): δ -293.5 ($^{1}J_{Se\text{-}P}$ = 502 Hz) ppm.

5.5 Conclusion

Reaction of a literature phosphine-imine[1] with hydrogen peroxide, elemental sulfur or selenium affords three bidentate ligands **2**-**4** that chelate via N and either O, S, or Se to metal atoms. In either $CDCl_3$, C_6D_6, or CD_3CN solutions these compounds undergo significant molecular rearrangement via tautomerism. ^{1}H, ^{13}C, and ^{31}P NMR spectroscopy shows some of the isomers including a major imine tautomer in all solutions with **2**-**4**, minor (E)- and (Z)-enamine tautomers, and compound **3** within CD_3CN solution gave rise

to what may be a fourth isomer visible by ^{31}P NMR spectroscopy; however, very low concentration made absolute assignment inconclusive for ^{1}H and ^{13}C NMR spectroscopy. This fourth isomer is expected to be an ylide with the acidic proton on the chalcogen in each case. DFT calculations of compound **2** based on single crystal structure cif files of the imine and (E)-enamine or a drawn model of the (Z)-isomer as each of the proposed isomers in the gas phase show the (Z)-enamine (0 kcal/mol) to be most stable with the similar conformation ylide rearranging into the (Z)-enamine. The imine was modelled in the same (Z)-isomer chelate structure, rearranging into a more stable conformation (+1.4 kcal/mol) with the (E)-enamine the next most stable (+3.8 kcal/mol). The ylide, modelled in the same conformation as the (E)-isomer, was the highest in energy (+23.5 kcal/mol). As phosphorus ylide are prone to electron delocalization, the resulting phosphonium secondary carbanion produced may play a crucial role within the dynamic dance in solution and is thought to exist as a transient intermediate species between the dominant imine/(E)-enamine/(Z)-enamine isomers. Compound **2** has been isolated as both the imine and (E)-enamine isomers, with the latter displaying hydrogen bonding from N-H…O'=P'.

Six novel dimethyl group 13 metallacycles with a ring structure of '-N-M-E-P-C=C-' (M = Al (**5**-**7**), In (**8**-**10**) and E = O (Ligand = **2**, Al = **5**, In = **8**), S (Ligand = **3**, Al =**6**, In = **9**), Se (Ligand = **4**, Al = **7**, In = **10**),) have been prepared. Each metallacycle is zwitterionic, has an anionic tetrahedral metal center and cationic phosphonium formed via electron delocalization and subsequent donation to the metal via the oxide, sulfide and selenide. These metallacycles are mostly 6-membered cyclic monomers; however, **8** forms as a 12-membered cyclic dimer as well. Compounds **6**-**7** and **9**-**10** represent the first

reported instances of 6-membered metallacycles of the structure '-N-M-E-P-C=C-' (E = S, Se M = Al, In) within the CSD. Exploration into these derivatives expands the list of known dimethyl organoaluminum complexes that can be studied further regarding the many potential applications as catalysts in ring-opening- or co-polymerization processes.

5.6 References

1. Masuda, J. D.; Wei, P.; Stephan, D. W. Nickel and palladium phosphinimine-imine ligand complexes. *Dalton Transactions* **2003**, 35-355.

2. Mindiola, D. Nacnac … Are You Still There? The Evolution of β-Diketiminate Complexes of Nickel. *Angewandte Chemie International Edition* **2009**, *48*, 6198-6200.

3. Cui, C.; Roesky, H. W.; Schmidt, H.; Noltemeyer, M.; Hao, H.; Cimpoesu, F. Synthesis and Structure of a Monomeric Aluminum(I) Compound [{HC(CMeNAr)$_2$}Al] (Ar=2,6–iPr$_2$C$_6$H$_3$): A Stable Aluminum Analogue of a Carbene. *Angewandte Chemie International Edition* **2000**, *39*, 4274-4276.

4. Zhong, M.; Sinhababu, S.; Roesky, H. W. The unique β-diketiminate ligand in aluminum(i) and gallium(i) chemistry. *Dalton Transactions* **2020**, *49*, 1351-1364.

5. Wilson, A. S. S.; Hill, M. S.; Mahon, M. F.; Dinoi, C.; Maron, L. Organocalcium-mediated nucleophilic alkylation of benzene. *Science* **2017**, *358*, 1168-1171.

6. Liang, L.; Chen, F.; Huang, M.; Cheng, L.; Li, C.; Lee, H. M. Aluminium complexes of bidentate N,O- and N,N-ligands derived from oxidative functionalization of amido phosphines: synthesis, structure and reactivity. *Dalton Transactions* **2010**, *39*, 9941-9951.

7. Qian, B.; Ward, D. L.; Smith, M. R. Synthesis, Structure, and Reactivity of β-Diketiminato Aluminum Complexes. *Organometallics* **1998**, *17*, 3070-3076.

8. Wei, Y.; Wang, S.; Zhou, S. Aluminum alkyl complexes: synthesis, structure, and application in ROP of cyclic esters. *Dalton Transactions* **2016**, *45*, 4471-4485.

9. Ajellal, N.; Carpentier, J.; Guillaume, C.; Guillaume, S. M.; Helou, M.; Poirier, V.; Sarazin, Y.; Trifonov, A. Metal-catalyzed immortal ring-opening polymerization of lactones, lactides and cyclic carbonates. *Dalton Transactions* **2010**, *39*, 8363-8376.

10. Castro-Osma, J. A.; Earlam, A.; Lara-Sánchez, A.; Otero, A.; North, M. Synthesis of Oxazolidinones from Epoxides and Isocyanates Catalysed by Aluminium Heteroscorpionate Complexes. *ChemCatChem* **2016**, *8*, 2100-2108.

11. Whiteoak, C. J.; Kielland, N.; Laserna, V.; Escudero-Adán, E. C.; Martin, E.; Kleij, A. W. A Powerful Aluminum Catalyst for the Synthesis of Highly Functional Organic Carbonates. *Journal of the American Chemical Society* **2013**, *135*, 1228-1231.

12. Andrea, K. A.; Plommer, H.; Kerton, F. M. Ring-opening polymerizations and copolymerizations of epoxides using aluminum- and boron-centered catalysts. *European Polymer Journal* **2019**, *120*, 109202.

13. Li, C.; Tsai, C.; Lin, C.; Ko, B. Synthesis, structural characterization and reactivity of aluminium complexes supported by benzotriazole phenoxide ligands: air-stable alumoxane as an efficient catalyst for ring-opening polymerization of l-lactide. *Dalton Transactions* **2011**, *40*, 1880-1887.

14. Ebrahimi, T.; Aluthge, D. C.; Patrick, B. O.; Hatzikiriakos, S. G.; Mehrkhodavandi, P. Air- and Moisture-Stable Indium Salan Catalysts for Living Multiblock PLA Formation in Air. *ACS Catalysis* **2017**, *7*, 6413-6418.

15. Clegg, W.; Harrington, R. W.; North, M.; Pasquale, R. Cyclic Carbonate Synthesis Catalysed by Bimetallic Aluminium-Salen Complexes. *Chemistry – A European Journal* **2010**, *16*, 6828-6843.

16. Herzog, H. J. *Carbon Capture;* The MIT Press: Cambridge, Massachusetts, 2018; *1*.

17. Nordheider, A.; Woollins, J. D.; Chivers, T. Organophosphorus–Tellurium Chemistry: From Fundamentals to Applications. *Chemical Reviews* **2015**, *115*, 10378-10406.

18. Zingaro, R. A. Tributylphosphine telluride. *Journal of Organometallic Chemistry* **1963**, *1*, 200.

19. MostafaHabibi-Khorassani, S.; Shahraki, M.; Mofarrah, E.; Mofarrah, E. Investigation of rotations in isomerism forms of a ylide of theophylline: Dynamic ^{1}H NMR study. *Oriental Journal of Chemistry* **2017**, *33*, 1182-1189.

20. Castro-Osma, J. A.; Alonso-Moreno, C.; Gómez, M. V.; Márquez-Segovia, I.; Otero, A.; Lara-Sánchez, A.; Fernández-Baeza, J.; Sánchez-Barba, L. F.; Rodríguez, A. M. Heteroscorpionate aluminium complexes as chiral building blocks to engineer helical architectures. *Dalton Transactions* **2013**, *42*, 14240-14252.

21. Yu, R.; Hung, C.; Huang, J.; Lee, H.; Chen, J. CCDC 201571: Experimental Crystal Structure Determination. **2003**.

22. Heeg, M. J.; Chou, H.; Oliver, J. P. CCDC 779775: Experimental Crystal Structure Determination. **2011**.

23. Normand, M.; Dorcet, V.; Kirillov, E.; Carpentier, J. CCDC 912299: Experimental Crystal Structure Determination. **2013**.

24. Groom, C. R.; Bruno, I. J.; Lightfoot, M. P.; Ward, S. C. The Cambridge Structural Database. *Acta Crystallographica*, *Section B* **2016**, *72*, 171-179.

25. APEX 3 (Bruker, 2018) Bruker AXS Inc., Madison, Wisconsin, USA.

26. SAINT (Bruker, 2016) Bruker AXS Inc., Madison, Wisconsin, USA.

27. SADABS (Bruker, 2016) Bruker AXS Inc., Madison, Wisconsin, USA.

28. Sheldrick, G. M. SHELXT– Integrated space-group and crystal-structure determination. *Acta Crystallographica. Section A* **2015**, *71*, 3-8.

29. Sheldrick, G. M. Crystal structure refinement with SHELXL. *Acta Crystallographica. Section C* **2015**, *71*, 3-8.

30. Hübschle, C. B.; Sheldrick, G. M.; Dittrich, B. ShelXle: a Qt graphical user interface for SHELXL. *Journal of Applied Crystallography* **2011**, *44*, 1281-1284.

31. Dolomanov, O. V.; Bourhis, L. J.; Gildea, R. J.; Howard, J. A. K.; Puschmann, H. OLEX2: a complete structure solution, refinement and analysis program. *Journal of Applied Crystallography* **2009**, *42*, 339-341.

32. Allen, F. H.; Kennard, O.; Watson, D. G.; Brammer, L.; Orpen, A. G.; Taylor, R. Tables of bond lengths determined by X-ray and neutron diffraction. Part 1. Bond lengths in organic compounds. *Journal of the Chemical Society, Perkin Transactions 2* **1987**, S1-S19.

Chapter 6: Future Work

This work involved a lot of troubleshooting that ultimately shed light on a very complex literature preparation in chapter 3 and the discovery of new procedures in chapters 4 and 5. There are many things about the work completed in Chapter 3 that deserve finishing. One of the most important would be reproduction of the solid molybdenum precursors and further exploration into what properties of this reaction lead to the observed results. Water is produced in the reaction, and exposing the ethylene glycol to air will absorb some as well. This can be removed via heating or lowering pressure; however, the effect of this on the final product is not well understood. Temperature is also important as temperature variation led to different products. The relationship between the monomeric $MoO_2(OC_2H_4OH)_2$ and the other compounds is also of interest, as the exact process of MoO_3 to these products is not understood. It could be that the brown oil and largest cluster is due to incomplete hydrolysis of the MoO_3, or it could be clustering of the monomers produced, or a mixture of the two processes. Use of THF also complicated things, as this seemed essential for isolating the single dimeric molybdenum compound, and it is uncertain whether the polymeric dimers require contact with THF to form. In general, the compounds that can come from highly similar reaction conditions need greater understanding if any one of them is the crucial key to forming directly electrodeposited MoS_2.

I believe crystalline molybdenum disulfide can be produced electrochemically; however, the variables are endless to tweak. An ideal synthesis would be easy, clean, reliable, controllable, and variable to alter the deposit for any given use. This is a very, very difficult task, and many people have failed to make this happen. I believe electrodeposition

may come from any number of alternate methods, and it is very difficult to predict what conditions would make for an ideal, non-amorphous deposit. It seems heat may be necessary; however, the lack of heat would be ideal with the expectation that proper application of applied current and voltage could overcome this energy barrier depending on the precursors used. I strongly feel like the ideal method to produce MoS_2 via electrodeposition requires a series of steps, especially when using MoO_x based precursors. Considering this, controlled monolayer electrodeposition of a molybdenum source that could be readily converted to the disulfide via a secondary treatment with a sulfur source may be a useful method of achieving this goal. Adhesion may be an issue as well, as electrodeposition will require some sort of material to be in contact with the bottom layer of sulfur atoms strongly, making electrode material an important variable to consider. Platinum was used for much of this project, ironically due to it is abundance in the lab compared to cheaper materials like glassy carbon.

The next projects in chapters 4 and 5 are thankfully clearer. Now that a variety of potential precursor materials have been identified, produced, and characterized in chapter 4, future projects includes continuing investigations of the phosphonium-fluorenide ligand to observe how other metals and main group elements interact with this type of bidentate chelating monoanionic ligand. Of most interest to me include Mg, Ca, Sr, Ba as a series study along with the transition metals from group 4 (Ti, Zr), group 5 (V), group 8 (Fe), group 9 (Co, Rh, Ir), group 10 (Ni), group 11 (Cu, Ag, Au), group 12 (Zn), group 13 (B, Al, Ga, In), group 15 (P, Bi). Group 17 was indirectly studied including the chloride, bromide, and triiodide salts mostly via SC-XRD with complete characterization of the

bromide salt as the primary precursor used within the project. Characterization of these other halide salts as alternate precursors for different types of reactions may be of value as well if used in reactions with metal precursors such as [K][$AuCl_4$] or [K][$NiCl_3$] to form intermediate [Ligand][Anionic metal cluster] species that may be reduced to valuable molecules via methods such stirring with Zn, KC_8, or Mg^0.

Chapter 5 resulted in the preparation of 6 compounds that are now prime candidates for catalytic testing. Dimethyl indium and aluminum have remarkable properties when it comes to ring-opening polymerization and co-polymerization. While exploring these avenues was out of the scope of this project, future work can be done testing these compounds following well defined literature procedures to gain knowledge about their efficacy, and more excitingly to further the comparison between the chalcogen substitution and how that plays a role in possible catalytic activity. The affinity of oxygen for aluminum may make the sulfur and selenium analogs highly effective due to preference for oxygen-based substrates to interact with the active metal center. I am especially interested in the sulfur analog. The sulfur-based ligand formed very easy to handle crystals, and both the dimethyl aluminum and indium analogs formed even better crystals for physical manipulation. This is valuable as it allows accurate weighing of small samples that is useful for small scale as catalyst loading can be as low as a few mol percent. Sulfur proved to be highly beneficial over similar oxygen analogs in tetrahedral dialkyl aluminum N/S chelates for co-polymerization of isocyanates and epoxides, that could be a first step to studying the possible value of the complexes prepared in chapter 5. It would also be very worthwhile to test out formation of Al(I) and In(I) complexes via reduction. Conversion of these dimethyl

complexes to a dihalide followed by subsequent reduction may allow for isolation of highly reactive carbene analogs of the group 13, open to much more exciting and novel chemistry along with possible use as organometallic ligands for larger metals such as platinum. The lack of steric bulk on one side of these proposed group 13(I) ligands may give rise to square planar group 11 dihalides.

Identification of Key Reaction Products from MoO_3 and Ethylene Glycol Mixtures Used for Attempted MoS_2 Electrodeposition and Synthesis of Bidentate Ligands and Related Group 1 and 13 Metal Complexes

By Tanner A. George

Supplementary Information

List of Figures

3. 3.7 Supplementary Information – Chapter 3

3.7.1 Molybdenum Oil Images

Figure 3.1 Images of **B3a** (gold, left), **B5a** (golden brown, middle), and **B6a** (brown, right) crude reaction mixtures of MoO_3 and ethylene glycol after heating, concentration in vacuo, and filtration through diatomaceous earth.

3.7.2 Crystal from Hydrolysis of D4a Black Solid

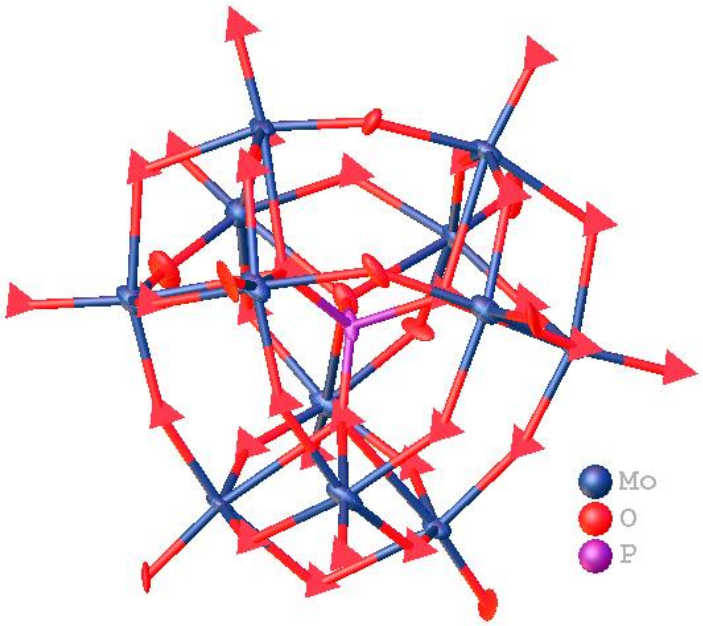

Figure 3.2 Olex 2 screenshot showing the large anionic heteroatom-containing cluster $[Mo_{12}O_{40}X]^{n-}$ where X is best modelled as phosphorus. This is the dataset derived from a single isolated blue crystal (**C4a**) from hydrolysis of **D4a** residue and freezing at -18 °C. Co-crystallized solvent and cations could not be modelled effectively and were removed for this image. Poor data resulted in only evidence of this cluster forming.

3.7.3 NMR Spectroscopy of Ionic Liquid, Precursors, and 1,4-Butanedithiol

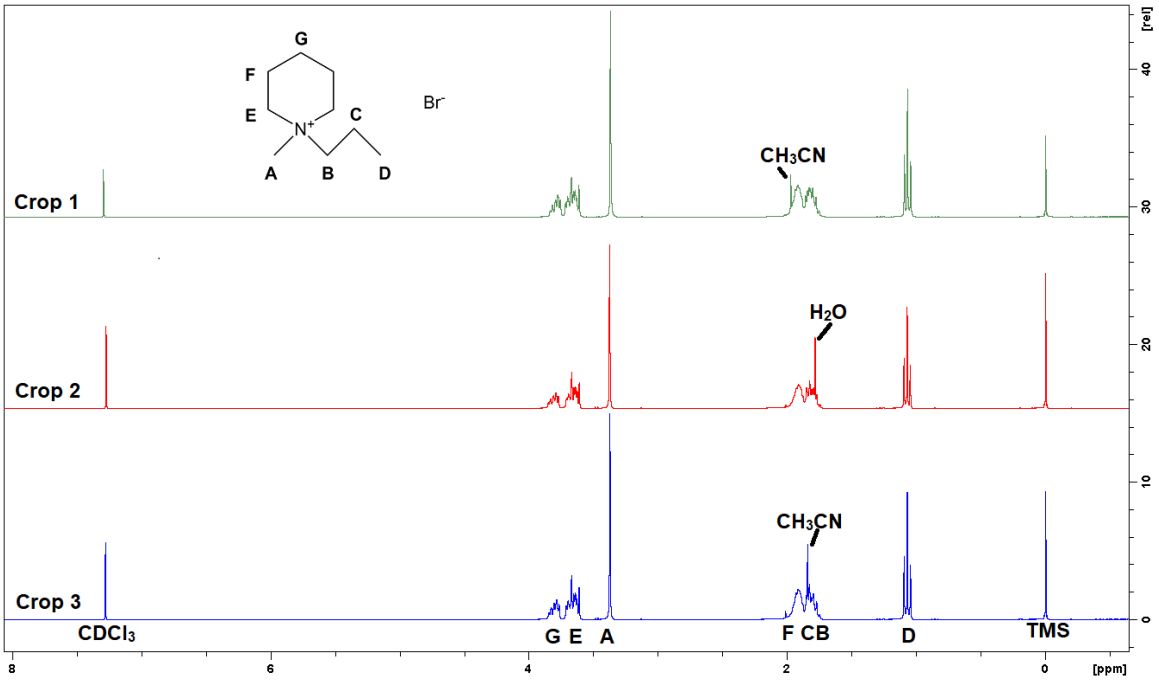

Figure 3.3 ^{1}H NMR spectra of [PP13][Br] in $CDCl_3$ (crops 1-3).

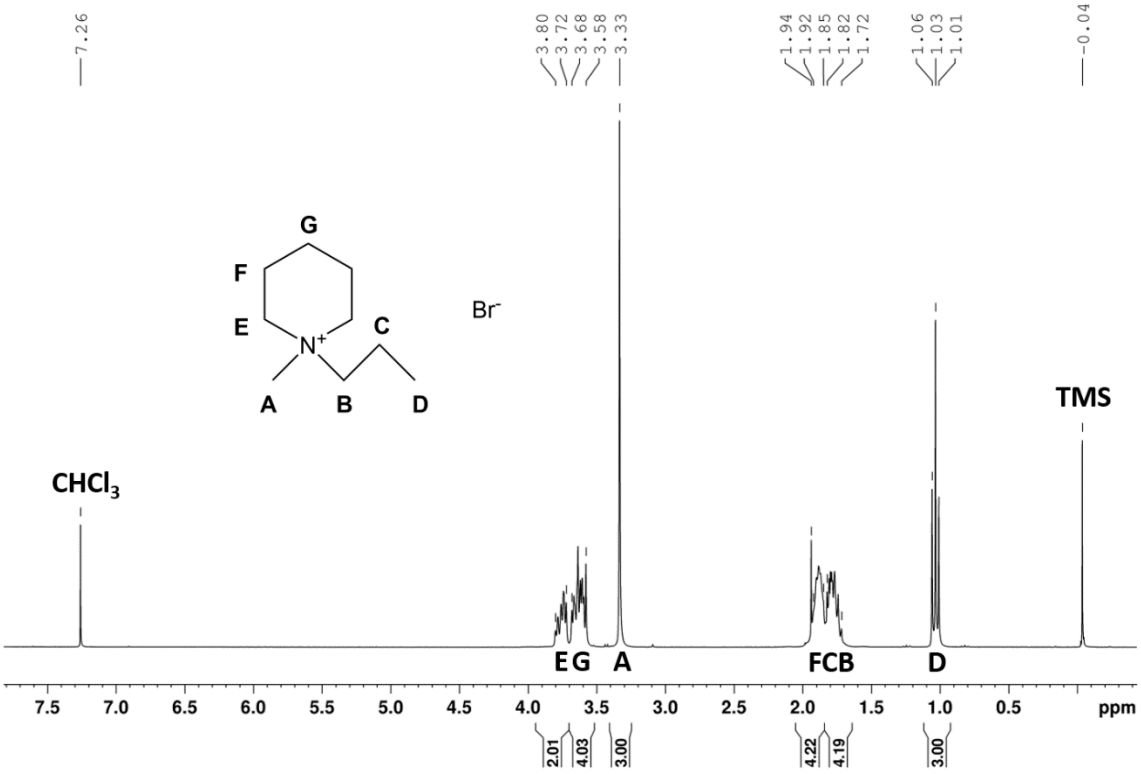

Figure 3.4 ^{1}H NMR spectra of [PP13][Br] in $CDCl_3$

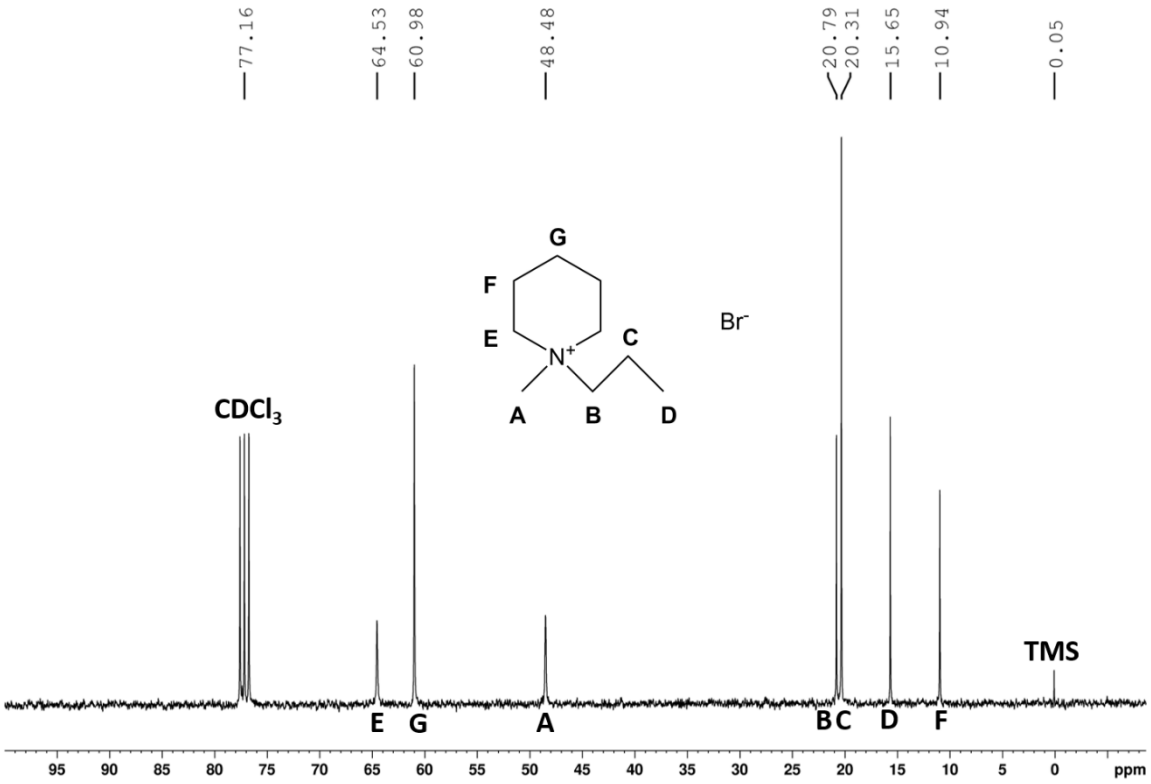

Figure 3.5 ^{13}C NMR spectra of [PP13][Br] in $CDCl_3$.

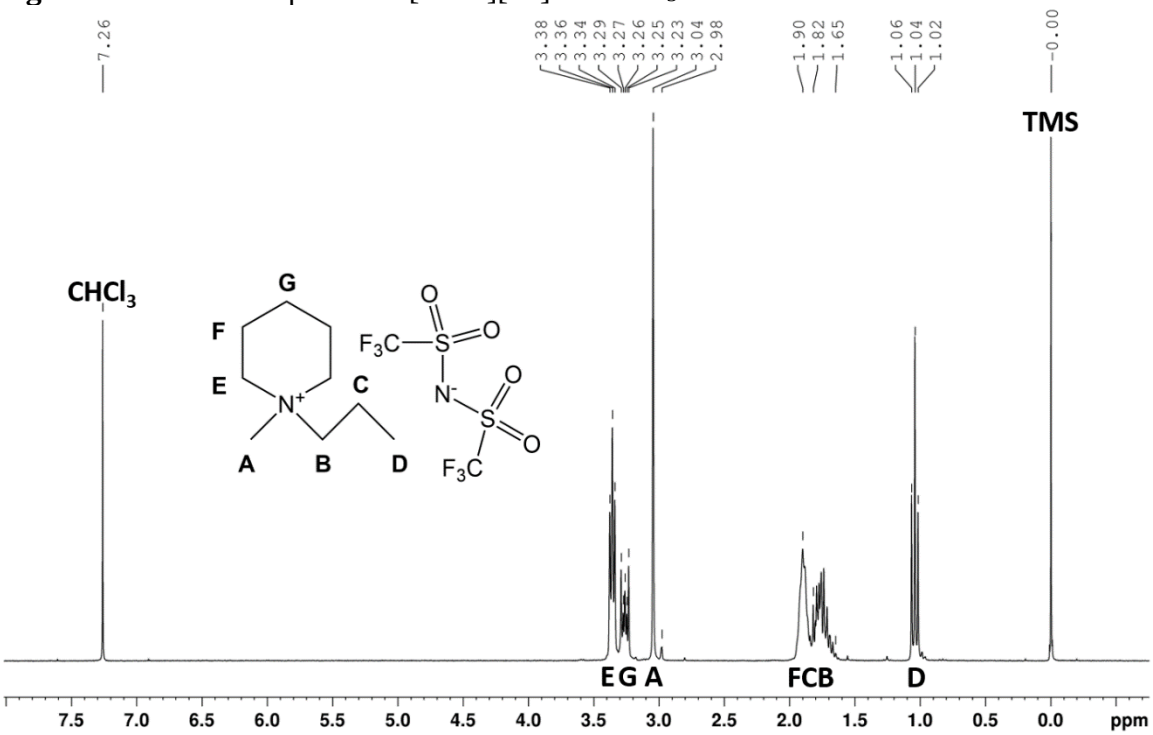

Figure 3.6 ^{1}H NMR spectra of [PP13][TFSI] in $CDCl_3$.

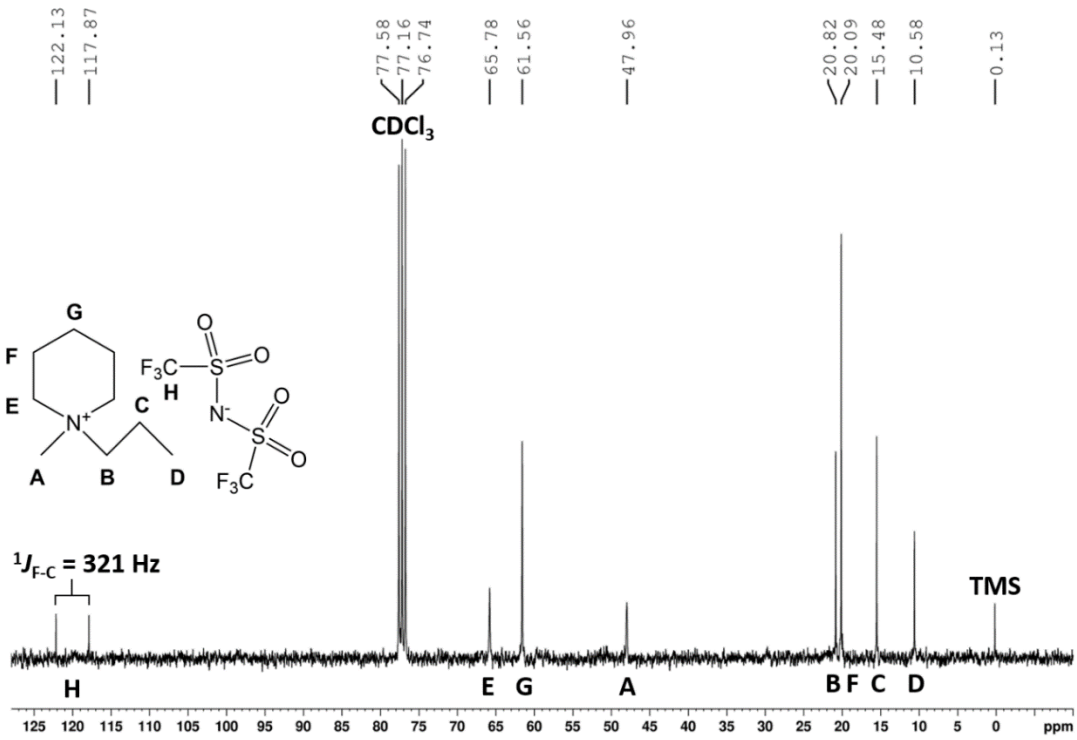

Figure 3.7 ^{13}C NMR spectra of [PP13][TFSI] in $CDCl_3$.

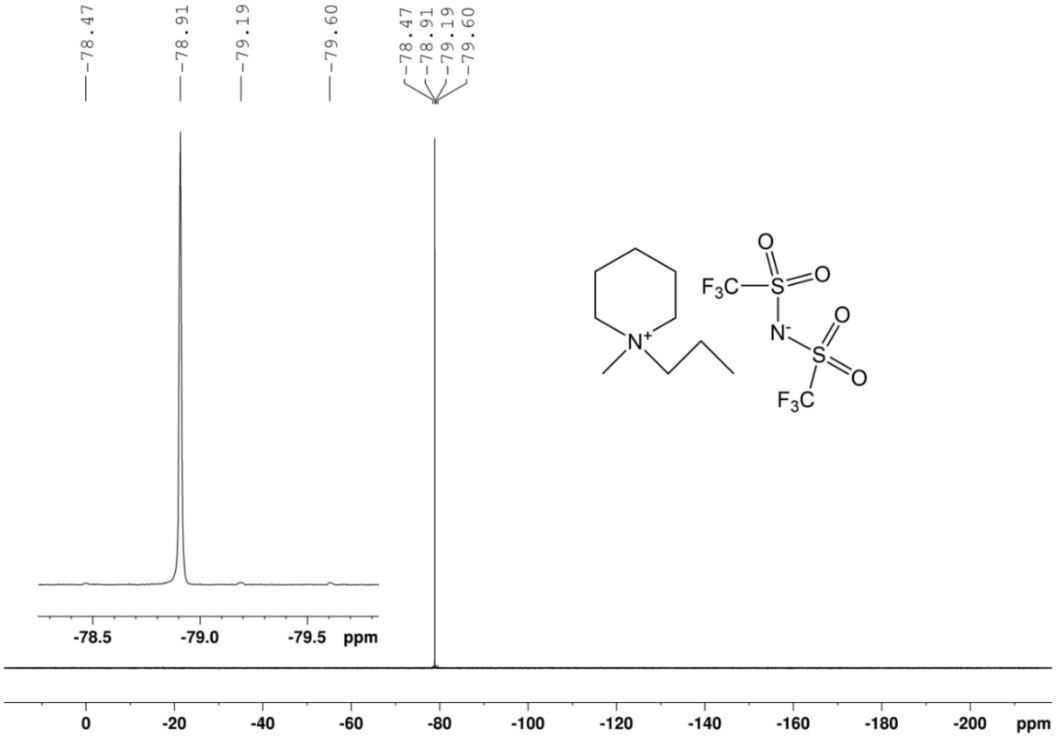

Figure 3.8 ^{19}F NMR spectra of [PP13][TFSI] in $CDCl_3$.

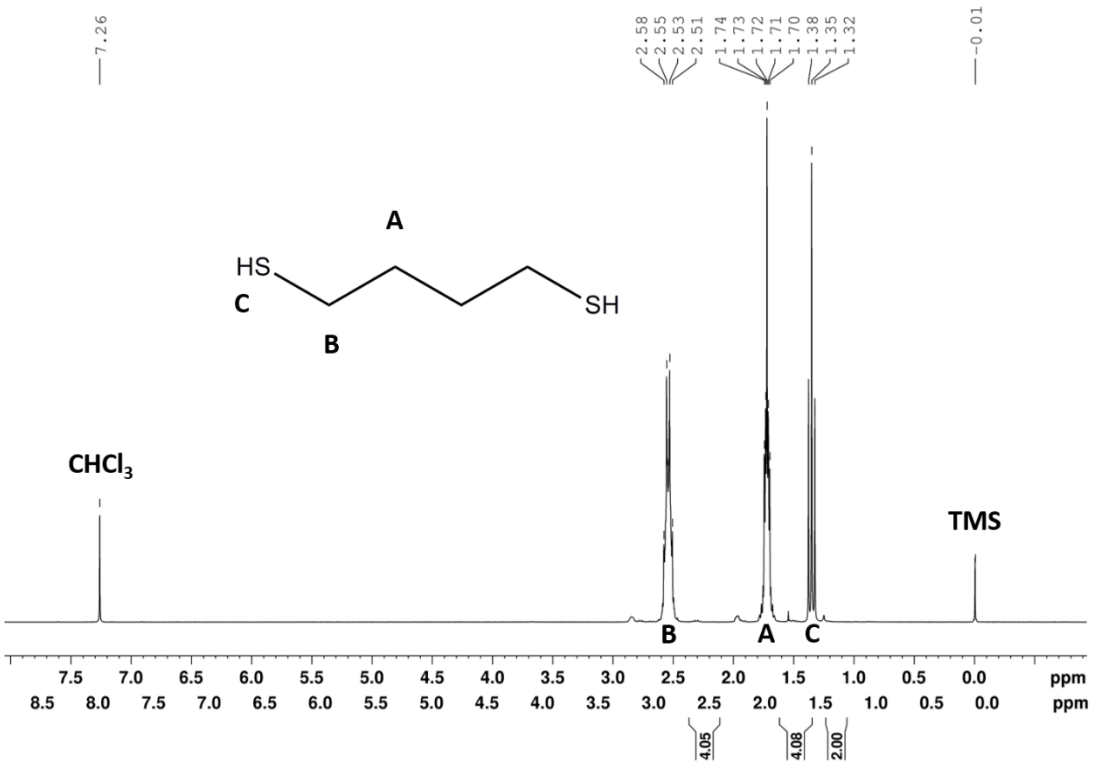

Figure 3.9 ^{1}H NMR spectra of 1,4-butanedithiol in $CDCl_3$.

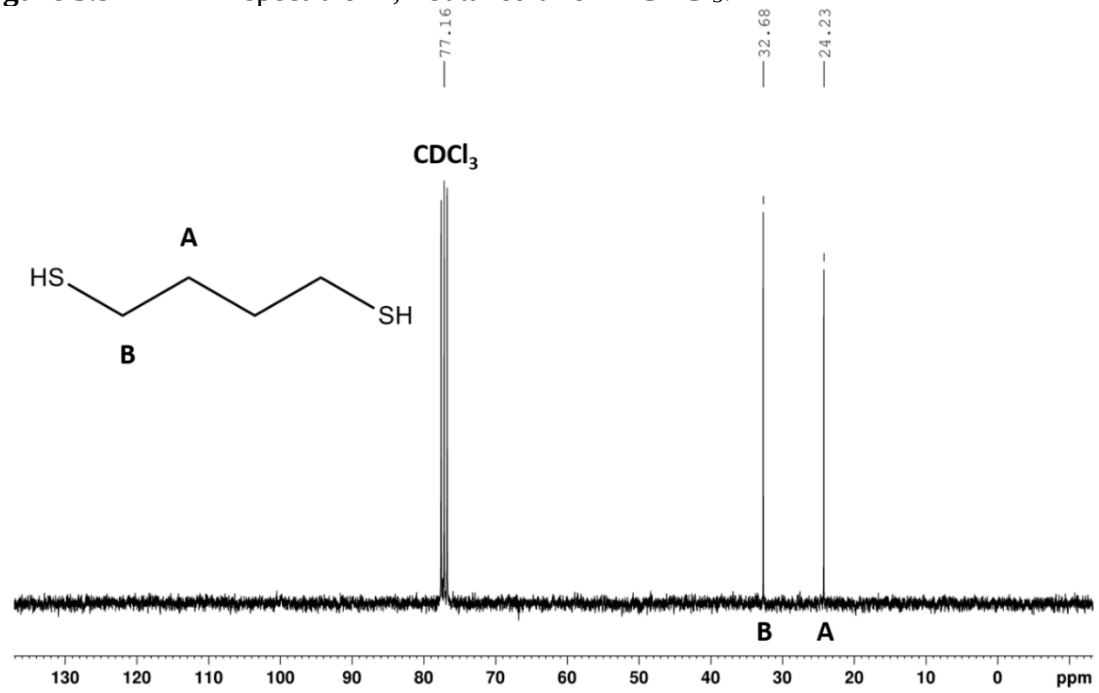

Figure 3.10 ^{13}C NMR spectra of 1,4-butanedithiol in $CDCl_3$.

3.7.4 SEM-EDX Analysis of Amorphous Mo-Containing Deposit

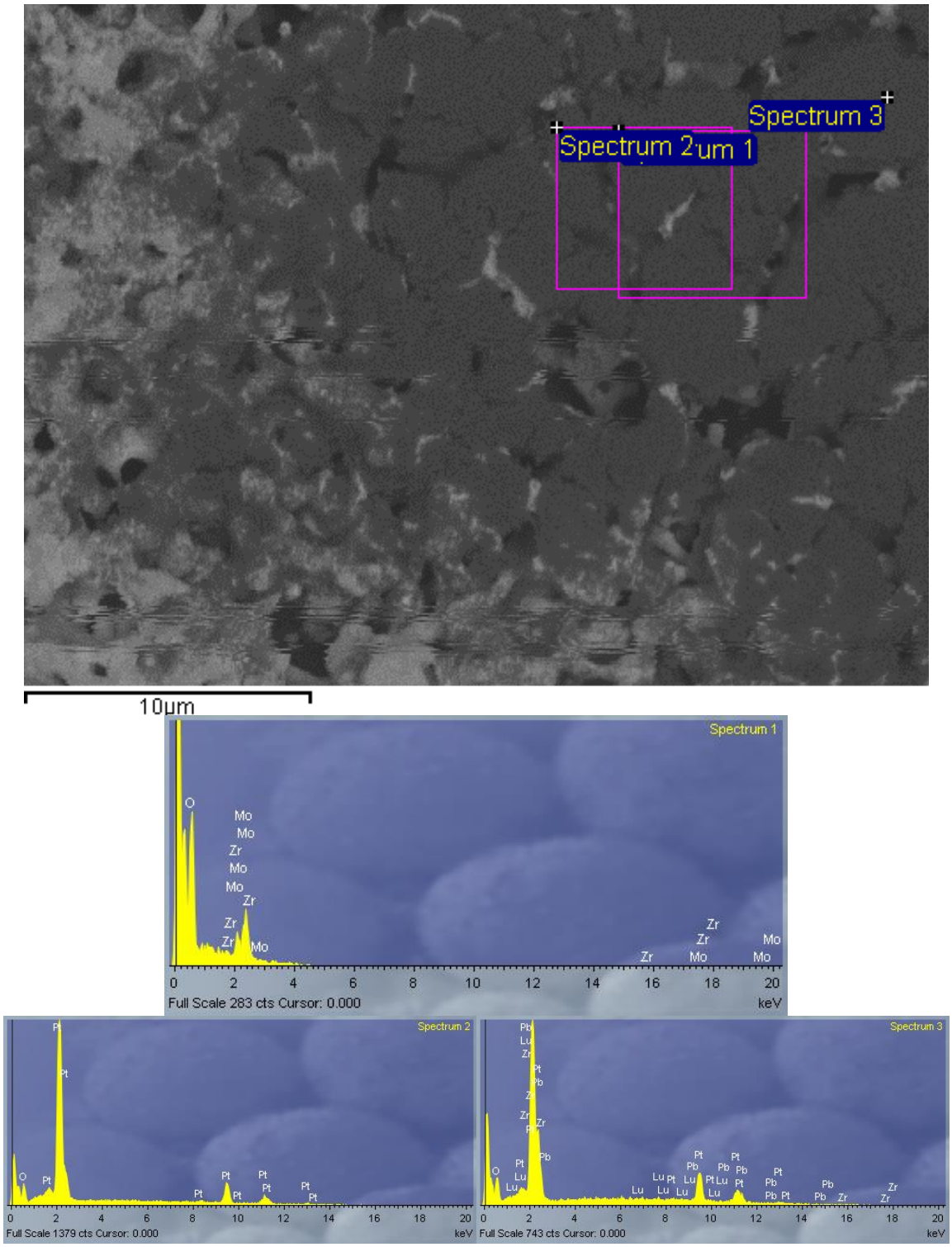

Figure 3.11 SEM-EDX analysis of Pt WE after CV of 0.05 mL **B6a** in 1.5 mL of 0.1 M PP13-TFSI in THF. Lu, Pb, and Zr are thought to be artifacts caused by Mo/Pt overlap.

3.7.5 Synthesis of Ionic Liquid and Precursors

3.7.5.1 Synthesis of PP13-Br cation precursor

In a 500 mL round bottom flask 15 mL 1-bromo propane, 20 mL N-methyl piperidine and 160 mL acetonitrile were heated to 70 °C for 2.5 hours with an air condenser open to air until solid began forming, then nitrogen was supplied for the remainder of the synthesis. At the 4-hour mark, aluminum foil was wrapped around the flask. The next day at the 23-hour mark, the solid had prevented stirring. This was filtered through a coarse glass frit and rinsed with 50 mL acetonitrile in 4 aliquots, transferred to a round bottom flask and dried at 42 °C under vacuum. A second crop was harvested by concentrating the solution until solid formed followed by cooling to 0 °C and filtering/rinsing as per crop 1. The third crop of crystals came from completely drying the filtrate to a yellow paste, triturating with 10 mL acetonitrile, then filtering and rinsed as before. The filtrate was disposed of, and the yield for each crop was 16.2, 8.2, and 4.9 g (44, 22, 13 % yield, total 79%) in succession after drying *in vacuo*. By ^{1}H NMR, each crop was pure PP13-Br with a trace of acetonitrile or water.

3.7.5.2 First Synthesis of PP13-TFSI Ionic Liquid

A solution of PP13-Br (0.9566 g) in 6 mL D.I. H_2O was slowly added to a solution of Li-TFSI (1.2362 g) in 6 mL D.I. H_2O with rapid stirring. And additional 2×2 mL D.I. H_2O was used to completely transfer the PP13-Br solution and left to stir over night. Upon initial addition, the solution of Li-TFSI became cloudy and translucent. Ceasing stirring allowed a biphasic layer to form with PP13-TFSI on the bottom with an aqueous top layer, which was decanted off. Rinsing the bottom layer with 3×5 mL D.I. H_2O with ~10 min stirring, settling, and decanting each time was followed by dissolution of PP13-TFSI in 6 mL DCM which was similarly rinsed with 3×5 mL D.I. H_2O. The next day, the organic

layer was dried over $MgSO_4$ and filtered through a diatomaceous earth pipette filter, rinsing 2× with ~3 mL $MgSO_4$ dried DCM. The final solution was dried *in vacuo* at 105 °C for 14 hours and the ionic liquid was pure by NMR, however when water was present, a shift was noticed clearly by ^{1}H NMR spectroscopy for the two -C*H*$_3$ groups with the shifted peaks disappearing with water loss. This indicates a strong interaction such as some sort of clustering or hydrogen bonding occurring between the ionic liquid and water.

3.7.5.3 Second Synthesis of PP13-TFSI Ionic Liquid

A 5.4601 g PP13-Br in 15 mL H_2O solution was added to a 7.0475g LiTFSI in 20 mL H_2O solution in a 50 mL Erlenmeyer flask and rinsed with 3×5 mL totaling 50 mL. Stirring overnight was followed by quick settling of the layers the next day. Decanting the water was followed by addition of 15 mL $CHCl_3$ was added to extract remaining product and was separated with a pipette to the ionic liquid bottom fraction. Triplicate washing of the organic fraction with 20 mL water with stirring, settling and decanting in between was followed by drying over $MgSO_4$ for 20 minutes and filtering through diatomaceous Earth with 3×3 mL $CHCl_3$ rinses and the combined solvent was removed *in vacuo* and heated the remaining thick colorless oil was heated to o 100 °C in two separate vials. One vial was dropped in the oil bath, losing the product. The remaining vial of PP13-TFSI when dried contained 0.1 eq H_2O and weighed 4.5g.

3.7.5.4 Third Synthesis of PP13-TFSI Ionic Liquid

In a 125 mL Erlenmeyer flask 9.818 g PP13-Br dissolved in 60 mL H_2O had a solution of 12.665 g Li-TFSI in 20 mL H_2O added followed by 20 mL used to rinse the beaker 3 times into the reaction flask. Stirring for 1.5 hours, then add 20 mL $CHCl_3$ and rapidly stir biphasic mixture for 2 minutes, followed by settling until no more visible tiny bubbles of $CHCl_3$ were suspended in the water layer. Decanting the water was followed

with triplicate washing the organic layer with three 25 mL portions. The organic phase was transferred to a separatory funnel with an additional 75 mL water, the organic phase washed once more and separated, dried over $MgSO_4$ for 20 min and filtered through diatomaceous Earth with 3×5 mL $CHCl_3$ rinses and the solvent was removed *in vacuo* and heated to 105 °C for 12 hours and store in a glovebox, total mass = 13.98 g (75 % yield)

3.7.5.5 Fourth Synthesis of PP13-TFSI Ionic Liquid

Two 10 mL water solutions were prepared containing 3.9630 g Li-TFSI and 3.1253 g PP13-Br. The PP13-Br solution was then added to the Li-TFSI solution, followed by 5 mL water to rinse. After 1.5 hours the biphasic mixture was allowed to settle, the aqueous phase was decanted, and the ionic liquid was washed 2× with 5 mL water by stirring for 0.5 hours. All three aqueous decantation's were combined. The PP13-TFSI had 2×10 mL DCM added transferring to a separatory funnel with the organic layer being separated into anhydrous $MgSO_4$ for further drying. Filtration through diatomaceous Earth into a 20 mL scintillation vial afforded 4.3161 g of PP13-TFSI after drying overnight in a vacuum desiccator. All glassware and the aqueous phase were extracted with an additional 50 mL, drying over the same $MgSO_4$ after separation from the aqueous phase. Filtration through a cotton plug into a round bottom flask was followed by solvent removal *in vacuo*, with a final transfer and drying *in vacuo* in a 20 mL scintillation vial using an additional 2×3 mL DCM. Drying overnight in a vacuum desiccator afforded a second crop of PP13-TFSI weighing 1.4327 g. Combined yield = 98% (1st = 73 %, 2nd = 25%)

3.7.6 Crystallography Table and Additional Refinement Details

Table 3.1 Data derived from single crystal X-ray diffraction of crystals of compounds **1**-**5** from the work in Chapter 3.

Compound reference	Compound **1**	Compound **2**	Compound **3**	Compound **4**	Compound **5**
Chemical formula	$C_4H_{10}MoO_6$	$C_8H_{18}Mo_2O_{10}$•C_4H_8O	$C_{16}H_{36}Mo_4O_{20}$	$C_{24}H_{54}Mo_8O_{32}$•2($C_2H_6O_2$)	$[Mo_6O_{19}]$•2[$C_9H_{20}N$]
Formula Mass	250.06	538.21	932.21	1746.32	1164.16
Crystal system	Tetragonal	Orthorhombic	Orthorhombic	Triclinic	Monoclinic
a/Å	9.46450(10)	16.7363(3)	34.2851(19)	8.5318(4)	9.4347(8)
b/Å	9.46450(10)	24.6210(5)	9.7131(5)	11.0284(5)	16.0288(12)
c/Å	17.3160(4)	8.8062(2)	8.4881(4)	14.5245(7)	10.9136(9)
α/°	90	90	90	81.706(2)	90
β/°	90	90	90	77.862(2)	101.838(3)
γ/°	90	90	90	69.992(2)	90
Unit cell volume/Å^3	1551.11(5)	3628.72(13)	2826.7(3)	1251.55(10)	1615.3(2)
Temperature/K	100.0	125.0	125	125.0	125.0
Space group	$P4_1$	$Fdd2$	$Pna2_1$	$P\bar{1}$	$P2_1/n$
No. of formula units per unit cell, *Z*	8	8	4	1	2
Radiation type	MoKα	MoKα	MoKα	MoKα	MoKα
Absorption coefficient, μ/mm^{-1}	1.675	1.436	1.819	2.040	2.339
No. of reflections measured	110585	39690	281817	126602	42434
No. of independent reflections	12760	7050	13709	10104	4095
R_{int}	0.0334	0.0568	0.0390	0.0407	0.0348
Final R_1 values ($I > 2\sigma(I)$)	0.0206	0.0309	0.0655	0.0219	0.0275
Final $wR(F^2)$ values ($I > 2\sigma(I)$)	0.0509	0.0467	0.1341	0.0528	0.0626
Final R_1 values (all data)	0.0221	0.0485	0.0683	0.0267	0.0293
Final $wR(F^2)$ values (all data)	0.0519	0.0508	0.1353	0.0554	0.0635

Compound **1** has four hydrogen bonding interactions between mono-deprotonated ethylene glycol ligands The asymmetric unit includes the O6-H6…O6 H-bond, while hydrogen bonds also occur between O12-H12…O11 across the symmetry element +Y,2-X,-0.25+Z, O4-H4…O3 across 2-X,1-Y,0.5+Z, and O10-H10…O5 across 2-X,1-Y,0.5+Z. Compound **2** has one intramolecular hydrogen bond between O6-H6…O3 across the symmetry element 0.75-X,0.25+Y,-0.25+Z. Compound **3** has two disordered ethylene glycol units in a 62:38 and 65:35 ratio. Compound **3** has five hydrogen bonding interactions with one (O14B-H14D…O20) across the symmetry element 1-X,1-Y,-0.5+Z. The other four interactions occur between O5-H5…O4, O14A-H14C…O15, O17-H17…O11, and O1B-H1B…O7. Compound **4** has one disorder ethylene glycol methylene fragment in a 72:38 ratio. Co-crystallized ethylene glycol solvent participates extensively in hydrogen

bonding within **4**. Intermolecular bonding occurs first from O13-H13…O17 from the compound to the ethylene glycol, and the same hydroxy group donates back to the compound via O17-H17…O12 with further intramolecular bonding from O12-H12…O8. The other end of the ethylene glycol is hydrogen bound to an adjacent molecule of **4** as O18-H18…O4 across the symmetry element -1+X,1+Y,+Z. Additional intramolecular hydrogen bonding between each molecule of **4** from O16-H16…O3 across 1-X,1-Y,1-Z exists, holding the symmetry equivalent halves of the structure together among other bonds. Compound **5** only experiences minor two component disorder in an 83:17 ratio within the quaternary N-methyl-N-propylpiperidinium cations with the minor component's methyl group shifting slightly closer to the $[Mo_6O_{19}]^{-2}$ anion.

4. 4.7 Supplementary Information – Chapter 4

4.7.1 NMR Spectroscopy of Compounds 2-6

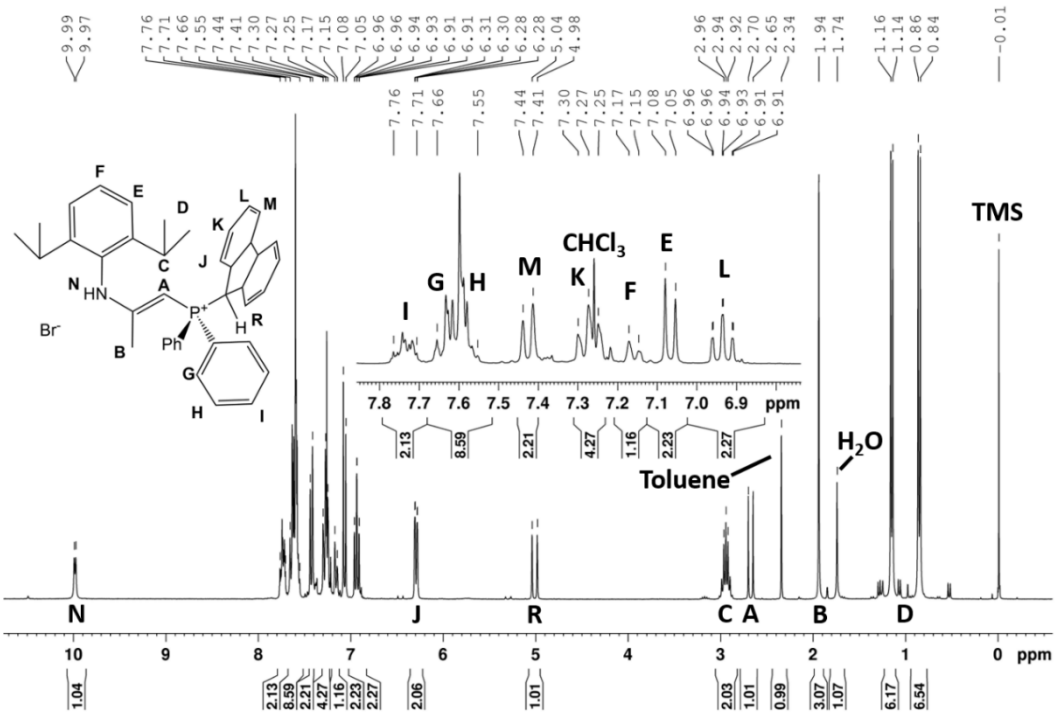

Figure 4.1 ^{1}H NMR spectrum (300 MHz) of compound **2** in $CDCl_3$.

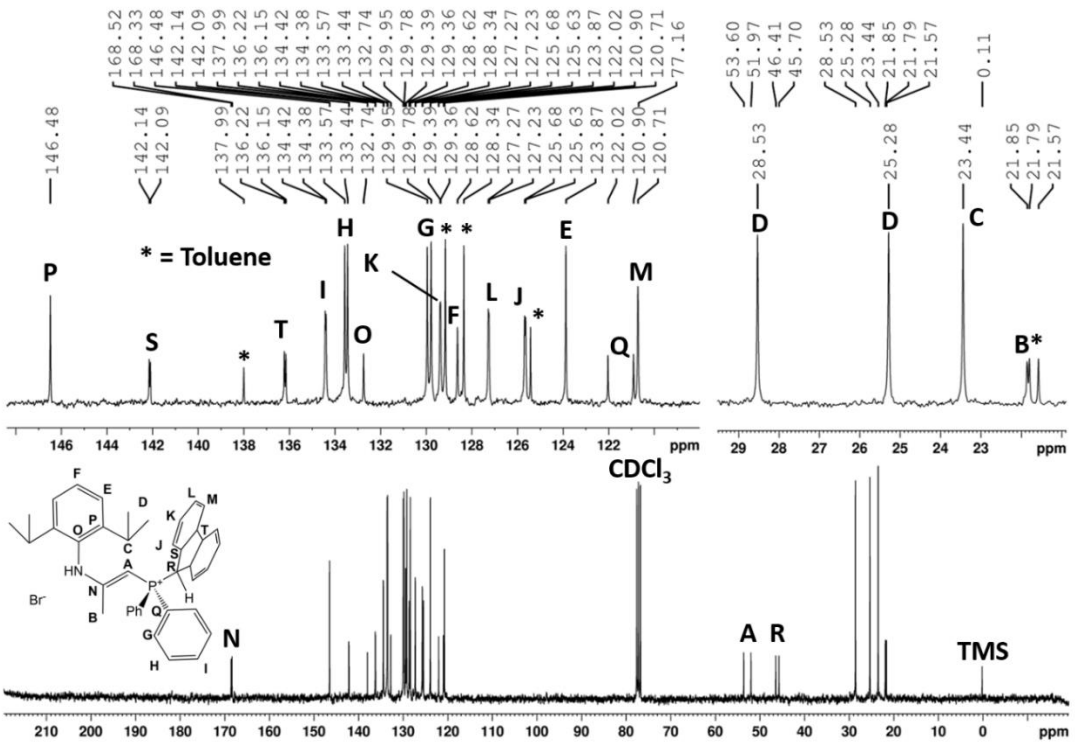

Figure 4.2 ^{13}C NMR spectrum (75 MHz) of compound **2** in $CDCl_3$.

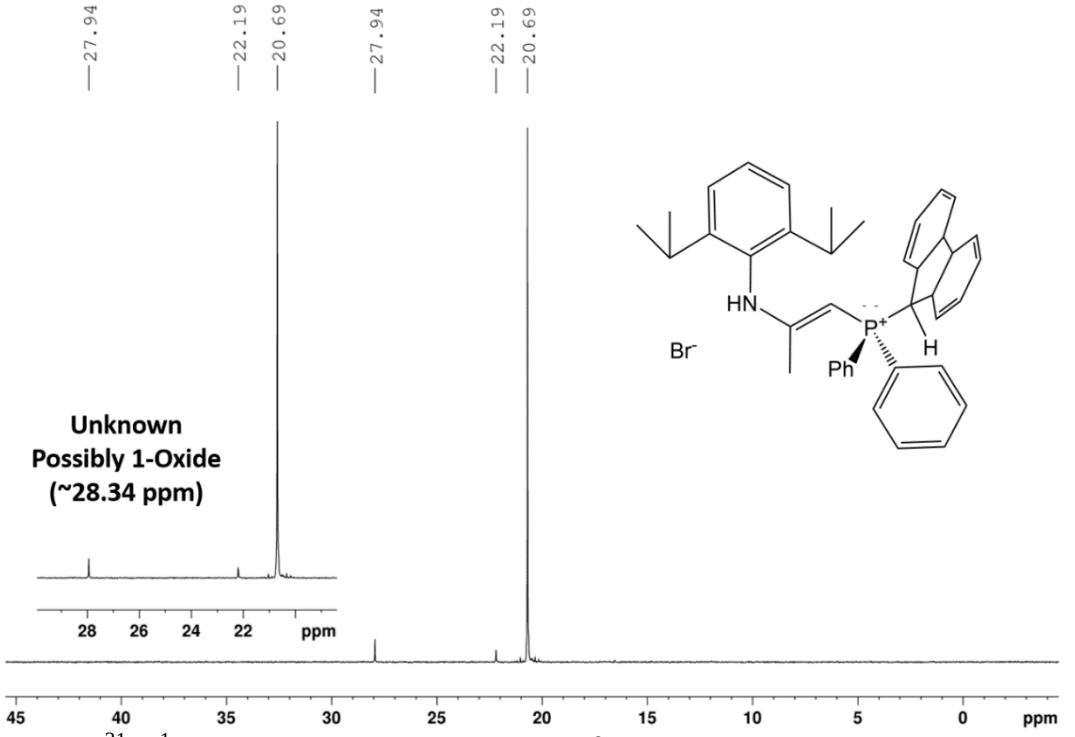

Figure 4.3 $^{31}P\{^{1}H\}$ NMR spectrum (121 MHz) of compound **2** in $CDCl_3$.

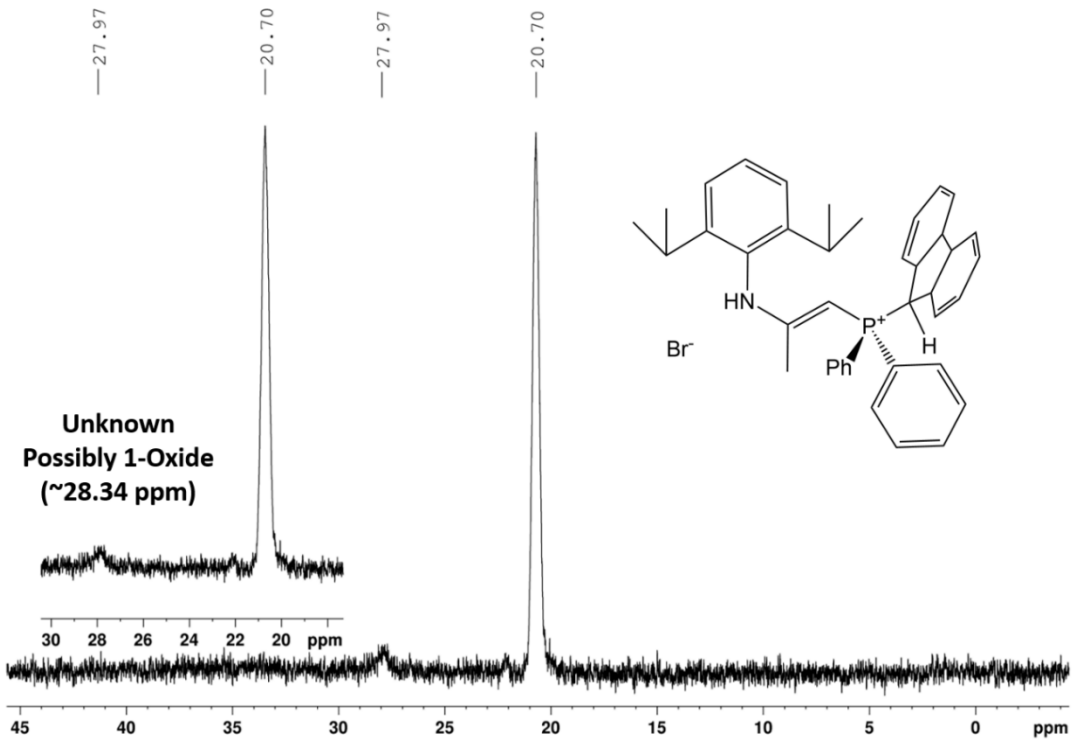

Figure 4.4 ^{31}P NMR spectrum (121 MHz) of compound **2** in $CDCl_3$.

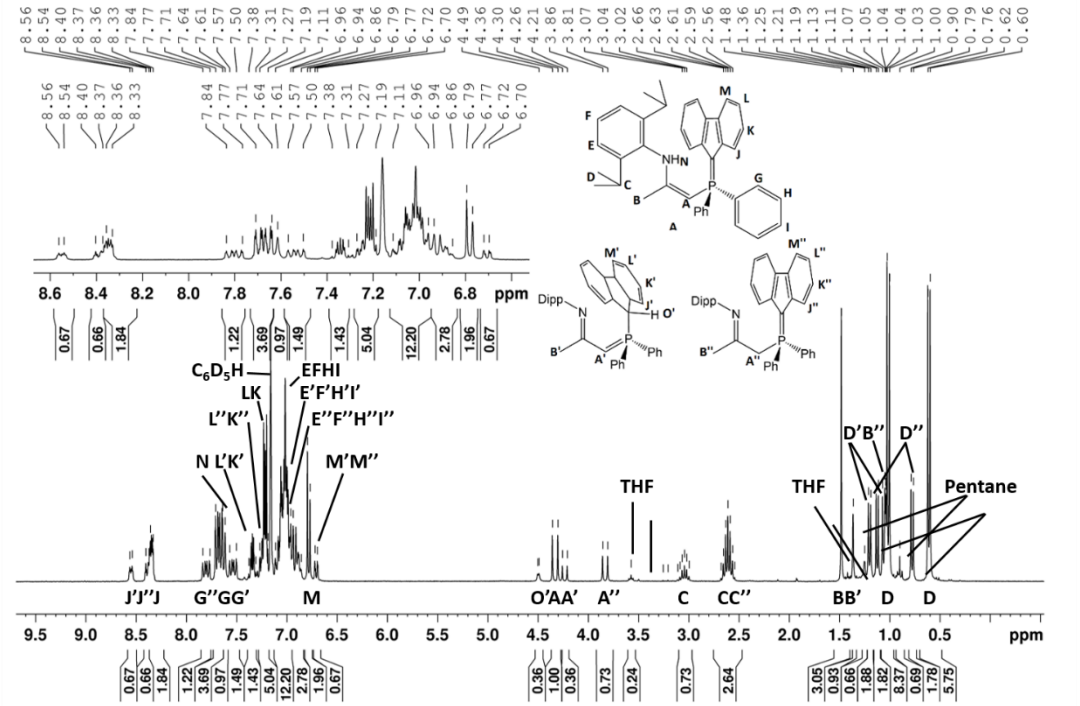

Figure 4.5 ^{1}H NMR spectrum (300 MHz) of compound **3** in C_6D_6.

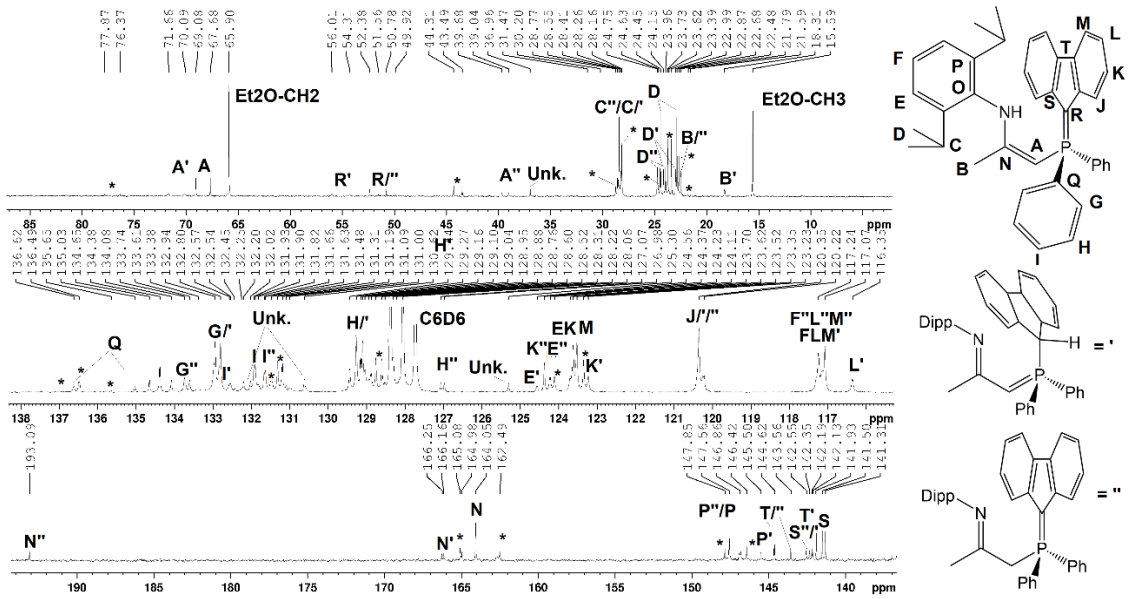

Figure 4.6 ^{13}C NMR spectrum (75 MHz) of compound **3** in C_6D_6. Each * indicates **1**-(**oxide**) impurity.

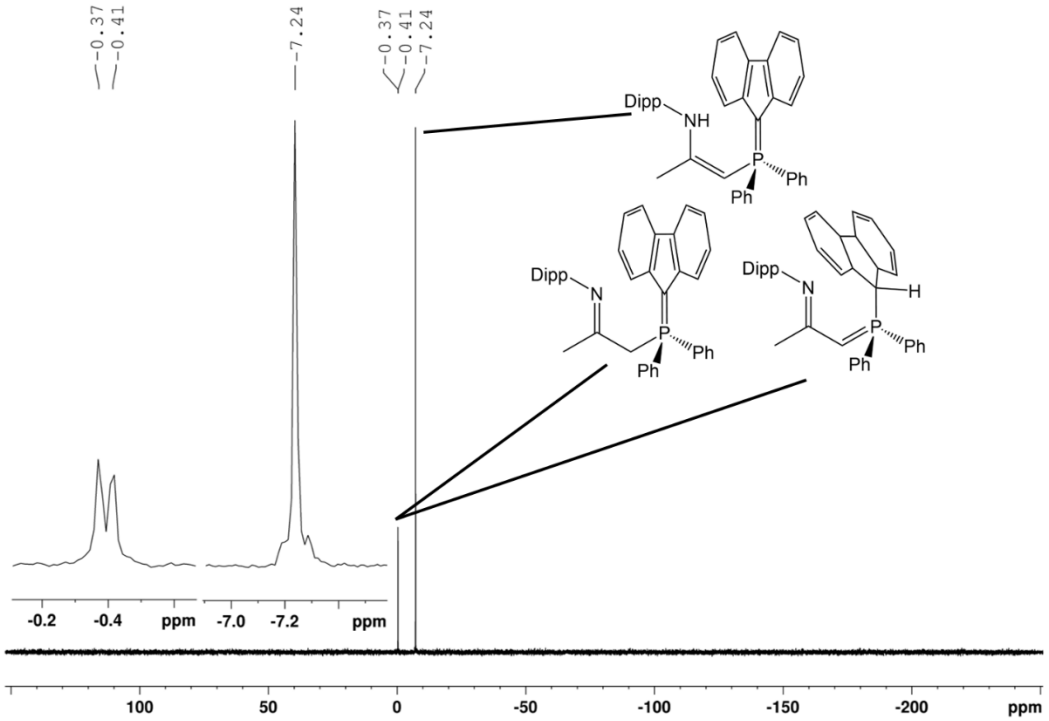

Figure 4.7 $^{31}P\{^1H\}$ NMR spectrum (121 MHz) of compound **3** in C_6D_6.

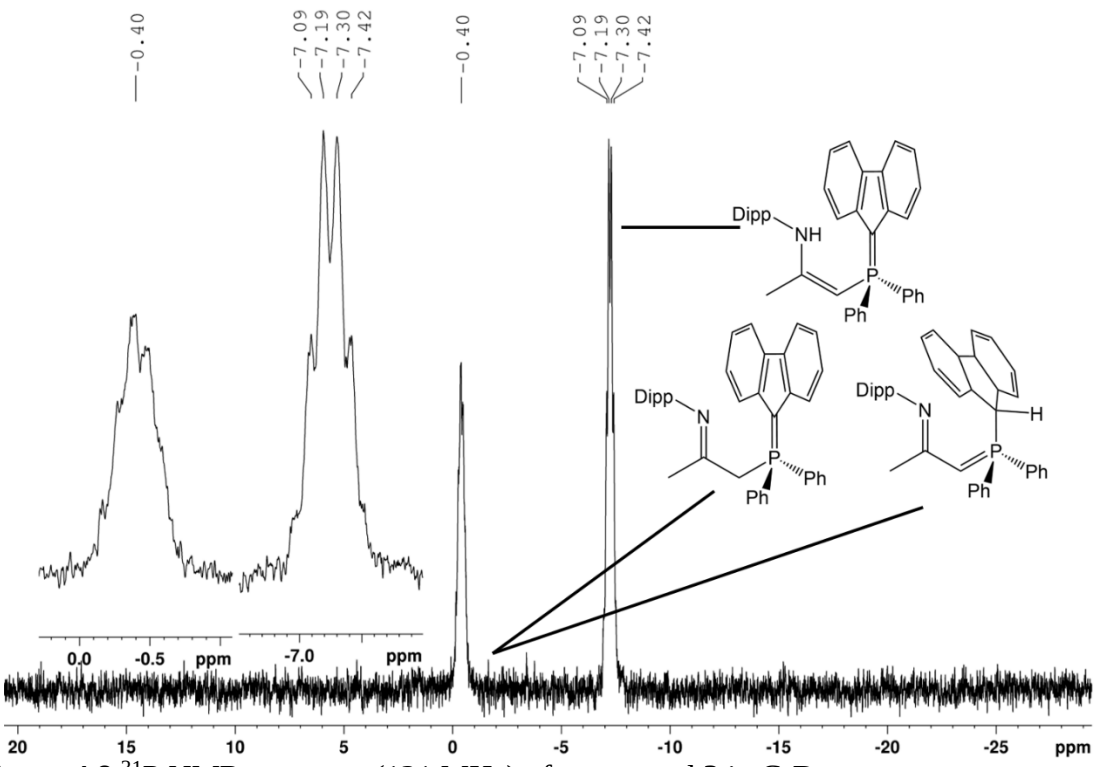

Figure 4.8 ^{31}P NMR spectrum (121 MHz) of compound **3** in C_6D_6.

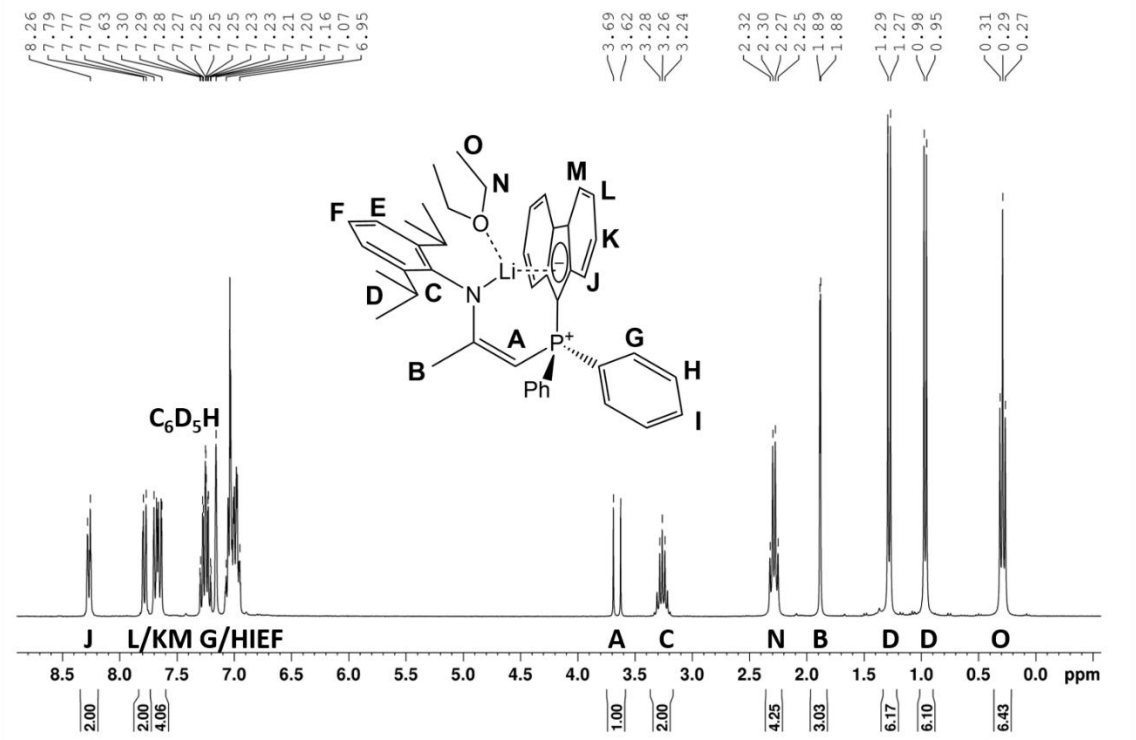

Figure 4.9 ^{1}H NMR spectrum (300 MHz) of compound **4a** in C_6D_6.

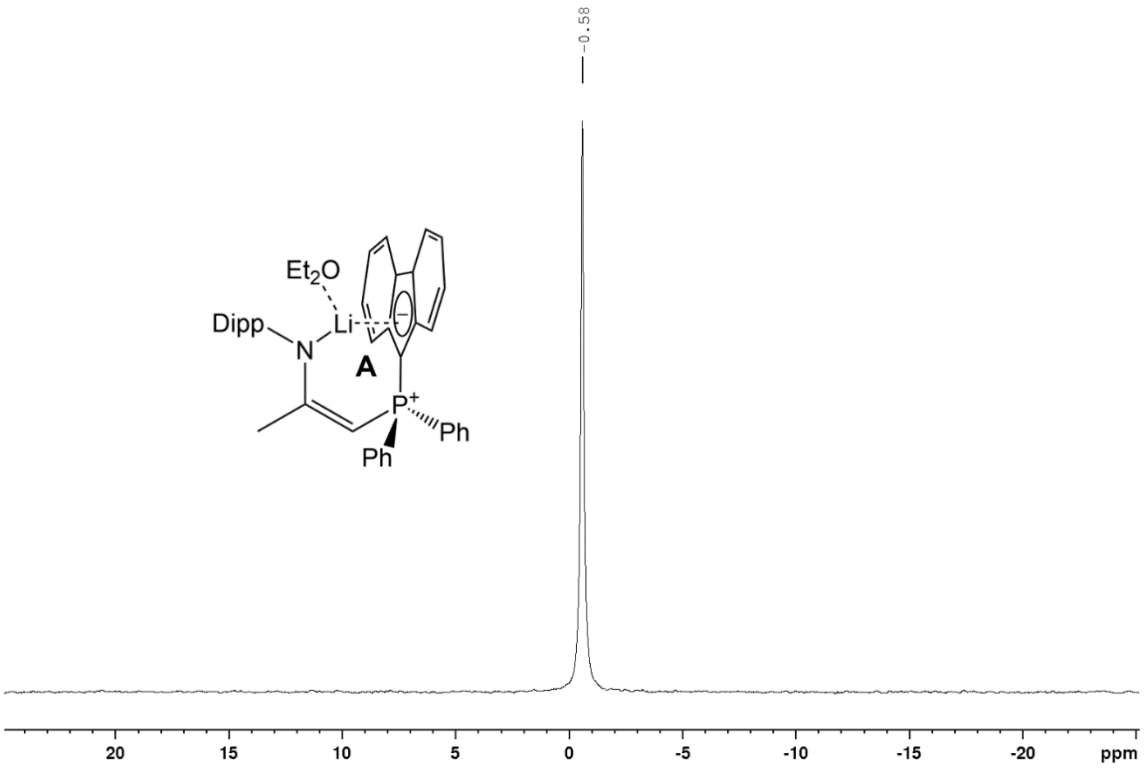

Figure 4.10 ^{7}Li NMR spectrum (117 MHz) of compound **4a** in C_6D_6.

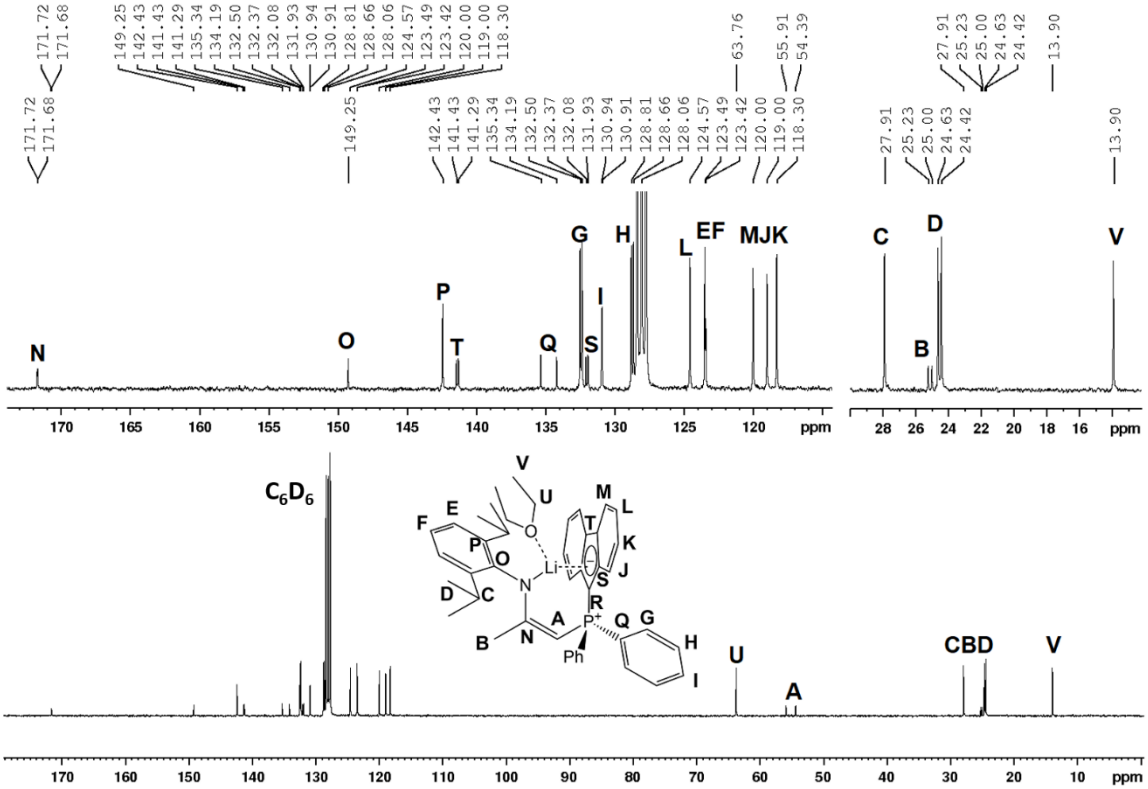

Figure 4.11 ^{13}C NMR spectrum (75 MHz) of compound **4a** in C_6D_6.

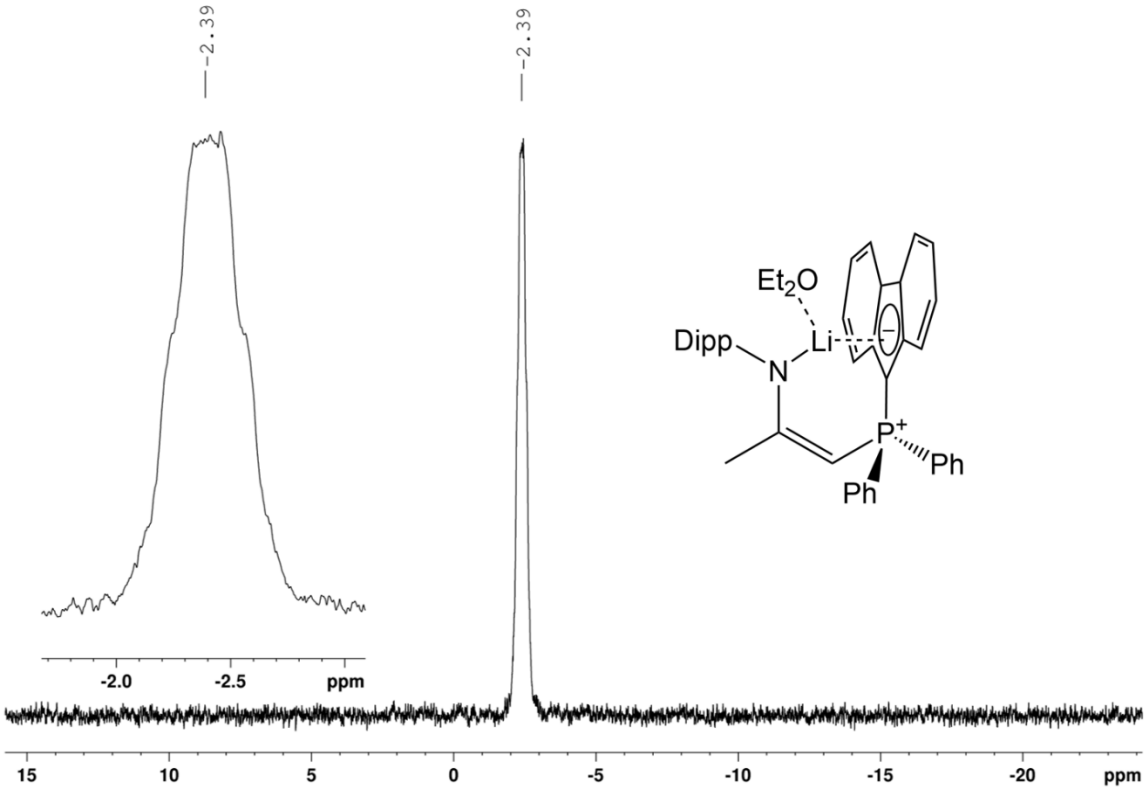

Figure 4.12 ^{31}P NMR spectrum (121 MHz) of compound **4a** in C_6D_6.

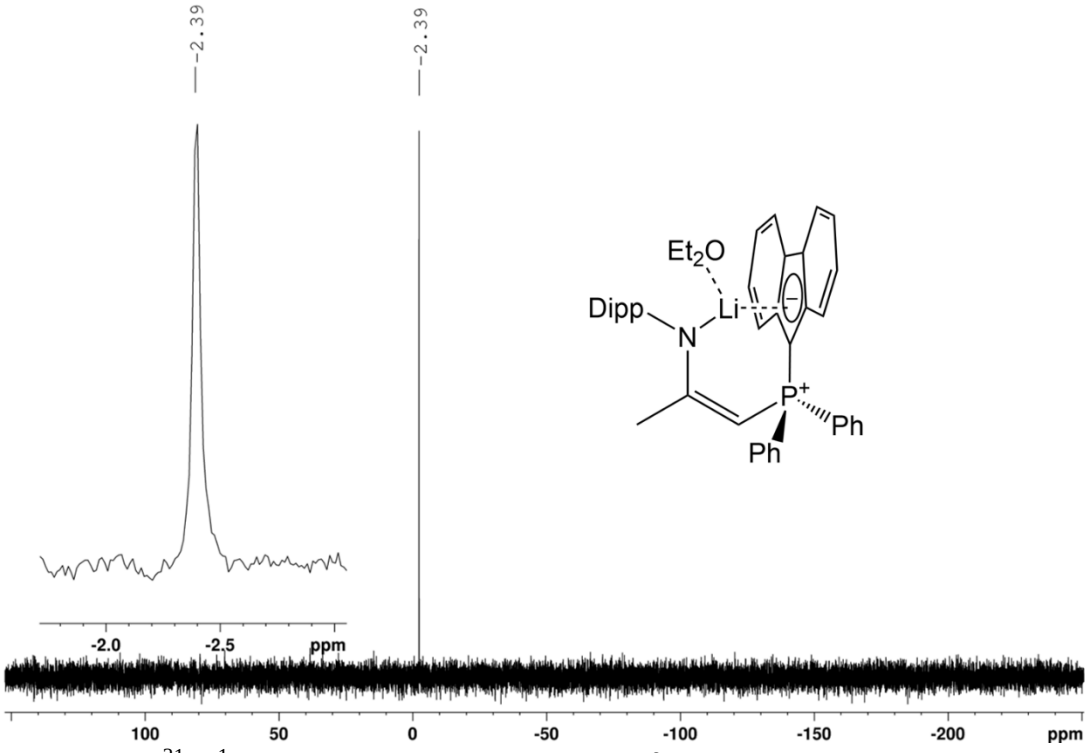

Figure 4.13 $^{31}P\{^{1}H\}$ NMR spectrum (121 MHz) of compound **4a** in C_6D_6.

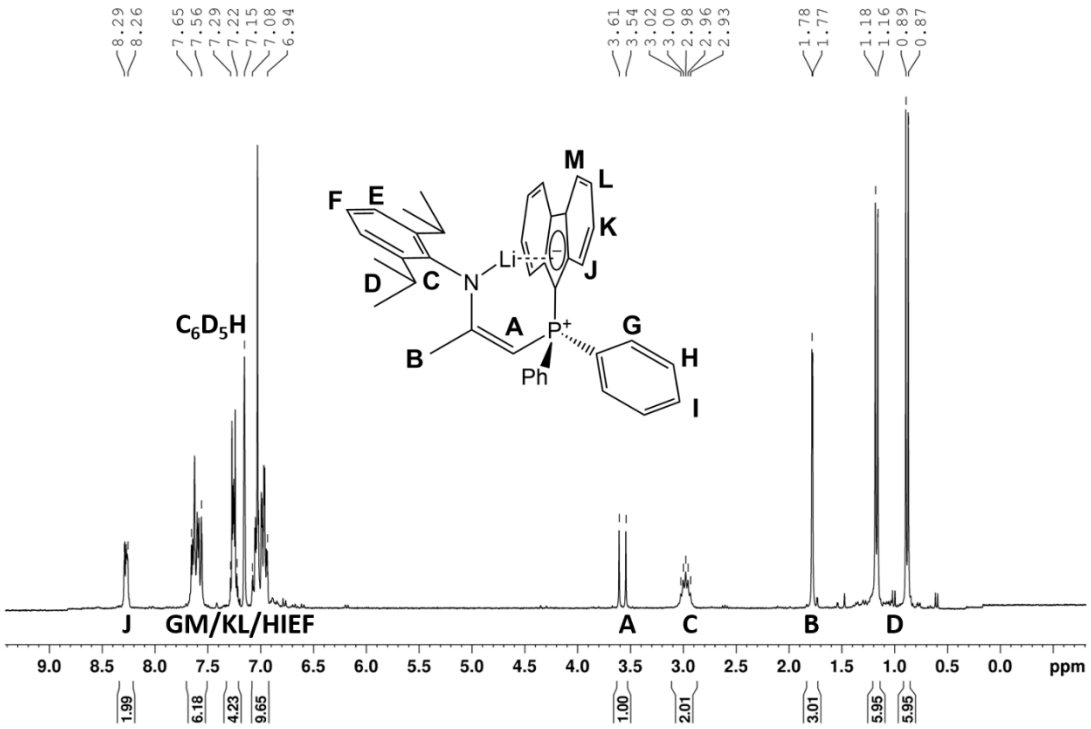

Figure 4.14 ^{1}H NMR spectrum (300 MHz) of compound **4b** in C_6D_6.

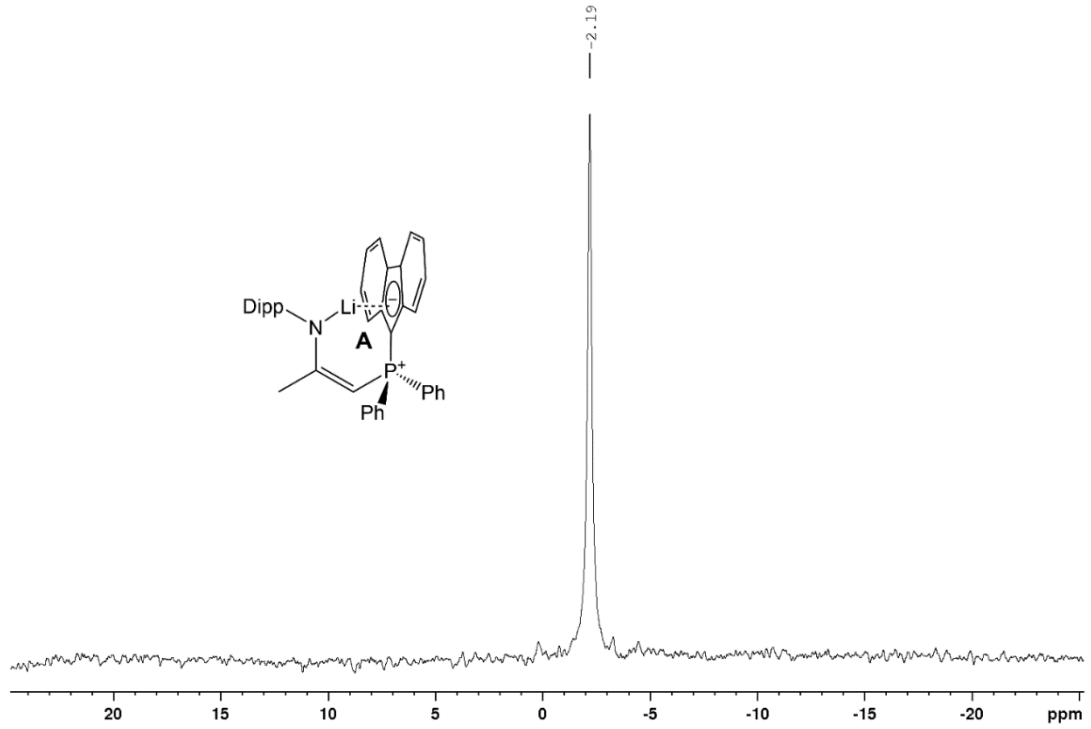

Figure 4.15 ^{7}Li NMR spectrum (117 MHz) of compound **4b** in C_6D_6.

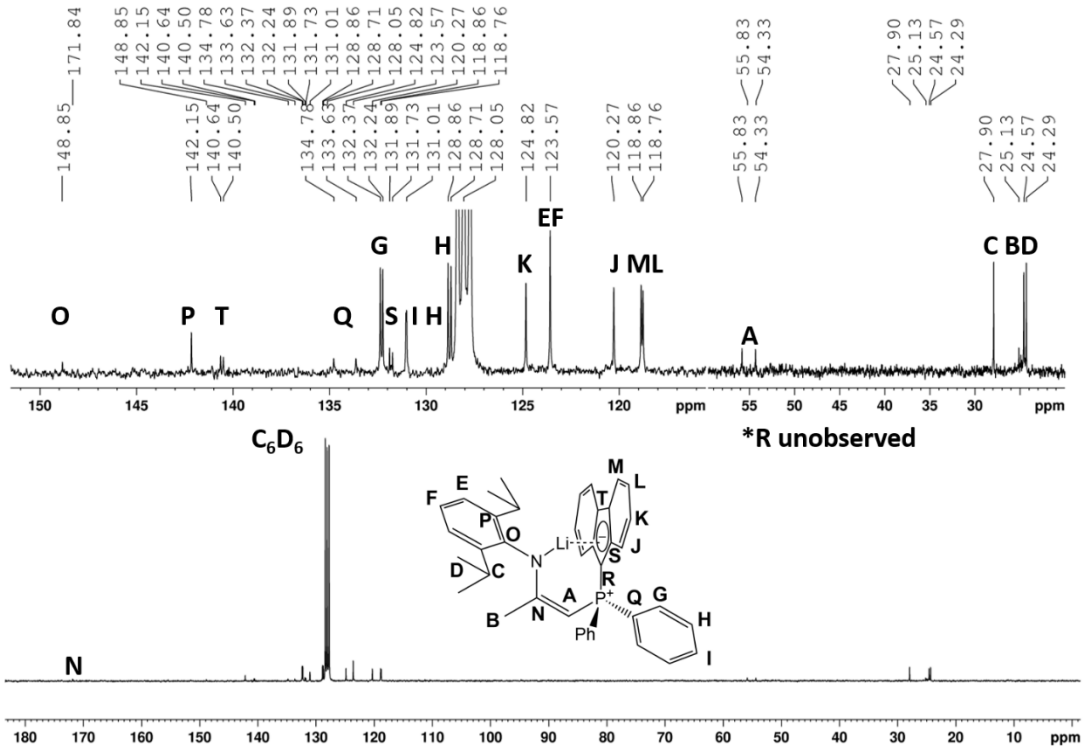

Figure 4.16 ^{13}C NMR spectrum (75 MHz) of compound **4b** in C_6D_6.

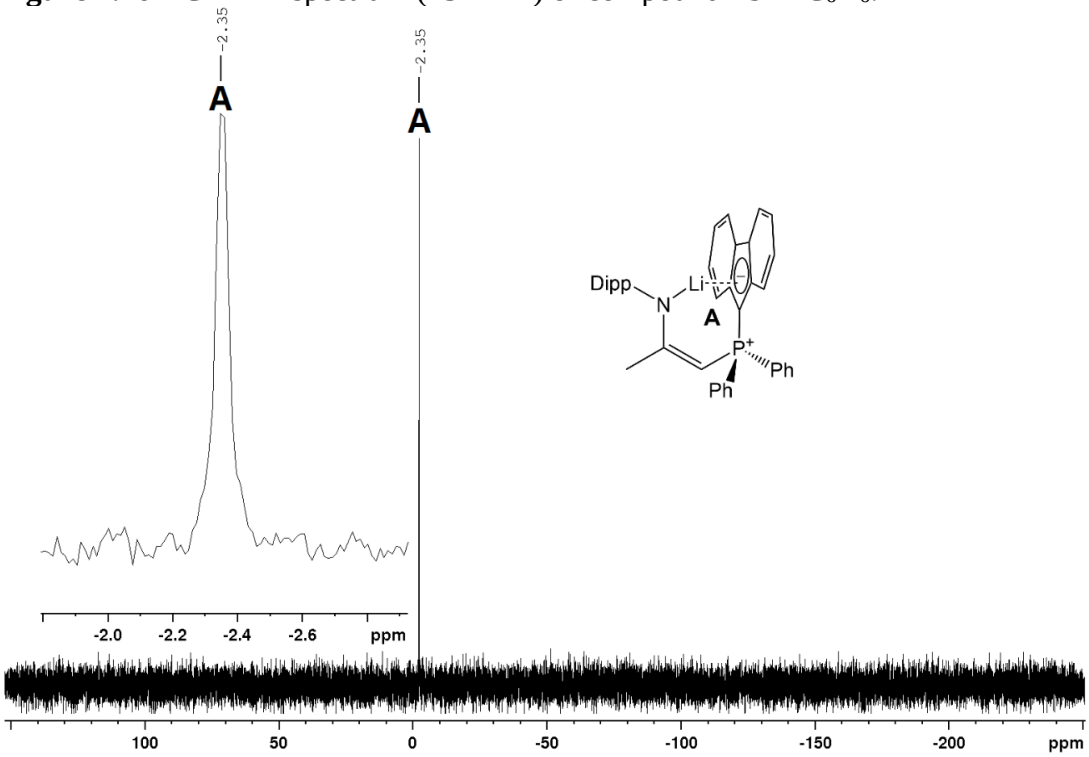

Figure 4.17 $^{31}P\{^{1}H\}$ NMR spectrum (121 MHz) of compound **4b** in C_6D_6.

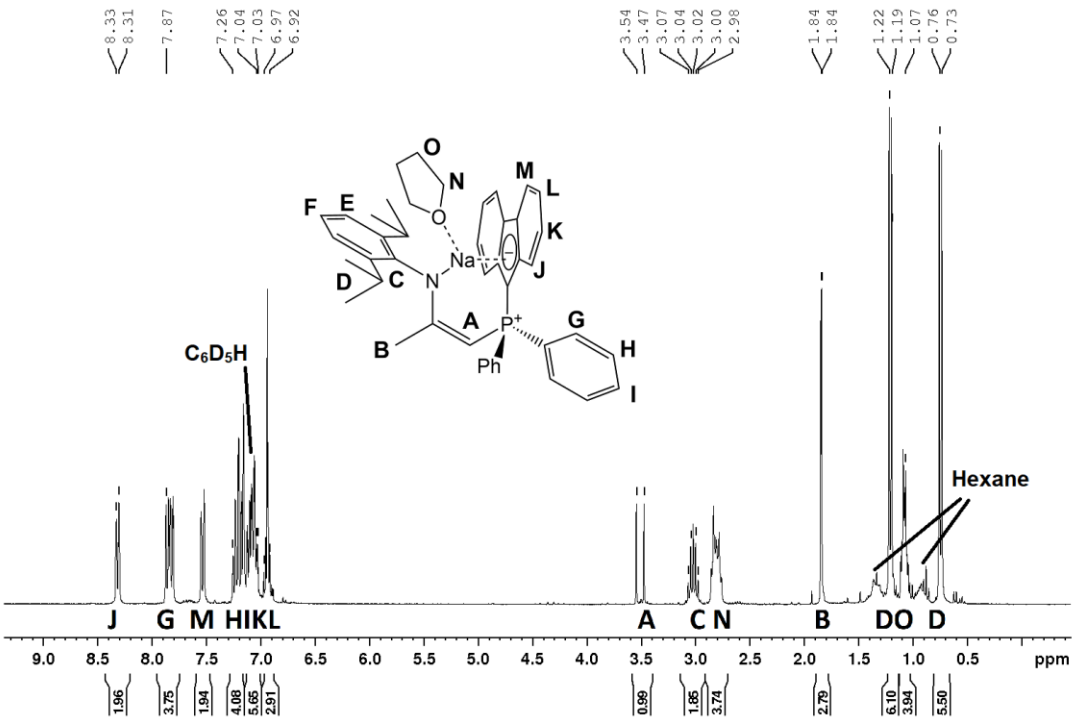

Figure 4.18 ^{1}H NMR spectrum (300 MHz) of compound **5** in C_6D_6.

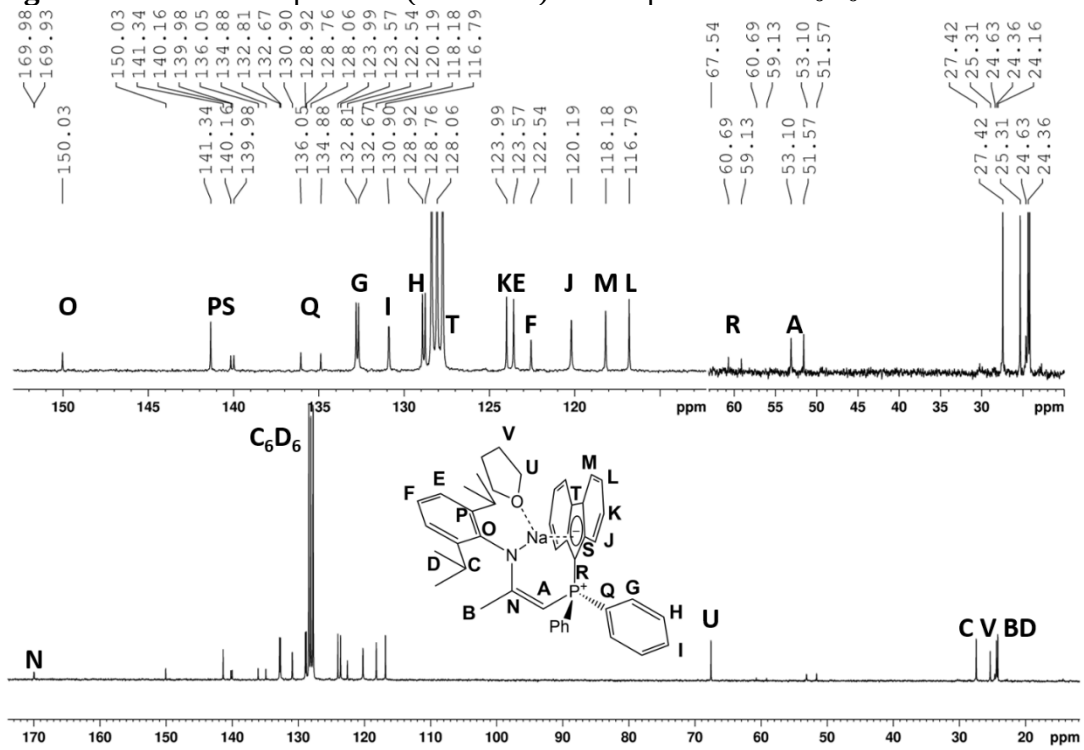

Figure 4.19 ^{13}C NMR spectrum (75 MHz) of compound **5** in C_6D_6.

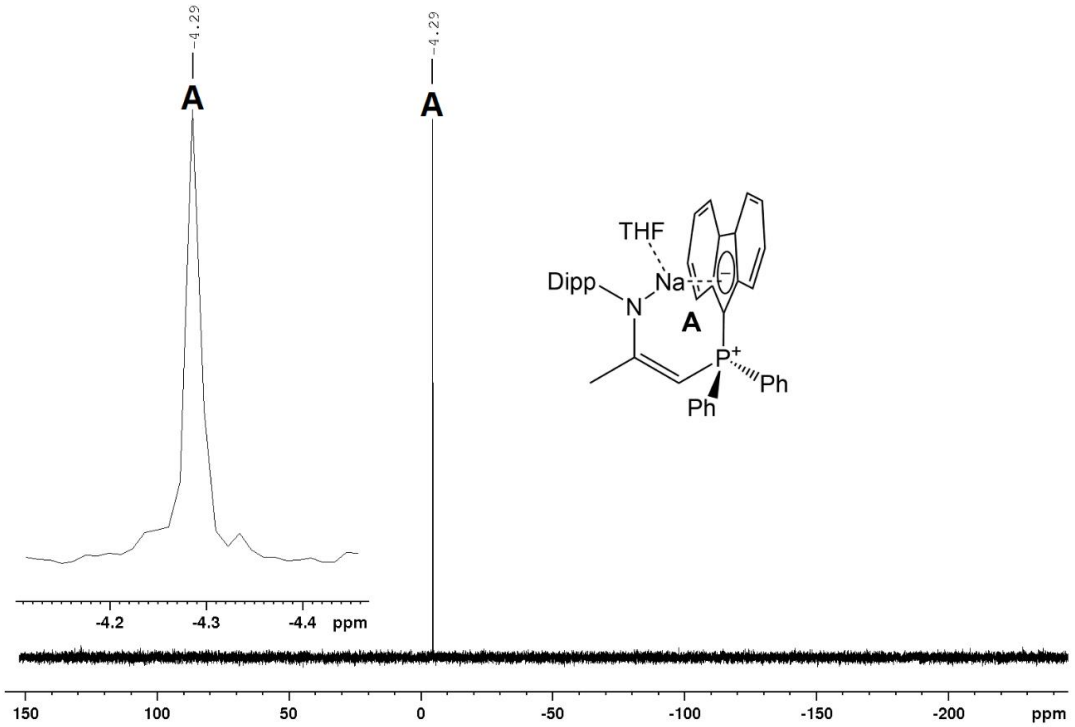

Figure 4.20 $^{31}P\{^{1}H\}$ NMR spectrum (121 MHz) of compound **5** in C_6D_6.

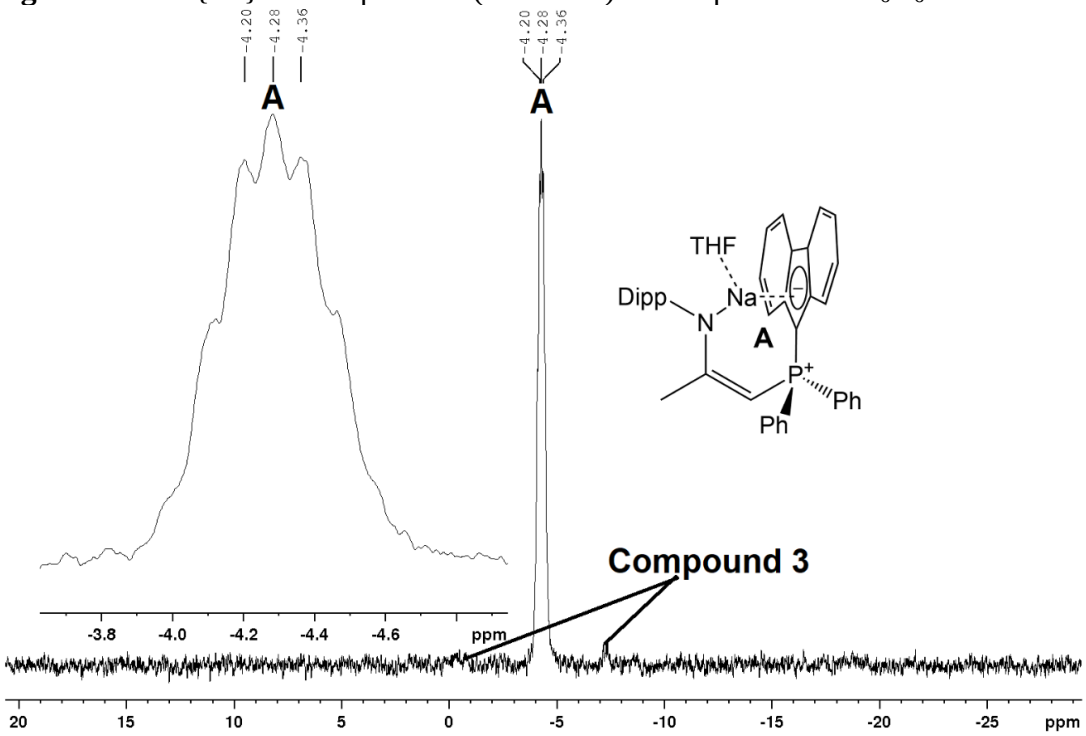

Figure 4.21 ^{31}P NMR spectrum (121 MHz) of compound **5** in C_6D_6.

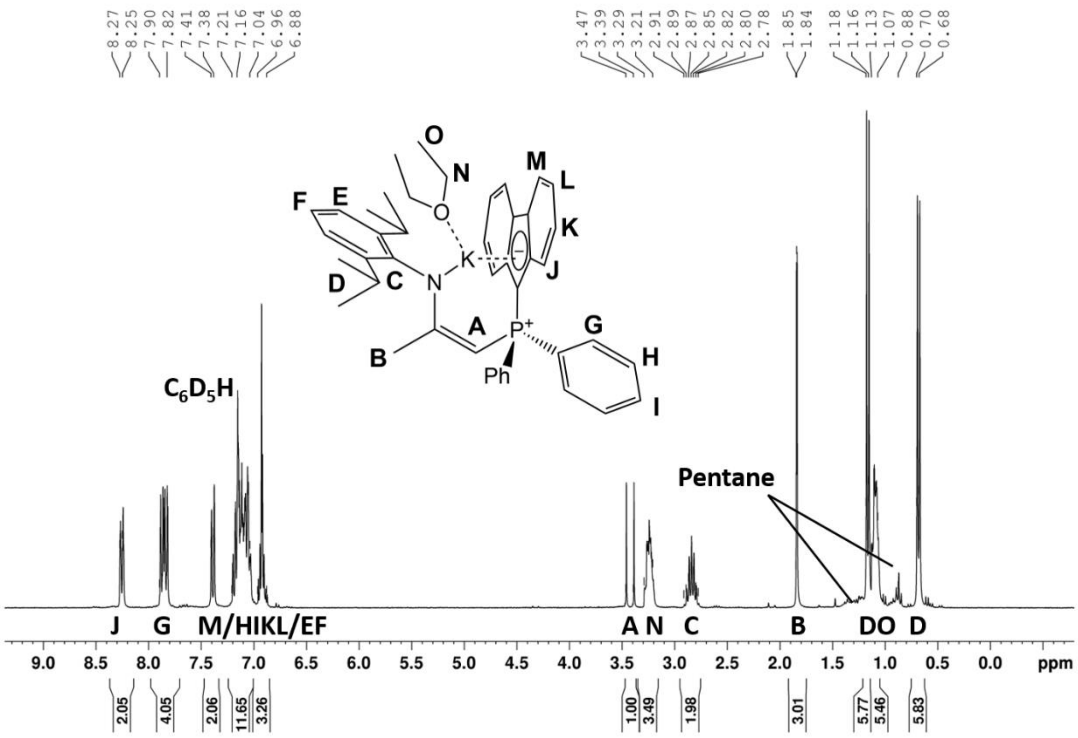

Figure 4.22 ^{1}H NMR spectrum (300 MHz) of compound **6a** in C_6D_6.

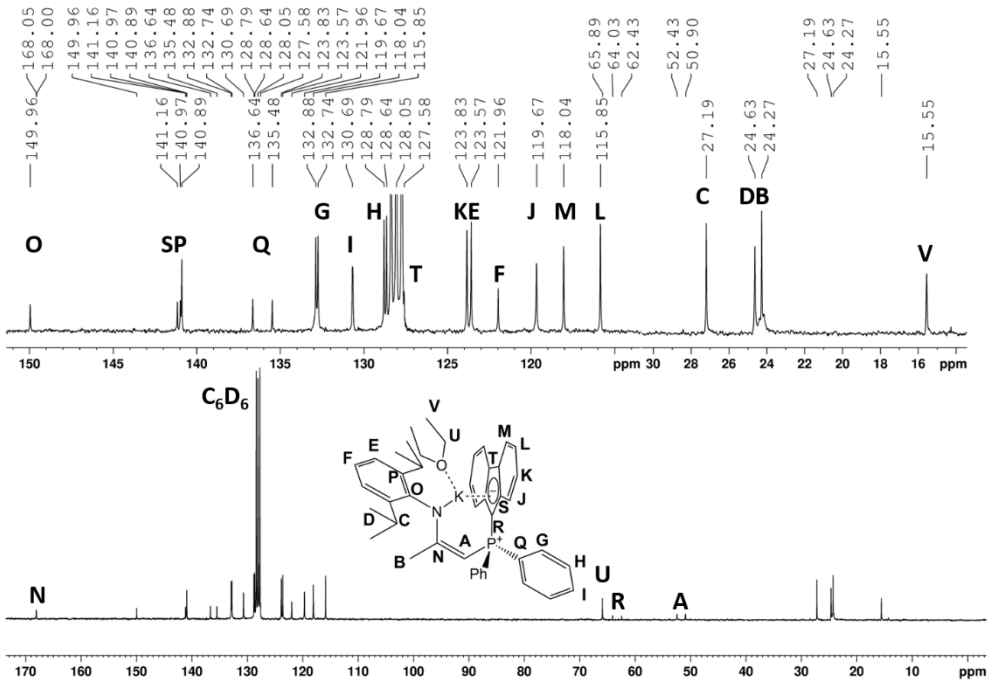

Figure 4.23 ^{13}C NMR spectrum (75 MHz) of compound **6a** in C_6D_6.

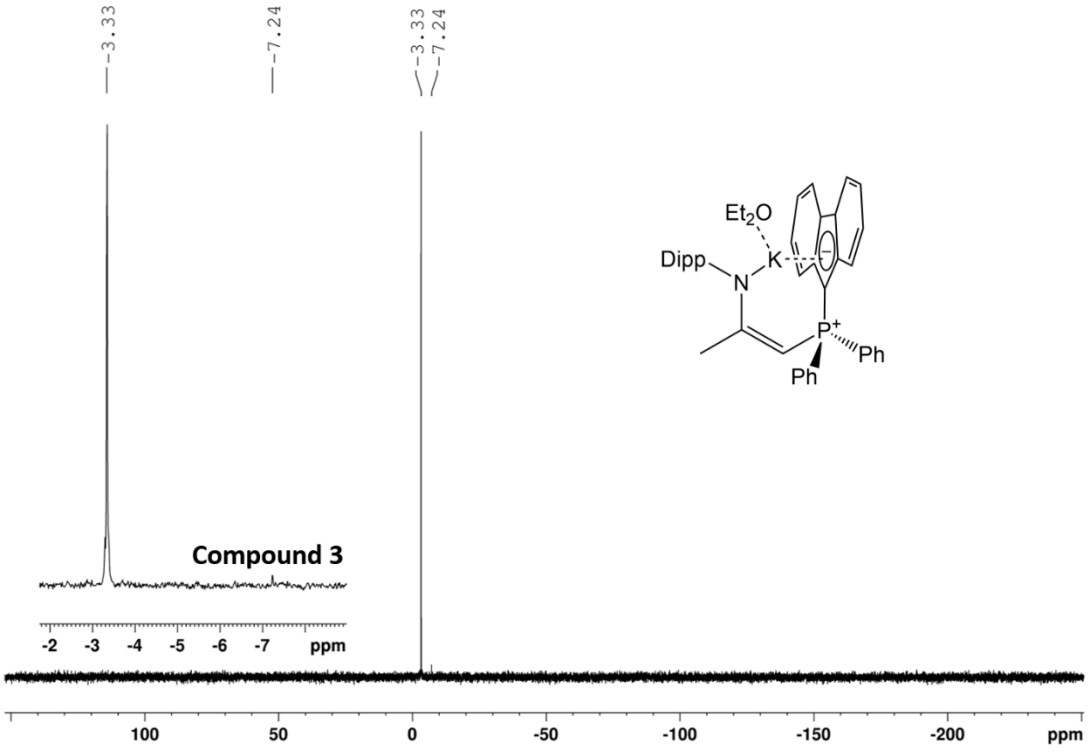

Figure 4.24 $^{31}P\{^{1}H\}$ NMR spectrum (121 MHz) of compound **6a** in C_6D_6.

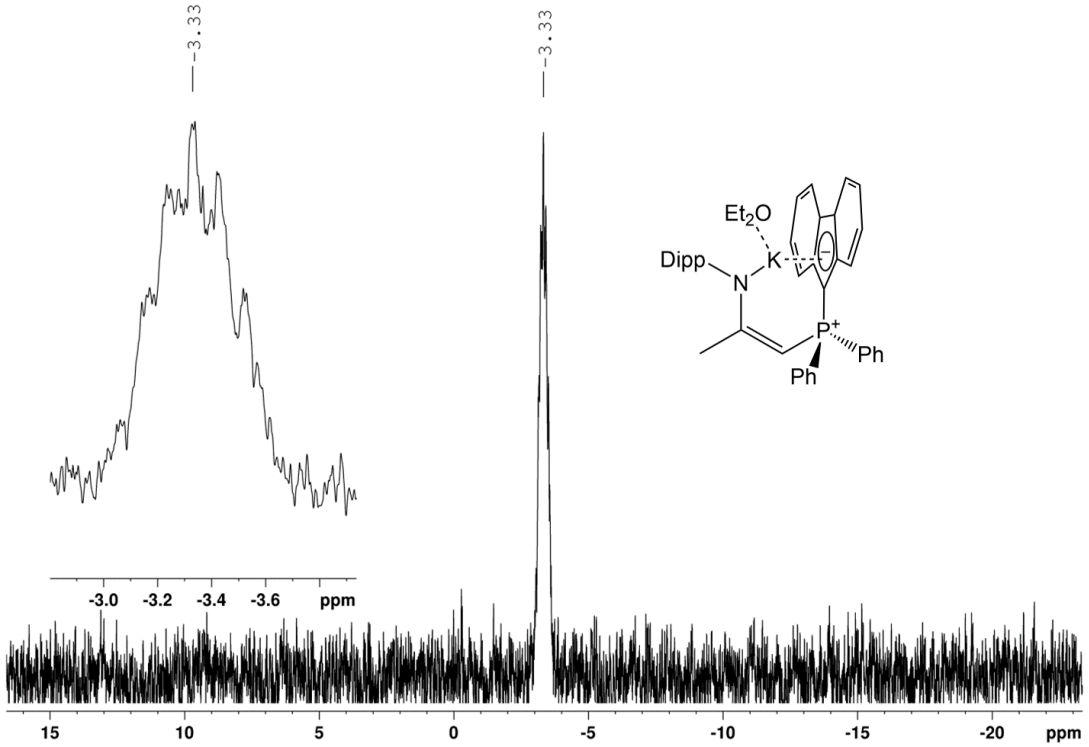

Figure 4.25 ^{31}P NMR spectrum (121 MHz) of compound **6a** in C_6D_6.

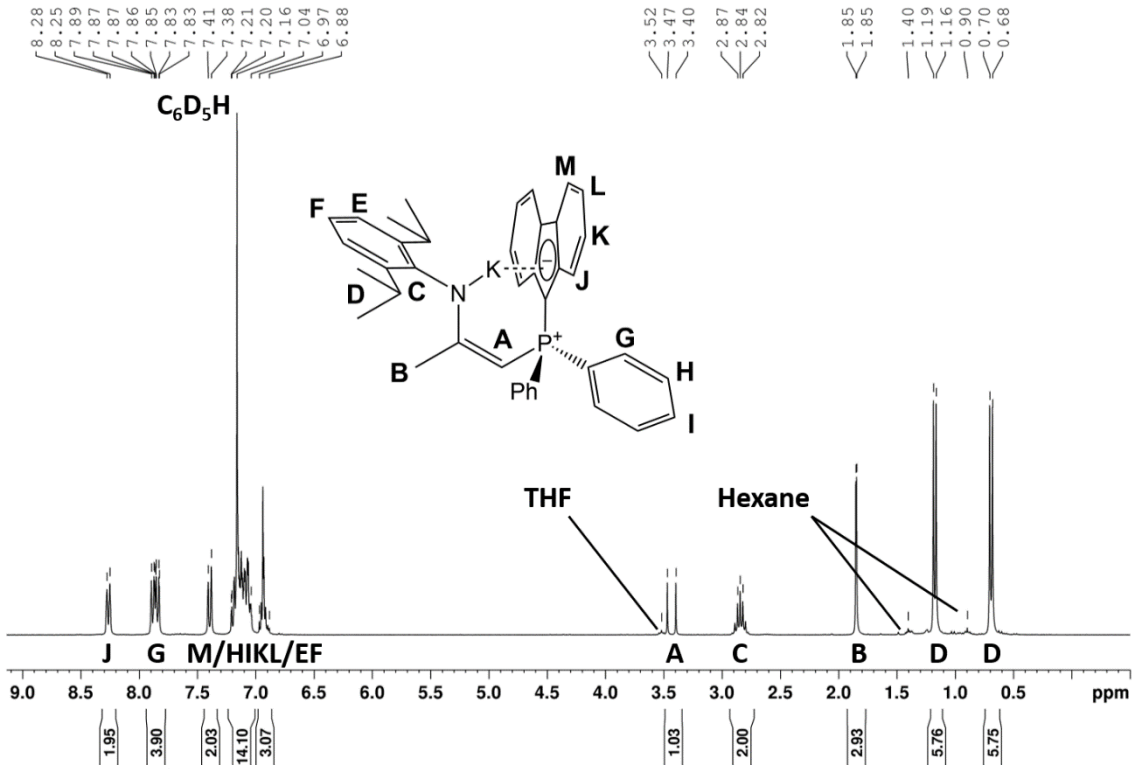

Figure 4.26 ^{1}H NMR spectrum (300 MHz) of compound **6b** in C_6D_6.

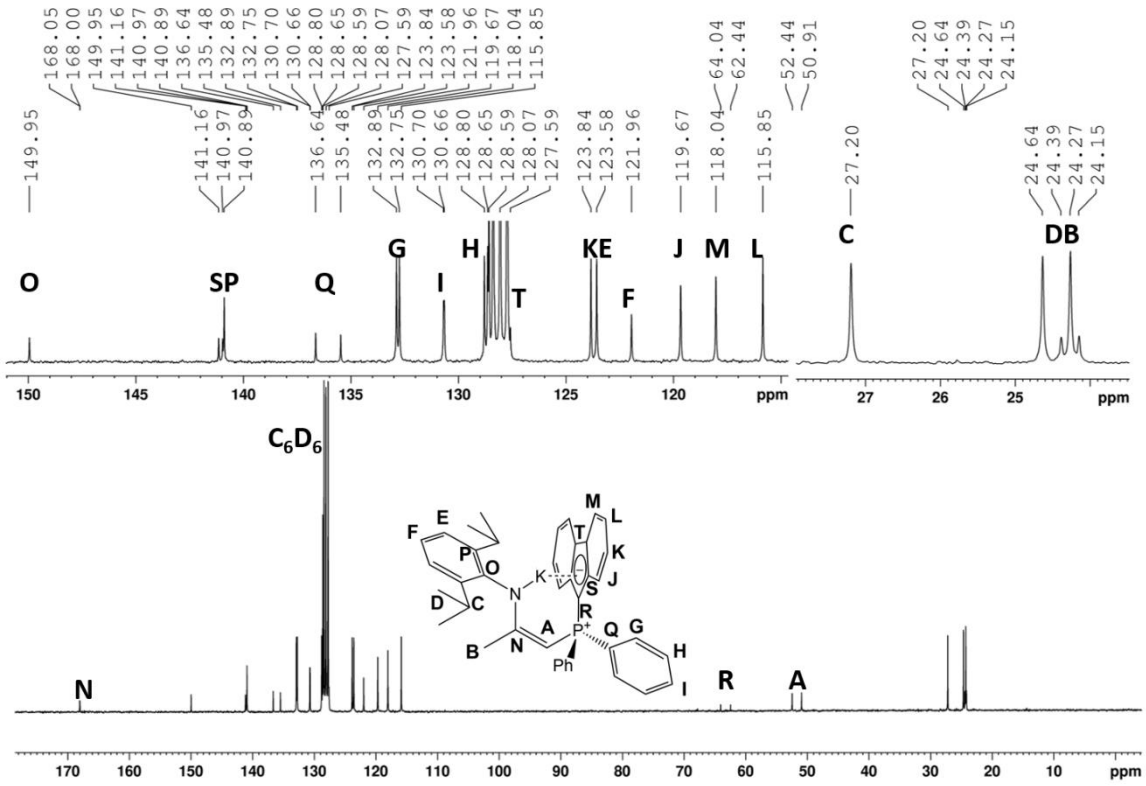

Figure 4.27 ^{13}C NMR spectrum (75 MHz) of compound **6b** in C_6D_6.

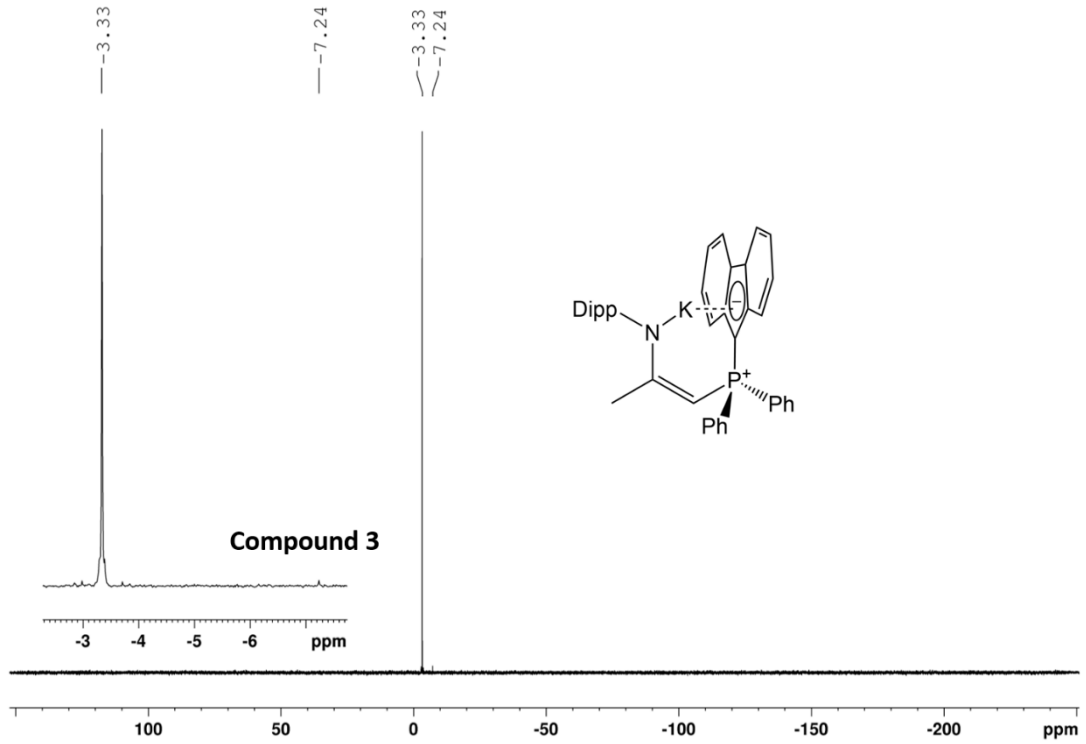

Figure 4.28 $^{31}P\{^{1}H\}$ NMR spectrum (121 MHz) of compound **6b** in C_6D_6.

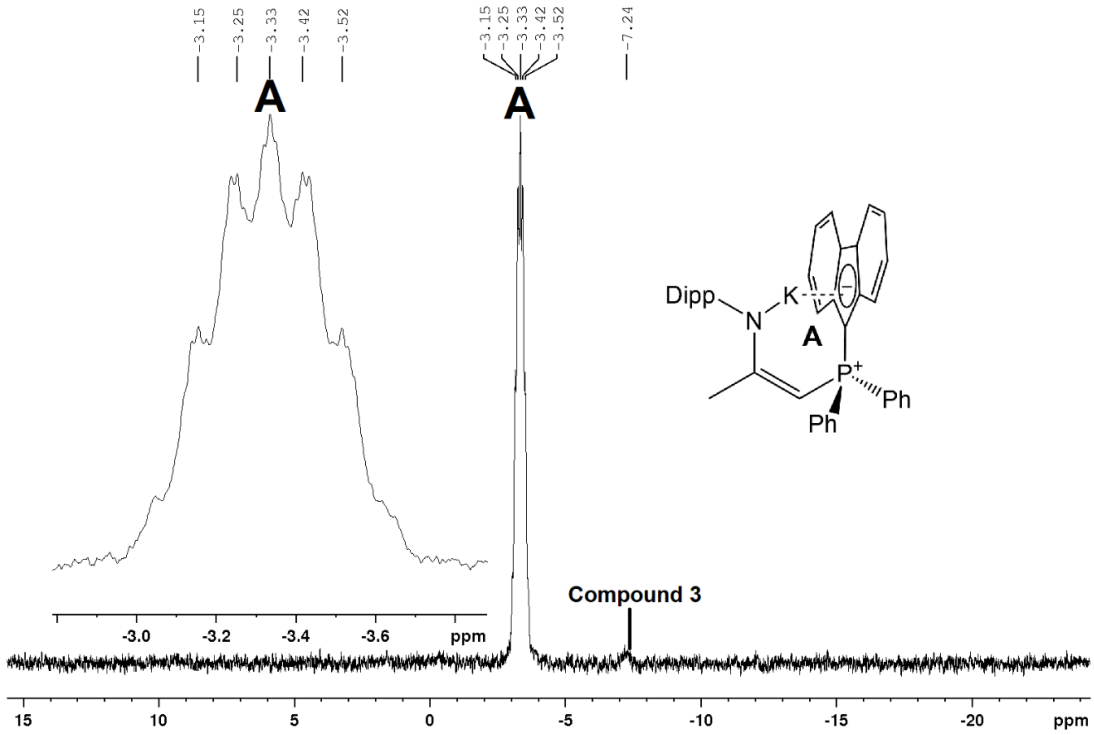

Figure 4.29 ^{31}P NMR spectrum (121 MHz) of compound **6b** in C_6D_6.

4.7.2 SC-XRD of Various Halide Salts Analogous to Compound 2 and Solvates

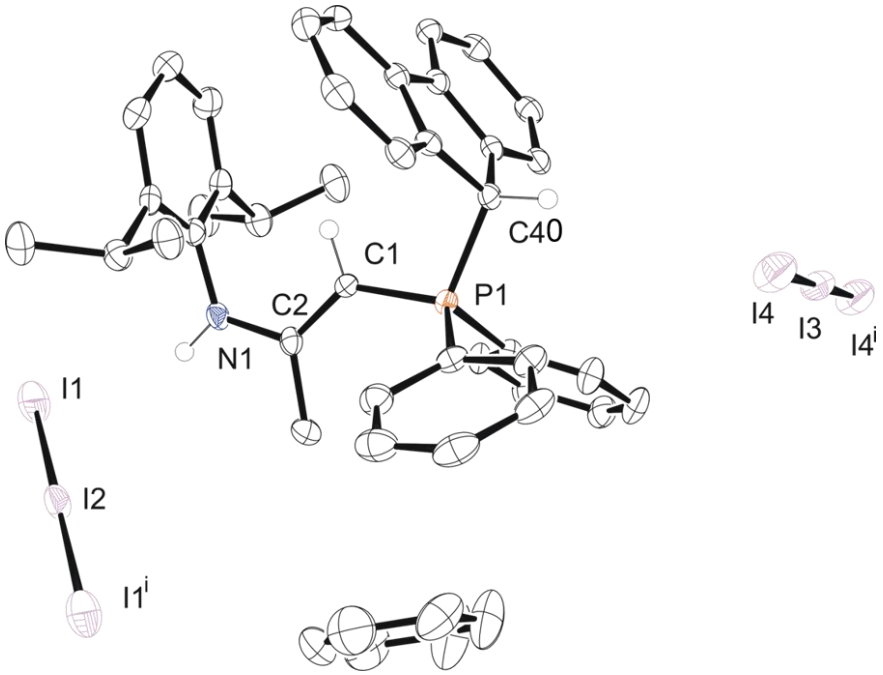

Figure 4.30 Molecular structure of the triiodide analog of compound **2** as a benzene solvate with anisotropic displacement ellipsoids projected at the 50% probability level. Hydrogen atoms except for C1-H, N1-H and C40-H have been omitted for clarity.

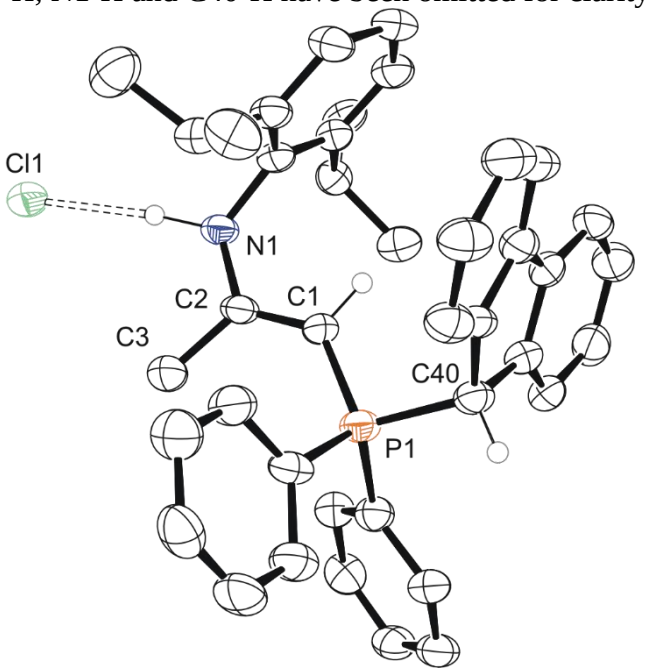

Figure 4.31 Molecular structure of the chloride analog of compound **2** as a benzene solvate with anisotropic displacement ellipsoids projected at the 50% probability level. Hydrogen atoms except for C1-H, N1-H and C40-H and C_6 have been omitted for clarity.

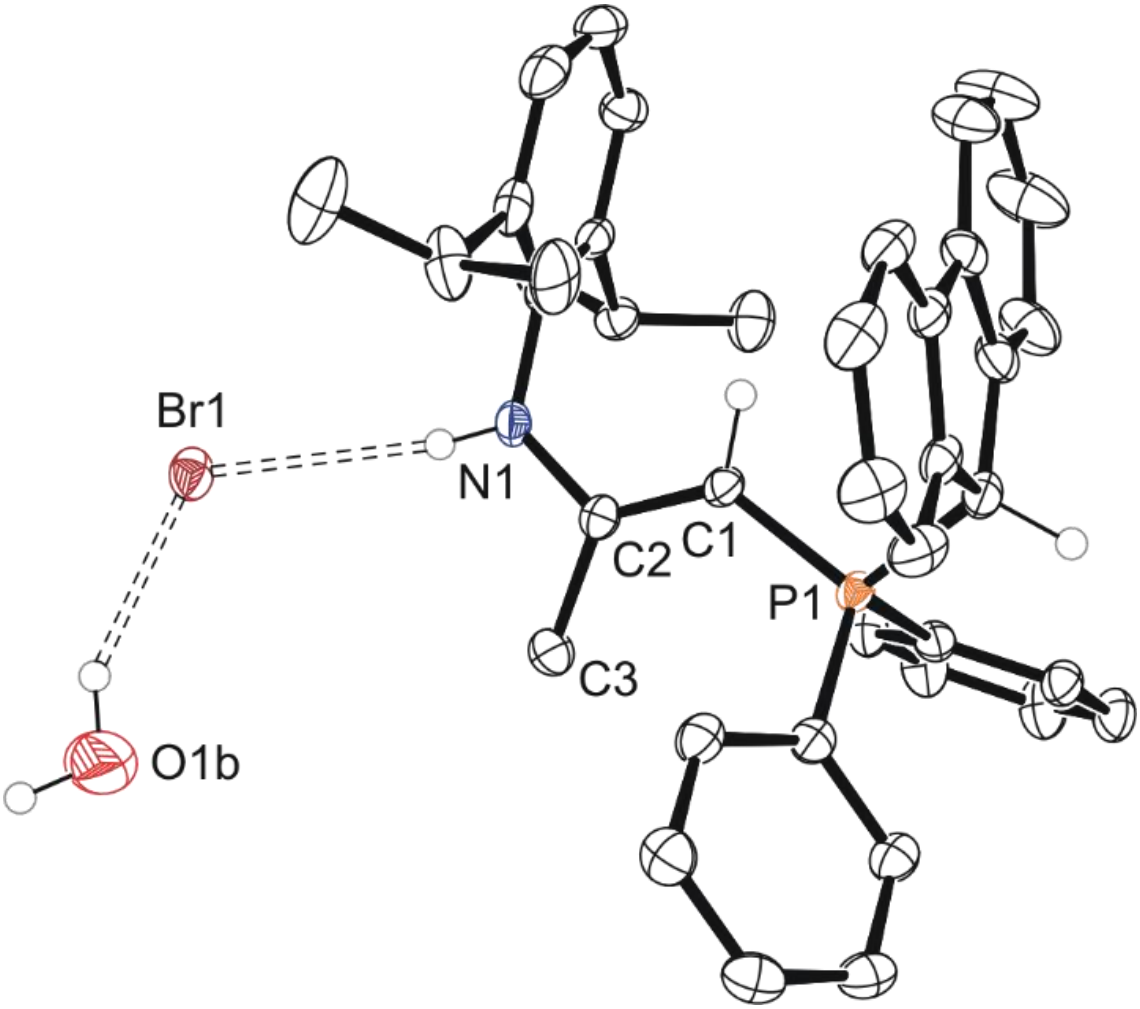

Figure 4.32 Molecular structure of compound **2•(H_2O)** with anisotropic displacement ellipsoids projected at the 50% probability level. Hydrogen atoms except for N1-H, C1-H, C40-H, and O1b-H have been omitted for clarity.

4.7.3 Crystallography Table and Additional Refinement Details

Table 4.1 Data derived from single crystal X-ray diffraction of crystals of compounds **2** and related halide salts from the work in Chapter 4.

Compound reference	Compound **2**	**2•(H_2O)**	**2-Cl•(C_6D_6)**	**2-(I_3)•(C_6H_6)**
Chemical formula	[Br]•$C_{40}H_{41}NP$	[Br]•$C_{40}H_{41}NP$•H_2O	[Cl]•$C_{40}H_{41}NP$•C_6D_6	[I_3]•$C_{40}H_{41}NP$•C_6H_6
Formula Mass	646.62	664.63	680.77	1025.51
Crystal system	Monoclinic	Monoclinic	Monoclinic	Triclinic
a/Å	12.741(2)	10.0975(5)	10.4185(11)	10.2940(4)
b/Å	16.807(3)	18.3601(9)	21.123(2)	11.6462(5)
c/Å	16.992(3)	18.9113(10)	17.2825(18)	18.0532(7)
α/°	90	90	90	100.312(2)
β/°	110.690(5)	101.673(2)	100.937(4)	91.631(2)
γ/°	90	90	90	98.080(2)
Unit cell volume/Å^3	3404.0(9)	3433.5(3)	3734.2(7)	2105.03(15)
Temperature/K	103.0	100.0	100.0	100.0
Space group	$P2_1/c$	$P2_1/n$	$P2_1/c$	$P\bar{1}$
No. of formula units per unit cell, *Z*	4	4	4	2
Radiation type	MoKα	MoKα	MoKα	MoKα
No. of reflections measured	67232	97324	93934	118810
No. of independent reflections	6946	7556	6898	12292
R_{int}	0.0939	0.0436	0.3469	0.0766
Final R_1 values ($I > 2\sigma(I)$)	0.0673	0.0340	0.0876	0.0361
Final $wR(F^2)$ values ($I > 2\sigma(I)$)	0.1666	0.0817	0.2000	0.0597
Final R_1 values (all data)	0.0945	0.0432	0.1684	0.0649
Final $wR(F^2)$ values (all data)	0.1809	0.0865	0.2576	0.0697

Table 4.2 Data derived from single crystal X-ray diffraction of crystals of compounds **3** and all solvates from the work in Chapter 4.

Compound reference	**3**	**3•(0.5 Et_2O)**	**3•(0.5 THF, 0.5 n-Hexane)**	**3•(3 THF)**
Chemical formula	$C_{40}H_{40}NP$	2($C_{40}H_{40}NP$)•$C_4H_{10}O$	2($C_{40}H_{40}NP$)•C_6H_{14}, C_4H_8O	$C_{40}H_{40}NP$•3(C_4H_8O)
Formula Mass	565.70	1205.51	1289.67	782.01
Crystal system	Monoclinic	Monoclinic	Triclinic	Triclinic
a/Å	37.6440(13)	12.564(3)	9.5712(7)	9.8426(3)
b/Å	9.8467(3)	14.284(3)	10.6830(8)	14.3465(5)
c/Å	18.9160(7)	19.167(4)	18.3305(13)	16.0750(5)
α/°	90	90	92.517(3)	88.7720(10)
β/°	116.6140(10)	97.293(7)	94.855(3)	88.3920(10)
γ/°	90	90	106.278(3)	74.9090(10)
Unit cell volume/Å^3	6268.7(4)	3412.2(12)	1788.2(2)	2190.52(12)
Temperature/K	100.0	100.0	100.0	125.0
Space group	$C2/c$	$P2_1/c$	$P\bar{1}$	$P\bar{1}$
No. of formula units per unit cell, *Z*	8	2	1	2
Radiation type	MoKα	MoKα	MoKα	MoKα
No. of reflections measured	19148	56231	139342	149719
No. of independent reflections	5778	7431	6537	14572
R_{int}	0.0260	0.0967	0.0684	0.0441
Final R_1 values ($I > 2\sigma(I)$)	0.0359	0.0949	0.0381	0.0507
Final $wR(F^2)$ values ($I > 2\sigma(I)$)	0.0864	0.2200	0.0917	0.1296
Final R_1 values (all data)	0.0403	0.1317	0.0428	0.0671
Final $wR(F^2)$ values (all data)	0.0898	0.2423	0.0960	0.1423

Table 4.3 Data derived from single crystal X-ray diffraction of crystals of compounds **4-6** from the work in Chapter 4.

Compound reference	Compound **4a**	**4•(THF, 0.5 C_6H_6)**	Compound **5**	Compound **6a**	**6b•0.5(C_6H_{14})**
Chemical formula	$C_{44}H_{49}LiNOP$	$C_{44}H_{47}LiNOP•C_3H_3$	$C_{44}H_{47}NNaOP$	$C_{44}H_{49}KNOP$	$C_{40}H_{39}KNP$ •0.5(C_6H_{14})
Formula Mass	645.75	682.79	659.78	677.91	646.88
Crystal system	Monoclinic	Monoclinic	Monoclinic	Triclinic	Monoclinic
a/Å	10.6480(3)	22.6988(8)	10.4778(3)	9.3756(5)	34.9632(12)
b/Å	14.3485(4)	9.1277(3)	20.5243(5)	10.5985(5)	10.2850(4)
c/Å	24.1158(8)	19.9525(7)	17.3436(5)	20.4307(8)	26.1626(10)
α/°	90	90	90	93.377(2)	90
β/°	90.8970(10)	112.0830(10)	102.9070(10)	100.264(2)	129.7780(10)
γ/°	90	90	90	104.180(2)	90
Unit cell volume/Å^3	3684.03(19)	3830.7(2)	3635.50(17)	1925.56(16)	7230.3(5)
Temperature/K	125.0	100.0	125.0	125.0	125.0
Space group	$P2_1/c$	$P2_1/c$	$P2_1/n$	$P\bar{1}$	$C2/c$
No. of formula units per unit cell, *Z*	4	4	4	2	8
Radiation type	MoKα	MoKα	MoKα	MoKα	MoKα
No. of reflections measured	168628	191561	121993	137752	265612
No. of independent reflections	16177	7119	8343	9776	10583
R_{int}	0.0441	0.1163	0.0853	0.0413	0.0645
Final R_1 values ($I > 2\sigma(I)$)	0.0375	0.0401	0.0503	0.0553	0.0468
Final $wR(F^2)$ values ($I > 2\sigma(I)$)	0.1027	0.0862	0.1039	0.1232	0.1152
Final R_1 values (all data)	0.0465	0.0598	0.0695	0.0643	0.0610
Final $wR(F^2)$ values (all data)	0.1090	0.0983	0.1121	0.1312	0.1265

Halide salts (except that of the I_3 anion) experience a hydrogen bonding interaction between the halide anion and the amine. Compound **2** has two component disorder in one of the isopropyl groups in a 63:37 ratio. The corresponding hydrate **2•(H_2O)** has the same disorder in a 59:41 ratio along with a disordered water molecule in an 81:19 ratio with both components hydrogen bound to the bromide anion. Within the structure of **3•(0.5 THF, 0.5 n-Hexane)** the molecule of n-hexane is split down the middle across the symmetry element -X,1-Y,1-Z and the n-hexane is modelled with two component wagging disorder for the C46 methylene group in a 73:27 ratio. Compound **3•(0.5 Et_2O)** has a molecule of diethyl ether split down the middle across the symmetry element -X,1-Y,2-Z and the diethyl ether is modelled with two component disorder in a 51:49 ratio. In the structure of **4•(THF, 0.5 C_6H_6)** the C_6H_6 in split in half down C45-C47 bonds across the symmetry element -X,-Y,-

Z. Compound **6a** has two component disorder in one of the isopropyl groups in a 69:31 ratio and the diethyl ether coordinated to potassium is highly disordered and modelled as two components in a 62:38 ratio, with no success modelling three component disorder (the 62% component remains with large thermal parameter). Within the structure of **6•(0.5 n-Hexane)** the molecule of n-hexane is split down the middle across the symmetry element 1-X,+Y,0.5-Z and the n-hexane is disordered however attempts to model two component disorder was unsuccessful and C43 has large anisotropic displacement ellipsoids and the C43-C43' bond length across the symmetry element is incorrectly short.

5. 5.7 Supplementary Information – Chapter 5

5.7.1 Infrared Spectroscopy

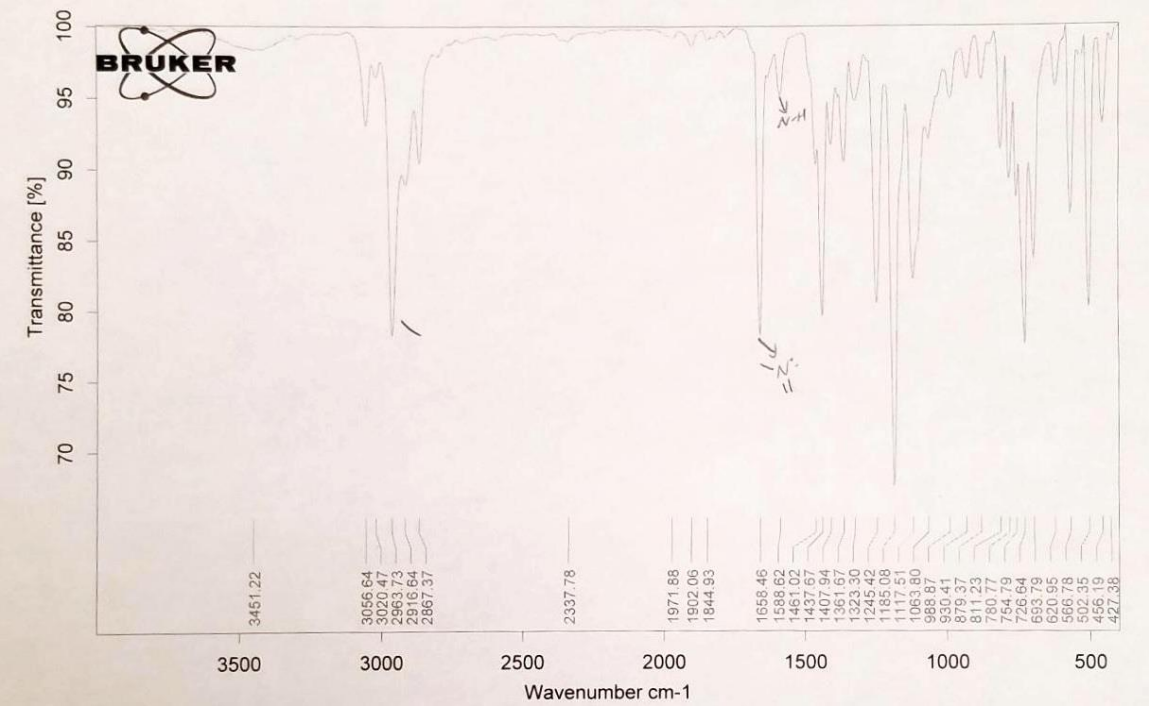

Figure 5.1 Infrared spectra of compound **2a** as a pressed KBr pellet.

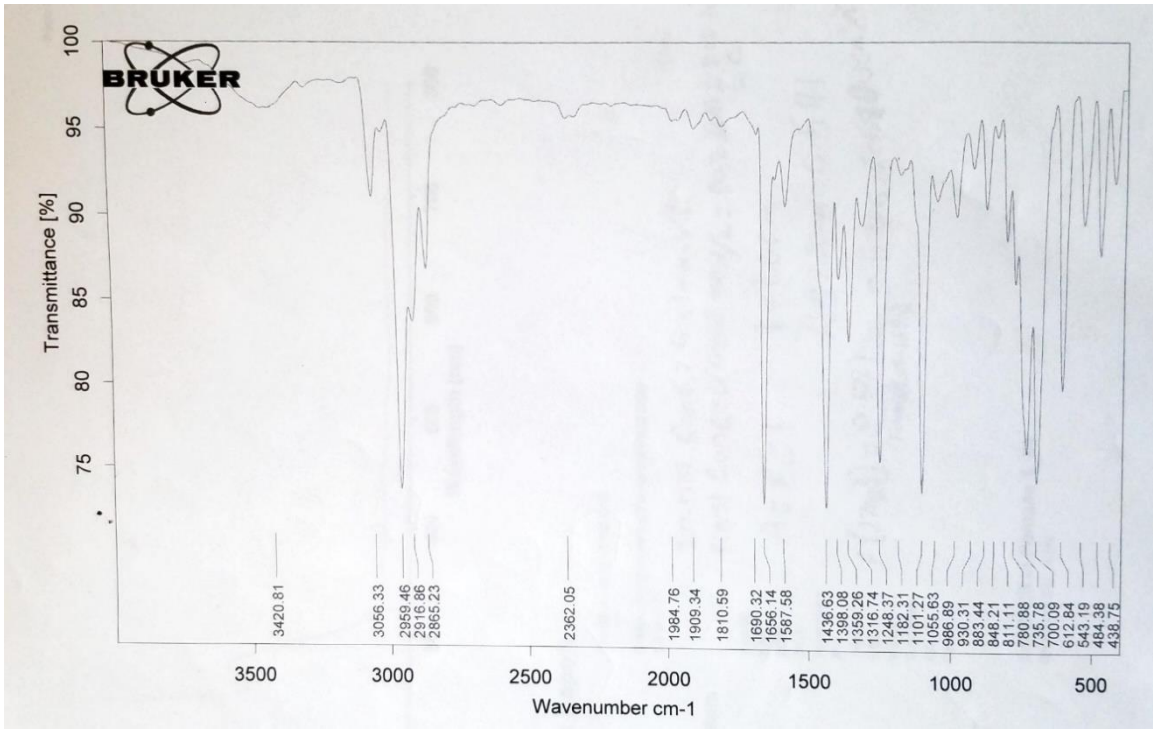

Figure 5.2 Infrared spectra of compound **3** as a pressed KBr pellet.

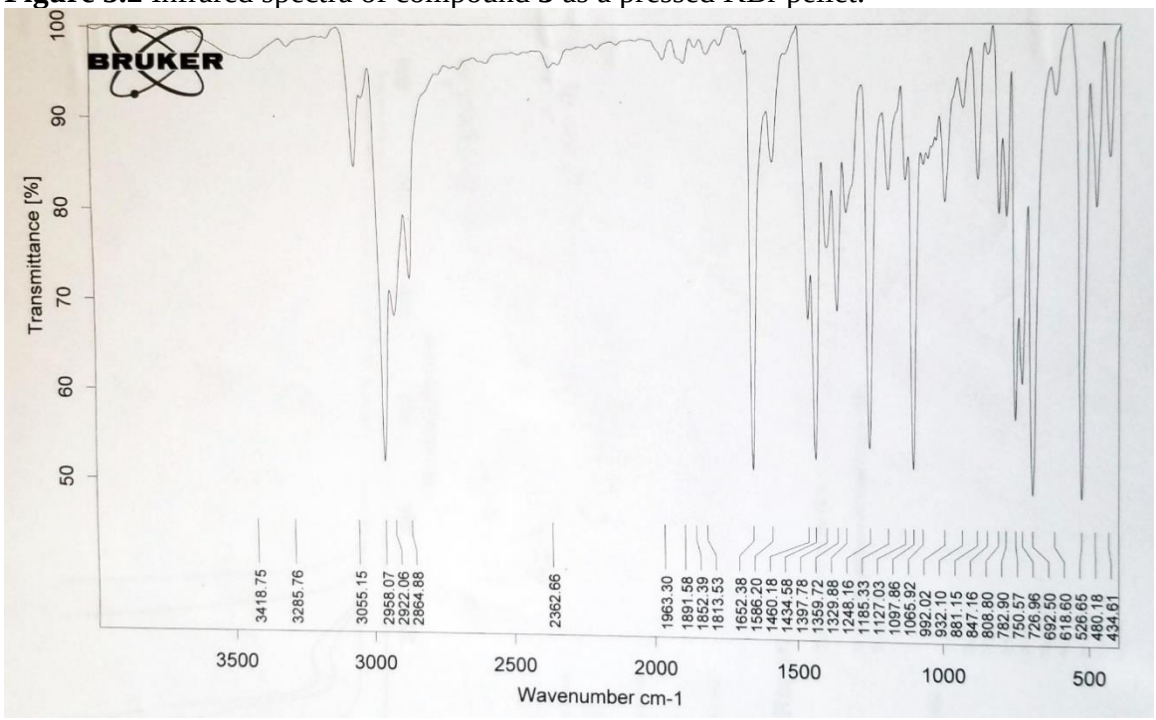

Figure 5.3 Infrared spectra of compound **4** as a pressed KBr pellet.

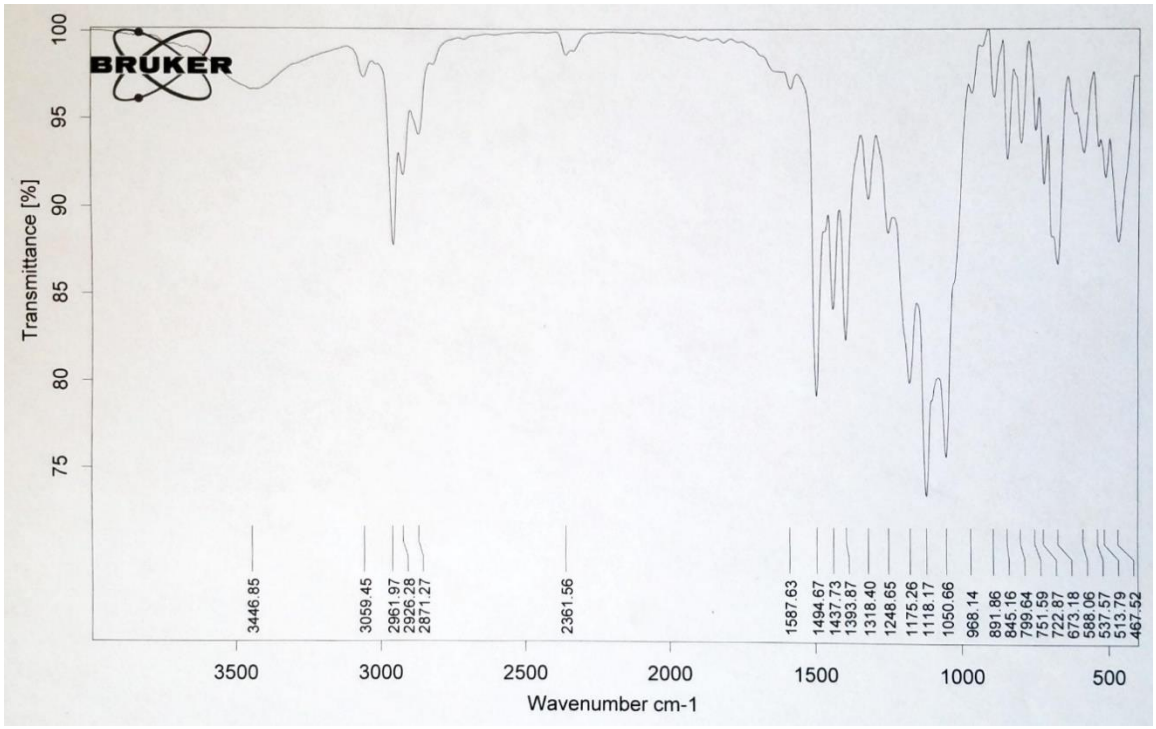

Figure 5.4 Infrared spectra of compound **5** as a pressed KBr pellet.

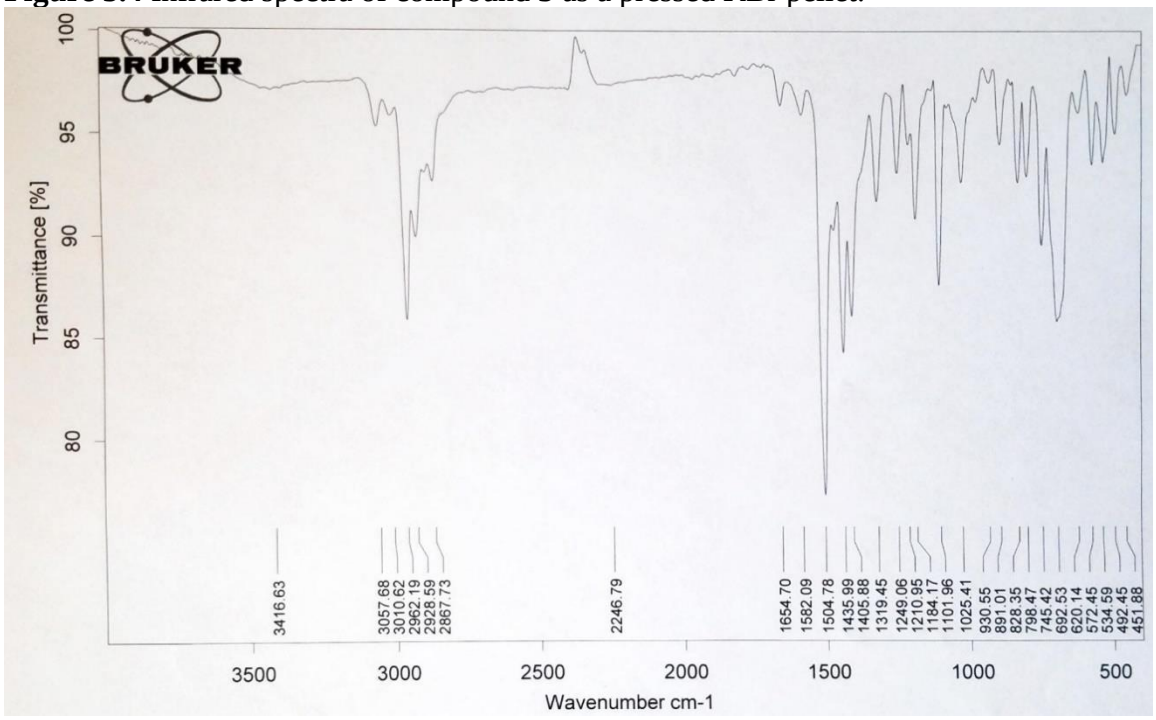

Figure 5.5 Infrared spectra of compound **6** as a pressed KBr pellet.

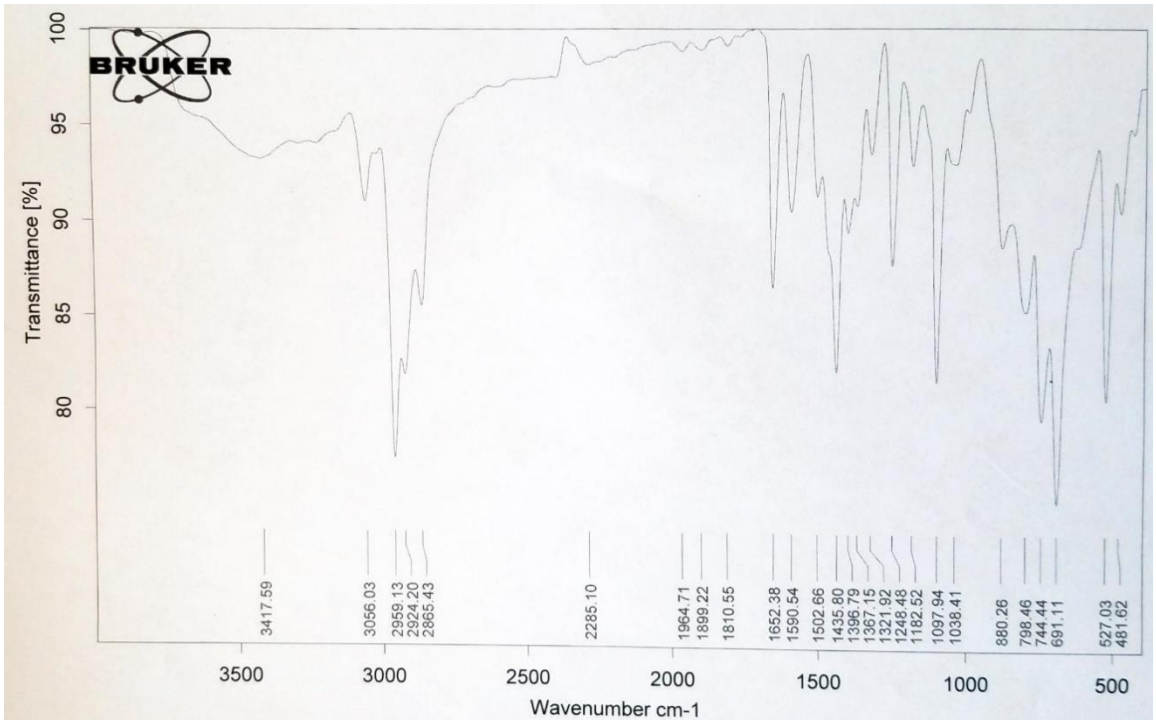

Figure 5.6 Infrared spectra of compound **7** as a pressed KBr pellet.

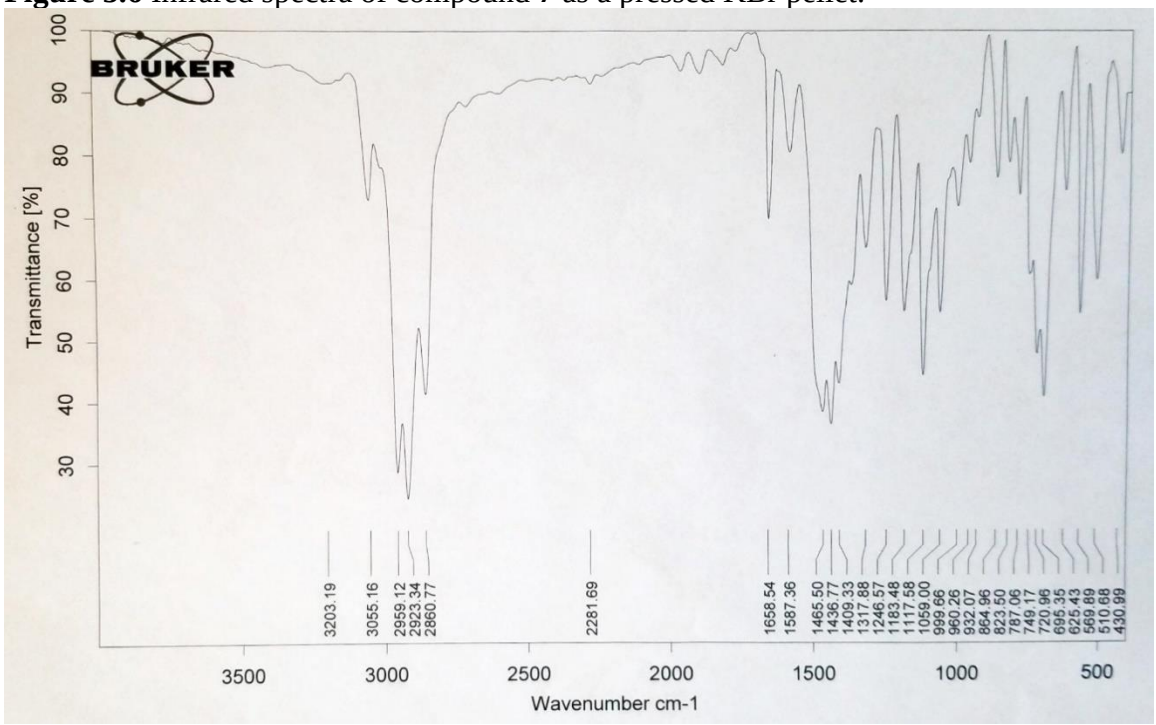

Figure 5.7 Infrared spectra of compound **8a** as a pressed KBr pellet.

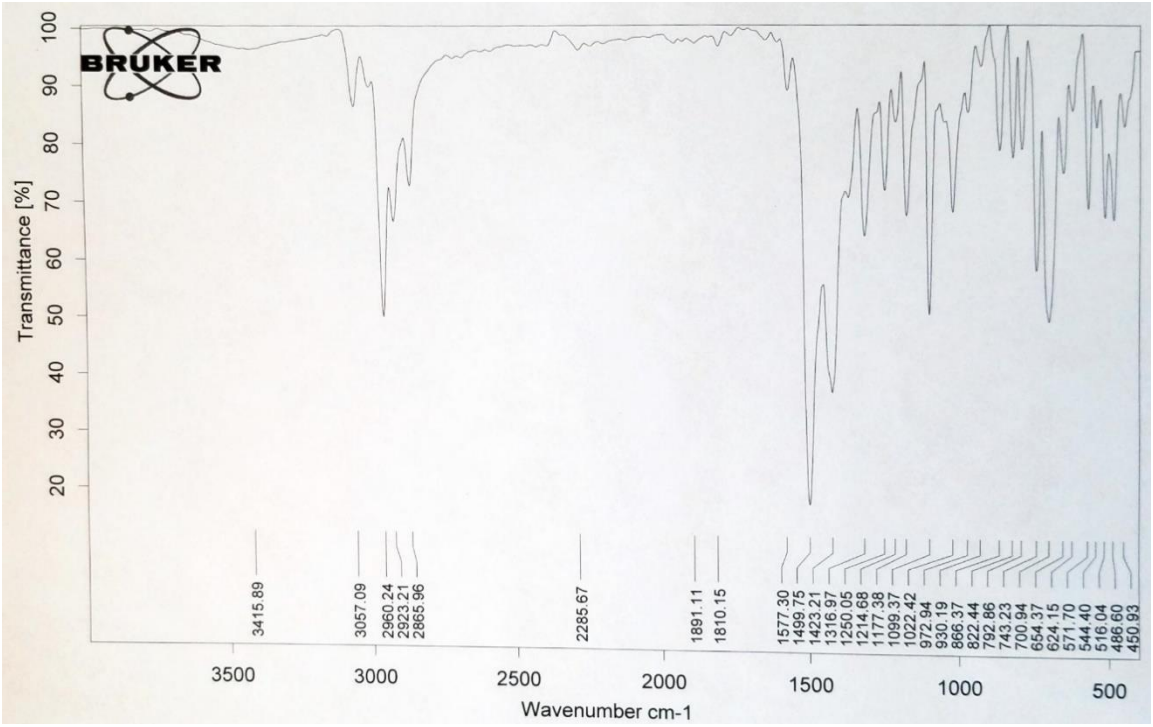

Figure 5.8 Infrared spectra of compound **9** as a pressed KBr pellet.

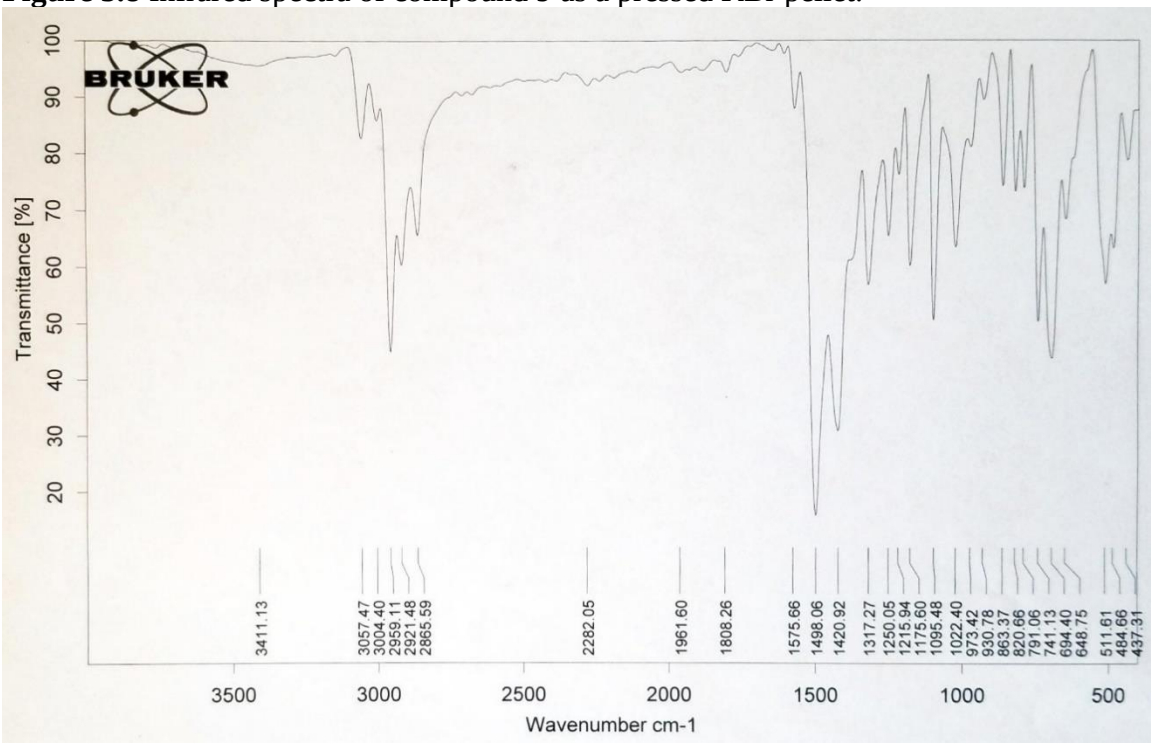

Figure 5.9 Infrared spectra of compound **10** as a pressed KBr pellet.

5.7.2 NMR Spectroscopy

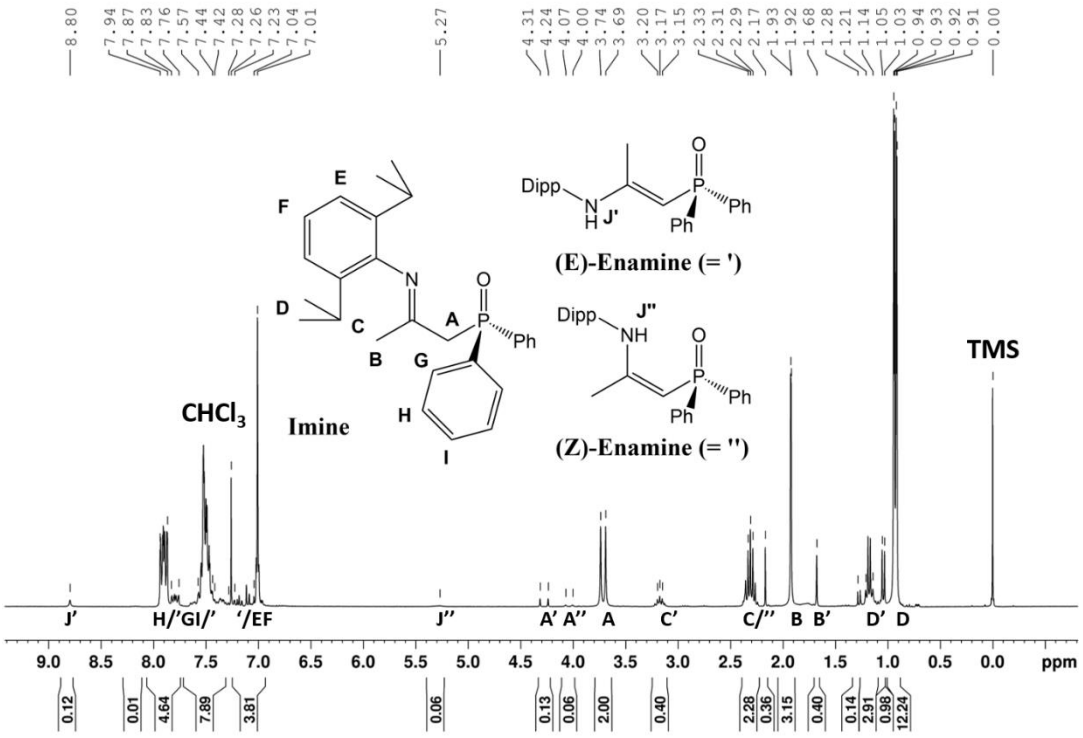

Figure 5.10 ^{1}H NMR spectrum of compound **2** recorded at 298K on a 300 MHz Bruker spectrometer in $CDCl_3$.

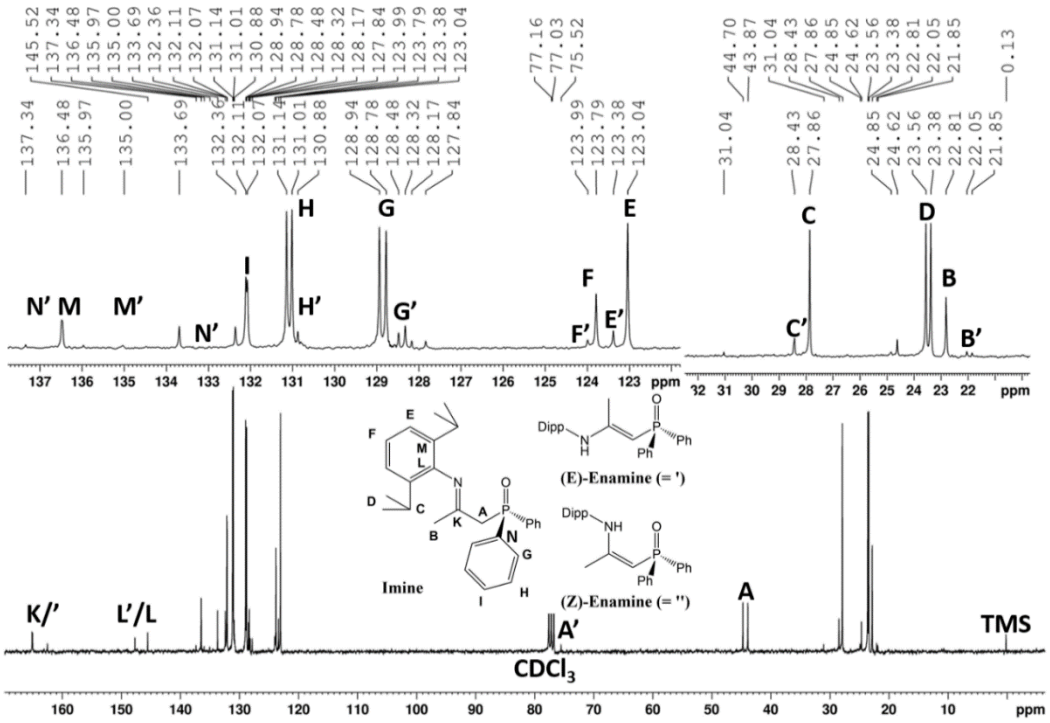

Figure 5.11 ^{13}C NMR spectrum of compound **2** recorded at 298K on a 300 MHz Bruker spectrometer in $CDCl_3$.

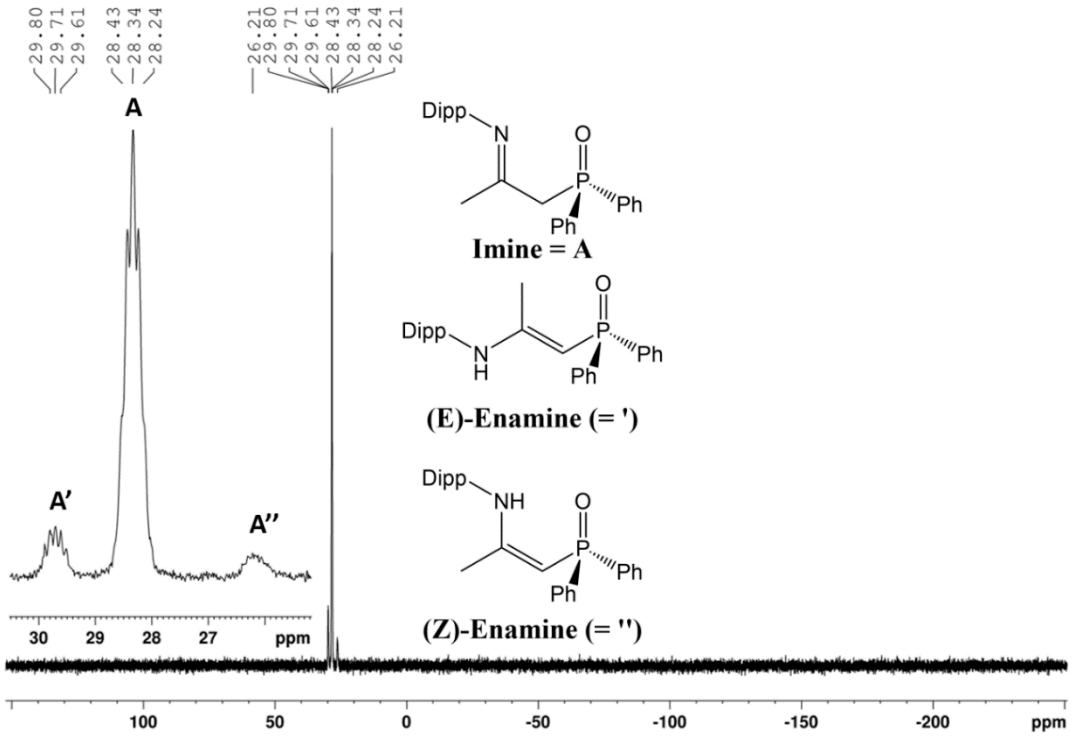

Figure 5.12 ^{31}P NMR spectrum (121 MHz) of compound **2** recorded at 298K on a 300 MHz Bruker spectrometer in $CDCl_3$.

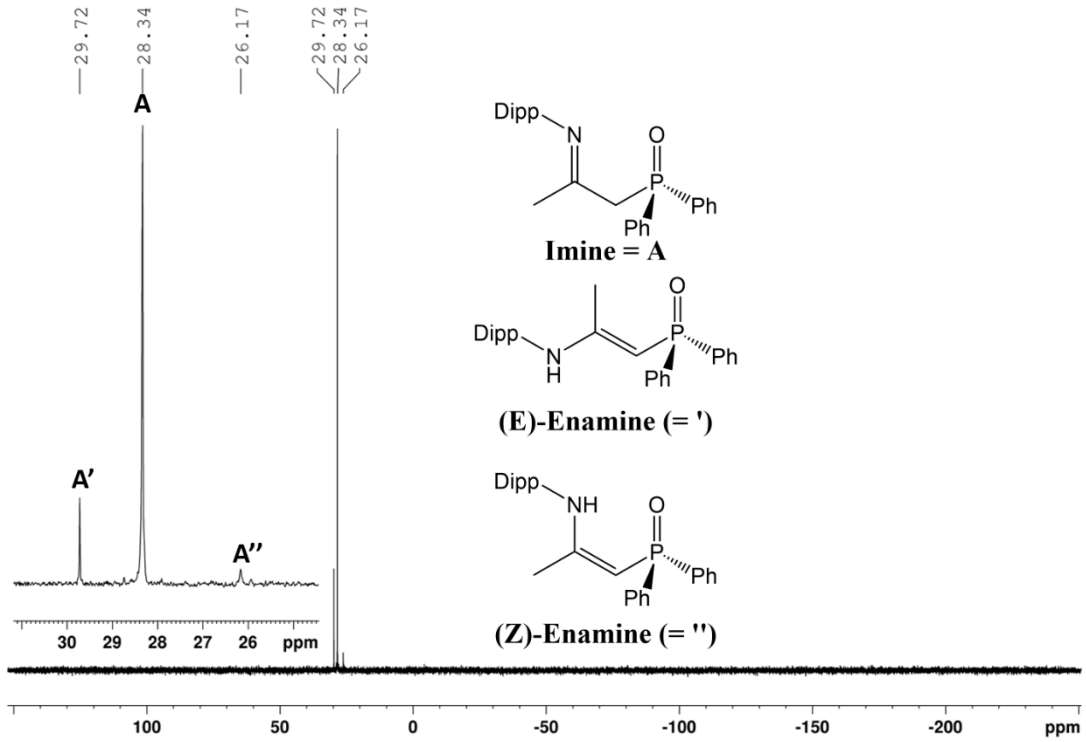

Figure 5.13 $^{31}P\{^{1}H\}$ NMR spectrum (121 MHz) of compound **2** recorded at 298K on a 300 MHz Bruker spectrometer in $CDCl_3$.

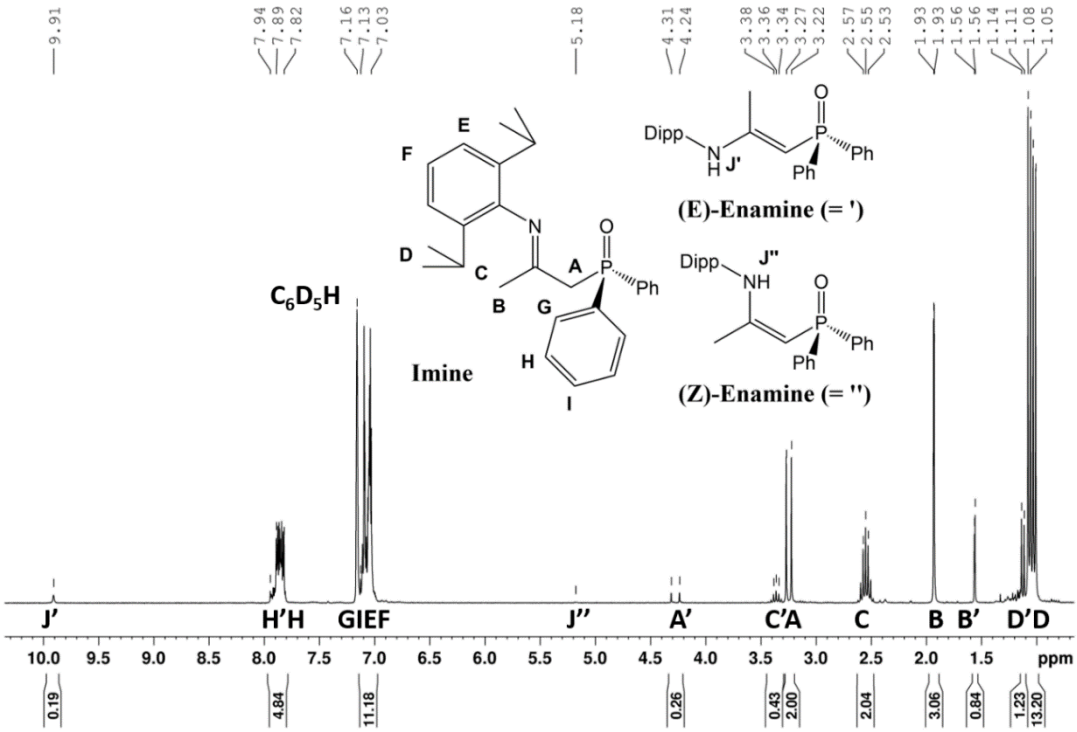

Figure 5.14 ^{1}H NMR spectrum of compound **2** recorded at 298K on a 300 MHz Bruker spectrometer in C_6D_6.

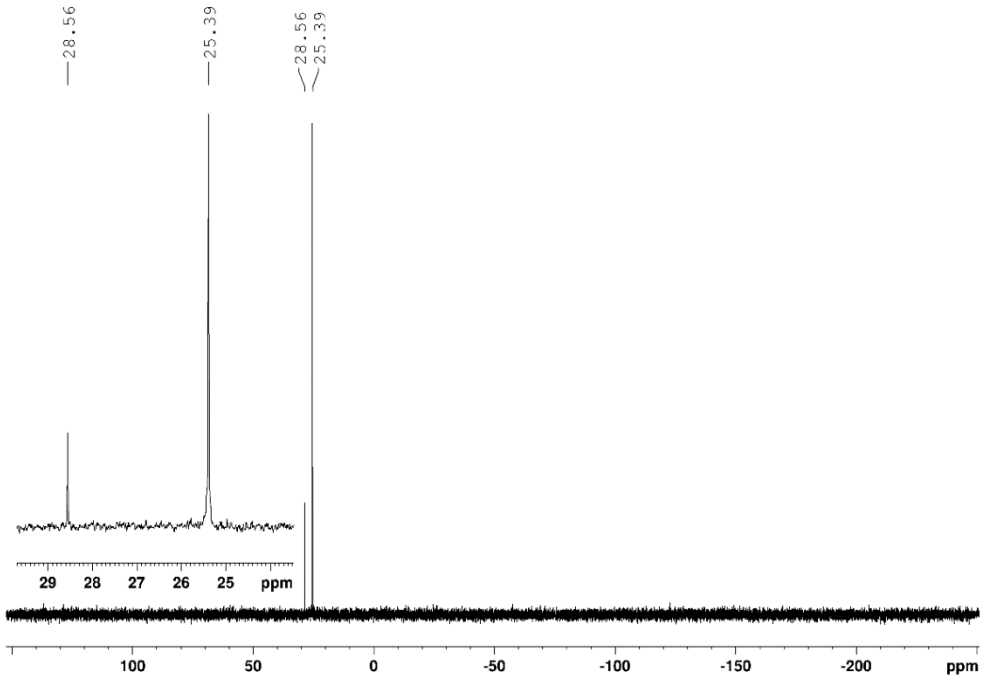

Figure 5.15 $^{31}P\{^{1}H\}$ NMR spectrum (121 MHz) of compound **2** recorded at 298K on a 300 MHz Bruker spectrometer in C_6D_6.

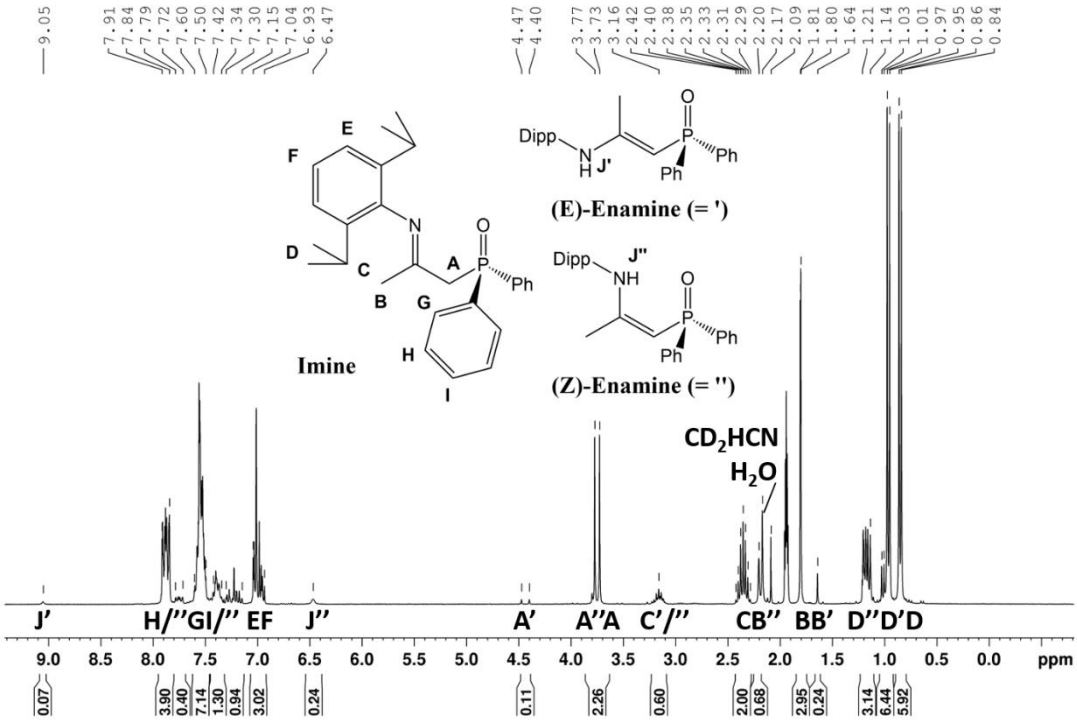

Figure 5.16 ^{1}H NMR spectrum of compound **2** recorded at 298K on a 300 MHz Bruker spectrometer in CD_3CN.

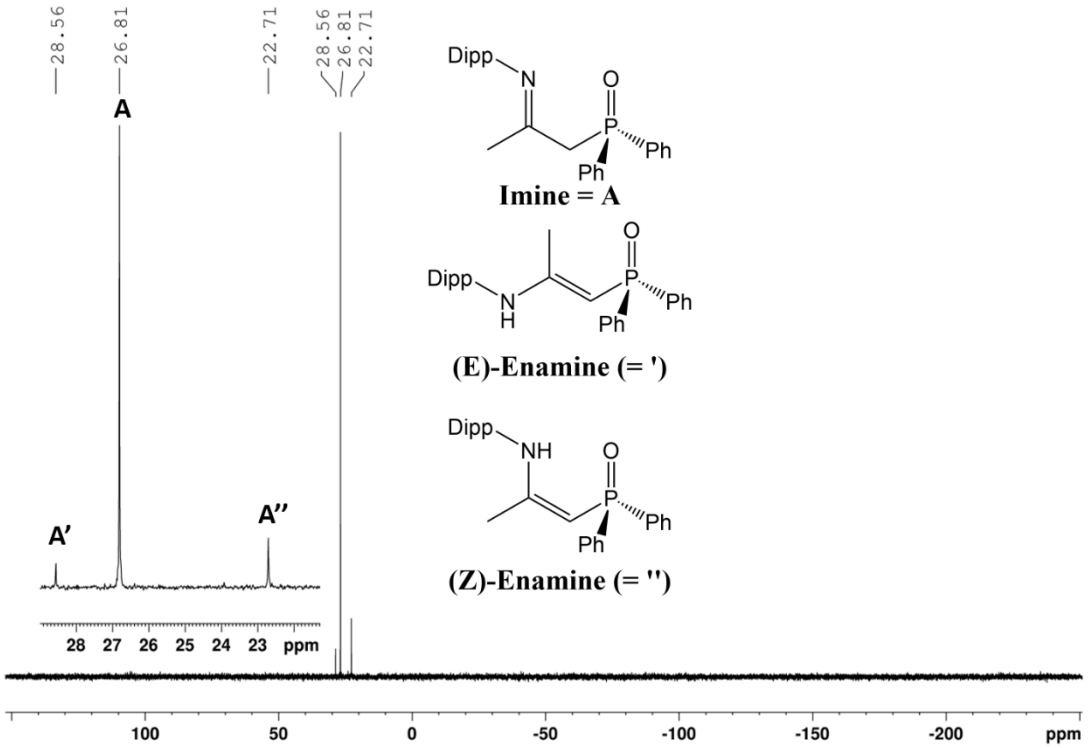

Figure 5.17 $^{31}P\{^{1}H\}$ NMR spectrum (121 MHz) of compound **2** recorded at 298K on a 300 MHz Bruker spectrometer in CD_3CN.

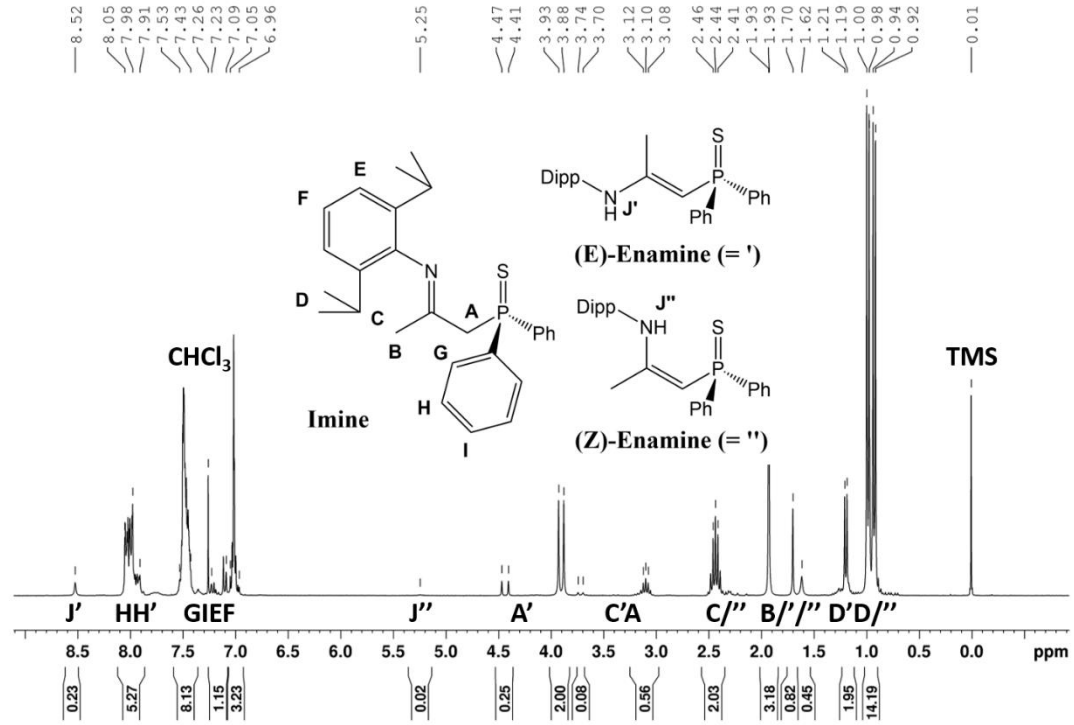

Figure 5.18 ^{1}H NMR spectrum of compound **3** recorded at 298K on a 300 MHz Bruker spectrometer in $CDCl_3$.

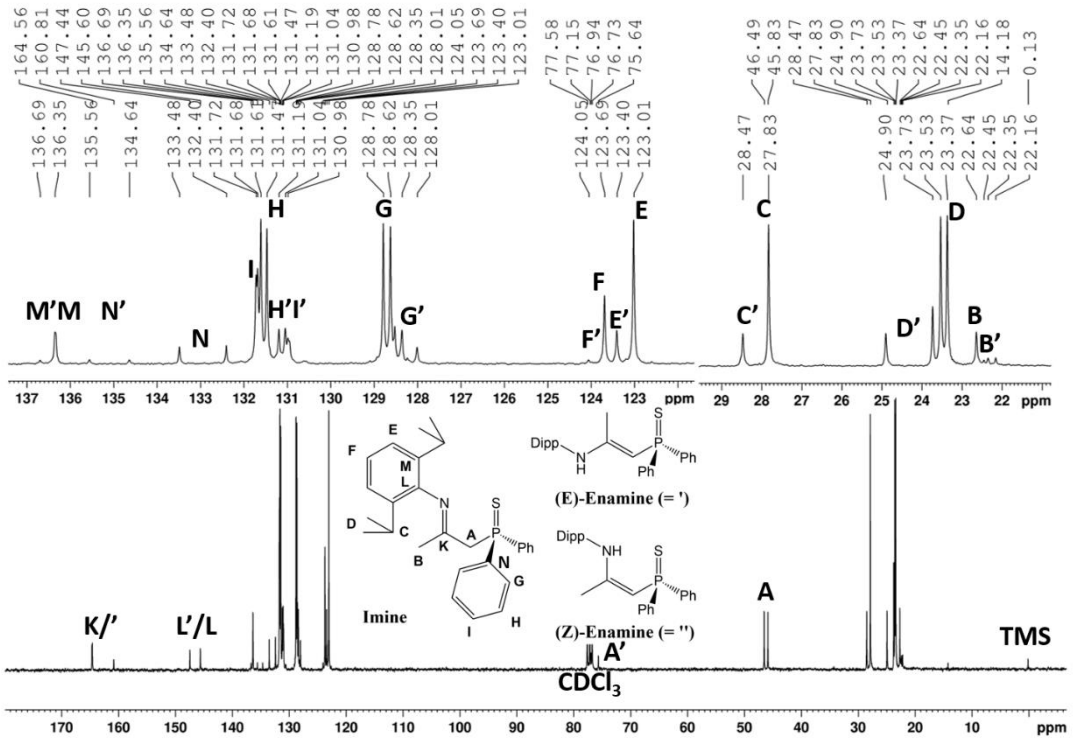

Figure 5.19 ^{13}C NMR spectrum of compound **3** recorded at 298K on a 300 MHz Bruker spectrometer in $CDCl_3$.

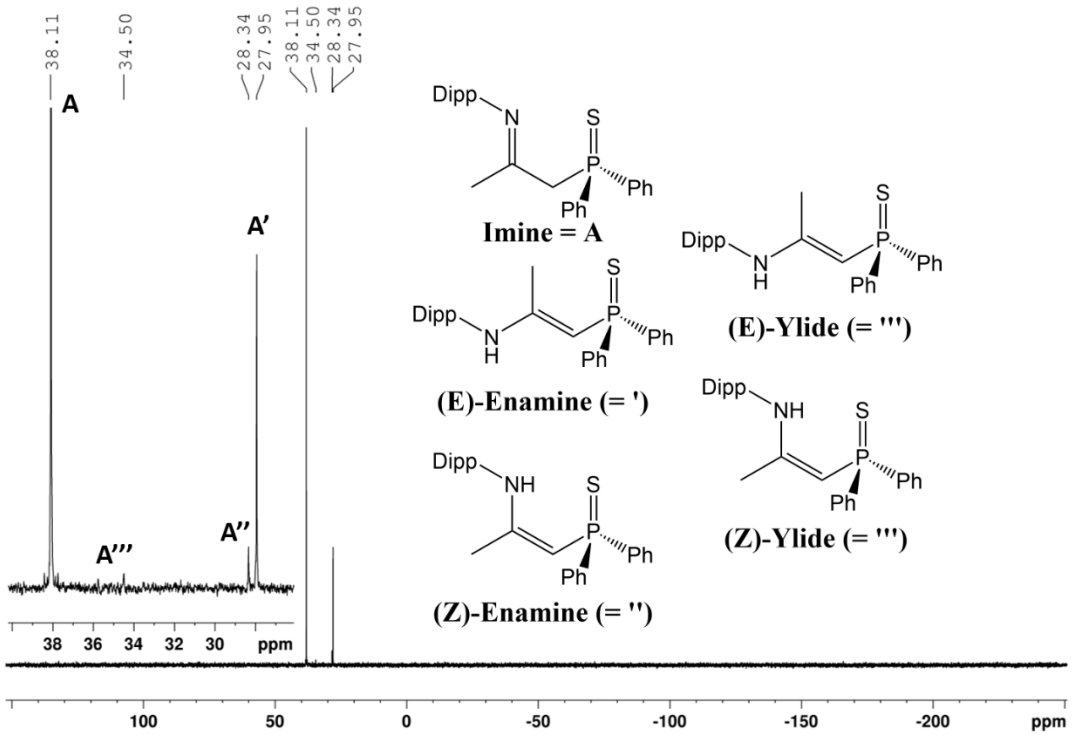

Figure 5.20 $^{31}P\{^{1}H\}$ NMR spectrum (121 MHz) of compound **3** recorded at 298K on a 300 MHz Bruker spectrometer in $CDCl_3$.

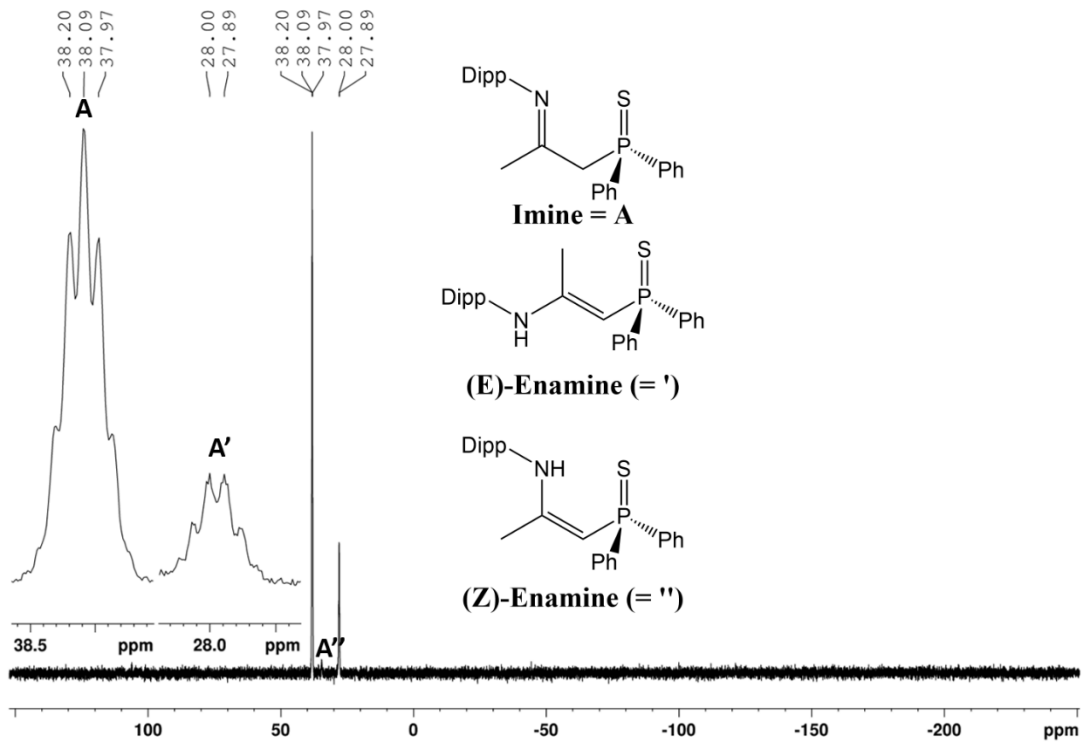

Figure 5.21 ^{31}P NMR spectrum (121 MHz) of compound **3** recorded at 298K on a 300 MHz Bruker spectrometer in $CDCl_3$.

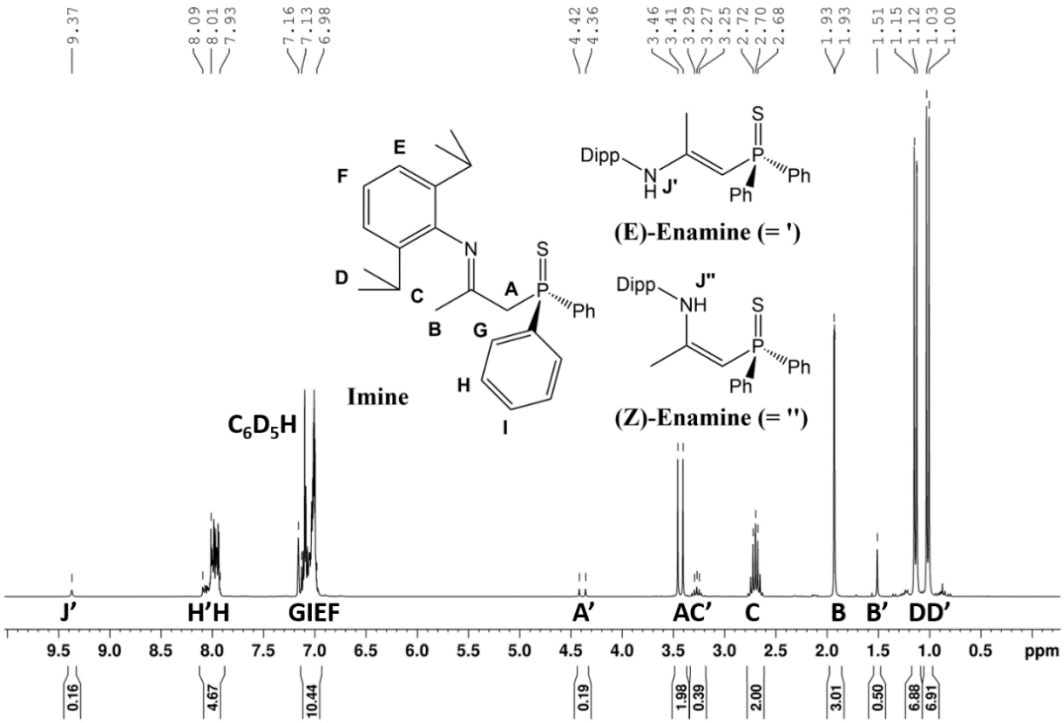

Figure 5.22 ^{1}H NMR spectrum of compound **3** recorded at 298K on a 300 MHz Bruker spectrometer in C_6D_6.

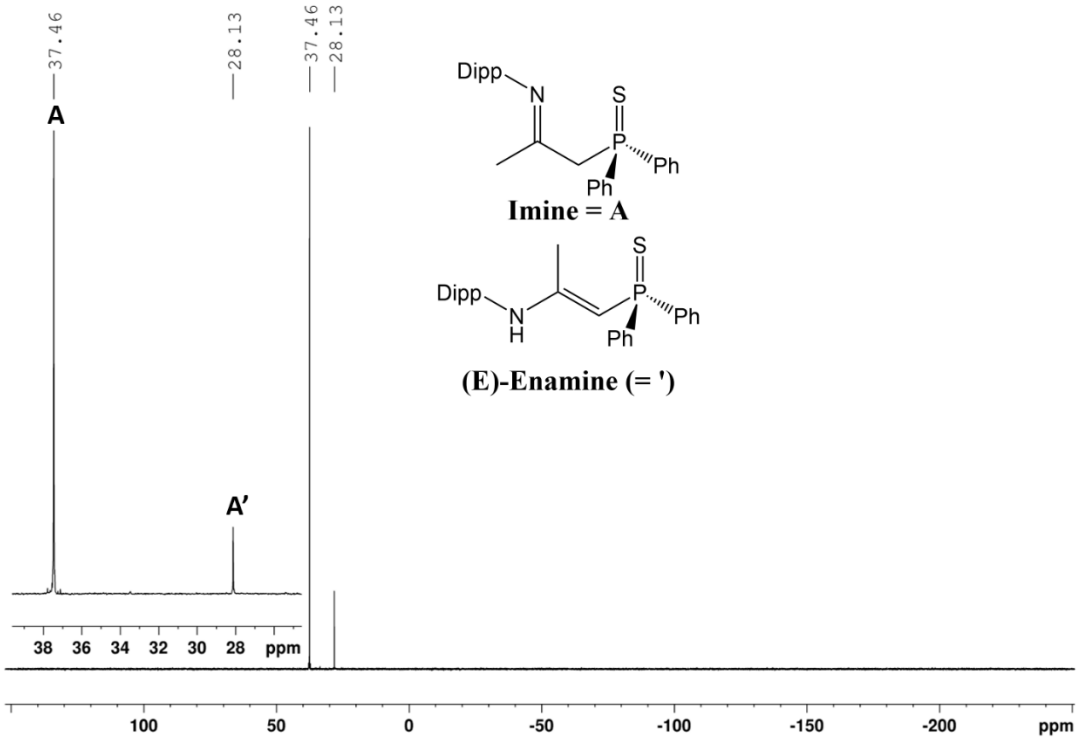

Figure 5.23 $^{31}P\{^{1}H\}$ NMR spectrum (121 MHz) of compound **3** recorded at 298K on a 300 MHz Bruker spectrometer in C_6D_6.

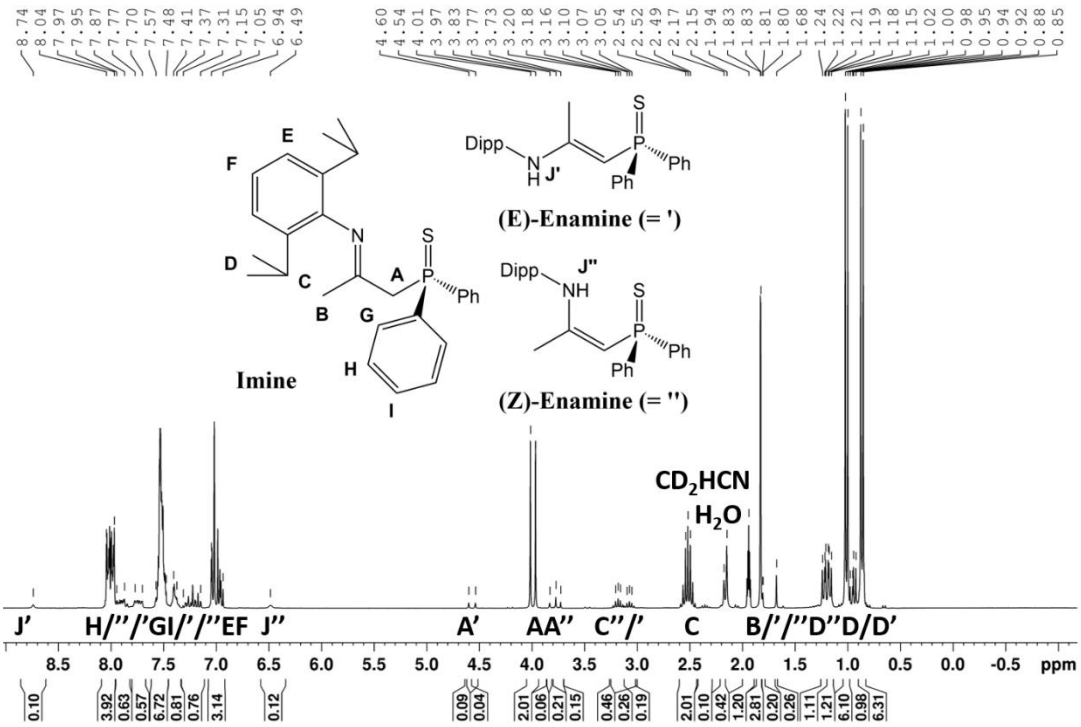

Figure 5.24 ^{1}H NMR spectrum of compound **3** recorded at 298K on a 300 MHz Bruker spectrometer in CD_3CN.

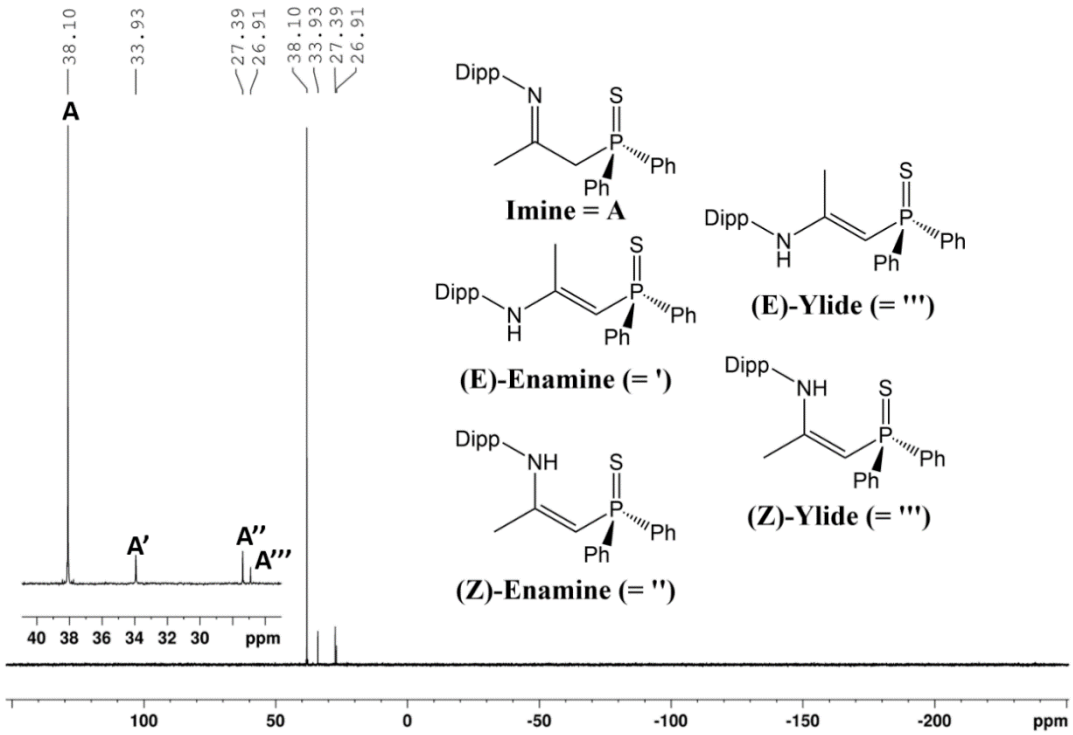

Figure 5.25 $^{31}P\{^{1}H\}$ NMR spectrum (121 MHz) of compound **3** recorded at 298K on a 300 MHz Bruker spectrometer in CD_3CN.

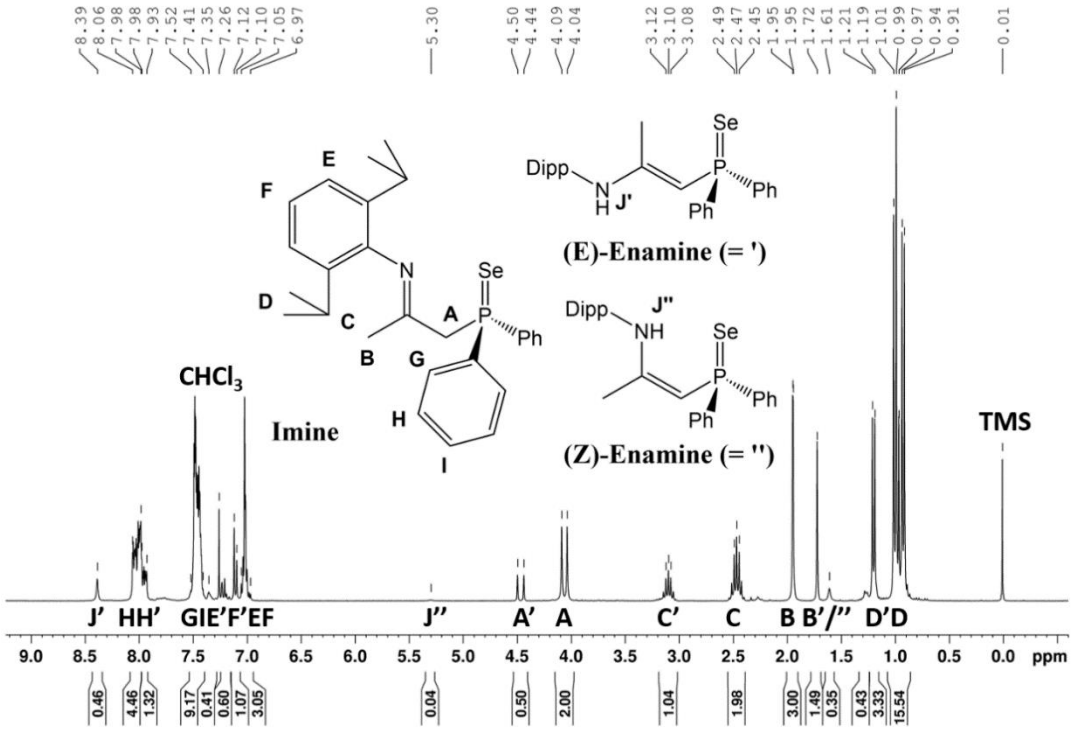

Figure 5.26 ^{1}H NMR spectrum of compound **4** recorded at 298K on a 300 MHz Bruker spectrometer in $CDCl_3$.

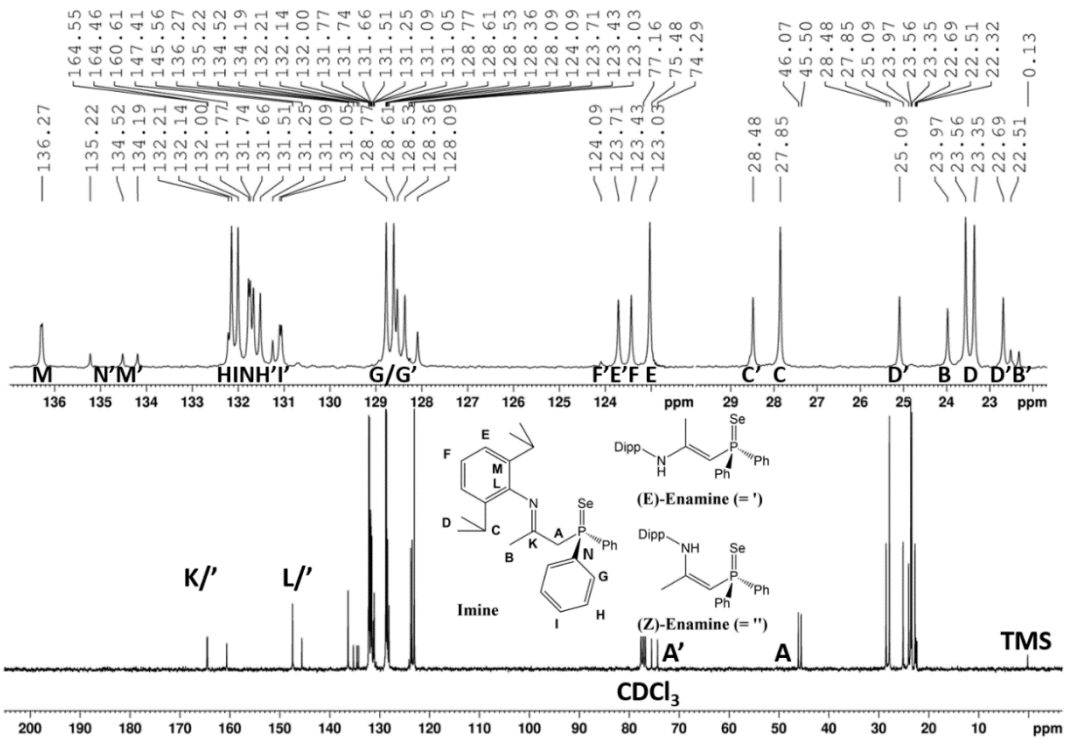

Figure 5.27 ^{13}C NMR spectrum of compound **4** recorded at 298K on a 300 MHz Bruker spectrometer in $CDCl_3$.

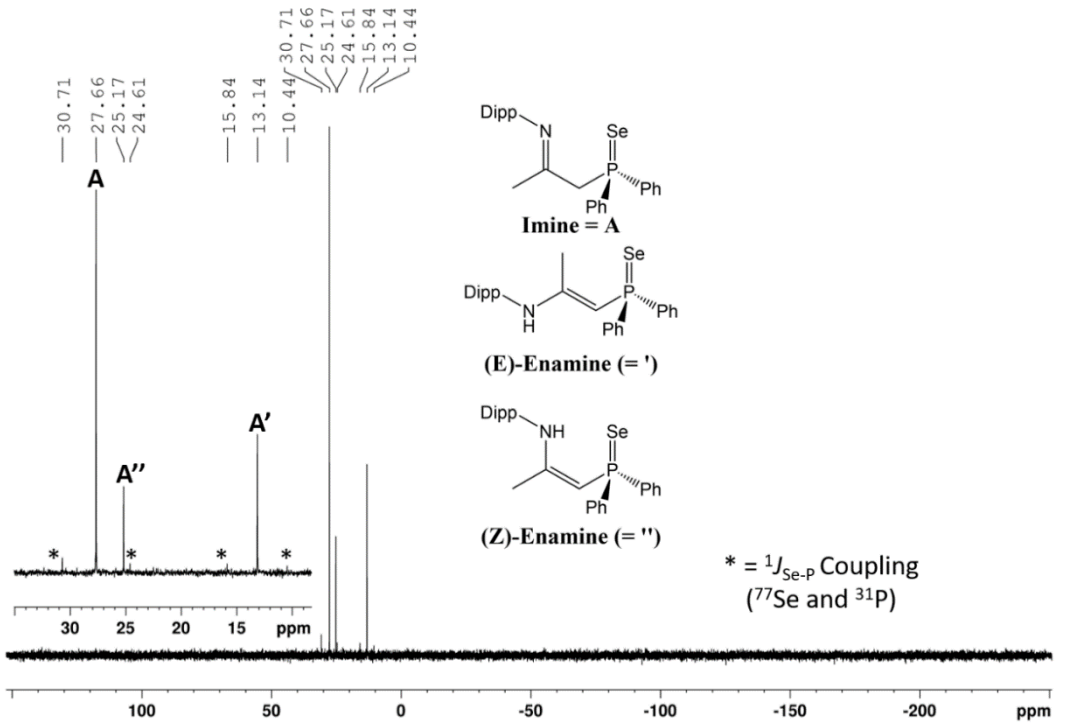

Figure 5.28 $^{31}P\{^{1}H\}$ NMR spectrum (121 MHz) of compound **4** recorded at 298K on a 300 MHz Bruker spectrometer in $CDCl_3$.

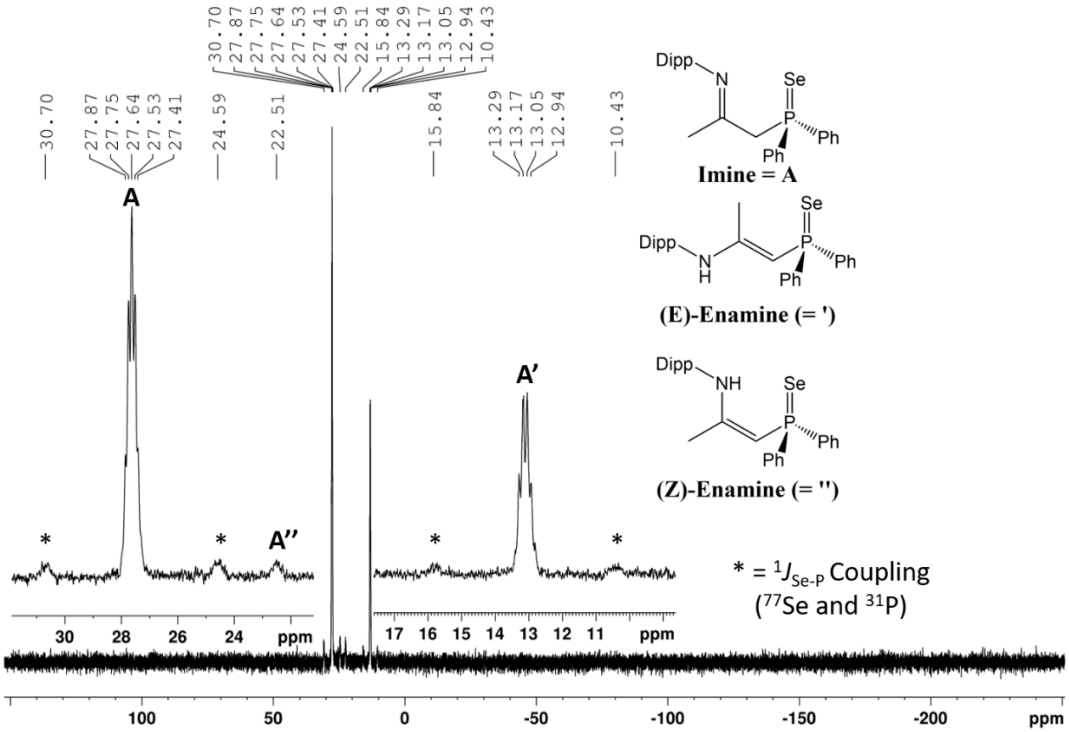

Figure 5.29 ^{31}P NMR spectrum (121 MHz) of compound **4** recorded at 298K on a 300 MHz Bruker spectrometer in $CDCl_3$.

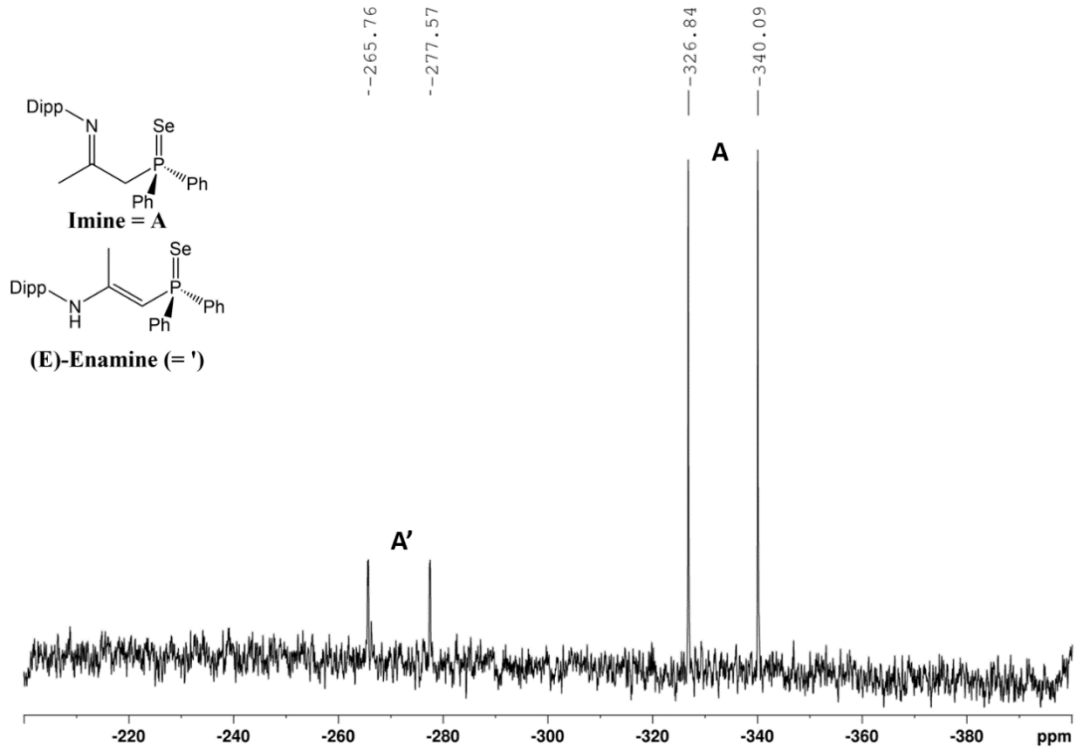

Figure 5.30 ^{77}Se NMR spectrum (57 MHz) of compound **4** recorded at 298K on a 300 MHz Bruker spectrometer in $CDCl_3$.

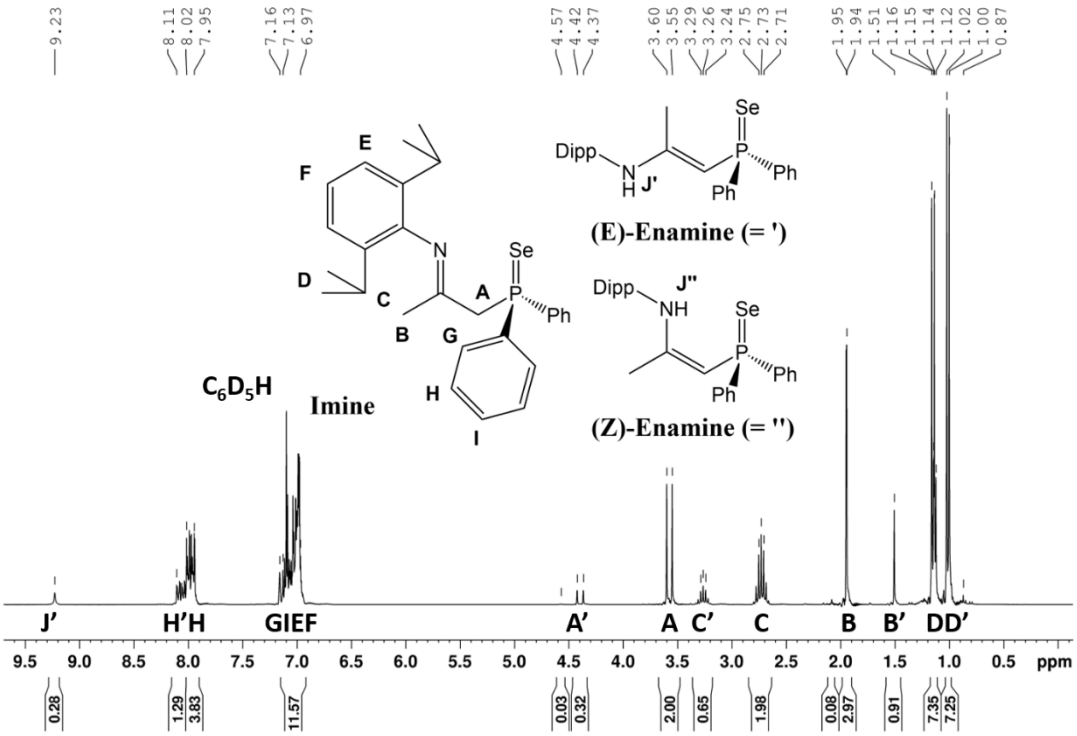

Figure 5.31 ^{1}H NMR spectrum of compound **4** recorded at 298K on a 300 MHz Bruker spectrometer in C_6D_6.

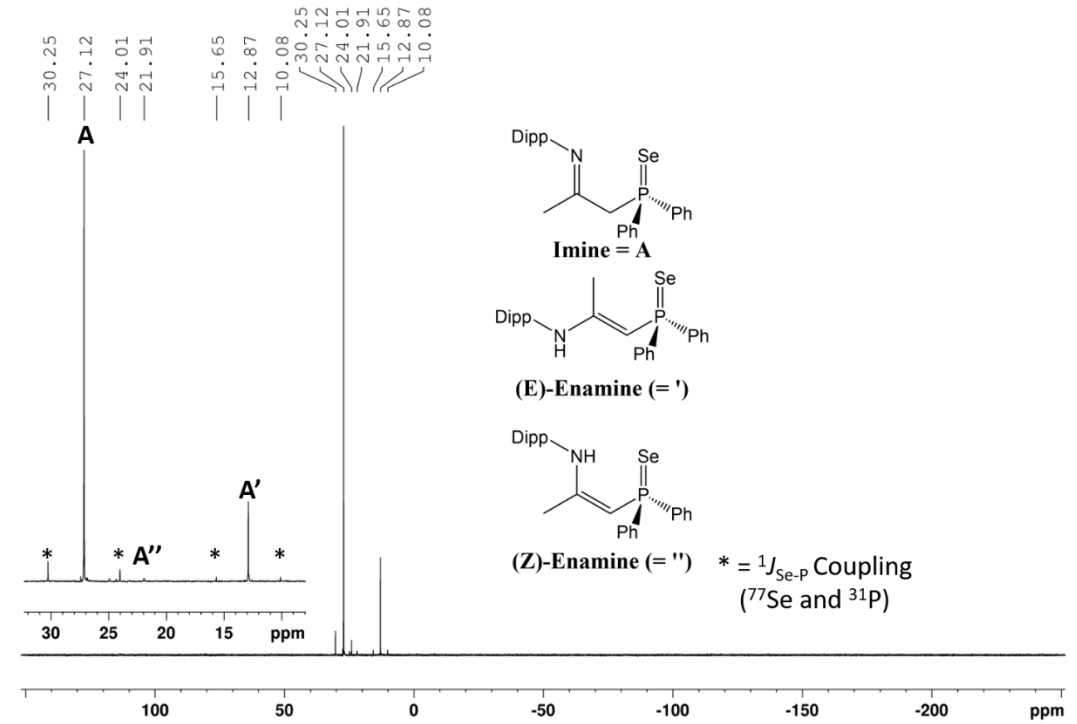

Figure 5.32 $^{31}P\{^{1}H\}$ NMR spectrum (121 MHz) of compound **4** recorded at 298K on a 300 MHz Bruker spectrometer in C_6D_6.

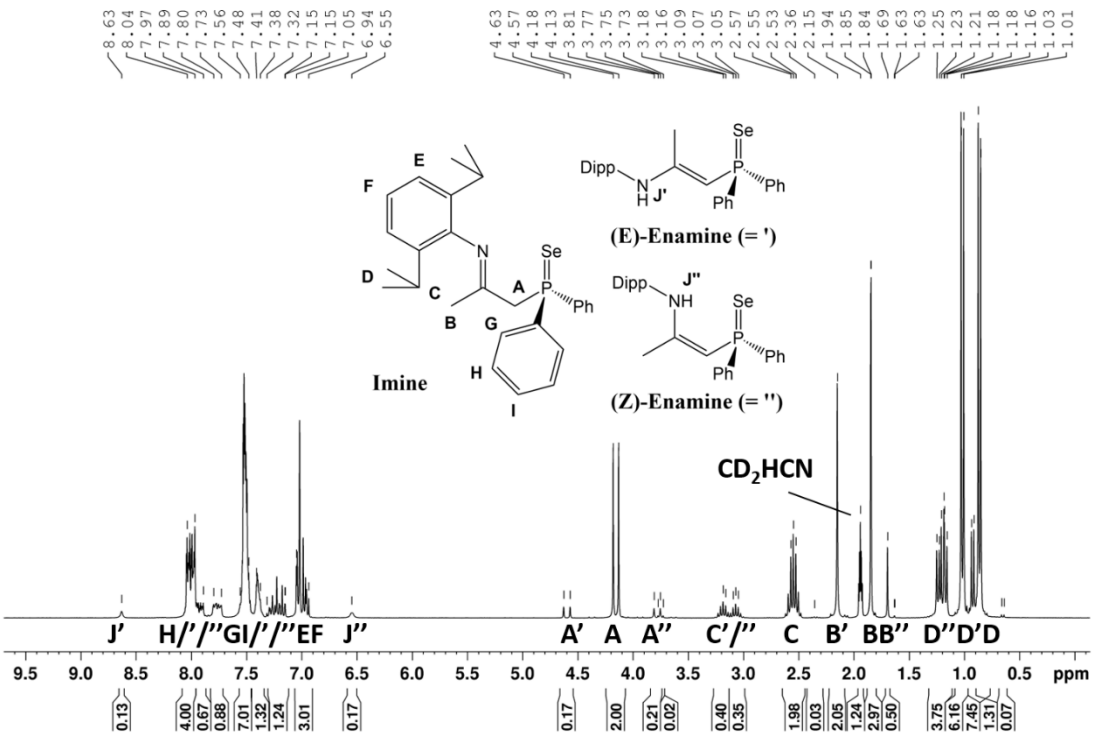

Figure 5.33 ^{1}H NMR spectrum of compound **4** recorded at 298K on a 300 MHz Bruker spectrometer in CD_3CN.

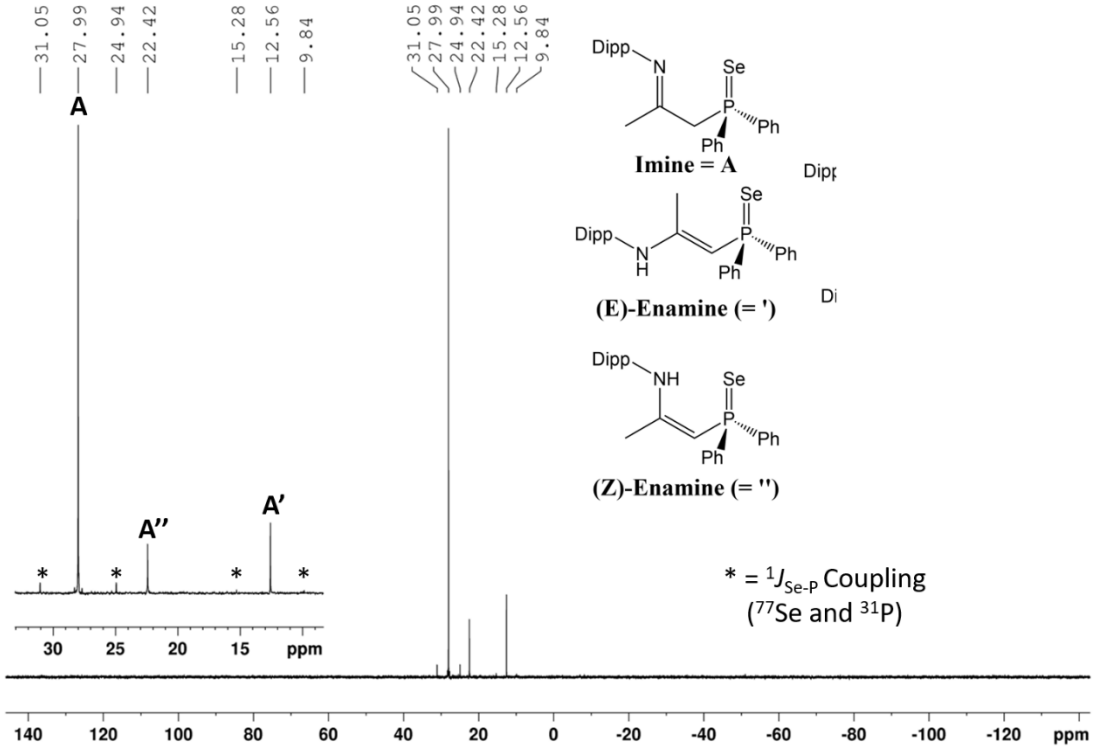

Figure 5.34 $^{31}P\{^{1}H\}$ NMR spectrum (121 MHz) of compound **4** recorded at 298K on a 300 MHz Bruker spectrometer in CD_3CN.

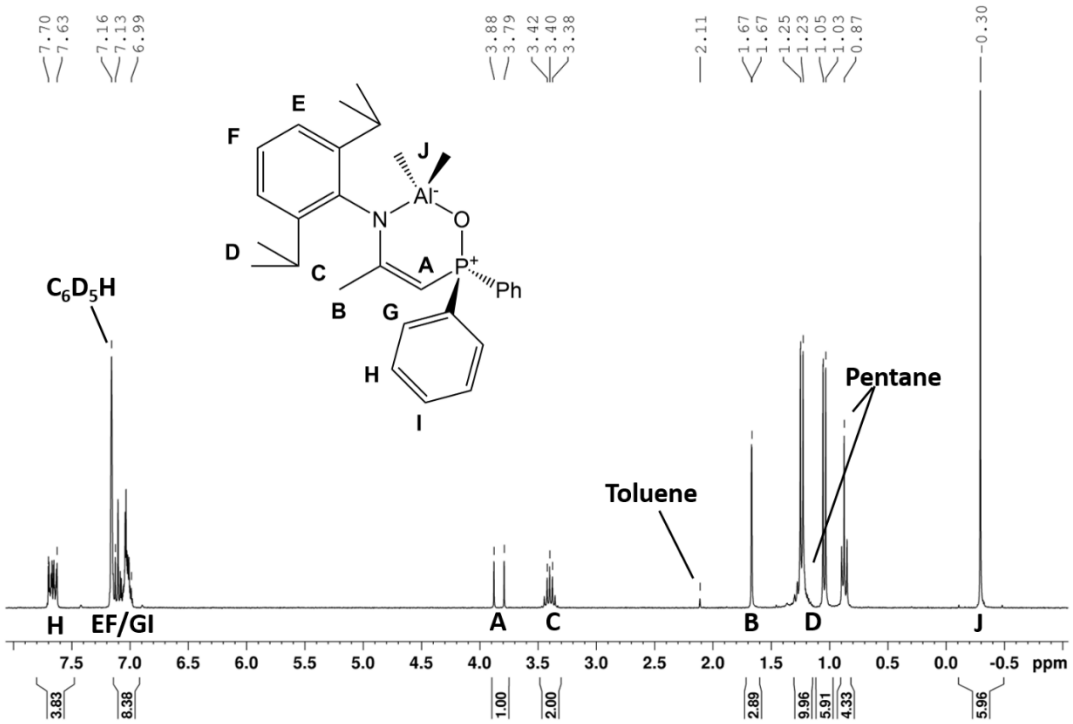

Figure 5.35 ^{1}H NMR spectrum of compound **5** recorded at 298K on a 300 MHz Bruker spectrometer in C_6D_6.

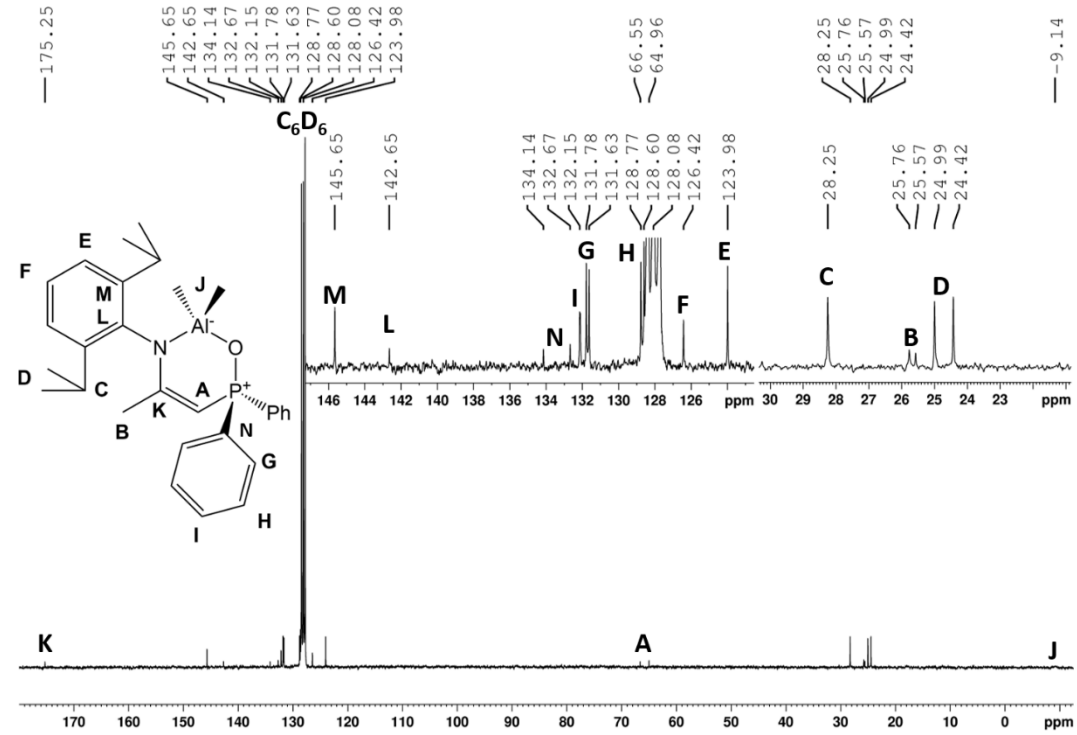

Figure 5.36 ^{13}C NMR spectrum of compound **5** recorded at 298K on a 300 MHz Bruker spectrometer in C_6D_6.

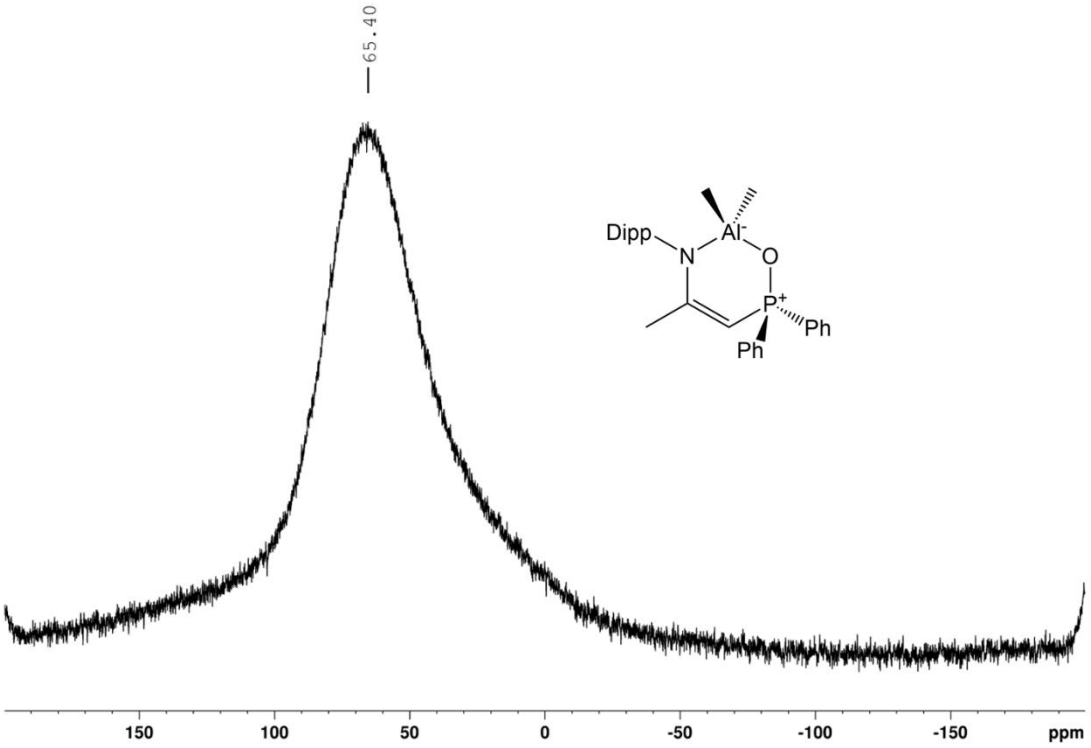

Figure 5.37 ^{27}Al NMR spectrum of compound **5** recorded at 298K on a 300 MHz Bruker spectrometer in C_6D_6.

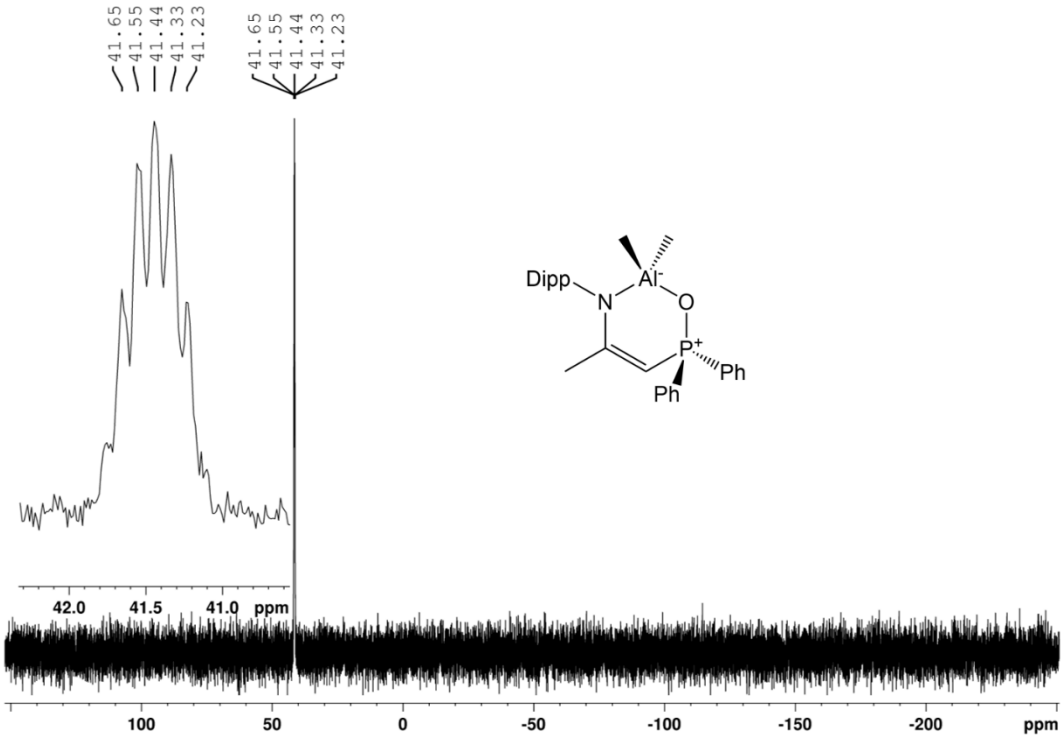

Figure 5.38 ^{31}P NMR spectrum of compound **5** recorded at 298K on a 300 MHz Bruker spectrometer in C_6D_6.

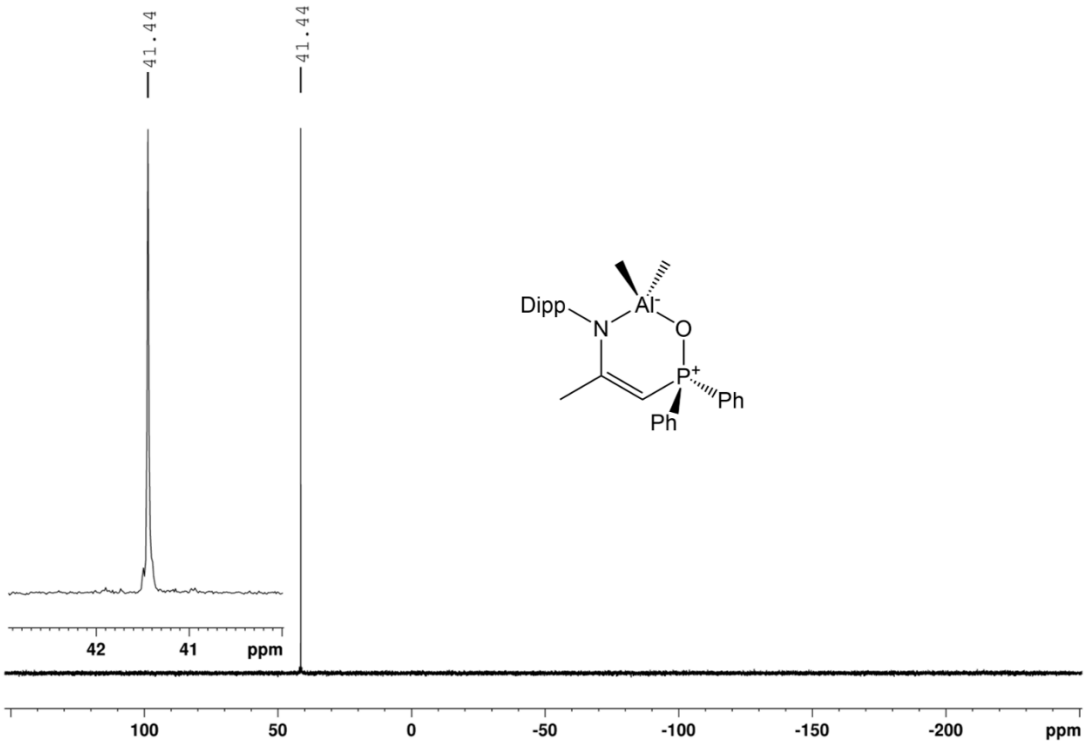

Figure 5.39 $^{31}P\{^{1}H\}$ NMR spectrum of compound **5** recorded at 298K on a 300 MHz Bruker spectrometer in C_6D_6.

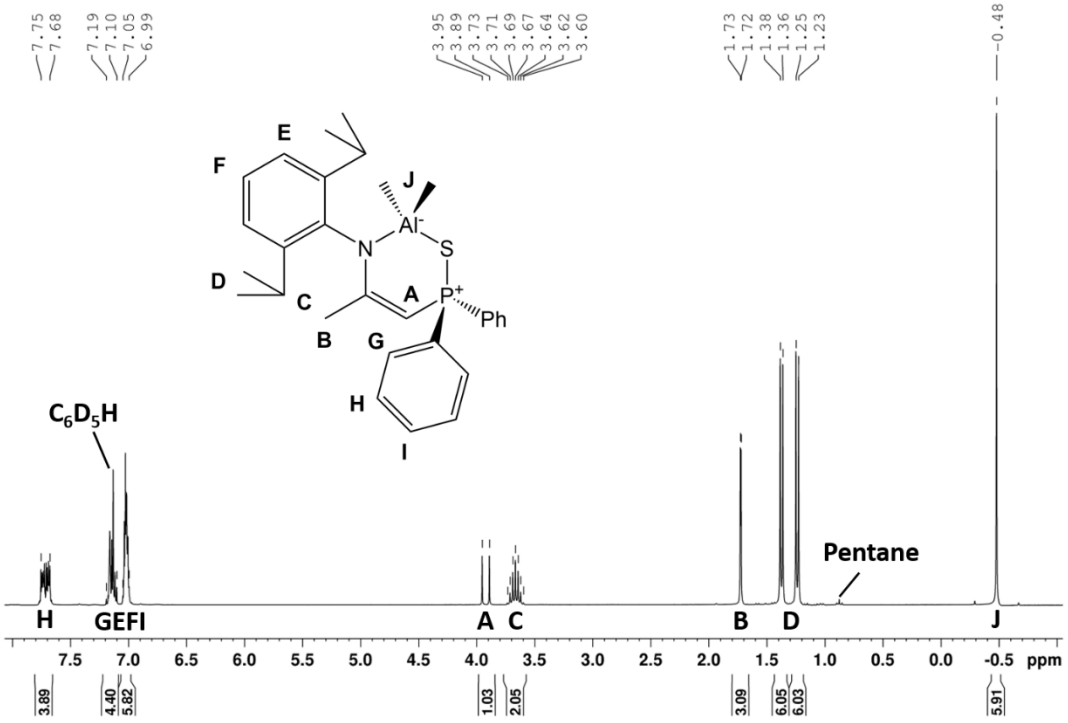

Figure 5.40 ^{1}H NMR spectrum of compound **6** recorded at 298K on a 300 MHz Bruker spectrometer in C_6D_6.

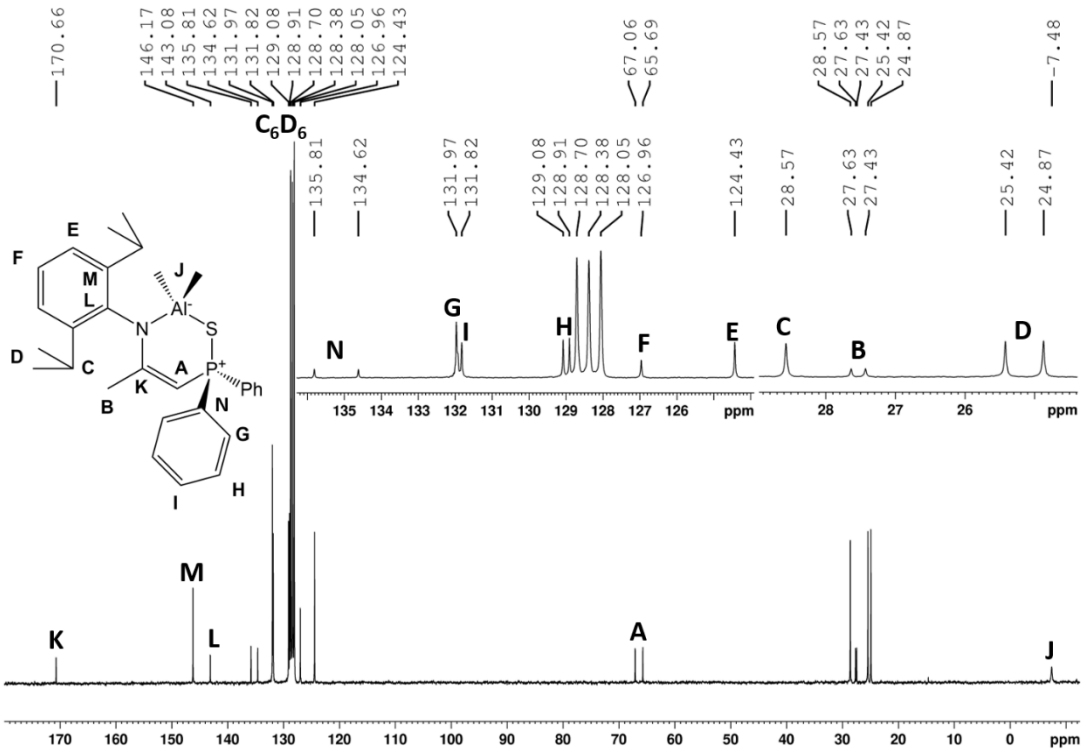

Figure 5.41 ^{13}C NMR spectrum of compound **6** recorded at 298K on a 300 MHz Bruker spectrometer in C_6D_6.

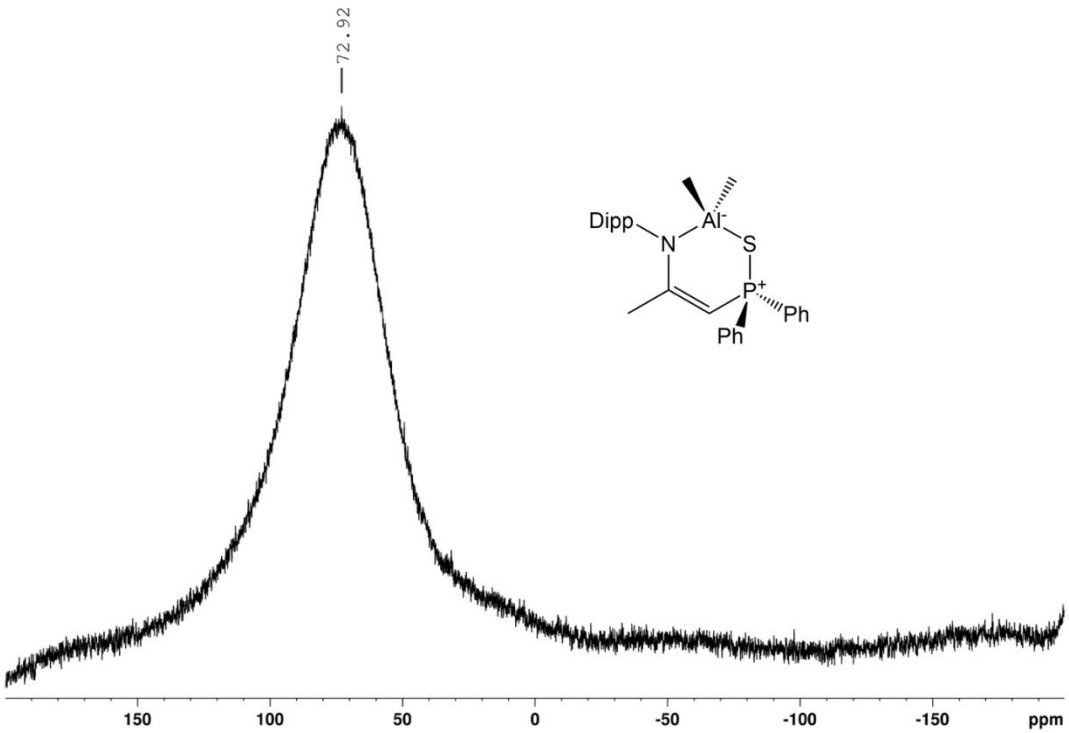

Figure 5.42 ^{27}Al NMR spectrum of compound **6** recorded at 298K on a 300 MHz Bruker spectrometer in C_6D_6.

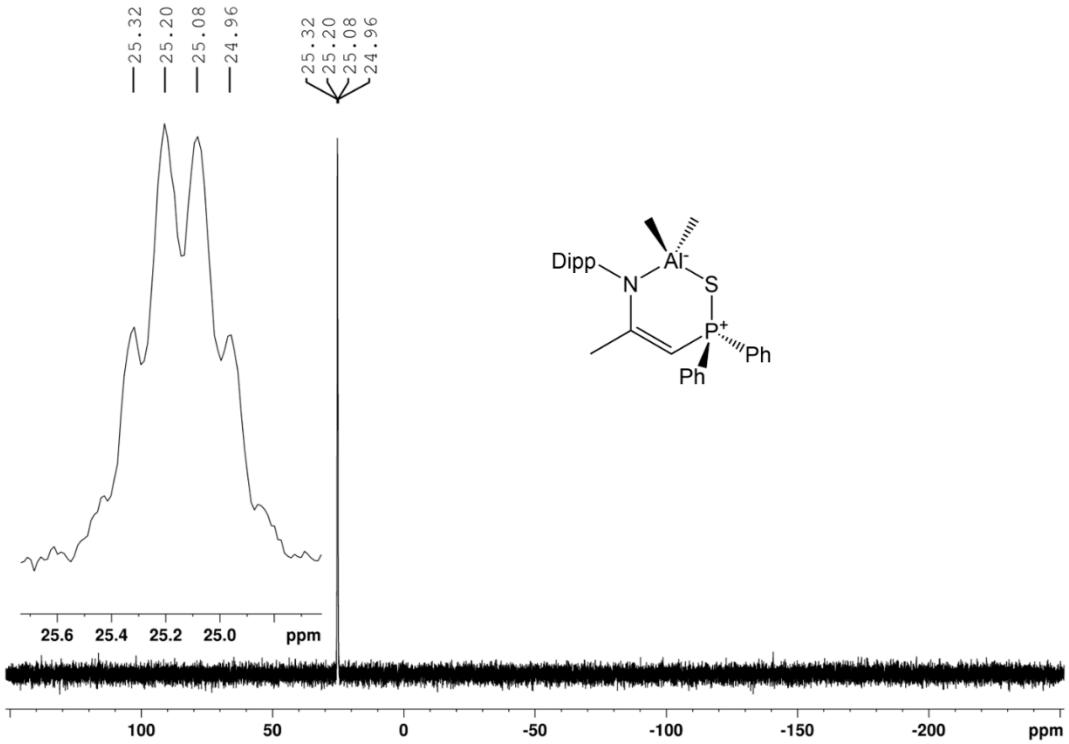

Figure 5.43 ^{31}P NMR spectrum of compound **6** recorded at 298K on a 300 MHz Bruker spectrometer in C_6D_6.

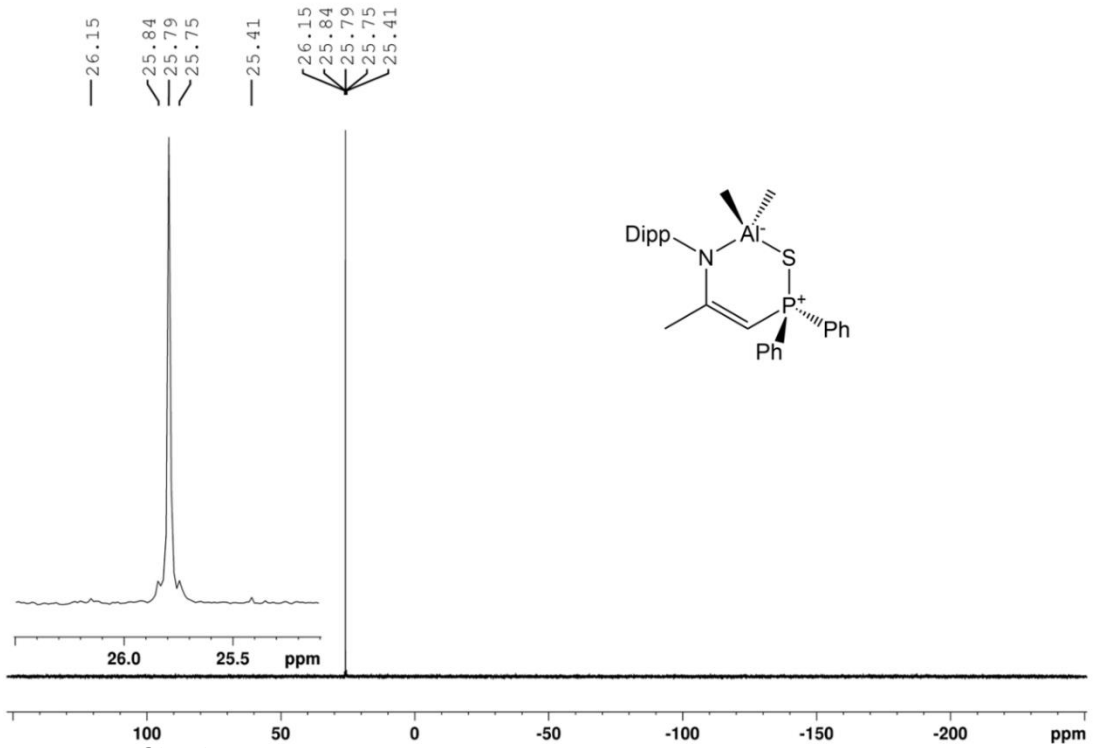

Figure 5.44 $^{31}P\{^{1}H\}$ NMR spectrum of compound **6** recorded at 298K on a 300 MHz Bruker spectrometer in C_6D_6.

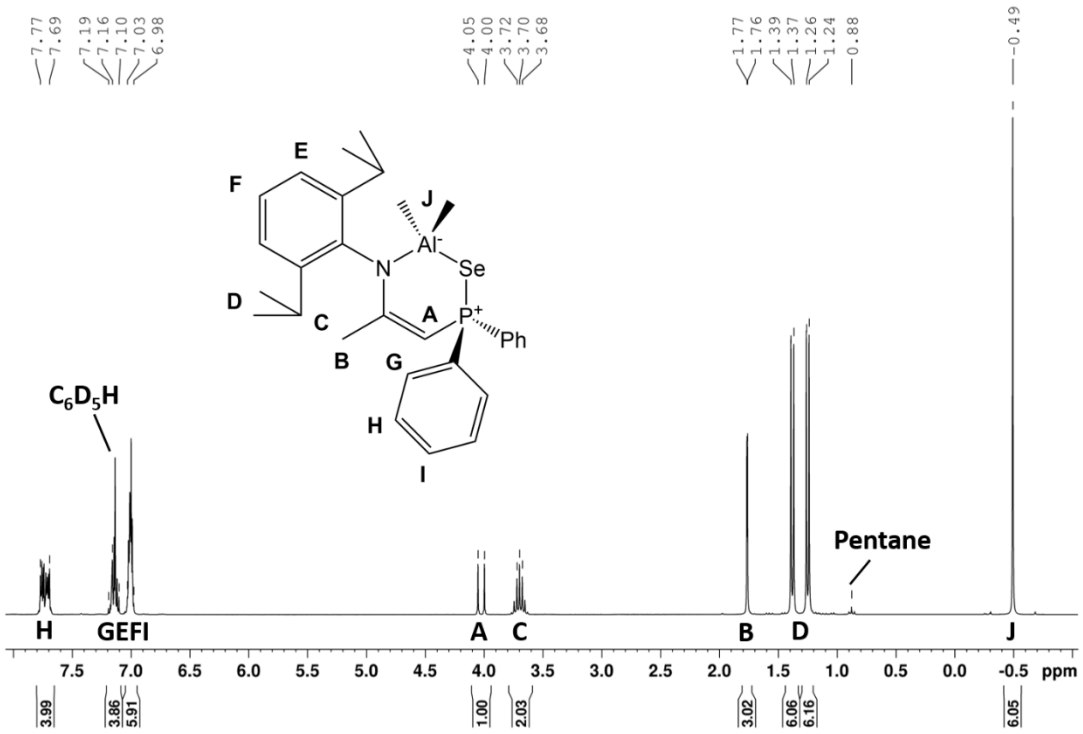

Figure 5.45 ^{1}H NMR spectrum of compound **7** recorded at 298K on a 300 MHz Bruker spectrometer in C_6D_6.

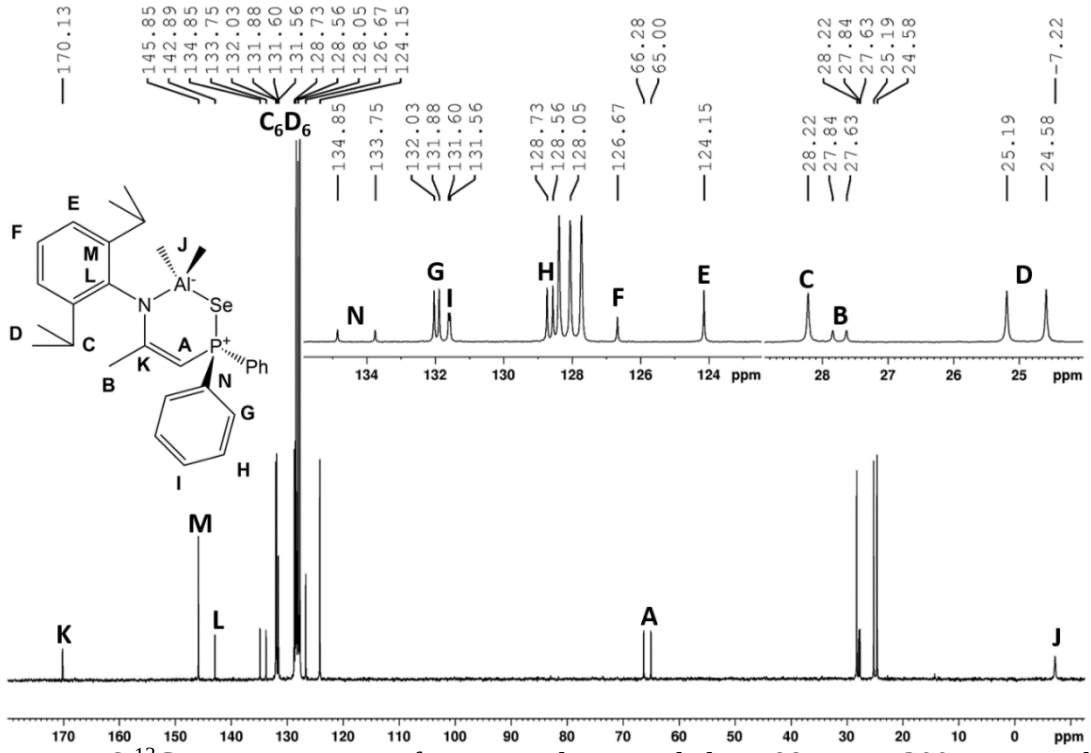

Figure 5.46 ^{13}C NMR spectrum of compound **7** recorded at 298K on a 300 MHz Bruker spectrometer in C_6D_6.

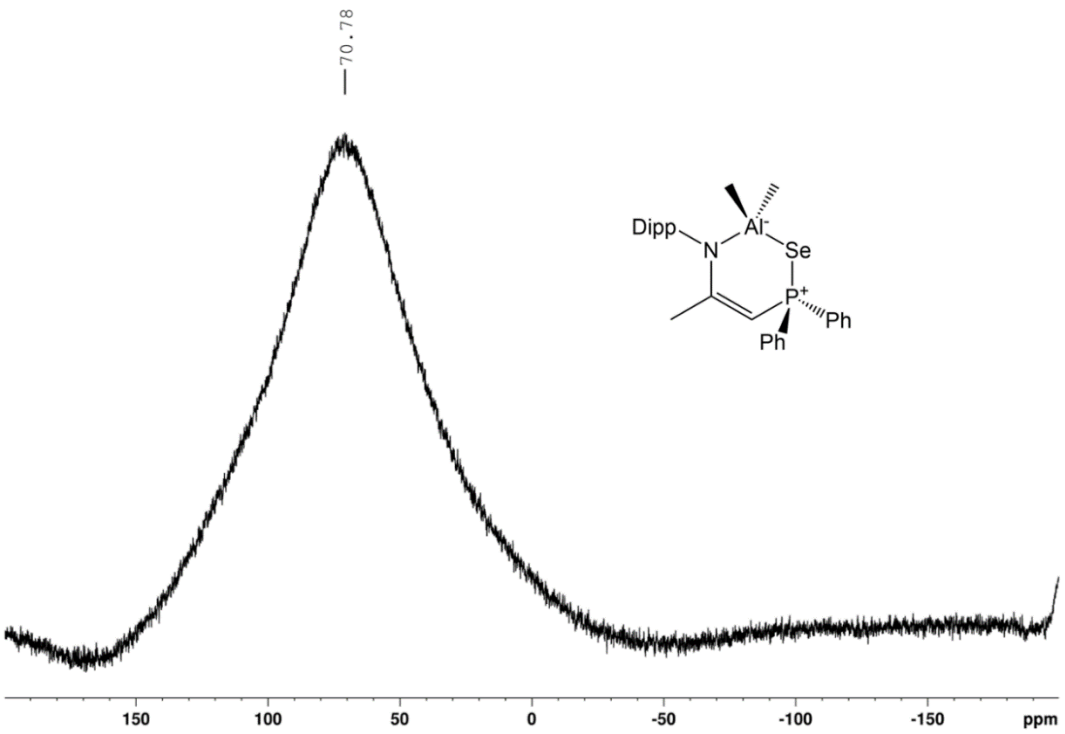

Figure 5.47 ^{27}Al NMR spectrum of compound **7** recorded at 298K on a 300 MHz Bruker spectrometer in C_6D_6.

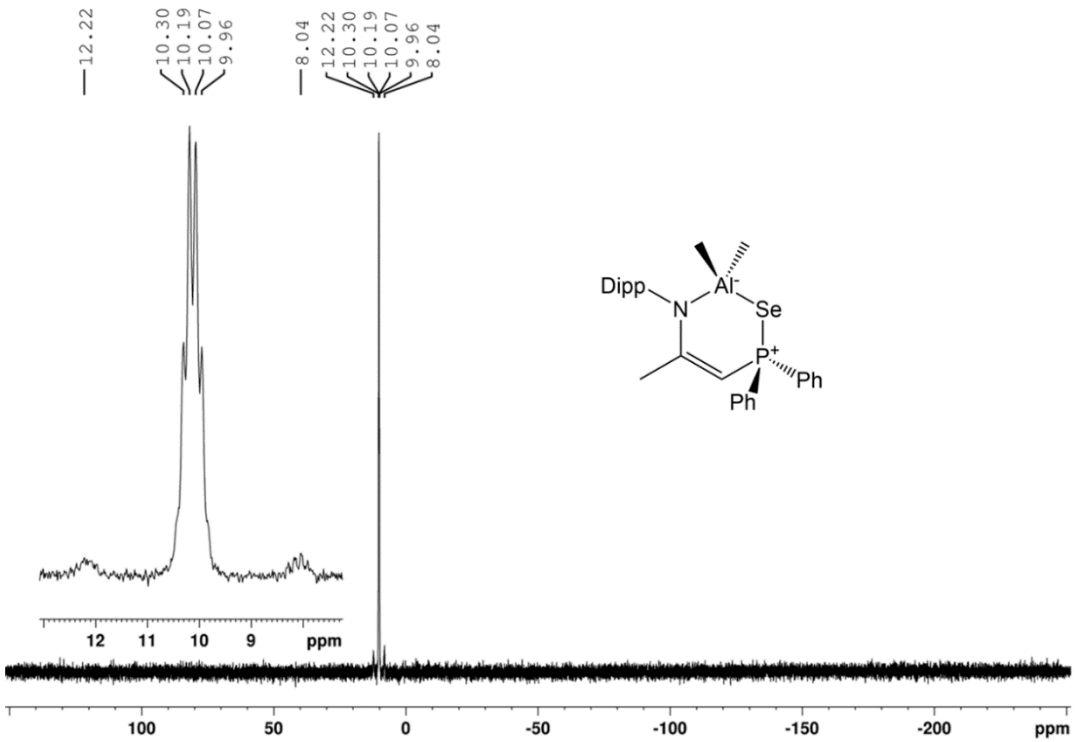

Figure 5.48 ^{31}P NMR spectrum of compound **7** recorded at 298K on a 300 MHz Bruker spectrometer in C_6D_6.

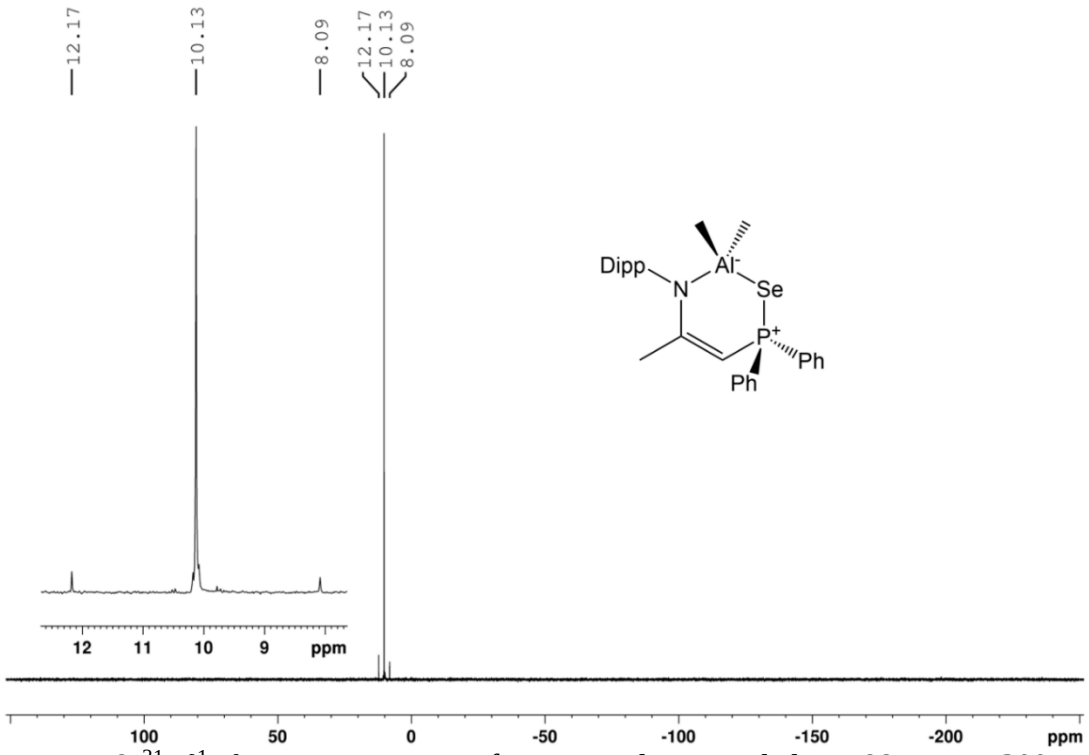

Figure 5.49 $^{31}P\{^{1}H\}$ NMR spectrum of compound **7** recorded at 298K on a 300 MHz Bruker spectrometer in C_6D_6.

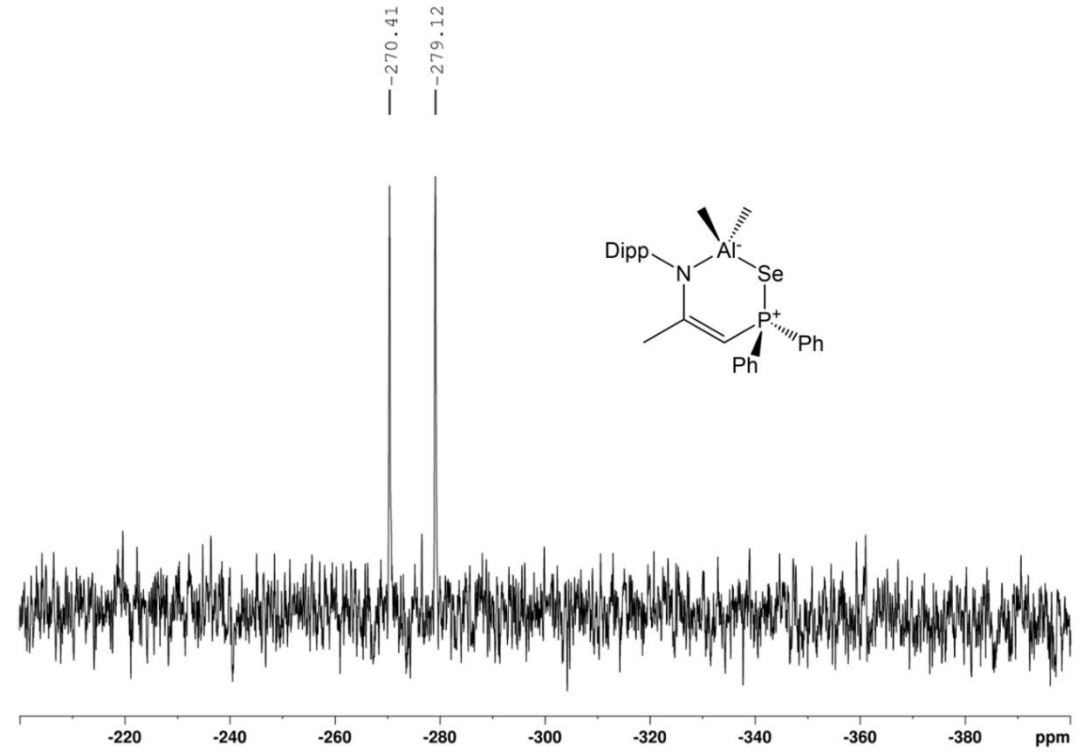

Figure 5.50 77Se NMR spectrum of compound **7** recorded at 298K on a 300 MHz Bruker spectrometer in C_6D_6.

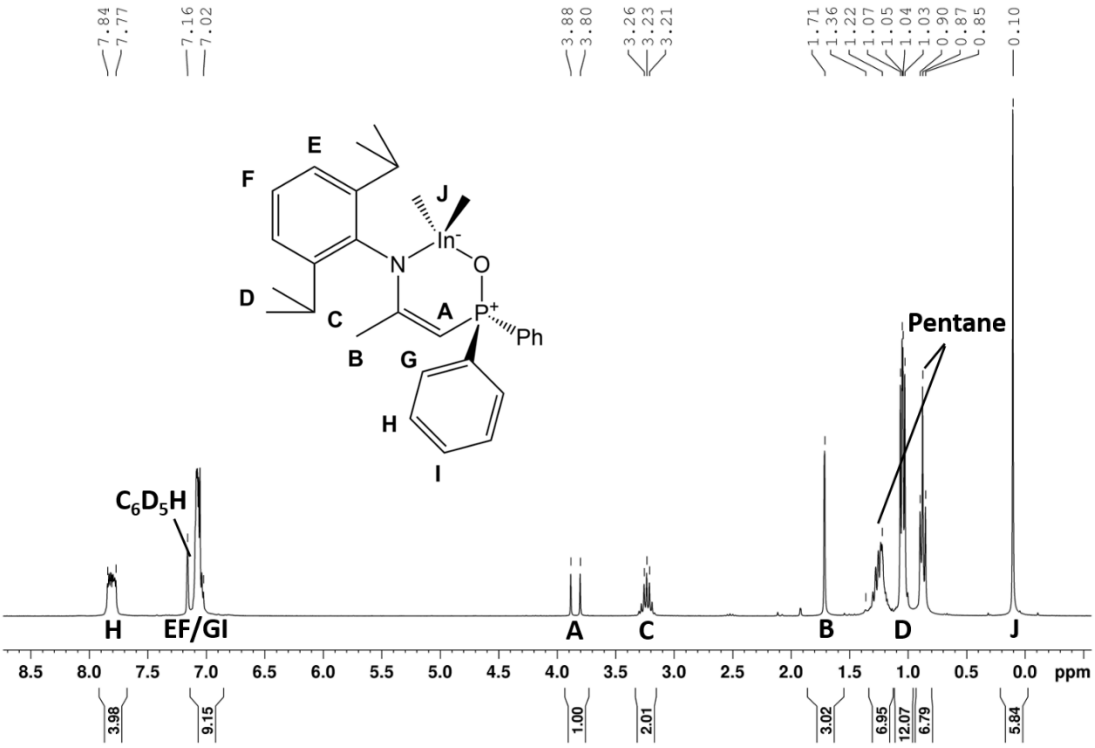

Figure 5.51 ^{1}H NMR spectrum of compound **8** recorded at 298K on a 300 MHz Bruker spectrometer in C_6D_6.

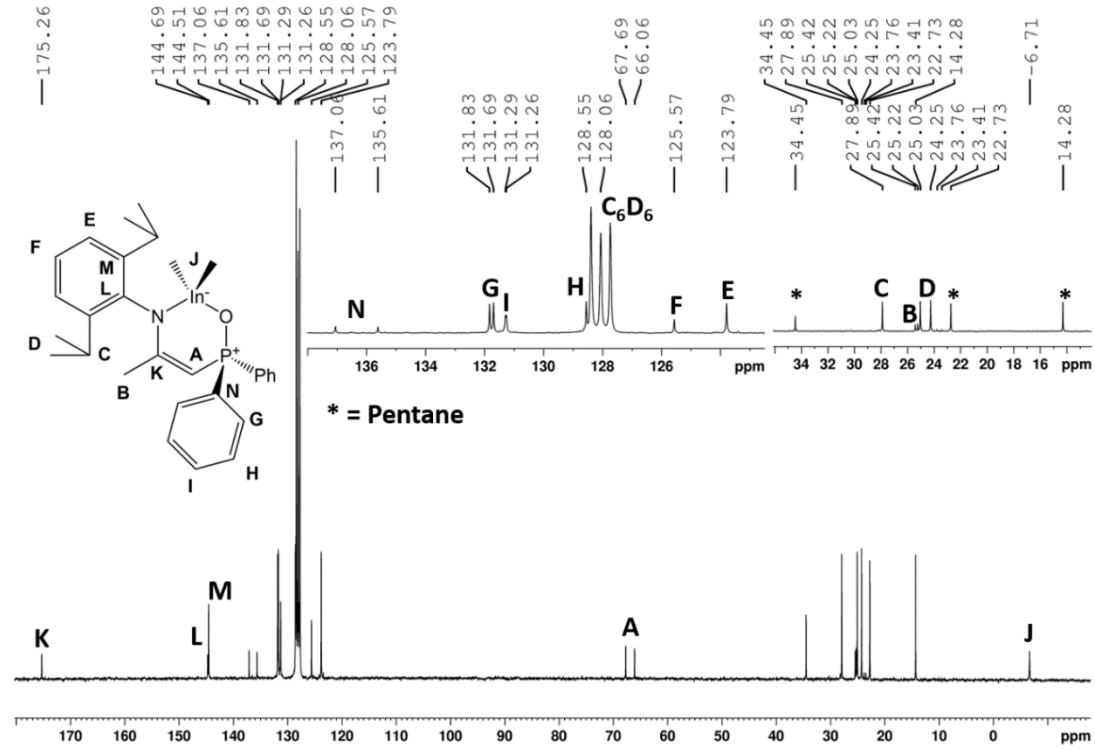

Figure 5.52 ^{13}C NMR spectrum of compound **8** recorded at 298K on a 300 MHz Bruker spectrometer in C_6D_6.

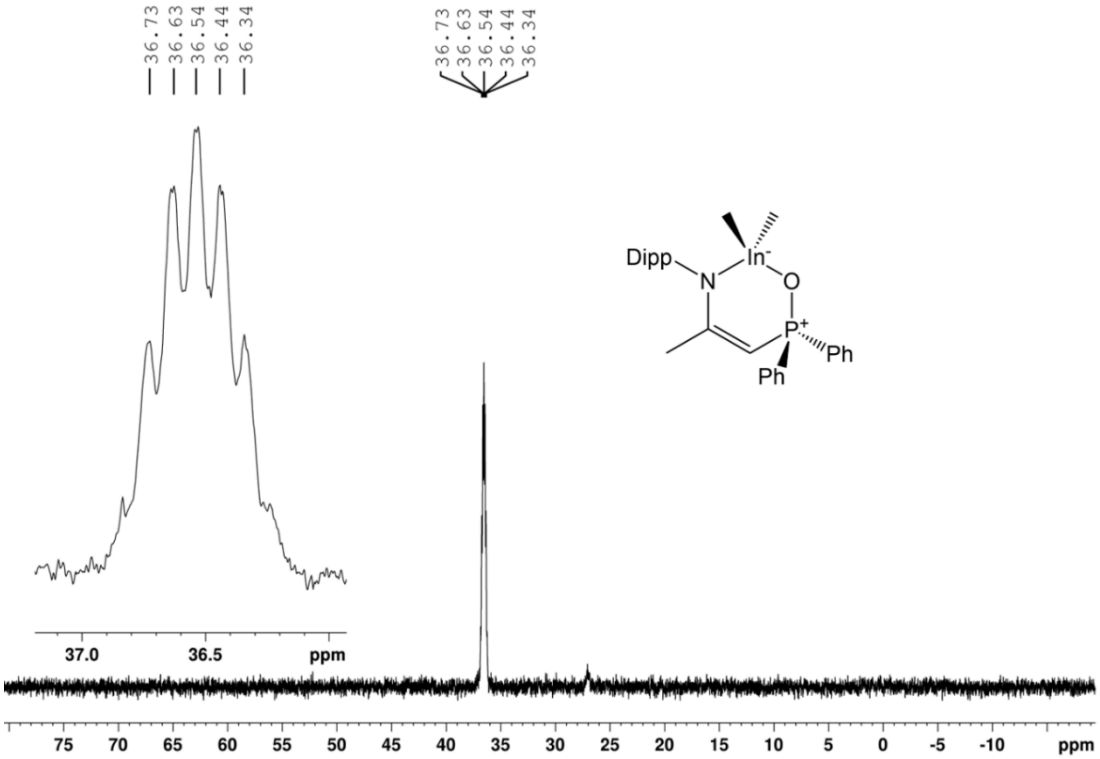

Figure 5.53 ^{31}P NMR spectrum of compound **8** recorded at 298K on a 300 MHz Bruker spectrometer in C_6D_6.

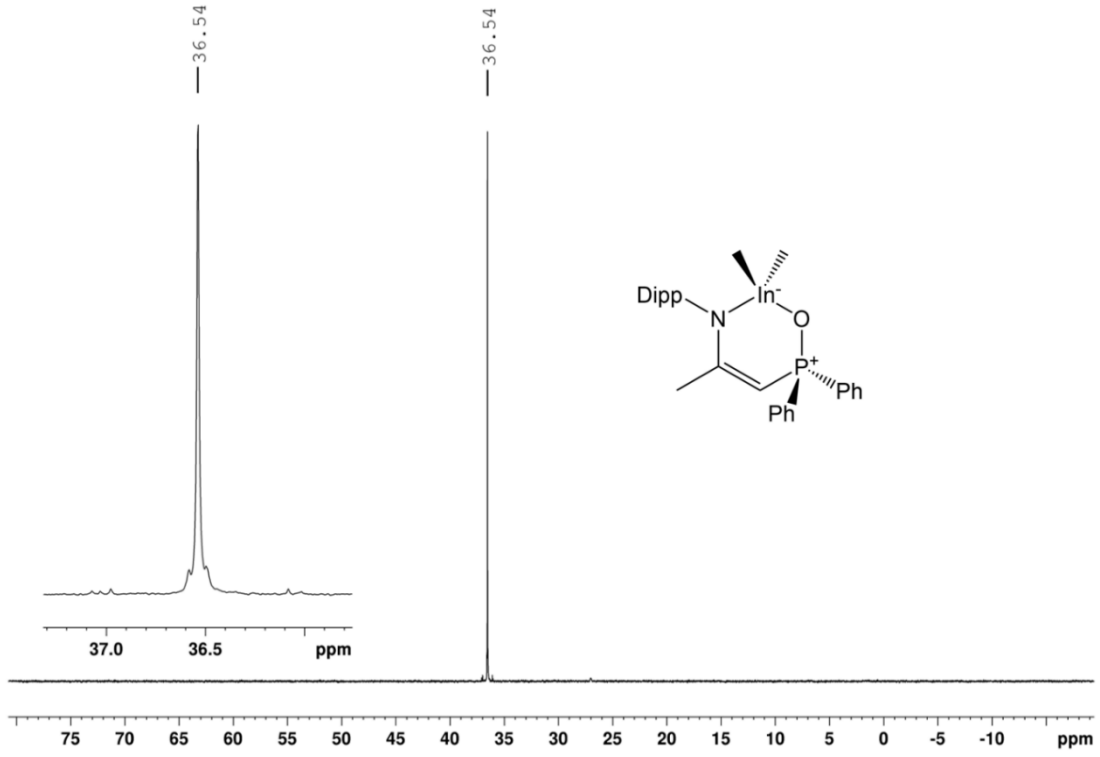

Figure 5.54 $^{31}P\{^{1}H\}$ NMR spectrum of compound **8** recorded at 298K on a 300 MHz Bruker spectrometer in C_6D_6.

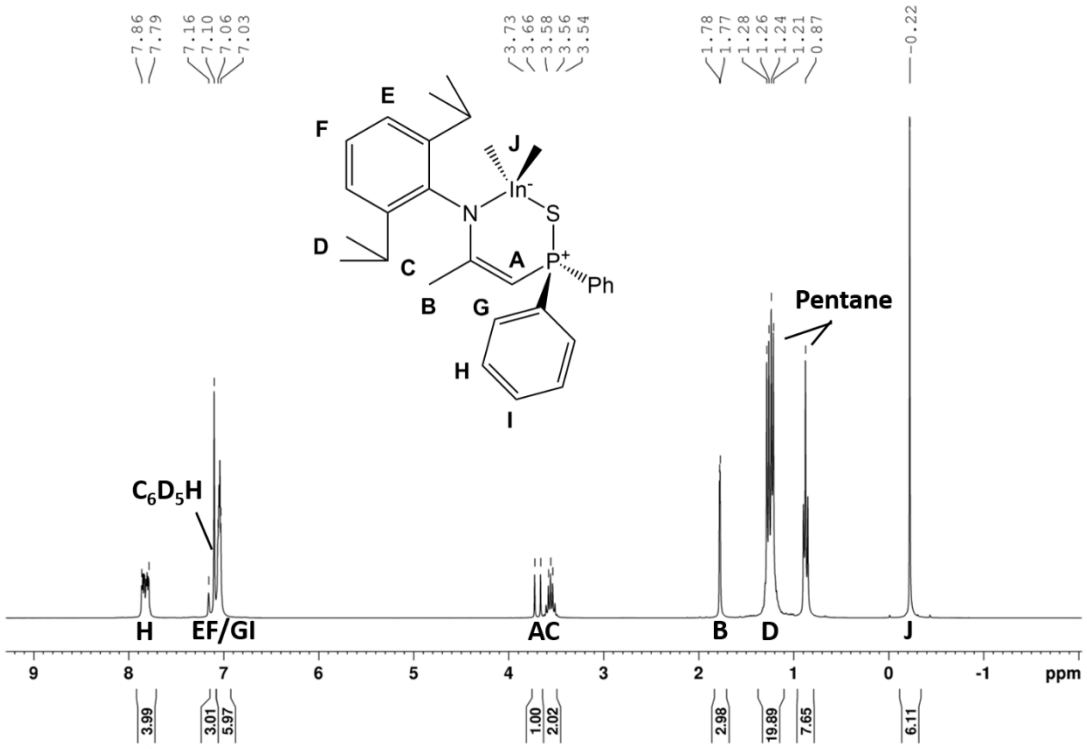

Figure 5.55 ^{1}H NMR spectrum of compound **9** recorded at 298K on a 300 MHz Bruker spectrometer in C_6D_6.

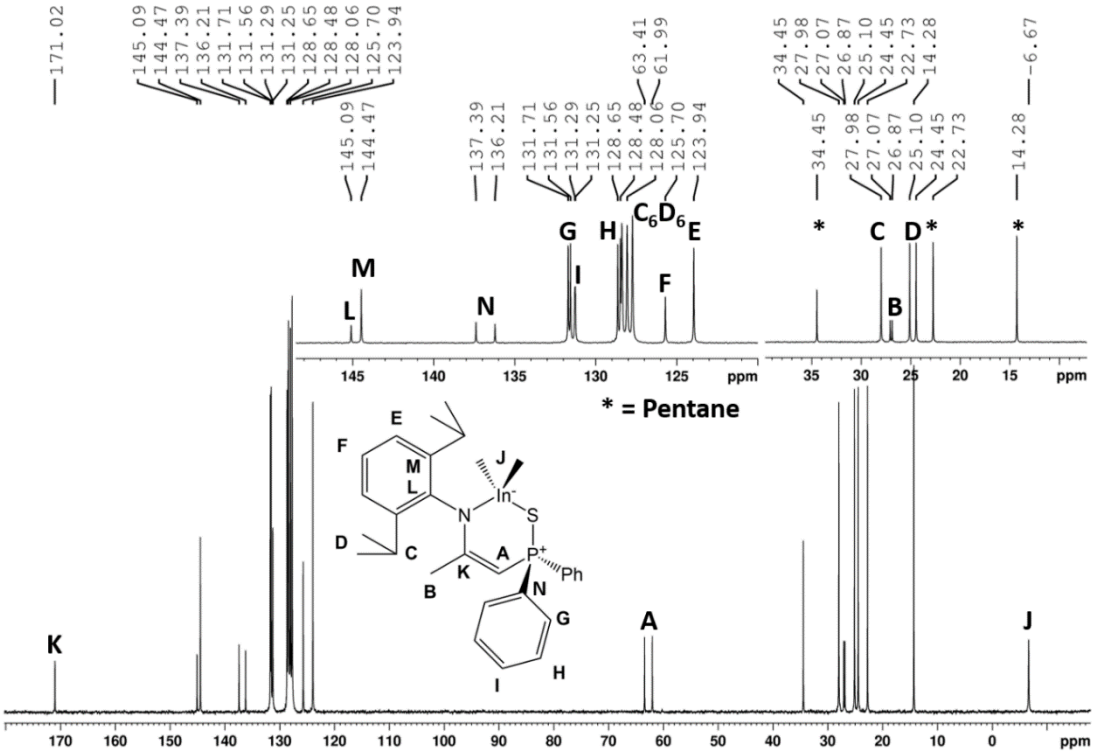

Figure 5.56 ^{13}C NMR spectrum of compound **9** recorded at 298K on a 300 MHz Bruker spectrometer in C_6D_6.

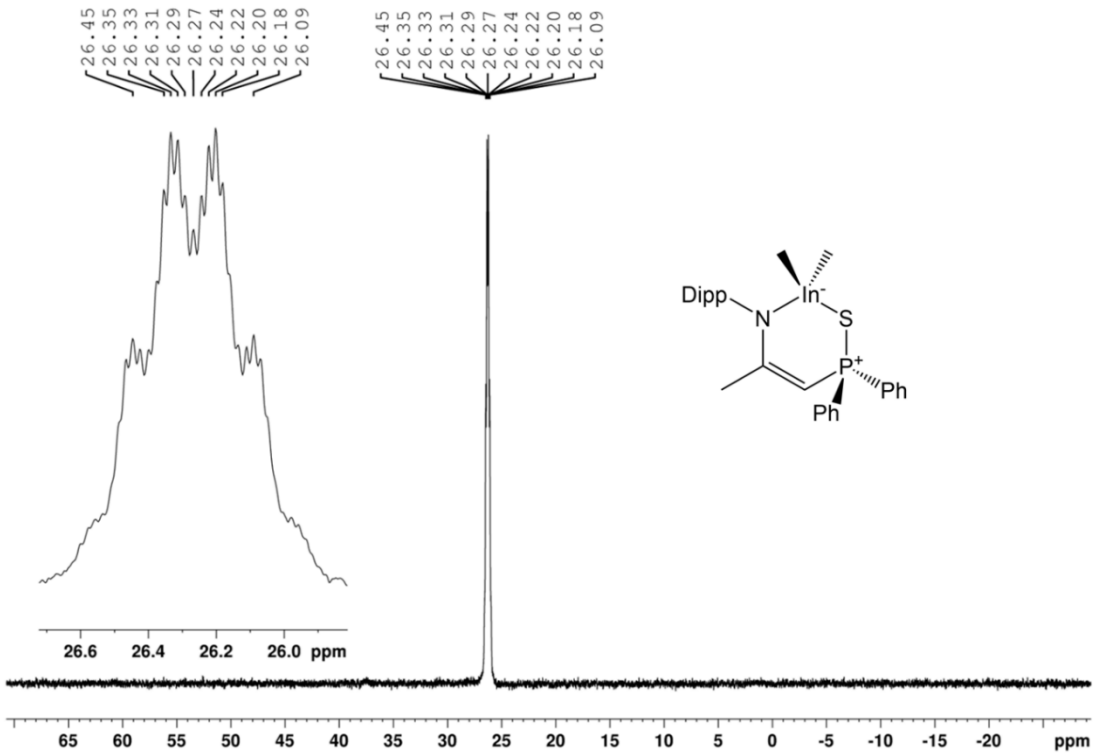

Figure 5.57 ^{31}P NMR spectrum of compound **9** recorded at 298K on a 300 MHz Bruker spectrometer in C_6D_6.

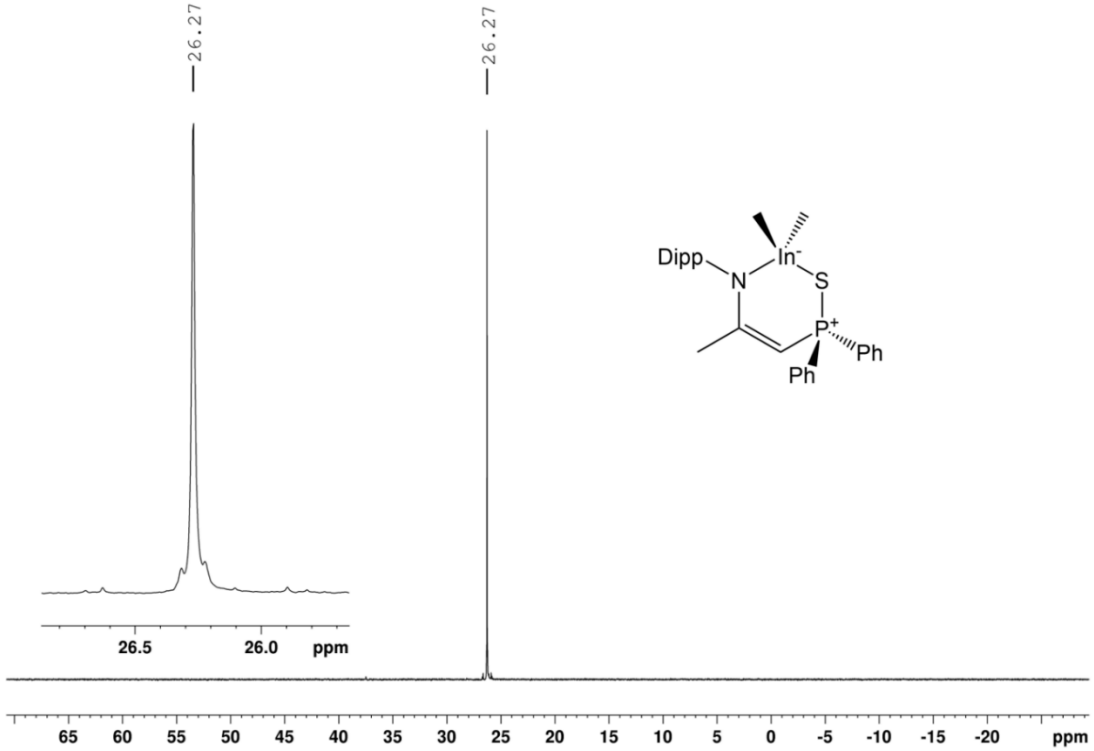

Figure 5.58 $^{31}P\{^{1}H\}$ NMR spectrum of compound **9** recorded at 298K on a 300 MHz Bruker spectrometer in C_6D_6.

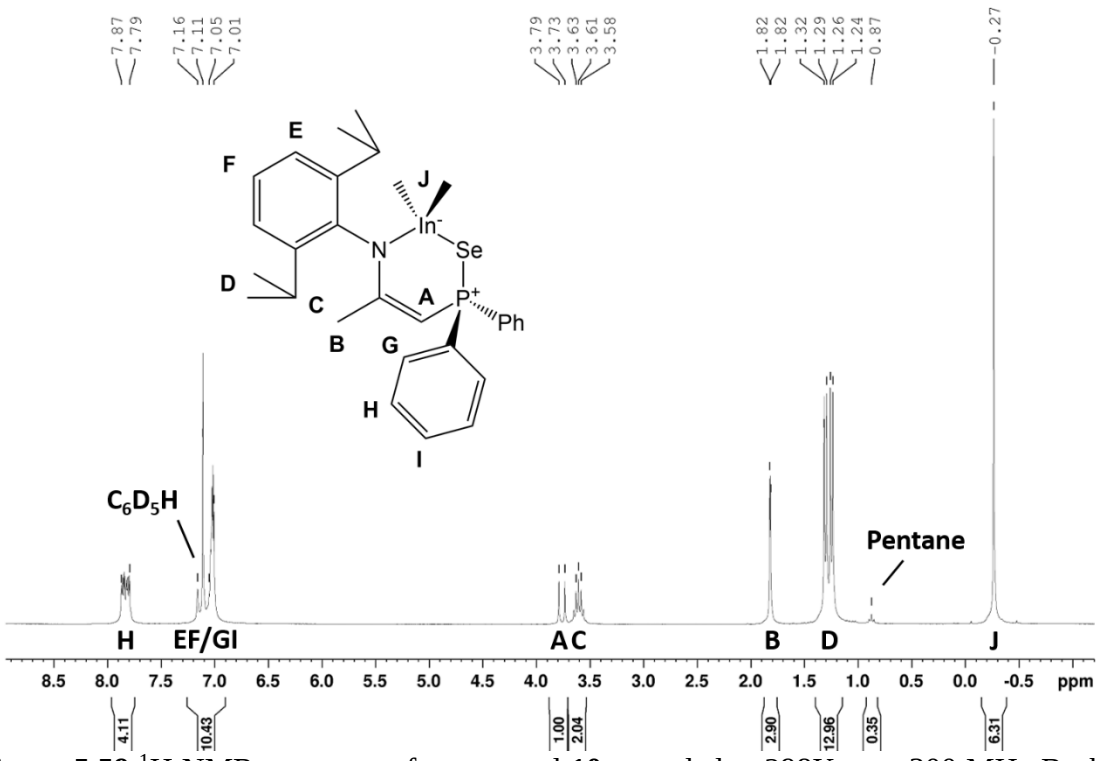

Figure 5.59 ^{1}H NMR spectrum of compound **10** recorded at 298K on a 300 MHz Bruker spectrometer in C_6D_6.

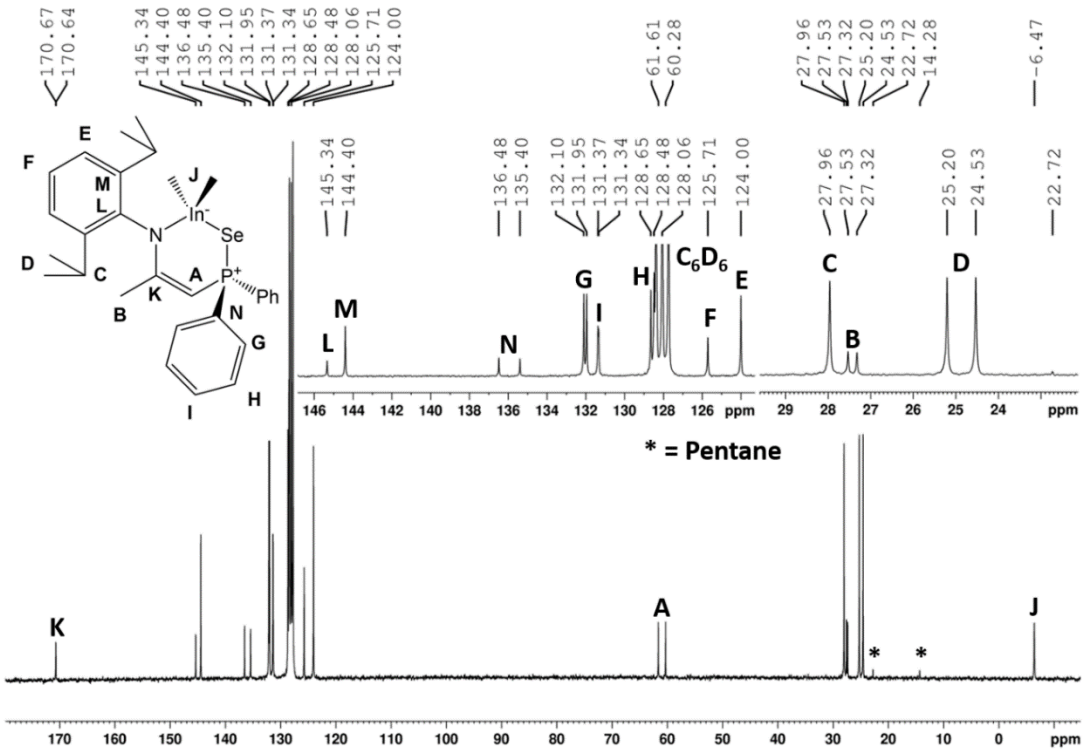

Figure 5.60 ^{13}C NMR spectrum of compound **10** recorded at 298K on a 300 MHz Bruker spectrometer in C_6D_6.

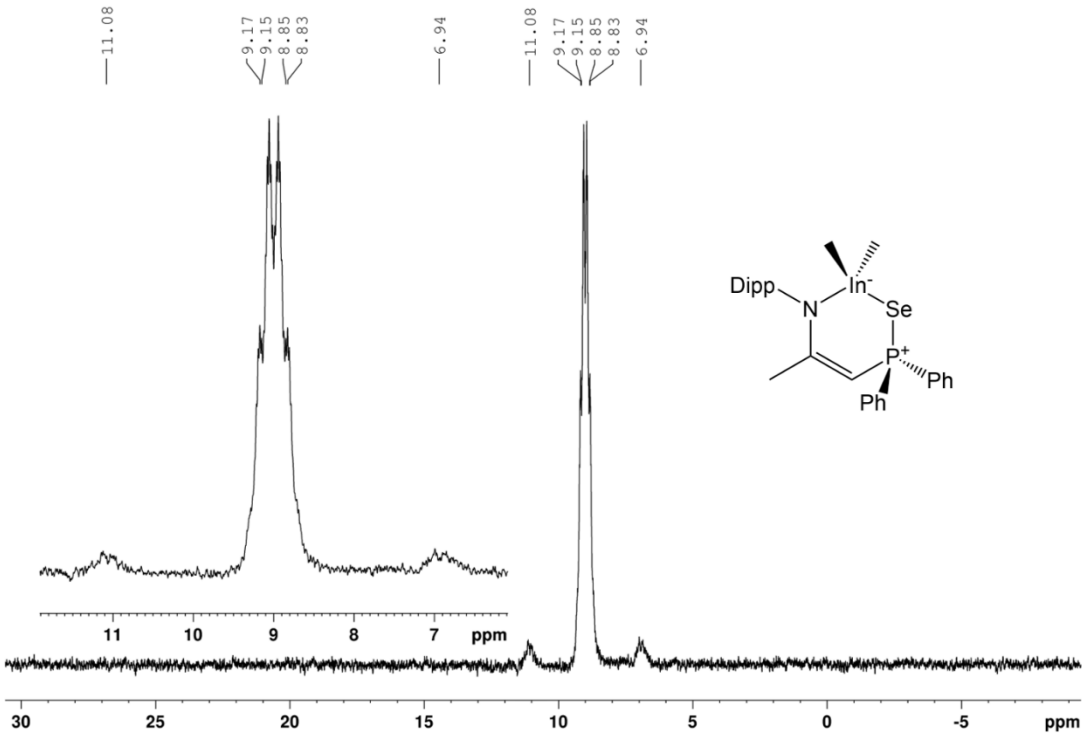

Figure 5.61 ^{31}P NMR spectrum of compound **10** recorded at 298K on a 300 MHz Bruker spectrometer in C_6D_6.

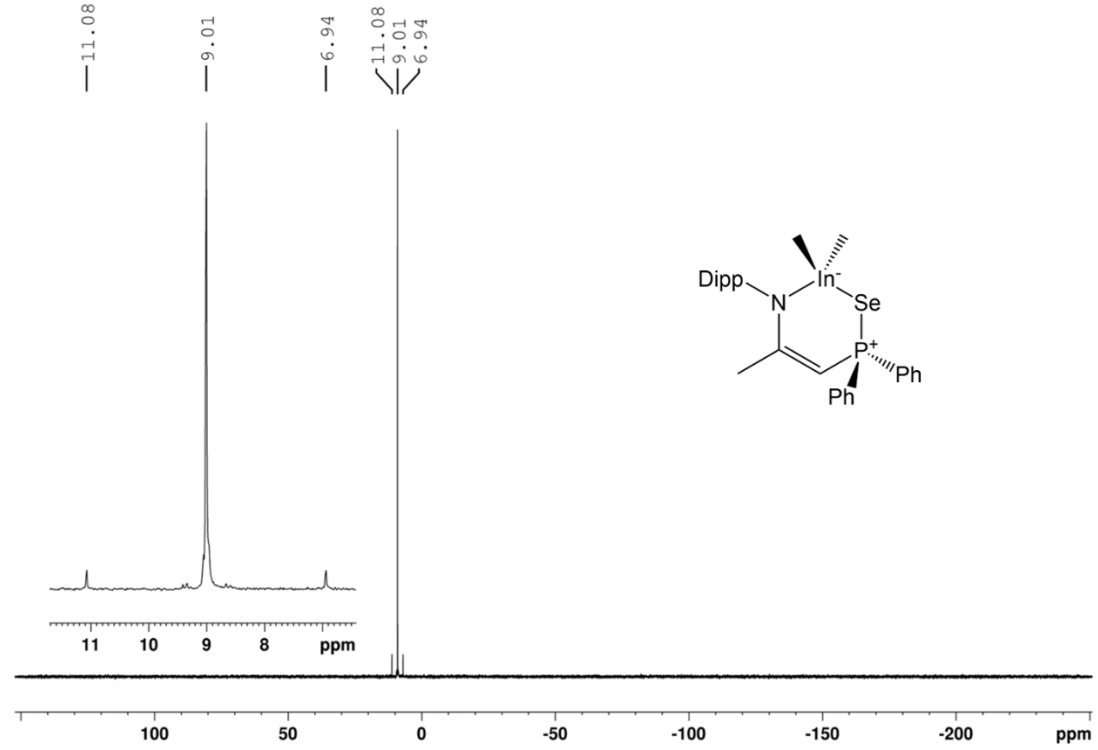

Figure 5.62 $^{31}P\{^{1}H\}$ NMR spectrum of compound **10** recorded at 298K on a 300 MHz Bruker spectrometer in C_6D_6.

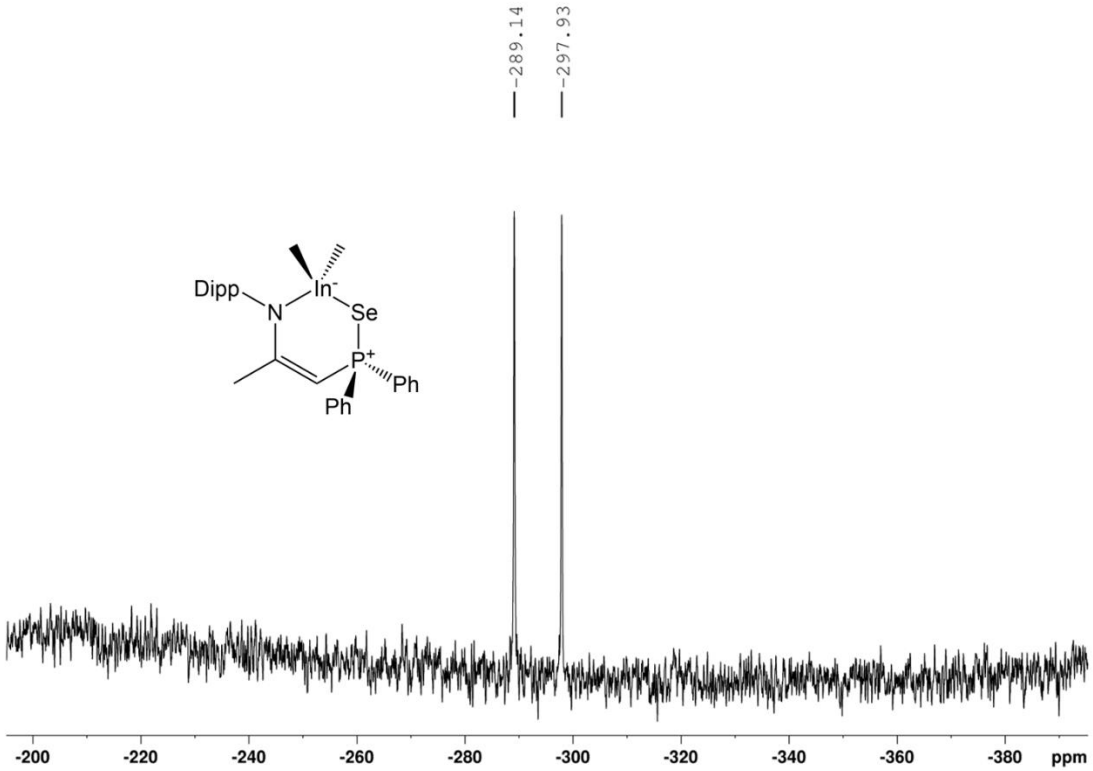

Figure 5.63 ^{77}Se NMR spectrum of compound **10** recorded at 298K on a 300 MHz Bruker spectrometer in C_6D_6.

5.7.3 SC-XRD of Compounds 2-10

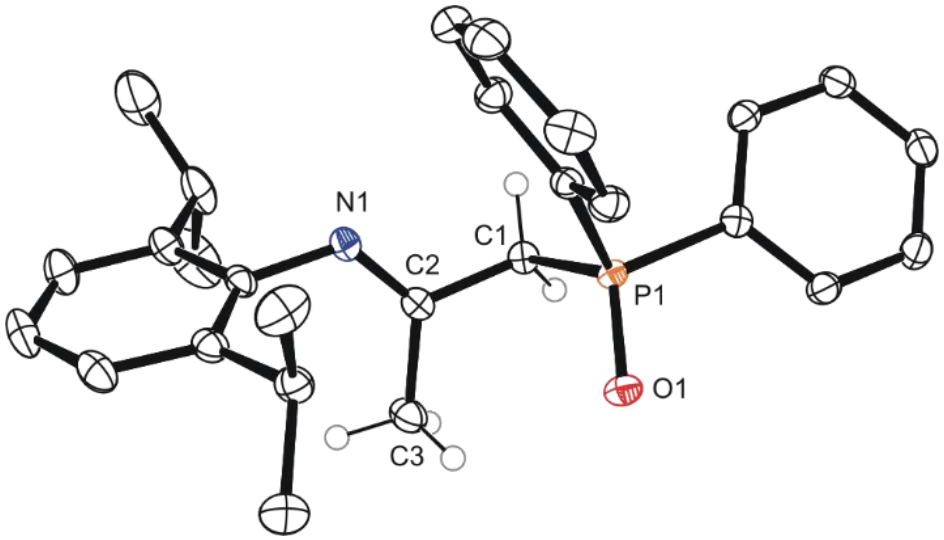

Figure 5.64 Single crystal structure of **2a** (imine isomer) in the solid state. Anisotropic displacement ellipsoids are set to 50 % probability and hydrogen atoms except for C1-H and C3-H are omitted for clarity.

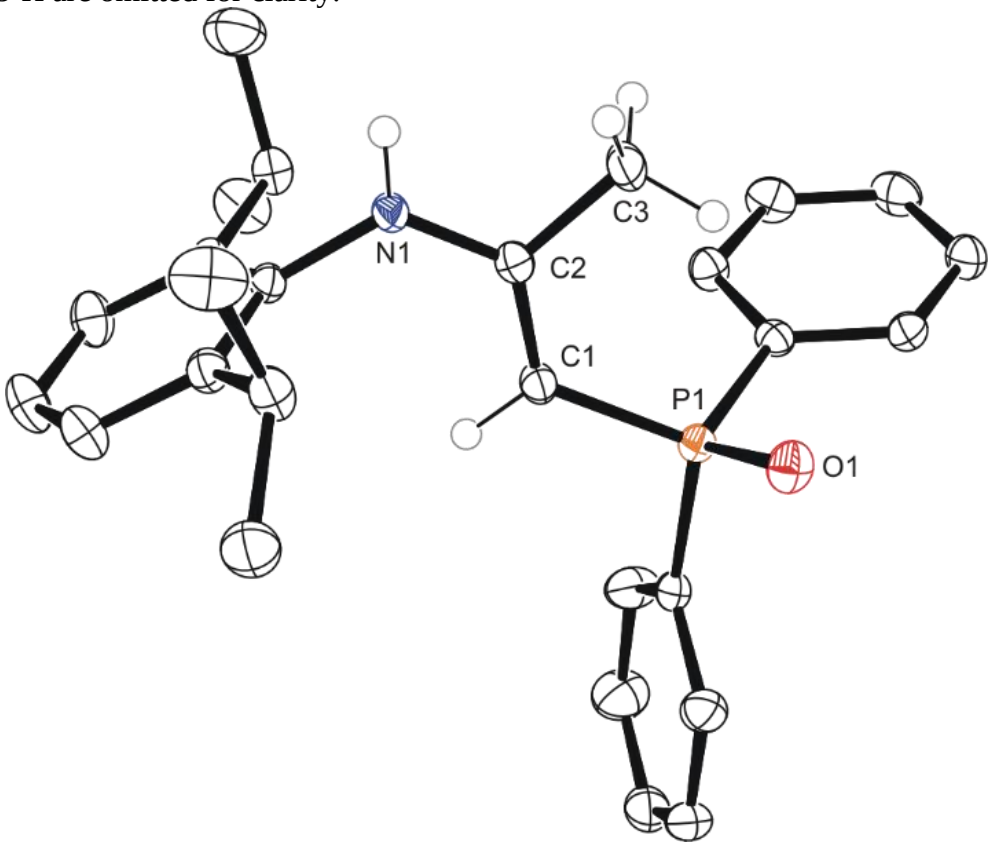

Figure 5.65 Single crystal structure of **2b** ((E)-enamine isomer) in the solid state. Anisotropic displacement ellipsoids are set to 50 % probability and hydrogen atoms except for C1-H and C3-H are omitted for clarity.

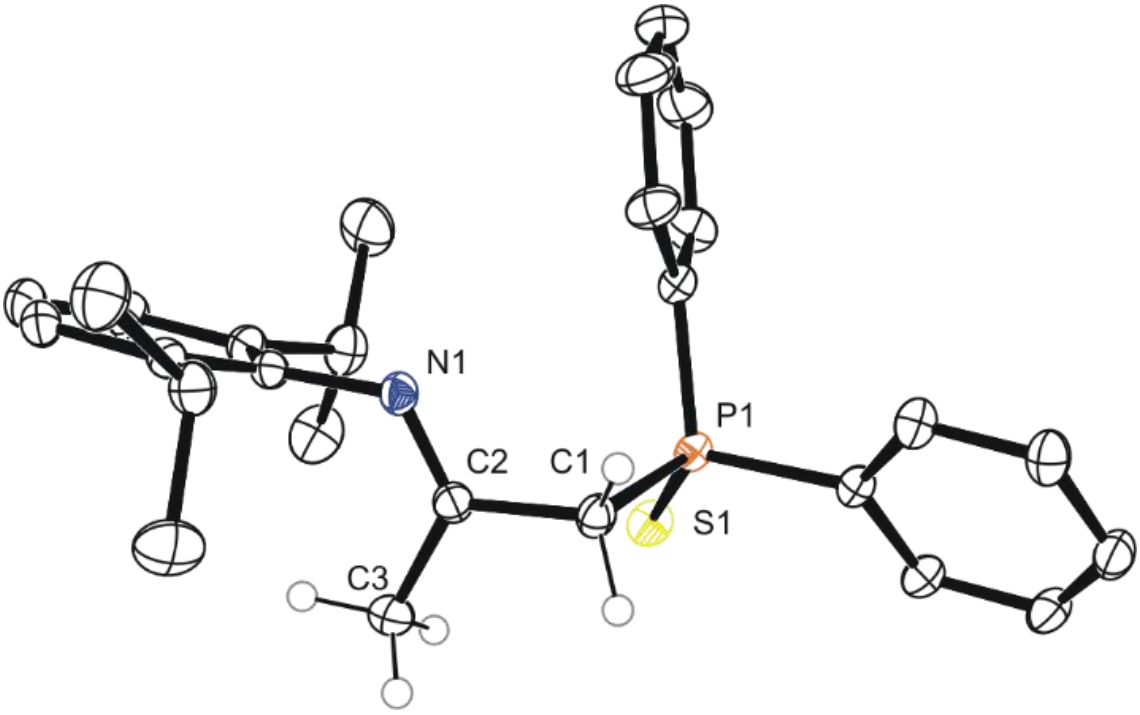

Figure 5.66 Single crystal structure of **3** in the solid state. Anisotropic displacement ellipsoids are set to 50 % probability and hydrogen atoms except for C1-H and C3-H are omitted for clarity.

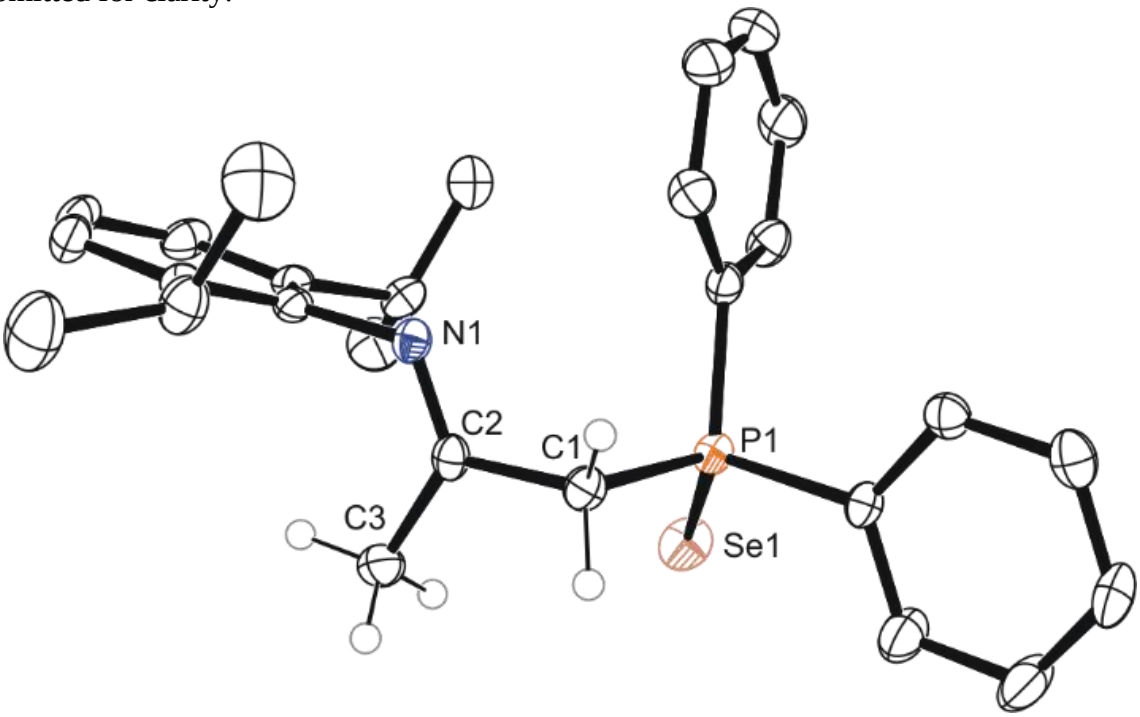

Figure 5.67 Single crystal structure of **4** in the solid state. Anisotropic displacement ellipsoids are set to 50 % probability and hydrogen atoms except for C1-H and C3-H are omitted for clarity.

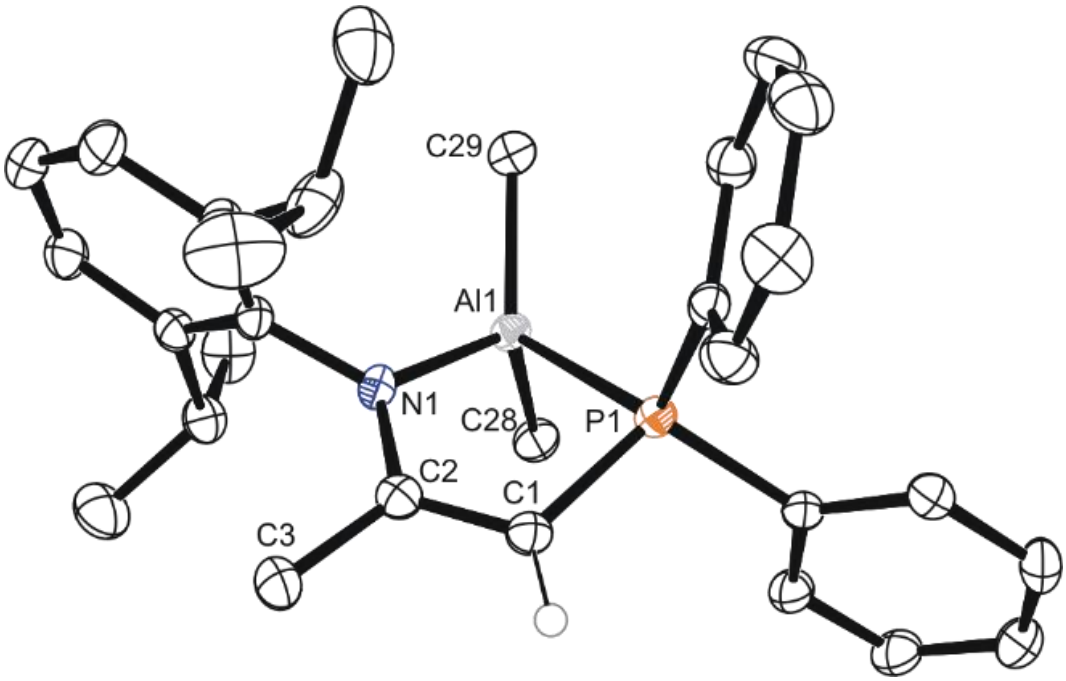

Figure 5.68 Single crystal structure of **1-AlMe2** in the solid state. Anisotropic displacement ellipsoids are set to 50 % probability and hydrogen atoms except for C1-H are omitted for clarity.

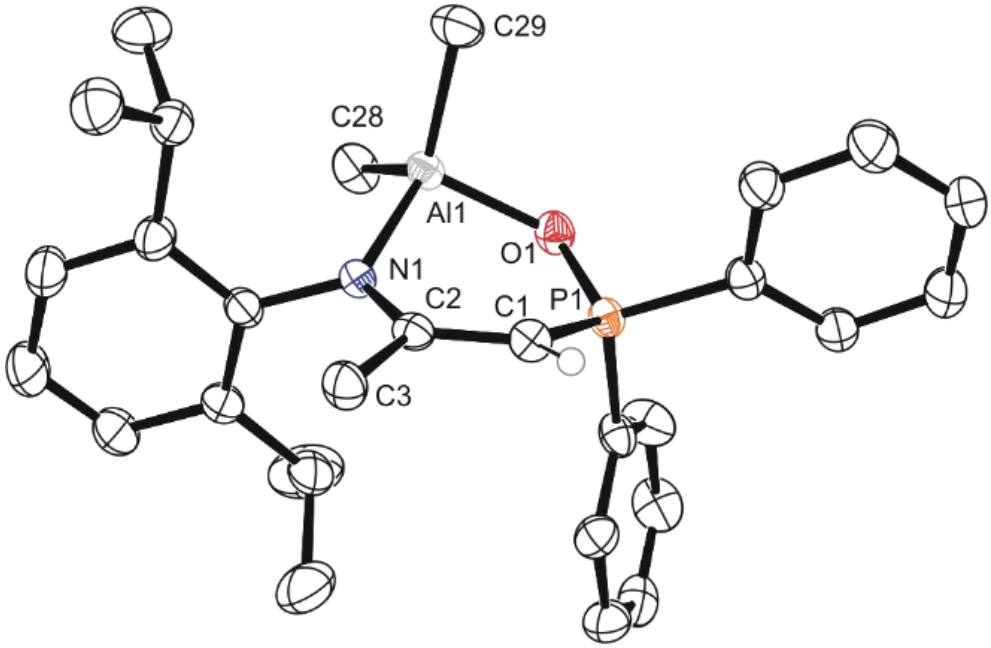

Figure 5.69 Single crystal structure of **5** in the solid state. Anisotropic displacement ellipsoids are set to 50 % probability and hydrogen atoms except for C1-H are omitted for clarity.

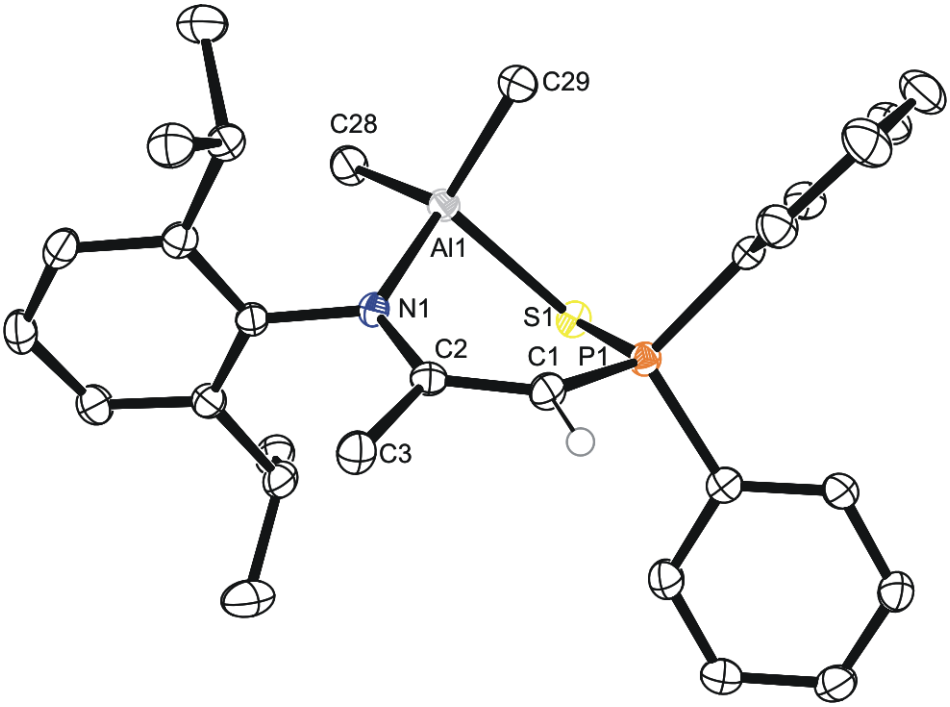

Figure 5.70 Single crystal structure of **6** in the solid state. Anisotropic displacement ellipsoids are set to 50 % probability and hydrogen atoms except for C1-H are omitted for clarity.

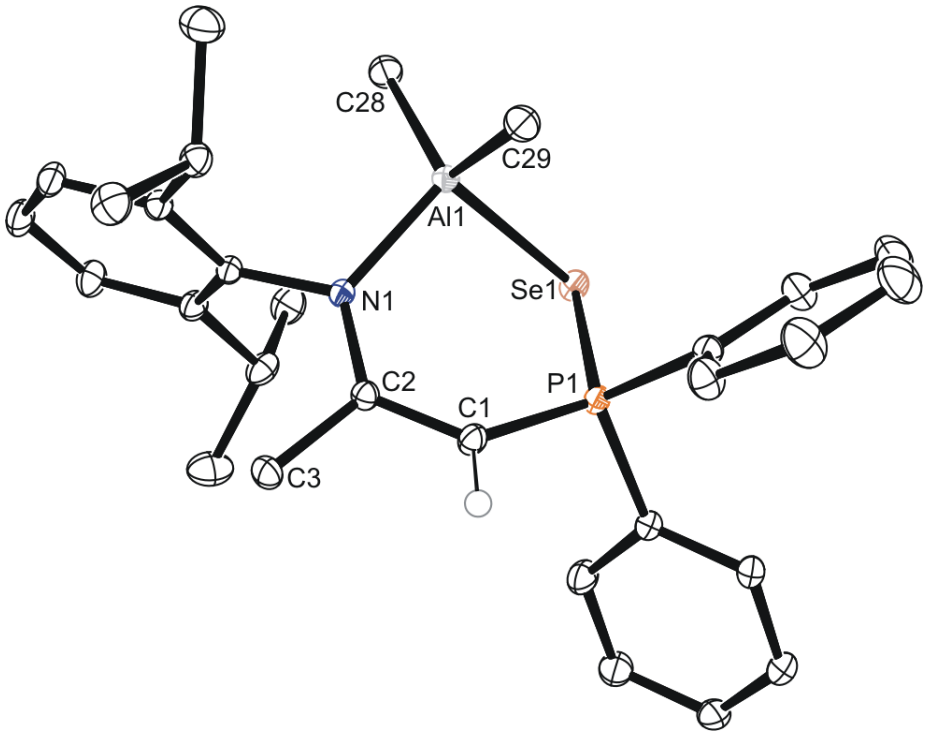

Figure 5.71 Single crystal structure of **7** in the solid state. Anisotropic displacement ellipsoids are set to 50 % probability and hydrogen atoms except for C1-H are omitted for clarity.

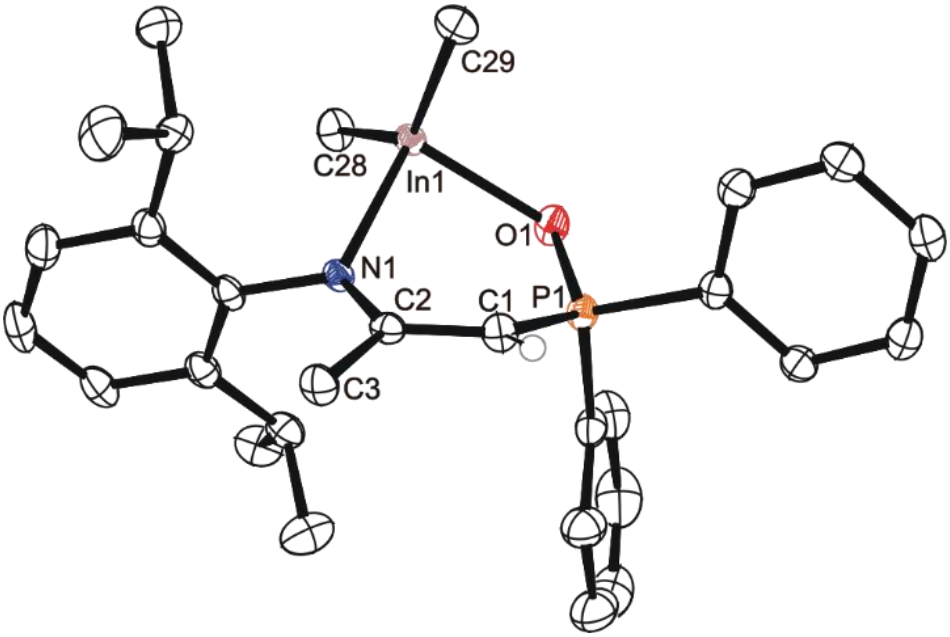

Figure 5.72 Single crystal structure of **8a** in the solid state. Anisotropic displacement ellipsoids are set to 50 % probability and hydrogen atoms except for C1-H are omitted for clarity.

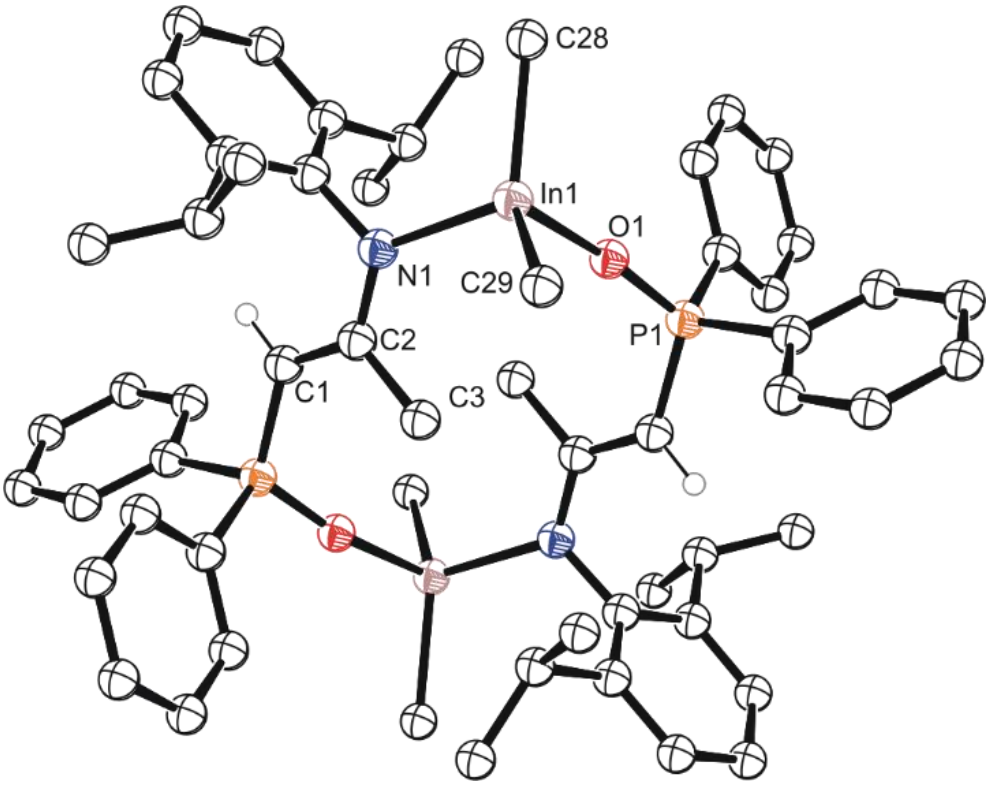

Figure 5.73 Single crystal structure of **8b** in the solid state. Anisotropic displacement ellipsoids are set to 50 % probability and hydrogen atoms except for C1-H are omitted for clarity.

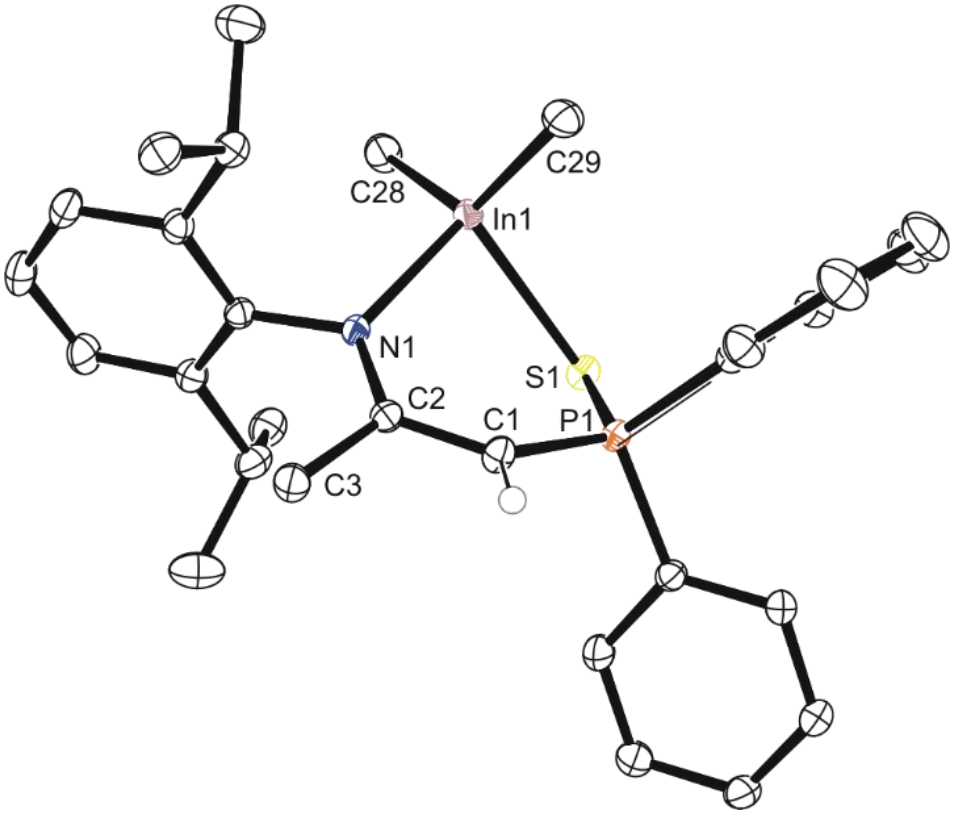

Figure 5.74 Single crystal structure of **9** in the solid state. Anisotropic displacement ellipsoids are set to 50 % probability and hydrogen atoms except for C1-H are omitted for clarity.

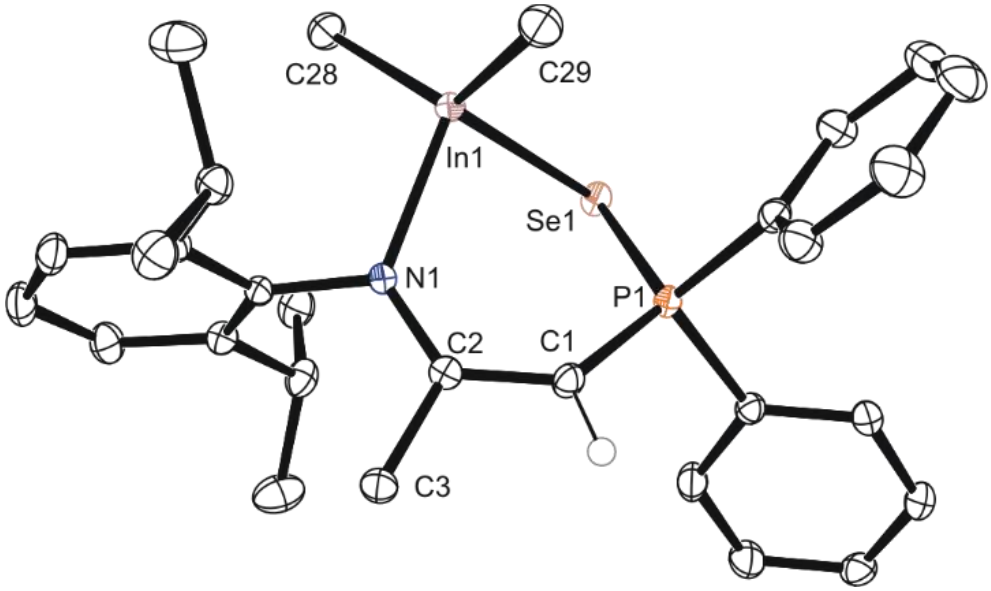

Figure 5.75 Single crystal structure of **10** in the solid state. Anisotropic displacement ellipsoids are set to 50 % probability and hydrogen atoms except for C1-H are omitted for clarity.

5.7.4 Crystallography Table and Additional Refinement Details

Table 4.1 Data derived from single crystal X-ray diffraction of crystals of compounds **2-10** and the dimethyl aluminium chelate of compound **1** from the work in Chapter 5.

Compound reference	**2a**	**2b**	**3**	**4**	**1-AlMe2**	**5**	**6**	**7**	**8a**	**8b**	**9**	**10**
Chemical formula	$C_{27}H_{32}NOP$	$C_{27}H_{32}NOP$	$C_{27}H_{32}NPS$	$C_{27}H_{32}NPSe$	$C_{29}H_{37}AlNP$	$C_{29}H_{37}AlNOP$	$C_{29}H_{37}AlNPS$	$C_{29}H_{37}AlNPSe$	$C_{29}H_{37}InNOP$	$C_{58}H_{74}In_2N_2O_2P_2$	$C_{29}H_{37}InNPS$	$C_{29}H_{37}InNPSe$
Formula Mass	417.50	417.50	433.56	480.46	457.54	473.54	489.60	536.50	561.38	1122.77	577.44	624.34
Crystal system	Monoclinic	Monoclinic	Monoclinic	Monoclinic	Triclinic	Monoclinic	Orthorhombic	Orthorhombic	Monoclinic	Monoclinic	Orthorhombic	Orthorhombic
a/Å	8.5833(3)	12.3073(3)	8.9711(4)	25.7547(14)	9.838(3)	33.496(2)	15.5886(12)	15.4976(3)	8.6720(5)	13.1361(4)	15.7440(7)	15.6585(2)
b/Å	25.7233(8)	9.7254(3)	23.6926(10)	21.8166(12)	10.549(3)	10.7213(7)	16.7550(13)	16.8142(4)	17.5977(8)	14.1548(5)	16.8069(6)	16.9162(2)
c/Å	11.4020(3)	20.0034(4)	12.4579(6)	17.7353(9)	13.541(4)	15.6598(11)	21.2732(17)	21.3983(4)	18.1245(10)	15.2502(6)	21.3702(10)	21.4668(4)
α/°	90	90	90	90	72.135(3)	90	90	90	90	90	90	90
β/°	111.2060(10)	90.1310(10)	110.367(2)	100.0610(10)	81.392(3)	103.480(2)	90	90	95.677(2)	99.9240(10)	90	90
γ/°	90	90	90	90	85.805(3)	90	90	90	90	90	90	90
Unit cell volume/Å^3	2346.99(13)	2394.27(11)	2482.4(2)	9811.9(9)	1321.9(6)	5468.8(7)	5556.3(8)	5576.0(2)	2752.4(3)	2793.18(17)	5654.7(4)	5686.18(14)
Temperature/K	100.0	125.0	125.0	125.46	125.01	125.0	100.0	100.0	125	100.0	100.0	100.0
Space group	$P2_1/c$	$P2_1/n$	$P2_1/c$	$P2_1/c$	$P\bar{1}$	$P2_1/c$	*Pbca*	*Pbca*	$P2_1$	$P2_1/n$	*Pbca*	*Pbca*
No. of formula units per unit cell, *Z*	4	4	4	16	2	8	8	8	4	2	8	8
Radiation type	MoKα	MoKα	MoKα	MoKα	MoKα	MoKα	MoKα	MoKα	MoKα	MoKα	MoKα	MoKα
No. of reflections measured	22736	36507	128850	117506	8868	361528	250697	223922	95735	439311	176943	48155
No. of independent reflections	4290	6023	9447	22525	4866	10011	5098	14895	12036	11172	9844	6914
R_{int}	0.0283	0.0507	0.0318	0.0649	0.0264	0.0774	0.1485	0.0457	0.0244	0.0346	0.0532	0.0198
Final R_1 values ($I > 2\sigma(I)$)	0.0356	0.0405	0.0321	0.0392	0.0403	0.0412	0.0308	0.0289	0.0158	0.0239	0.0255	0.0150
Final $wR(F^2)$ values ($I > 2\sigma(I)$)	0.0870	0.0893	0.0898	0.0781	0.0848	0.1022	0.0746	0.0671	0.0414	0.0630	0.0513	0.0376
Final R_1 values (all data)	0.0384	0.0574	0.0354	0.0757	0.0570	0.0509	0.0458	0.0398	0.0160	0.0261	0.0392	0.0165
Final $wR(F^2)$ values (all data)	0.0888	0.0998	0.0925	0.0901	0.0931	0.1108	0.0827	0.0711	0.0416	0.0654	0.0603	0.0383

Compound **2b** is the (E)-enamine isomer of **2**. In the crystal structure hydrogen bonding between the donor N1-H and acceptor O1 across the symmetry element 0.5-X,0.5+Y,1.5-Z and 0.5-X,-0.5+Y,1.5-Z is observed forming a chain structure. The C3 methyl group in this structure is modelled with two component rotational disorder about the C3-C2 bond in a 59:41 ratio.